Universitat de Lleida

Availability of metal ions and ZnO nanoparticles in aqueous media

Sara Cruz González

Universitat
de Lleida

Availability of metal ions and ZnO nanoparticles in aqueous media

Memoria presentada por Sara Cruz González para optar al grado de

Doctora por la Universitat de Lleida

Trabajo realizado en el Departamento de Química de la Universitat

de Lleida bajo la dirección del Dr. Jaume Puy i Llorens y el Dr. Carlos Rey Castro

Lleida, marzo del 2015

A todas las personas que han estado a mi lado

Agradecimientos

La realización de esta tesis ha podido ser posible gracias al apoyo incondicional de muchas personas, por ello, me gustaría mostrar mis agradecimientos a todas y cada una de ellas:

A la Universidad de Lleida y el Ministerio de Economía y Competitividad por la el soporte económico recibido para la realización del presente trabajo, a través de la concesión de la beca de Formación de Personal Investigador y de las ayudas para la realización de actividades complementarias de investigación y formación.

A mis directores de tesis: el Dr. Jaume Puy y el Dr. Carlos Rey, por ser mis mentores durante estos 4 años de formación. Les doy las gracias por su constante apoyo, ánimos, sus sabios consejos y por haber atendido a todas mis dudas solucionando todo tipo de problemas que han surgido en el desarrollo de la tesis doctoral, lo cual me ha permitido realizar con éxito todo este trabajo. Les tengo que agradecer profundamente tanto el hecho de haberme ayudado en el ámbito profesional como en el personal, puesto que han demostrado en todo momento tener una excelente calidad humana, por ello, os doy las gracias.

A la resta de profesores del grupo, Josep, Pepe y Encarna por su completa disposición a resolver cualquier problema que se haya podido plantear.

A las personas con las que he compartido el día a día en el laboratorio. Mireia, David, Calin, Diana y Sandrine. Mireia y David, mis apoyos, confidentes, con quienes he compartido los mejores y peores momentos de estos años…por ello os considero unos grandes amigos, cada uno de vosotros sabéis lo que significáis para mí :), siempre os llevaré en mi corazón. A Calin por ser un compañero y persona excelente, el cual me ha ofrecido su desinteresada ayuda durante el trabajo diario, mostrándose accesible en todo momento, siempre con una sonrisa, siendo capaz de solucionar cualquier tipo de problema, muchas gracias ;). A aquellas personas que formaron parte de esta etapa temporalmente, aunque dejaron una gran huella, Mayela y en especial a Daniela por todos los buenos momentos que pasamos.

A mi amigo Ferran por haber estado siempre a mi lado, por saber escuchar cuando ha sido necesario, por sus buenos consejos y por todas las risas que hemos compartido durante estos 4 años… Me llevo un gran amigo al que siempre tendré presente y espero forme parte de mi vida.

También agradecer a las nuevas generaciones: Marjan, Martín y Alex, sus ánimos, consejos y optimismo.

A los compañeros de la Facultad de Agrónomos y en especial a los del laboratorio de orgánica, Olalla, Anna, Silvia, Albert, Pau, Toni, Alexis y Edinson y a aquellos que han emprendido otros caminos, por su amistad, por los buenos momentos que he pasado en su compañía y por haber ofrecido su ayuda siempre que ha sido necesario.

A todo el personal de los Servicios Científico-técnicos, en especial a Silvia, Mireia y Maria por su total colaboración, ayuda y paciencia.

Finalmente, agradecerle a mi hermano Juan Manuel por haber confiado en mi capacidad para finalizar este trabajo y animarme hasta el final, a mis padres por apoyarme en todas las decisiones que he tomado a lo largo de la vida, hayan sido buenas o malas, y enseñarme a luchar por lo que quiero, a mi abuela por haber estado siempre a mi lado y seguir estándolo allí donde esté… y en especial a Jay, por su apoyo, sus ánimos, su optimismo, por sacarme una sonrisa en los peores momentos, además de su paciencia por las ausencias a cualquier día y hora del año.

Muchas gracias a todos por haber formado parte de esta etapa de mi vida, la cual no olvidaré jamás…

Summary

The presence of certain metals, either in the form of free metal, forming complexes with ligands or as nanoparticles has negative effects on the environment. For this reason, the study of the availability of metals is important in determining its environmental impact.

In this work a technique for measuring availability has been studied and applied to a particular system. This system contains metal oxide nanoparticles in dispersion. A first part of the study focuses on the physical and chemical characterization of synthetic dispersions of nanoparticles. This part examines the effect of environmental conditions (pH, salinity, organic matter content, etc.) in the behavior of ZnO nanoparticles. Processes such as aggregation, solubilisation and sedimentation, are studied as a function of environmental conditions. All these processes play an important role in the fate of nanoparticles and their toxicity.

The second part of this thesis focuses on the application of the analytical technique DGT (Diffusive Gradients in Thin films) for measuring the flux of available metals in aqueous solutions. In the present study, the metal availability in aqueous dispersions of nanoparticles has been determined and compared with the solubility at equilibrium. Moreover, the DGT technique has been studied from a physical-chemical point of view. The contribution of complexes to the overall metal flux has been evaluated with a parameter, the lability degree, which takes into account the dissociation constants of the complexes and their diffusion coefficients. The accumulations of metals which in solution are present predominantly as electrically charged complexes have been studied. If this charge is negative, the accumulation decreases with the decrease of the ionic strength (and vice versa in the opposite case). This phenomenon is explained by the electrostatic repulsion between the negatively charged resin disk and the complex when it is partially labile. In conclusion, the resin seems to play a more active role in the accumulation of metals in DGT than previously thought.

Resum

La presència de determinats metalls, ja sigui en forma del metall lliure, formant complexos amb lligands o en forma de nanopartícules té efectes negatius en el medi ambient. Per aquest motiu, l'estudi de la disponibilitat de metalls és important per determinar el seu impacte mediambiental.

En aquest treball s'ha estudiat una tècnica per a la mesura de la disponibilitat i s'ha aplicat a un sistema en particular, consistent en dispersions de nanopartícules d'òxids metàl·lics. Una primera part de l'estudi, doncs, s'enfoca a la caracterització físic-química d'aquestes dispersions sintètiques de nanopartícules. Aquesta part estudia l'efecte que tenen les condicions del medi (pH, salinitat, contingut de matèria orgànica, etc.) en el comportament de nanopartícules de ZnO. S'han determinat processos com són l'agregació, solubilització i sedimentació, en funció de les condicions del medi. Tots aquests processos juguen un paper important en el destí de les nanopartícules i en la seva toxicitat.

La segona part d'aquesta tesi es centra en l'aplicació de la tècnica analítica DGT (Diffusive Gradients in Thin films) per la mesura de fluxos de metall disponibles en solucions aquoses. En el present treball, s'ha determinat la disponibilitat de metall en dispersions aquoses de nanopartícules i s'ha comparat amb la solubilitat en equilibri. Per altra banda s'ha estudiat la tècnica DGT des d'un punt de vista físic-químic. Les contribucions dels fluxos de complexos s'avaluen amb un paràmetre que té en compte les constants de dissociació dels complexos així com la seva difusió. S'han estudiat les acumulacions de metalls que en solució tenen com especies dominants complexos carregats elèctricament. Si aquesta càrrega és negativa, l'acumulació disminueix en baixar la força iònica (i a l'inrevés en el cas contrari). Aquest fenomen s'explica per la repulsió electrostàtica entre la càrrega negativa del disc de resina i el complex quan aquest és parcialment làbil. En conclusió, la resina sembla jugar un paper més actiu del que es pensava en l'acumulació de metalls en DGT.

Resumen

La presencia de determinados metales, ya sea en forma del metal libre, formando complejos con ligandos o en forma de nanopartículas tiene efectos negativos en el medio ambiente. Por este motivo, el estudio de la disponibilidad de metales es importante para determinar su impacto medioambiental.

En este trabajo se ha estudiado una técnica para la medida de la disponibilidad y se ha aplicado a un sistema en particular, consistente en dispersiones de nanopartículas de óxidos metálicos. Una primera parte del estudio se enfoca, pues, a la caracterización físico-química de dichas dispersiones sintéticas de nanopartículas. Esta parte estudia el efecto que tienen las condiciones del medio (pH, salinidad, contenido de materia orgánica, etc) en el comportamiento de nanopartículas de ZnO. Se han determinado procesos como son la agregación, solubilidad y sedimentación, en función de las condiciones del medio. Todos estos procesos juegan un papel importante en el destino de las nanopartículas y en su toxicidad.

La segunda parte de esta tesis se centra en la aplicación de la técnica analítica DGT (*Diffusive Gradients in Thin films*) para la medida de flujos de metal disponibles en soluciones acuosas. En el presente trabajo, se ha determinado la disponibilidad de metal en dispersiones acuosas de nanopartículas y se ha comparado con su solubilidad en equilibrio. Por otra parte se ha estudiado la técnica DGT desde un punto de vista físico-químico. Las contribuciones de los flujos de complejos se evalúan con un parámetro que tiene en cuenta las constantes de disociación de los complejos así como su coeficiente de difusión. Se han estudiado las acumulaciones de metales que en solución tienen como especies dominantes complejos cargados eléctricamente. Si esta carga es negativa, la acumulación disminuye al bajar la fuerza iónica (y viceversa en el caso contrario). Este fenómeno se explica por la repulsión electrostática entre la carga negativa del disco de resina y el complejo cuando éste es parcialmente lábil. En conclusión, la resina parece jugar un papel más activo de lo que se pensaba en la acumulación de metales en DGT.

Table of contents

Chapter 1. Introduction

Chapter 2. Behavior of ZnO nanoparticles in aqueous media

Chapter 3. Interaction of ZnO nanoparticles with dissolved organic matter

Chapter 4. Determination of the DGT-labile fraction of zinc in dispersions of nano-ZnO

Chapter 5. Measurement of Metals Using DGT: Impact of Ionic Strength and Kinetics of Dissociation of Complexes in the Resin Domain

Chapter 6. Additional evidences of kinetic and electrostatic effects on DGT devices

Chapter 1

Introduction

1.1. Nanoecotoxicology

Nanoecotoxicology is referred to the study of the toxicological effects of nanomaterials on the ecosystems, which integrates nanomaterials, ecology and environmental chemistry.

Due to the rapid development of nanotechnology in the recent years, the industrial production and use of nanomaterials, *i.e.*, materials with one or more dimensions in a submicron scale (nanoparticles, nanorods, etc.) is greatly increasing. These substances possess a number of advantageous features that make them particularly interesting in a number of industrial applications (*1*,*2*). Due to these properties and its widespread use, it is expected that significant quantities of nanomaterials will be released into the natural environment, where their behavior (for example, interaction with living organisms) and fate are largely unknown (*3*).

Nowadays, there is a growing concern among health and safety regulators in the EU and other countries, to develop laws and methods of risk assessment including toxicological and environmental impact of nanomaterials (*4*). This concern has resulted in the development of funding mechanisms for public research in the area of nanosecurity, such as the EU ENNSATOX project ("Engineered Nanoparticle Impact on Aquatic Environments: Structure, Activity and TOXicology", www.ennsatox.eu), and the CTM2009-14612-C02-01 project from the Spanish Ministerio de Economia y Competitividad, which are the frameworks in which part of this work has been developed.

1.1.1. Characteristics of nanomaterials

The most common engineered nanomaterials belong to one of these five groups: carbon nanomaterials, metal oxide nanoparticles, zero-valence metal nanoparticles, quantum dots (QDs) and dendrimers (*5*).

The present work is focused on metal oxide nanoparticles (NPs). Nano is a prefix referred to extremely small, 10^{-9} m. Nanomaterials are defined as materials with at least one dimension below 100 nm. The current opinion of the European Commission on the definition of nanomaterials (Official Journal of the European Union, recommendation 2011/696/EU) states that: "*Nanomaterial* means a natural, incidental or manufactured material containing particles, in an unbound state or as an aggregate or as an agglomerate and where, for 50 % or more of the particles in the number size distribution, one or more external dimensions is in the size range 1 nm-100 nm". The Commission recognizes that 100 nm "is commonly used by general consensus, but there is no scientific evidence to support the appropriateness of this value". There is no unequivocal scientific basis to justify this 50% fraction in the particle size distribution either, but this value is adopted as a convention for use in a regulatory context.

The physico-chemical properties of NPs are some of the most important factors that regulate their behavior in the environment (*6*). These properties are attributable to their nanosized dimensions (large specific surface area and small size distribution), chemical composition (purity, crystallinity, electronic properties), surface structure (surface reactivity, surface groups, inorganic or organic coatings), solubility, shape, aggregation, etc. (*7,8*). The high surface to volume ratio makes NPs potentially more reactive than larger particles. Properties like solubility, transparency, colour, conductivity, melting points and catalytic behavior may depend on the particle size.

Despite the success of nanotechnology, ecotoxicological data are just emerging. There is a lack of information about the potential health and environmental risks associated with NPs (*9,10*). Some recent studies have focussed on the behavior of NPs in the environment and their ecotoxicology (*11-15*). These works also try to determine whether the toxicological effects are due to the NPs themselves, to the dissolved metal fraction released from them, or both. For instance, Morones *et al*. (*16*) have shown that bactericidal (to Gram-Negative bacteria) properties of the AgNPs were related mainly to direct effects of particles, which were found to accumulate intracellularly and at the cell membrane. Buffet *et al*. reported ecotoxicity effects to marine invertebrates that seem to be related to Cu NPs themselves (*17*). Some other authors affirm that the effect is related to the dissolved ions, such as Ma *et al*. (*18*). While other studies, like the one published by Navarro *et al*. (*19*), conclude that free Ag^+ plays an important role for the toxicity of AgNP but also significant interactions of nanoparticles with algae were found. Nevertheless, further studies are needed to evaluate the nanoecotoxicology of these relatively novel materials.

1.1.2. Metal oxide nanoparticles. Uses and applications

Data on the production of engineered nanomaterials estimate that the production of engineered nanomaterials was 2.000 tons in 2004 and is expected to increase to 58.000 tons between 2011 and 2020 (*20*).

In the report "The Nanotechnology Consumer Products Inventory" (*21*), the most common type of nanomaterial mentioned was carbon, which included fullerenes and nanotubes. Silver was the second most referenced (25 products), followed by silica (14), titanium dioxide (8), zinc oxide (8), and cerium oxide (1). These nanomaterials are being used in a variety of areas such as electronic, cosmetic, pharmaceutical, biomedical and catalytic applications, among others.

Metal oxide NPs are some of the most commonly used nanomaterials (*1*,*2*). For instance, Al_2O_3 derivatives are widely employed for catalysis or to improve the mechanical characteristics of different materials (*5*). ZnO and TiO_2 are also broadly exploited in sunscreens, cosmetics and coatings, due to their ultraviolet absorption properties. Iron oxide nanoparticles (Fe_2O_4 and Fe_2O_3) are used for biomedical applications and manufacturing of pigments.

Other relevant metal oxide NPs are based on cerium dioxide (CeO_2), chromium dioxide, (CrO_2), molybdenum trioxide (MoO_3), bismuth trioxide (Bi_2O_3) and binary oxides (e.g., lithium-cobalt dioxide ($LiCoO_2$) or indium-tin oxide (ITO)). CeO_2 is finding major uses as a combustion catalyst in diesel fuels to improve emission quality (*22*) as well as in solar cells, gas sensors, oxygen pumps, and metallurgical and glass or ceramic applications.

In the past few years, ZnO nanoparticles (nano-ZnO), on which this work is focused, have attracted the attention of researchers because of their properties. Nano-ZnO is a semiconductor that can be introduced in optoelectronic and electronic devices and in a wide range of other products due to their function as UV absorber (sunscreens, personal care products, textiles, paints, industrial coatings, antibacterial agents, wastewater treatments, electronic components, etc.) (*23*-*26*).

1.1.3. Interaction with aqueous environment

NPs are present in the environment through intentional as well as unintentional releases such as atmospheric emissions and solid or liquid waste streams. The entry of nanomaterials may be by anthropogenic and natural causes (*6*). Incidental emissions coming from anthropogenic sources are due to industrial and nanotechnological activities (*12*) as well as combustion processes in diesel and gasoline-fueled vehicles, while natural emissions come from volcanic eruptions, forest fires, biological processes, and physical and chemical weathering, among other sources.

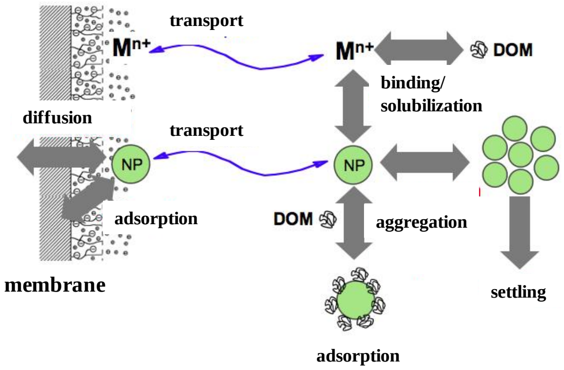

Figure 1.1. Conceptual overview of the environmental fate processes of metal oxide nanoparticles in aqueous media.

Once in the aqueous media, metal oxides are often unstable and may lead to the formation of larger aggregates and agglomerates (*27*). The kinetics of aggregation in these systems depends on environmental conditions such as pH, salinity, particle concentration, etc. Given the relatively high density of these materials compared to the water, aggregates may settle more or less rapidly, depending on its structure (porosity). Moreover, metal oxide NPs can also solubilize and the existence of organic matter in natural waters, or proteins in biological media (*28*), may result in the formation of organic coatings on the NPs (due to the large specific surface area), which alter their surface charge, hydrophobicity, etc., which in turn affects the processes of aggregation, sedimentation, and finally their persistence in the aqueous media. All the above phenomena (solubilisation, aggregation, transport) are interrelated, and they largely condition the transport of NPs on the aqueous media. These environmental transformation processes are represented in Figure 1.1.

Nanoparticles could also interact with microorganisms or even be toxic to them, and may give rise to bioaccumulation in the food chain and arrive to humans. Humans can be either directly influenced by NP through exposure to air, soil or water or, indirectly, by consuming plants or animals which have accumulated NP. Health effects are still being investigated (*29*).

1.1.4. Relevance of physicochemical characterization of nanoparticles for bioavailability and toxicological studies

Many bibliographic examples show that, in conventional toxicological assays, NPs can aggregate and change their physical characteristics when they are exposed to different culture media (*30*), which makes it very difficult to estimate the real dose at which the organism or tissue is exposed. The usual procedure in the *in vitro* experiments with plated cells is to add an aliquot of the liquid dispersion of NPs to the culture media in contact with the tissue and incubate the sample for a defined period of time. The effect on cell viability depends on the exposure of cells to the amount of NPs (mass, number, area, etc.) that comes into contact with the cell per unit time. In general, it is assumed that the suspensions are well dispersed and stable in the culture media as a result of diffusion (Brownian motion), so that the concentration of nanoparticles in the solution boundary layer in contact with the cell surface is assumed to be the same as the initial concentration in the culture media. In the case that this assumption does not hold, the real exposure dose would be completely different from the one estimated in homogeneous conditions.

For example, in the case that the nanoparticles settle within the time scale of the experiment, the total concentration of NPs close to the cell surface may be greater than the initial concentration, which could lead to an increased cellular uptake, as has been shown in a recent study published in Nature (*31*), where uptake of gold NPs is compared between identical cultures exposed to the same dispersion but in opposite orientations (standard or inverted). Since cellular uptake is directly related to the concentration of nanoparticles (*32*), the results of studies that do not consider the transport and aggregation could be inaccurate.

To cite another example, we can mention the work of Wittmaack (*33*) about the effect of sedimentation on the uptake of NPs of different metal oxides by LA-4 mice cell cultures. For this study, it was used NPs from commercially available powder, which showed numerous micron sized aggregates after ultrasonication in water or in cell culture media. The sonicated nanoparticles sedimented rapidly in all the aqueous media tested. At the bottom, the probability of contact of the particles with the cells could be enhanced by a factor of more than 1000 compared to the theoretical concentration of NPs (assuming homogeneous dispersion).

These high levels of exposure may lead to overload effects, which are often misinterpreted as evidence of cytotoxicity. Although recent theoretical studies have considered the effect of sedimentation and diffusion of nanoparticles on the dosimetry (*34*), there are still not many data on the comparison with experimental results.

Moreover, the aggregation kinetics of NPs can take place in a time scale comparable to the sedimentation and diffusion processes, which means that the size and density of the nanoparticles may also vary during the experiments. However, the model mentioned above (*34*) does not include either aggregation kinetics or the polydispersity of the sample. In the literature on NP toxicity tests, the experimental procedures described often do not include the aggregation state of the NPs in the culture media during the time of contact with the tissues or microorganisms, with the exception of recent studies (*35*). The latter work is one of the first studies to examine the effect of the aggregation of gold NPs in the cellular uptake. The authors prepared different aggregated samples that mimicked the progressive aggregation of NPs in biological media. They concluded that the absorption patterns are different between individual nanoparticles and aggregates. There was a 25 % decrease in the uptake of nanoparticles added to HeLa and A549 cells compared to the individual and monodisperse nanoparticles. However, there was an increased uptake of 2 times in MDA-MB 435 for larger aggregates. These results suggest that the cell type and the mechanism of interaction may play an important role. However, predicting the response of a cell to a sample of heterogeneous and asymmetric aggregates is difficult since it depends on a number of parameters such as receptor expression, the endocytosis mechanism and the cell phenotype.

Finally, as mentioned above, there is a debate about whether the toxicity of soluble NPs is due to their nanoscale properties, or rather to the ions released in the solution. Also, the release of metal ions from the NPs follows a time course that is generally unknown. However, the experimental study of the solubility is hampered by the fact that the separation of the particles from the liquid phase is often difficult due to the extremely small size of the NPs.

1.1.5 ZnO nanoparticles

The nanomaterials on which this research work is focused are synthetic ZnO nanoparticles (nano-ZnO), a relatively common nanomaterial which is being incorporated in a wide range of products. Simultaneously with the development of new nano-ZnO applications, the study of the toxicity of these NPs has been increasing. In recent years, researchers have been studying various adverse effects of these NPs in bacteria, alga, phytoplankton, plants (*36,37*), fish and human cell lines (*38-41*) using *in vitro* (*42,43*) and *in vivo* tests (*39,44,45*). Compared with other NPs, ZnO has often been found to be among the most toxic (*46,47*). To cite an example, in a recent study of acute toxicity in *E. coli* versus seven different metal oxide nanoparticles, Hu *et al*. (2009) (*48*), have found that ZnO had the highest toxicity, with a 50% lethal dose (LD_{50}) of 21.1 mg L^{-1}.

In order to assess the environmental and toxicological risks of these nanomaterials, it is essential to study, first, how they are transported and transformed in the environment, culture media and biological fluids (*28,49*). This information is essential for the development of models to estimate how much of these materials reach the living organisms and interact with them to cause adverse effects (*34,50,51*).

In the particular case of ZnO NPs, the significant release of free Zn^{2+} ions may play an important role in the toxic effects of these NPs (*39,52*). Adam *et. al.* (*52*) concluded that the toxicological effects of ZnO nanoparticles at the chronic level could be largely attributed to the dissolved fraction rather than the nanoparticles or initially formed aggregates. Nevertheless, other studies suggest that both NPs and free Zn^{2+} ions have a toxic effect, but with different modes of action (*53*).

Even today it is not fully clarified what is the relative role of the particles themselves and their released metal ions on the overall toxic effect of nano-ZnO.

The behavior of ZnO NPs, both in natural water and in culture media, depends on its specific physicochemical properties (electrostatic charge, solubility, specific surface area, etc.). These properties, in turn, depend on pH, salinity and dissolved organic matter of the media, etc.

To understand the aggregation and settling of different nanoparticles under environmentally relevant conditions some studies have been performed (*54,55*). The influence of particle size and pH on the solubility (*56,57*) has been studied, as well as the influences of organic and inorganic ligands on the sedimentation and other physical effects that determine the environmental fate and toxicological implications. Recently, in our work group, it has been developed an electroanalytical technique, AGNES, which has been used to obtain a direct measure of free Zn^{2+} ions in ZnO dispersions prepared in simple electrolyte solutions (*56*) as well as ZnO incubated in culture media (*57*). An alternative and complementary technique, the DGT (Diffusion Gradients in Thin Films) technique (*58*) offers the possibility to measure selectively, continuously and in situ the labile zinc fraction in solution without the necessity of sampling and separating the solid phase from the liquid one, as explained below. This technique is very promising for ecotoxicological studies to discriminate the influence of the proportion of dissolved metal on the effective toxicity of metal oxide NPs.

There are few examples in the literature about the application of theoretical models of aggregation, solubilisation and transport oriented to modelling the behavior of NPs in natural waters. A recent study of Arvidsson *et al*. (*50*) presents a theoretical model based on the classical equations of aggregation kinetics and sedimentation of colloids, but it does not provide comparison with experimental data. Also recently, Quik *et al*. (*51*) proposed a similar model but offered some limited comparisons with available experimental data. In any case, more experimental data are needed regarding sedimentation and dissolution of NPs in relevant environmental conditions.

One of the main objectives of this work is the experimental study and the corresponding modelling of the solubility, aggregation and sedimentation of nano-ZnO as a function of the conditions of the aqueous media (pH, salinity, presence of dissolved organic matter, etc.).

1.2. Availability of metals measured by DGT

The Diffusive Gradients in Thin Films (DGT) technique allows the measurement *in situ* of metal fluxes in aqueous media. This is relevant for the knowledge of the availability of metals and for the understanding of the ecotoxicology of metals in natural aqueous media.

The DGT technique is a method of analysis that emerged in the nineties (*59*). DGT devices accumulate metal ions in an ion exchange resin gel by letting the sample analytes diffuse thorough a hydrogel of known diffusional characteristics. The devices are deployed in contact with the sample during a given period of time and are analyzed upon retrieval. From the mass of metals accumulated in the device, the concentration of metals in the sample solution can be subsequently calculated.

In the present work, the measurement of the availability of metals in synthetic aqueous solutions has been performed using this technique.

1.2.1. Theory

The DGT technique is based on two phenomena: the diffusional characteristics of metal ions through a hydrogel and the ion exchange properties of a binding agent. The DGT device accumulates metal cations that reach the resin domain as a result of the diffusive transport of the free metal ions, as well as the diffusion and dissociation of dissolved inorganic complexes and small labile organic complexes from the sample solution (*60*). The binding agent consists of an ion exchange resin (Chelex-100 for most metal cations, but other binding resins are also available for inorganic anions) which is selective for the ions of interest. The resin is immobilized in a thin layer of hydrogel and serves as a sink for labile metal species. The resin layer is separated from the solution by a diffusion domain with a well-defined thickness, *g*, that consists of three parts: a hydrogel layer (the diffusive gel), a membrane filter and a double boundary layer or DBL (explained below). These layers are permeable to the cations and dissolved complexes which diffuse thorough them. The purpose of the membrane filter is to protect the hydrogel surface from the particles present in the solution (*59,61,62*). The three layers (resin disk, diffusive gel and filter) are mounted in a plastic sampling device with an opening exposed to the sampling medium (see figure 1.2 a). Between the diffusive gel and the bulk solution there is a diffusive boundary layer (DBL), the layer of fluid adjacent to the surface, of thickness δ, where transport of ions is solely by molecular diffusion. In high-velocity fluids such as streams, the DBL thickness can be negligible relative to the gel thickness. The DGT devices are submerged in the analysis solution. Within a few minutes of immersion, and due to the presence of a metal sink in the resin, a stable steady-state concentration gradient between the solution and the resin gel is established (Figure 1.2 b). By interpretation of this simple steady state condition, the DGT technique can be used to measure *in situ* the availability of metal cations. DGT represents, therefore, a new approach for determining the labile metal species (free or weakly complexed species), or "available" fraction, that may be present in aqueous aquatic systems.

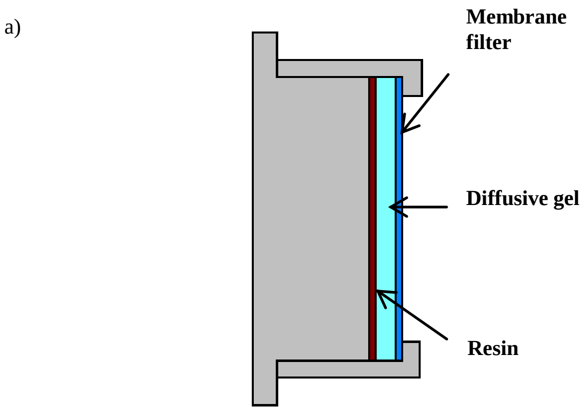

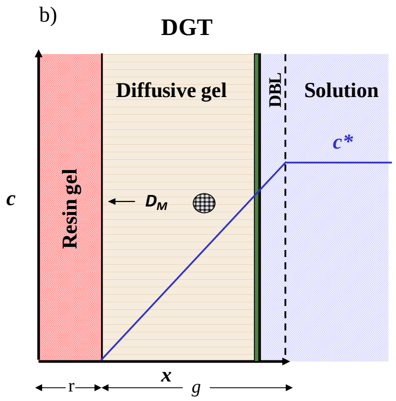

Figure 1.2. a) Scheme of the parts that compose a typical DGT device; b) Schematic cross-section through a DGT device in contact with the sample solution. It represents the concentration profile of solute within the sensor in the simplest case, where only free metal ions are present in solution.

Calculation of the available metal ion concentration is based on the measurement of the metal flux through the gel. Based on the Fick's first law of diffusion and the characteristics of the diffusive layer in the DGT device, for the simplest system that only contains a metal, the flux, *J*, can be expressed as:

$$J = D\frac{dc}{dx} \tag{1.1}$$

where *D* is the temperature-corrected molecular diffusion coefficient for the metal of interest (m^2 s^{-1}), *c* is the concentration of metal (mol m^{-3}) and *dc/dx* the concentration gradient (mol m^{-4}).

Then, the flux in steady state conditions can be rewritten as:

$$J = D\frac{c*}{g} \tag{1.2}$$

Where c^* is the metal ion concentration in bulk solution, and g is the thickness of the diffusion domain, typically 1.13 x 10^{-3} m. Notice that in Eqn. 1.2 we are assuming that the metal concentration at the resin-gel interface drops to zero, *i.e.*, the resin acts as a perfect sink, providing a fast and irreversible binding of the metal to the resin sites.

The DGT device is exposed to the target solution for a known time, t. Then, it is removed and disassembled, and the analytes are eluted from the binding layer, followed by determination using ICP-OES or ICP-MS. For the most common Chelex-DGT device, nitric acid is recommended as eluent. From the mass of metal accumulated experimentally on the resin, and applying equation 1.3, the number of moles of metal, n, are obtained (taking into account the elution efficiencies, f_e, which in this work are considered as 1 (*63*)):

$$n = \frac{c_e(\mathrm{v}_e + \mathrm{v}_r)}{f_e} \tag{1.3}$$

where c_e is the concentration of the analyte in the eluate, V_e is the volume of eluent (1 mL) and V_r, the volume of the binding hydrogel layer (typically 0.18 mL). Although the first published papers on DGT (*58*) considered the volume of the resin gel as negligible, this parameter is not so small compared to the volume of nitric acid (1 mL) required for the elution of Chelex. Here, the volume of the resin layer has been taken into account for the calculation of the moles of metal accumulated by the DGT sensor.

In a general system, Eqn. 1.2 is no longer valid since there are different complexes which diffuse and dissociate at a particular rate. However, it can still be used by replacing the metal concentration in bulk solution with an effective concentration, *i.e.*: the DGT labile metal concentration, which can be then calculated from the accumulation, n, as (*60*):

$$c_{DGT} = \frac{ng}{DtA} \tag{1.4}$$

where t is the deployment time (s), A is the area of the DGT window, with a value of 3.14 x 10^{-4} m^2, and n are the number of mols of metal accumulated during the deployment.

c_{DGT} can then be understood as an apparent concentration of free metal that will result in the same accumulation in the system. c_{DGT} differs from the total metal concentration in solution due to the particular values of the diffusion coefficient of the complexes present in the system and to the presence of inert or partially labile metal complexes whose dissociation at the resin gel interface is not complete even when the free metal concentration drops to zero.

1.2.2. Definition of lability of a metal complex and calculation of the lability degree from DGT measurements

The measurement of the metal availability depends on the flux of all the metal species present in solution. This flux is influenced by the interaction of metal ions with ligands present in solution and, in particular, by the lability of the corresponding complexes. The DGT device collects metal ions from the solution. The resulting flux (uptake) can be limited by the diffusion of the complex (in excess of ligand, the transport due to the free metal is negligible in comparison to that of the complex) and/or by its kinetics of dissociation.

Metal complexes can partially dissociate within the diffusion layer of the DGT sensor and, consequently, contribute to the net metal flux. The lability degree, ξ, allows the quantification of this contribution (*64-67*). Thus, the lability degree, corresponds to the ratio of the actual contribution of the complex to the metal flux with respect to the maximum contribution reached if the complex was fully labile (*68*).

A system is termed *fully labile* when kinetics is so fast that the metal flux is limited only by diffusion of the complex through the hydrogel thickness. During the diffusion, the complex dissociates and arrives to the resin as separated ligand and metal ions, being zero the concentration of metal and complex at the resin interface. Therefore, the lability degree of the complex is equal to 1. This case comprises the major part of inorganic complexes and a few organic complexes (*63,69,70*).

A system is inert when complex dissociation is so slow that its contribution to the metal flux is negligible. The metal complex diffuses through the diffusive layer and arrives in its metal complex form to the resin. This is the case of very stable complexes such as those of EDTA (*63,70*). The amount of metal accumulated in this case, corresponds only to the free metal concentration present in solution. In this case the lability degree of the complex is equal to 0.

In the case of partially labile complexes, they have an intermediate behavior between the two limiting cases mentioned above. The amount of metal accumulated by the DGT is, therefore, higher than the theoretical value corresponding to the free metal ion concentration, and smaller than that resulting from the total metal concentration, since only a part of the complex is able to dissociate within the time and length scale of the measurements. In this situation, the lability degree of the complex ranges between 0 and 1. This is the case, *e.g.*, of the complexes with humic and fulvic acids (*63,66*).

Metal complexation can be represented generically by a simple equilibrium relationship:

$$\mathrm{M} + \mathrm{L} \underset{k_d}{\overset{k_a}{\rightleftharpoons}} \mathrm{ML} \tag{1.5}$$

where M, L and ML are the free metal, ligand and metal complex species, respectively. The equilibrium constant for this reaction can be defined as:

$$K = \frac{k_\mathrm{a}}{k_\mathrm{d}} = \frac{c^*_\mathrm{ML}}{c^*_\mathrm{M} c^*_\mathrm{L}} \tag{1.6}$$

The rate constants for association and dissociation, k_a and k_d, respectively, are related with each other, through the complex stability constant *K*.

The conservation equations can be established as equations 1.7 (*66,70,71*). The first term (in the right hand side) refers to the diffusion of the species (according to the second Fick's law), and the following terms refer to the chemical reactions in which this species take part (*72*).

$$\frac{\partial c_M}{\partial t} = D_M \frac{\partial^2 c_M}{\partial x^2} + k_d c_{ML} - k_a c_M c_L \ - k_{a,R} c_M c_R$$

$$\frac{\partial c_L}{\partial t} = D_L \frac{\partial^2 c_L}{\partial x^2} + k_d c_{ML} - k_a c_M c_{ML} \tag{1.7}$$

$$\frac{\partial c_{ML}}{\partial t} = D_{ML} \frac{\partial^2 c_{ML}}{\partial x^2} - k_d c_{ML} + k_a c_M c_L$$

where D_M, D_L and D_{ML} are the diffusion coefficients of metal, ligand and complex, respectively. These equations have to be solved in all the diffusion domain which includes both the diffusive gel and the resin. Notice that the forth term in the right hand side of the metal equation indicates that the free metal disappears in the resin domain by complexation to the resin sites. The solution of the set of equations 1.7 allows finding the concentration profiles and the corresponding fluxes for each species in the gel domain within the DGT device. In general, this solution should be numerical, but approximate analytical expressions can be found for some particular cases which usually consider steady state, excess of ligand conditions and zero free metal concentration inside the resin domain (perfect sink conditions).

A general expression for the moles of metal accumulated in presence of N metal complexes can be written as:

$$n = \left(\frac{D_M c_M^*}{g} + \sum_{i=1}^{N} \frac{D_{ML,i}\, c_{ML,i}^*}{g} \xi_i\right) A\, t \qquad (1.8)$$

This equation can be easily understood as the total metal flux corresponding to the free metal concentration (first term in the r.h.s.) plus the addition of the maximum flux of each complex multiplied by its corresponding lability degree, which is just the fraction of the current metal flux with respect to the maximum one. The expression of the lability degree in terms of the system parameters requires the solution of the set of equations 1.7.

Alternatively, when only one complex is present in the system, the lability degree can be easily measured if the complex is the dominant species in the system. Indeed, when $D_M c_M^* << D_{ML}\, c_{ML}^*$, the first term in the r.h.s. of Eqn. 1.8 can be neglected and

$$n = \left(\xi \frac{D_{ML}\, c^*_{ML}}{g} \right) A\, t \tag{1.9}$$

In absence of ligand,

$$n(no\ L) = \left(\frac{D_M c^*_M}{g} \right) A\, t \tag{1.10}$$

So, at the same total metal concentration, the quotient

$$\xi = \frac{n}{n(noL)} = \left(\frac{D_{ML}}{D_M} \right) \tag{1.11}$$

allows the experimental determination of the lability degree of the complex.

1.2.3. Experimental

DGT sensors

The DGT holders, made of polyethylene, are based on a simple tight-fitting piston design consisted of a backing cylinder of 2.5 cm and a front cap with a 1.7 cm diameter window and were purchased from DGT Research Ldt. (Lancaster, UK, http://www.dgtresearch.com). The resin gel layer, of 0.4 mm thickness, consists of an agarose polyacrylamide gel with iminodiacetate chelating resin embedded in it (Chelex-100, Bio-Rad Laboratories). Diffusive gels, of 0.8 mm were also purchased from DGT Research Ldt. Two diffusive gels with different permeability, both with the same thickness, were used, whose characteristics are explained below. Cellulose nitrate membrane filters were purchased from Whatman (pore size: 0.45 µm, nominal thickness: 0.125 mm).

For each device, the resin gel is placed on the holder piston surface with the resin beads facing upwards. On top of it, the diffusive gel is placed, and then the filter membrane, following the scheme presented on Figure 1.2a. The front cap is pressed down tightly until a good seal is achieved.

Diffusive gels

Two different gels have been used. The thicknesses of both gels are the same, but they possess different pore sizes. To achieve different pore sizes, the composition of the gels is varied. The open pore gels, *OP*, consist of a hydrophilic network of polyacrylamide cross-linked with the agarose derivative AcrylAide. This material is known as APA gel. These gels have a pore size of about 2-5 nm. Restricted gels, *RG*, with a smaller pore size about 1 nm (*73,74*), consist of a polyacrylamide gel cross-linked with N,N'-methylenebysacrylamide (*75*).

The diffusion coefficients of metals in the open pore and restricted pore gels are about 85 % and 60% of those in water, respectively.

DGT exposure chamber

Different samples have been analyzed using the DGT technique with the objective of determine the labile metal fraction present in them. All the immersion solutions are placed in a cylindrical 5 L polyethylene bucket (see Figure 1.3). A volume of 2 L of sample solution has been used to avoid having a change in metal concentration during the deployment time.

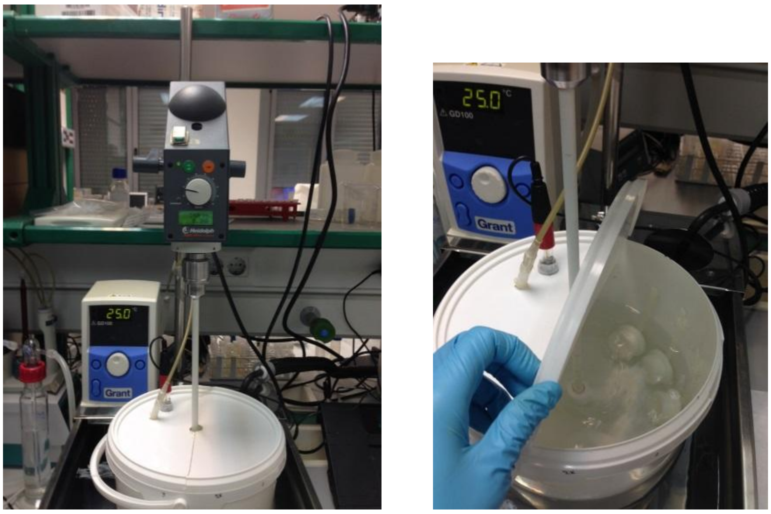

Figure 1.3. DGT setup corresponding to the description in Section 1.2.3.

The flow is kept constant by agitation (210-240 rpm). The stirring is very important because it may change the thickness of the diffusive boundary layer from one sensor to another. For this reason, a circular exposure chamber with a centered homogeneous agitation is needed to overcome this problem.

Temperature is fixed to 25 ± 0.1 °C, controlled by using a thermostatic bath where the immersion solution bucket is introduced. It is important to keep the temperature constant because of changes on temperature may cause changes in the sample speciation.

The pH has been recorded continuously throughout each experiment with a glass electrode connected to a computer with a data acquisition program, and it was readjusted if it was necessary. Keeping a constant pH during the deployment time is also very important, because a small change can cause important changes on sample speciation (*33*).

During the deployment time, aliquots of the immersion solution were taken at regular intervals of time at the height of the sensors to control the total amount of metals.

DGT retrieval and analysis procedures

After a certain time of contact with the solution, sensors are removed, washed with MilliQ water and disassembled. Resin gels are immersed in 1 mL of concentrated nitric acid (34.5 %, Fluka) for at least 24 h, in order to elute the metal ions bound to the resin. The preconcentration process resulting from the combination of the DGT deployment and elution steps has two advantages. First, the method allows very low detection limits, with the effective sensitivity increasing with deployment time. Second, since DGT metals are extracted into nitric acid, which is desirable for direct injection into most analytical instruments (*e.g.*, ICP-MS and ICP-OES), problems associated with matrix effects are obviated. In the present work, the concentration of metal is determined by Inductively Coupled Plasma Optical Emission Spectroscopy (ICP-OES) (Activa-S, Horiba Scientific) or Inductively Coupled Plasma Mass Spectrometry (ICP-MS) (7700 Series, Agilent) techniques. Additionally, samples of the immersion solution were acidified with HNO_3 solution and total metal was subsequently analyzed by ICP (OES or MS).

1.3. Outline of this thesis

As explained above, this thesis deals with the study of the availability of nanoparticles and metal cations in natural systems. In particular, systems containing engineered nanoparticles of ZnO are studied. The physico-chemical phenomena that determine the stability of aqueous dispersions of commercial ZnO NPs of different sizes are discussed. Phenomena studied range from solubility to aggregation and settling of ZnO NPs. These set of phenomena are essential to assess the fate of NPs in the natural aquatic environment and their toxicity. In a second part, the availability of metal ions is studied. DGT devices are used to determine the availability of metal ions released from ZnO NPs of different primary particle sizes within a range of environmentally relevant pH values. A second application describes the influence of the ionic strength on the availability of metal ions in systems that contain an excess of ligands, including the effect of the electric charge of the metal complexes.

Within this general purpose, the content of the thesis is structured into different chapters, according to the specific objectives, as follows:

Chapter 2 is focused on determining the effect of environmental parameters on the behavior of nano-ZnO aqueous dispersions: ionic strength, pH and nanoparticle concentration. With this purpose Dynamic Light Scattering, Laser Doppler Electrophoresis and TEM techniques have been implemented.

Chapter 3 assesses the influence of DOM on the stability of nano-ZnO dispersions. The stability has been studied with sedimentation experiments contrasted with theoretical models.

Chapter 4 is focused on the measurement of the labile metal fraction released from nano-ZnO by the implementation of the Diffusive Gradients in Thin Films (DGT) technique.

Chapter 5 deals with the impact of the medium ionic strength on the determination of the lability degree of a metal complex, and the effects of the charge and thickness of the DGT resin disc.

Chapter 6 presents a study of the effect that the charge of the resin beads embedded in the binding layer of the DGT can have on the accumulation of metals released from the dissociation of positively charged complexes in systems with different ionic strengths.

Chapter 7 discusses the results obtained throughout the Thesis.

Chapter 8 summarizes the main conclusions of the Thesis.

1.4. References

1. Ju-Nam, Y.; Lead, J. R. Manufactured nanoparticles: An overview of their chemistry, interactions and potential environmental implications. *Sci Total Environ* **2008,** *400*, 396.

2. Aitken, R. J.; Chaudhry, M. Q.; Boxall, A. B. A.; Hull, M. Manufacture and use of nanomaterials: current status in the UK and global trends. *Occupational Medicine-Oxford* **2006,** *56*, 300.

3. Ostiguy, C.; Laponite, G.; Trottier, M.; Menard, L.; Cloutier, Y.; Boutin, M.; Antoun, M.; Normand, C. *Health Effects of Nanoparticles. IRSST Report,* **2008**.

4. Bridges, J.; De Jong, W.; Jung, T.; Rydzynski, K. Risk assessment of products of nanotechnologies. *Scientific Committee on Emerging and Newly Identified Health Risks, EU* **2009**.

5. Farre, M.; Sanchis, J.; Barcelo, D. Analysis and assessment of the occurrence, the fate and the behavior of nanomaterials in the environment. *Trac-Trend Anal Chem* **2011,** *30*, 517.

6. Klaine, S. J.; Alvarez, P. J. J.; Batley, G. E.; Fernandes, T. F.; Handy, R. D.; Lyon, D. Y.; Mahendra, S.; McLaughlin, M. J.; Lead, J. R. Nanomaterials in the environment: Behavior, fate, bioavailability, and effects. *Environ Toxicol Chem* **2008,** *27*, 1825.

7. Nel, A.; Xia, T.; Madler, L.; Li, N. Toxic potential of materials at the nanolevel. *Science* **2006,** *311*, 622.

8. Hassellov, M.; Readman, J. W.; Ranville, J. F.; Tiede, K. Nanoparticle analysis and characterization methodologies in environmental risk assessment of engineered nanoparticles. *Ecotoxicology* **2008,** *17*, 344.

9. Owen, R.; Depledge, M. Nanotechnology and the environment: Risks and rewards. *Marine Pollution Bulletin* **2005,** *50*, 609.

10. Owen, R.; Handy, R. Formulating the problems for environmental risk assessment of nanomaterials. *Environ Sci Technol* **2007,** *41*, 5582.

11. Helland, A.; Wick, P.; Koehler, A.; Schmid, K.; Som, C. Reviewing the environmental and human health knowledge base of carbon nanotubes. *Ciencia & Saude Coletiva* **2008,** *13*, 441.

12. Biswas, P.; Wu, C. Y. 2005 Critical Review: Nanoparticles and the environment. *Journal of the Air & Waste Management Association* **2005,** *55*, 708.

13. Wiesner, M. R.; Lowry, G. V.; Alvarez, P.; Dionysiou, D.; Biswas, P. Assessing the risks of manufactured nanomaterials. *Environ Sci Technol* **2006,** *40*, 4336.

14. Colvin, V. L. The potential environmental impact of engineered nanomaterials. *Nat Biotechnol* **2003,** *21*, 1166.

15. Moore, M. N. Do nanoparticles present ecotoxicological risks for the health of the aquatic environment? *Environ Int* **2006,** *32*, 967.

16. Morones, J. R.; Elechiguerra, J. L.; Camacho, A.; Holt, K.; Kouri, J. B.; Ramirez, J. T.; Yacaman, M. J. The bactericidal effect of silver nanoparticles. *Nanotechnology* **2005,** *16*, 2346.

17. Buffet, P. E.; Tankoua, O. F.; Pan, J. F.; Berhanu, D.; Herrenknecht, C.; Poirier, L.; Amiard-Triquet, C.; Amiard, J. C.; Berard, J. B.; Risso, C.; Guibbolini, M.; Romeo, M.; Reip, P.; Valsami-Jones, E.; Mouneyrac, C. Behavioural and biochemical responses of two marine invertebrates Scrobicularia plana and Hediste diversicolor to copper oxide nanoparticles. *Chemosphere* **2011,** *84*, 166.

18. Ma, H. B.; Williams, P. L.; Diamond, S. A. Ecotoxicity of manufactured ZnO nanoparticles - A review. *Environ Pollut* **2013,** *172*, 76.

19. Navarro, E.; Piccapietra, F.; Wagner, B.; Marconi, F.; Kaegi, R.; Odzak, N.; Sigg, L.; Behra, R. Toxicity of Silver Nanoparticles to Chlamydomonas reinhardtii. *Environ Sci Technol* **2008,** *42*, 8959.

20. Maynard, A. Nanotechnology: A Research Strategy for Addressing Risk. *Project on Emerging Nanotechnologies. Woodrow Wilson International Center for Scholars,* **2006**.

21. Maynard, A.; Michelson, E. The Nanotechnology Consumer Products Inventory. *Project on Emerging Nanotechnologies. Woodrow Wilson International Center for Scholars,* **2006**.

22. Laosiripojana, N.; Sutthisripok, W.; Asabumrungrat, S. Synthesis gas production from dry reforming of methane over CeO2 doped Ni/Al2O3: influence of the doping ceria on the resistance toward carbon formation. *Chemical Engineering Journal* **2005,** *112*, 13.

23. Wang, Z. L. Nanostructures of zinc oxide. *Materials Today* **2004,** *7*, 26.

24. Becheri, A.; Durr, M.; Lo Nostro, P.; Baglioni, P. Synthesis and characterization of zinc oxide nanoparticles: application to textiles as UV-absorbers. *J Nanopart Res* **2008,** *10*, 679.

25. Navarro, E.; Baun, A.; Behra, R.; Hartmann, N. B.; Filser, J.; Miao, A. J.; Quigg, A.; Santschi, P. H.; Sigg, L. Environmental behavior

and ecotoxicity of engineered nanoparticles to algae, plants, and fungi. *Ecotoxicology* **2008,** *17*, 372.

26. Miller, R. J.; Lenihan, H. S.; Muller, E. B.; Tseng, N.; Hanna, S. K.; Keller, A. A. Impacts of Metal Oxide Nanoparticles on Marine Phytoplankton. *Environ Sci Technol* **2010,** *44*, 7329.

27. Miller, R.; Lenihan, H. S.; Muller, E.; Tseng, N.; Hanna, S.; Keller, A. A. Impacts of metal oxide nanoparticles on marine phytoplankton. *Environ Sci Technol* **2010,** *44*, 7329.

28. Monopoli, M.; Walczyk, D.; Campbell, A.; Elia, G; Lynch, I.; Bombelli, F.; Dawson, K. Physical-chemical aspects of protein corona: relevance to in vitro and in vivo biological impacts of nanoparticles. *J Am Chem Soc* **2011,** *133*, 2525.

29. Oberdorster, G.; Oberdorster, E.; Oberdorster, J. Concepts of Nanoparticle Dose Metric and Response Metric. *Environ Health Perspect* **2007,** *115*, A290.

30. Sager, T.; Ported, D.; Robinson, V.; Lindsley, W.; Schwegler-Berry, D.; Castranova, V. Improved method to disperse nanoparticles for in vitro and in vivo investigation of toxicity. *Nanotoxicology* **2007,** *1*, 118.

31. Cho, E. C.; Zhang, Q.; Xia, Y. N. The effect of sedimentation and diffusion on cellular uptake of gold nanoparticles. *Nat Nanotechnol* **2011,** *6*, 385.

32. Xu, C.; Tung, G; Sun, S. Size and Concentration Effect of Gold Nanoparticles on X-ray Attenuation As Measured on Computed Tomography. *Chem Mater* **2008,** *20*, 4167.

33. Wittmaack, K. Excessive Delivery of Nanostructured Matter to Submersed Cells Caused by Rapid Gravitational Settling. *Acs Nano* **2011,** *5*, 3766.

34. Hinderliter, P. M.; Minard, K. R.; Orr, G.; Chrisler, W. B.; Thrall, B. D.; Pounds, J. G.; Teeguarden, J. G. ISDD: A computational model of particle sedimentation, diffusion and target cell dosimetry for in vitro toxicity studies. *Part Fibre Toxicol* **2010,** *7*, 36.

35. Albanese, A.; Chan, W. C. W. Effect of Gold Nanoparticle Aggregation on Cell Uptake and Toxicity. *Acs Nano* **2011,** *5*, 5478.

36. Demir, E.; Kaya, N.; Kaya, B. Genotoxic effects of zinc oxide and titanium dioxide nanoparticles on root meristem cells of Allium cepa by comet assay. *Turkish Journal of Biology* **2014,** *38*, 31.

37. Rico, C. M.; Majumdar, S.; Duarte-Gardea, M.; Peralta-Videa, J. R.; Gardea-Torresdey, J. L. Interaction of Nanoparticles with Edible Plants and Their Possible Implications in the Food Chain. *J Agr Food Chem* **2011,** *59*, 3485.

38. Hackenberg, S.; Zimmermann, F.; Scherzed, A.; Friehs, G.; Froelich, K.; Ginzkey, C.; Koehler, C.; Burghartz, M.; Hagen, R.; Kleinsasser, N. Repetitive Exposure to Zinc Oxide Nanoparticles Induces DNA Damage in Human Nasal Mucosa Mini Organ Cultures. *Environmental and Molecular Mutagenesis* **2011,** *52*, 582.

39. Franklin, N. M.; Rogers, N. J.; Apte, S. C.; Batley, G. E.; Gadd, G. E.; Casey, P. S. Comparative toxicity of nanoparticulate ZnO, bulk ZnO, and ZnCl2 to a freshwater microalga (Pseudokirchneriella subcapitata): The importance of particle solubility. *Environ Sci Technol* **2007,** *41*, 8484.

40. Huang, Y.; Huang, C.; Aronstam, R.; Chen, D.; Huang, Y Oxidative stress, calcium homeostasis, and altered gene expression in human lung epithelial cells exposed to ZnO nanoparticles. *Toxicology in Vitro* **2010,** *24*, 45.

41. Dagong, G.; Hongsheng, B.; Bing, L.; Qiuxin, W.; Daoguang, W.; ui, Y Reactive oxygen species-induced cytotoxic effects of zinc oxide nanoparticles in rat retinal ganglion cells. *Toxicology in Vitro* **2013,** *27*, 731.

42. Xia, T.; Kovochich, M.; Liong, M.; Madler, L.; Gilbert, B.; Shi, H. B.; Yeh, J. I.; Zink, J. I.; Nel, A. E. Comparison of the Mechanism of Toxicity of Zinc Oxide and Cerium Oxide Nanoparticles Based on Dissolution and Oxidative Stress Properties. *Acs Nano* **2008,** *2*, 2121.

43. Kasemets, K.; Ivask, A.; Dubourguier, H. C.; Kahru, A. Toxicity of nanoparticles of ZnO, CuO and TiO2 to yeast Saccharomyces cerevisiae. *Toxicology in Vitro* **2009,** *23*, 1116.

44. Wong, S. W. Y.; Leung, P. T. Y.; Djurisic, A. B.; Leung, K. M. Y. Toxicities of nano zinc oxide to five marine organisms: influences of aggregate size and ion solubility. *Anal Bioanal Chem* **2010,** *396*, 609.

45. Ma, H. B.; Bertsch, P.; Glenn, T.; Kabengi, N.; Williams, R. Toxicity of manufactured zinc oxide nanoparticles in the nematode Caenorhabditis elegans. *Environ Toxicol Chem* **2009,** *28*, 1324.

46. Aruoja, V.; Dubourguier, H. C.; Kasemets, K.; Kahru, A. Toxicity of nanoparticles of CuO, ZnO and TiO2 to microalgae Pseudokirchneriella subcapitata. *Sci Total Environ* **2009,** *407*, 1461.

47. Adams, L. K.; Lyon, D. Y.; Alvarez, P. J. Comparative eco-toxicity of nanoscale TiO2, SiO2, and ZnO water suspensions. *Water Res* **2006,** *40*, 3527.

48. Hu, X. K.; Cook, S.; Wang, P.; Hwang, H. M. In vitro evaluation of cytotoxicity of engineered metal oxide nanoparticles. *Sci Total Environ* **2009,** *407*, 3070.

49. Zhang, Y.; Chen, Y. S.; Westerhoff, P.; Crittenden, J. Impact of natural organic matter and divalent cations on the stability of aqueous nanoparticles. *Water Res* **2009,** *43*, 4249.

50. Arvidsson, R.; Molander, S.; Sanden, B. A.; Hassellov, M. Challenges in Exposure Modeling of Nanoparticles in Aquatic Environments. *Hum Ecol Risk Assess* **2011,** *17*, 245.

51. Quik, J. T. K.; Vonk, J. A.; Hansen, S. F.; Baun, A.; Van de Meent, D. How to assess exposure of aquatic organisms to manufactured nanoparticles? *Environ Int* **2011,** *37*, 1068.

52. Adam, N.; Schmitt, C.; Galceran, J.; Companys, E.; Vakurov, A.; Wallace, R.; Knapen, D.; lust, R. The chronic toxicity of ZnO nanoparticles and ZnCl2 to Daphnia magna and the use of different

methods to assess nanoparticle aggregation and dissolution. *Nanotoxicology* **2014,** *8*, 709.

53. Poynton, H. C.; Lazorchak, J. M.; Impellitteri, C. A.; Smith, M. E.; Rogers, K.; Patra, M.; Hammer, K.; Allen, H.; Vulpe, C. D. Differential gene expression in Daphnia magna suggests distinct modes of action and bioavailability for ZnO nanoparticles and Zn ions. *Environ Sci Technol* **2011,** *45*, 762.

54. Mackay, C. E; Johns, M.; Salatas, J. H.; Bessinger, B.; Perri, M. Stochastic probability modeling to predict the environmental stability of nanoparticles in aqueous suspension. *Integr Environ Assess Manag* **2006,** *2*, 293.

55. Buffle, J.; Wilkinson, K. J.; Stoll, S.; Filella, M.; Zhang, J. W. A generalized description of aquatic colloidal interactions: The three-colloidal component approach. *Environ Sci Technol* **1998,** *32*, 2887.

56. David, C.; Galceran, J.; Rey-Castro, C.; Puy, J.; Companys, E.; Salvador, J.; Monne, J.; Wallace, R.; Vakourov, A. Dissolution Kinetics and Solubility of ZnO Nanoparticles Followed by AGNES. *The Journal of Physical Chemistry C* **2012,** *116*, 11758.

57. Mu, Q.; David, C.; Galceran, J.; Rey-Castro, C.; Krzeminski, L.; Wallace, R.; Bamiduro, F.; Milne, S.; ondow, N.; rydson, R.; izcay-Barrena, G.; outledge, M.; euken, L.; rown, A. Systematic investigation of the physicochemical factors that contribute to the toxicity of ZnO nanoparticles. *Chem Res Toxicol* **2014,** *27*, 558.

58. Zhang, H.; Davison, W. Performance-Characteristics of Diffusion Gradients in Thin-Films for the in-Situ Measurement of Trace-Metals in Aqueous-Solution. *Anal Chem* **1995,** *67*, 3391.

59. Davison, W.; Zhang, H. In-Situ Speciation Measurements of Trace Components in Natural-Waters Using Thin-Film Gels. *Nature* **1994,** *367*, 546.

60. Scally, S.; Davison, W.; Zhang, H. In situ measurements of dissociation kinetics and labilities of metal complexes in solution using DGT. *Environ.Sci.Technol.* **2003,** *37*, 1379.

61. Zhang, H.; Davison, W. Performance-characteristics of diffusion gradients in thin- films for the in-situ measurement of trace-metals in aqueous- solution. *Anal.Chem.* **1995,** *67*, 3391.

62. Buffle, J.; Horvai, G. In situ monitoring of acuatic systems. *Chemical Analysis and Speciation* **2000**.

63. Mongin, S. Contributions to the study of the availability of metal ions in aquatic systems. *Doctoral Thesis* **2012**.

64. Galceran, J.; Puy, J.; Salvador, J.; Cecilia, J.; van Leeuwen, H. P. Voltammetric lability of metal complexes at spherical microelectrodes with various radii. *J Electroanal Chem* **2011,** *505,* 85.

65. Puy, J.; Cecilia, J.; Galceran, J.; Town, R. M.; van Leeuwen, H. P. Voltammetric lability of multiligand complexes: the case of ML2. *J Electroanal Chem* **2004,** *571*, 121.

66. Salvador, J.; Puy, J.; Cecilia, J.; Galceran, J. Lability of complexes in steady-state finite planar diffusion. *J Electroanal Chem* **2006,** *588*, 303.

67. Salvador, J.; Garces, J. L.; Galceran, J.; Puy, J. Lability of a mixture of metal complexes under steady-state planar diffusion in a finite domain. *J Phys Chem B* **2006,** *110,* 13661.

68. Uribe, R.; Mongin, S.; Puy, J.; Cecilia, J.; Galceran, J.; Zhang, H.; Davison, W. Contribution of Partially Labile Complexes to the DGT Metal Flux. *Environ Sci Technol* **2011,** *45*, 5317.

69. Gimpel, J.; Zhang, H.; Hutchinson, W.; Davison, W. Effect of solution composition, flow and deployment time on the measurement of trace metals by the diffusive gradient in thin films technique. *Anal Chim Acta* **2001,** *448*, 93.

70. Tusseau-Vuillemin, M. H.; Gilbin, R.; Taillefert, M. A dynamic numerical model to characterize labile metal complexes collected with diffusion gradient in thin films devices. *Environ Sci Technol* **2003,** *37*, 1645.

71. Lehto, N. J.; Davison, W.; Zhang, H.; Tych, W. An evaluation of DGT performance using a dynamic numerical model. *Environ Sci Technol* **2006,** *40*, 6368.

72. Levy, J. L.; Zhang, H.; Davison, W.; Puy, J.; Galceran, J. Assessment of trace metal binding kinetics in the resin phase of diffusive gradients in thin films. *Anal Chim Acta* **2012,** *717*, 143.

73. Zhang, H.; Davison, W. Diffusional characteristics of hydrogels used in DGT and DET techniques. *Anal.Chim.Acta* **1999,** *398*, 329.

74. Davison, W.; Zhang, H. In-Situ Speciation Measurements of Trace Components in Natural-Waters Using Thin-Film Gels. *Nature* **1994,** *367*, 546.

75. Garmo, O. A.; Davison, W.; Zhang, H. Interactions of trace metals with hydrogels and filter membranes used in DET and DGT techniques. *Environ Sci Technol* **2008,** *42*, 5682.

Chapter 2

Behavior of ZnO nanoparticles in aqueous media

2.1. Abstract

Metal oxide nanoparticles (NPs) are used in a wide range of commercial products and it is expected a high increase of their applications in the next years. It is, then, urgent a better knowledge of the risks of nanomaterials for human health as well as their impact on the environment. The fate and impact of nanomaterials on the environment depends on many factors such as dissolution, homo and heteroaggregation, settling, interactions with cations, particles and contaminants presents in the system, pH, ionic strength, etc. ZnO NPs (nano-ZnO) have been selected as a model of metal oxide NPs. Here, the stability of these NPs (with average primary particle sizes of 71 and 20 nm) is studied by DLS and zeta potential meaurements. The attachment efficiencies are calculated from the experimental aggregation kinetics and compared with Derjaguin-Landau-Verwey-Overbeek (DLVO) theory predictions. The effect of ionic strength, pH and concentration of nano-ZnO on the aggregation is characterized. Measurements confirmed that the behavior of both NPs is affected by the NP concentration and ionic strength of the solution, while minimal influence of pH has been shown.

2.2. Introduction

Because of their advantageous properties, ZnO nanoparticles are being incorporated in a wide range of consumer products (*1*,*2*). This increasing use makes necessary the study of the risks these materials pose to humans and ecosystems (*3*-*5*). The stability, mobility, bioavailability and toxicity of NPs epend, among other processes, on the aggregation (*6*). Therefore, the study of the aggregation is fundamental to understand the behavior and fate of NPs in the environment. The stability of NPs is given by solution chemistry: pH, ionic strength and the presence of natural organic matter. Many studies of metal NPs aggregation are being conducted these days. Investigations have shown that the increase of the ionic strength promote the aggregation of CeO_2 (*7*), AgNPs (*8*), and also ZnO (*2,9*) NPs. Furthermore, aggregation is also affected by NPs concentration as has been seen for TiO_2, SiO_2 and ZnO (*10*) NPs.

The classic DLVO theory (*11*) of colloidal stability has been employed to explain the aggregation behavior of the charged nanoparticles in presence of electrolytes. Particles are surrounded by a diffuse electrostatic double layer (EDL) and the balance between the van der Waals attraction forces and the electrostatic repulsion forces determines their stability (*8*).

The objective of this chapter is to investigate and model the aggregation kinetics of two ZnO NPs of different size (71NP and 20NP) in the presence of different concentrations of KCl, pH and concentration of NPs. These results provide information to understand the stability of nano-ZnO in water and to assess their fate in the environment. To carry out this study several instrumental techniques such as DLS (Dynamic Light Scattering), Laser Doppler Electrophoresis and TEM (Transmission Electron Microscopy) are being used.

The aggregation kinetics of the nano-ZnO dispersions has been studied using DLS technique. The surface charge of nano-ZnO, in relation with the surrounding conditions, has been determined using Laser Doppler Electrophoresis technique and, finally, the aggregate morphology has been studied by TEM.

2.3. Theory

2.3.1. Aggregation kinetics

The model used in this work for the semi-quantitative description of the average size of the aggregates as a function of time was based on the classical theory of Smoluchowski, as is described in J. Gregory, *"Particles in water. Properties and Processes"* (*12*).

The model assumes an initial dispersion of N_0 identical spherical aggregates that after a period of time t, contains agglomerates of various sizes and different concentrations N_i, where i represents the "size" of the particles (number of primary particles contained in the aggregate). It is assumed that aggregation is a second-order process where the rate of collision is proportional to the product of the concentrations of the two species in collision (the collision of three bodies are only relevant at very high particle concentrations). The "effective" collisions fraction or attachment efficiency, α (see 2.3.2.), which leads to the irreversible formation of an aggregate is assumed to be 1, which corresponds to completely unstable dispersions where aggregation is controlled by mass transport. Assuming that the particle diffusion process is Brownian, and that collisions occur between particles of similar size, we can deduce the following approximate expression for the average aggregation number ($\bar{k}$) which is given by the ratio of the initial number of primary particles, N_0, to the total particle number at some stage in the aggregation process, N_T:

$$\bar{k} = \frac{N_0}{N_T} \tag{2.1}$$

at time *t*, the average number of primary particles contained in the aggregates is:

$$\bar{k} = 1 + \frac{t}{\tau} \tag{2.2}$$

where τ is a characteristic time called clotting time (or average life) of the aggregation process, when the total particle concentration is reduced to half of the original concentration, and is defined as:

$$\tau = \frac{1}{k_a N_0} \tag{2.3}$$

Early stage aggregation kinetics can be described by the rate of doublet formation, which dominates over other higher order aggregate formation. The loss in primary particles during the early stage of aggregation can be expressed as a rate equation of second order, where N_T is the concentration of primary particles as a function of time *t*:

$$\frac{dN_T}{dt} = -k_a N_T^2 \tag{2.4}$$

The integration of the expression gives the total number concentration at time t:

$$N_T = \frac{N_0}{1 + k_a N_0 t} \tag{2.5}$$

where k_a (m^3 s^{-1}) is the absolute aggregation rate constant which only depends on the media temperature and viscosity (μ), defined as (*12*)

$$k_a = \frac{4 k_B T}{3\mu} \tag{2.6}$$

where k_B is the Boltzmann constant. For water at 25 ºC, k_a= 6.13 x 10^{-18} m^3 s^{-1}.

The hydrodynamic diameter of the aggregates, *d,* is the parameter experimentally determined by DLS. It can be related to the average particle number $\bar{k}$ of the aggregates when an approximate expression that takes into account the aggregate structure is used. The simplest expression is (*13*):

$$d = d_0 \sqrt[FD]{\bar{k}} \tag{2.7}$$

where d and d_0 represent the mean diameters of the aggregate and primary particle, respectively, and *FD* is the fractal dimension that characterizes the aggregate structure. In practice, *FD* can be considered as an empirical parameter indicating how compact the aggregate is (*FD*= 3 represents a compact aggregate, and *FD*= 1 corresponds to a linear chain of primary particles).

By replacing Eqn. 2.2 in Eqn. 2.7, an explicit expression for the time dependence of the average diameter of the aggregates is obtained

$$d = d_0 \sqrt[FD]{1 + \frac{t}{\tau}} \tag{2.8}$$

which will be used to fit the *FD* .

2.3.2. Attachment efficiency and critical coagulation concentration

The aggregation kinetics of nanoparticles can be evaluated using DLS measurements. DLS provide the hydrodynamic diameter of the particle aggregates as a function of time (t). The initial rate of change of hydrodynamic diameter is proportional to $k_a N_0$, which can be written as (*14-16*):

$$\left(\frac{\mathrm{d}d}{\mathrm{d}t}\right)_{\mathrm{t}\to 0} \propto k_a N_0 \tag{2.9}$$

Where k_a is the aggregation rate constant and N_0 the initial particle number concentration. The attachment efficiency (α), otherwise known as the inverse stability ratio, 1/*W*, describes the fraction of effective particle collisions that result in the formation of an aggregate. It is related with the effective aggregation rate of the nanoparticles and can be estimated by comparison with the aggregation kinetic rate constant in situations controlled purely by diffusion (*17,18*).

For suspensions with the same nanoparticle concentration, attachment efficiencies are determined by normalizing the measured aggregation rate constant, determined at any electrolyte concentration, *k*, to the diffusion-limited aggregation rate constant, k_{fast} determined under favourable aggregation conditions (18):

$$\alpha = \frac{k}{k_{fast}} \tag{2.10}$$

Based on the initial slope of the *d*-*t* curve determined experimentally by DLS, the attachment efficiency can be obtained without having to determine the absolute aggregation rates. At fixed N_0, the ratio of the initial slope of the *d* versus time graph to that in the fast regime is proportional to k/k_{fast} (15).

The critical coagulation concentration (CCC) is the electrolyte concentration at which the attachment efficiency is close to unit and energy barrier is just eliminated. Above this CCC, the variation of the particle size is independent of electrolyte concentration.

Plotting α as function of the ionic strength and extrapolating the data to α= 1, the minimum concentration at which fast aggregation occurs is obtained. This concentration corresponds to the CCC (*16*).

2.3.3. DLVO calculations

The Derjaguin-Landau-Verwey-Overbeek (DLVO) theory (*11*) is used in this study to interpret the aggregation behavior of nano-ZnO as a function of the ionic strength. In the classical DLVO, total interaction energy is determined by the sum of the van der Waals energies, V_{vdw}, and the electric double layer (EDL) potential V_{EDL} (*12*) that exist between particles as they undergo Brownian motion:

$$V_T = V_{vdw} + V_{EDL} \tag{2.11}$$

where the V_{vdw} and V_{EDL} , for equal spheres of diameter d and zeta potential ζ, are expressed as follows:

$$V_{vdw} = -\frac{Ad}{24h} \tag{2.12}$$

$$V_{EDL} = \pi\varepsilon\, d\, \zeta^2 exp(-\kappa h) \tag{2.13}$$

where A is the Hamaker constant, which characterizes the van der Waals interactions between two colloidal particles in a liquid medium and depends on the particle geometry and medium composition. For ZnO, A, has a value of 1.9 x 10^{-20} J (*19*). d (m) is the diameter of particles and h (m) is the distance between surfaces of two interacting particles. The negative sign indicates an attraction. In our experiments we will use the value of the average diameter of the initial aggregates as d. $\varepsilon=\varepsilon_r\varepsilon_0$ is the dielectric constant where ε_r is the relative dielectric constant of the medium (78.54 for water at 298.13K), and ε_0 is the permittivity in vacuum (8.85 x 10^{-12} $C^2J^{-1}m^{-1}$). ζ is the zeta potential of the charged aggregates, κ is the reciprocal of the double layer thickness and can be computed as 2.32 x 10^9 x $(\sum C_iZ_i^2)^{1/2}$ m^{-1} where C_i is the concentration of each ion and Z_i is its charge value.

The total interaction energy, V_T, becomes:

$$V_T = \pi\,\varepsilon\,d\,\zeta^2 exp(-\kappa h) - \frac{Ad}{24h} \tag{2.14}$$

expressed in units of k_BT. Because of the assumptions made, this expression will only apply for fairly low values of ζ, for a relatively close approach ($h<<d$), and at separations where retardation is not significant (h<5 nm).

2.4. Experimental section

2.4.1. Reagents

Two different ZnO nanomaterials were used, labelled as 71NP and 20NP. 71NP has a 71 nm nominal average primary particle diameter (Sigma-Aldrich) and 20NP has an average size of 20 nm (IoLiTec, Ionic Liquid Technologies GmbH). Nano-ZnO stock solutions (1g L^{-1}) were prepared form dry ZnO powder, in Milli-Q water (Synergy UV, Millipore) without any additive or background electrolyte and sonicated in an ultrasonic bath (Branson 3210, 100W) for 30 min. The 20NP nano-ZnO stock was previously prepared at 4 g L^{-1} and sonicated for 30 min. As the dispersion is not stable and settles down, the precipitate (which also contains some impurities) is discarded and the remaining supernatant is quantified reaching a concentration of 1 g L^{-1}. The stock was stored for a maximum period of 1 week at room temperature and it was sonicated at least 30 minutes before its use in order to obtain an initial dispersion of nanoparticles as homogeneous as possible. Diluted solutions of nano-ZnO were prepared by dilution of the stock solutions.

Potassium chloride was used as inert supporting electrolyte and prepared from solid KCl (Fluka).

To maintain fixed the pH, solutions were buffered with tris(hydroxymethyl)aminomethane, Tris (Merck).

The ionic strength in the dispersion samples was fixed by adding an aliquot of a concentrated stock solution (1 M KCl plus 0.2 M Tris).

Standard 0.1 M solution of KOH and HCl (Fluka) were added to fix the pH at the desired values.

2.4.2. Instrumentation

Nano-ZnO was characterized with different techniques. Transmission electron microscopy (TEM) was used to determine the size and morphology of nanoparticles. Surface properties of nano-ZnO were probed using the surface sensitive technique BET (Brunauer, Emmett and Teller) porosimetry from which BET surface area of the nano-ZnO was measured.

The sedimentation of nano-ZnO was determined by monitoring the changes in the optical absorbance using a Perkin-Elmer Lambda XLS (from Analytik Jena UK) UV-Vis spectrophotometer. In particular, changes in the optical absorbance at 372 nm and 362 nm, for 20NP and 71NP, respectively, were obtained as a function of time as the nanoparticles settled.

Dynamic Light Scattering (DLS) was used to evaluate the hydrodynamic diameter of the particles in the sample. During the measurement, a laser beam passes through a particle suspension, and the fluctuations of the light intensity scattered by the particles over time are used to measure the diffusion coefficient of the particles. These fluctuations come from Brownian motion of the particles and from the fact that neighbouring particles can have constructive or destructive interference of the scattered light intensity in a certain direction (*20*). The hydrodynamic diameters of the particles can be determined from the diffusion coefficients in terms of the Stoke-Einstein equation. Detailed information on DLS, including their physical principles, mathematical models, and limitations can be found elsewhere (*21*). The mean particle size measured by DLS is the so-called “z-average” diameter, which is weighted by the intensity of light scattered by the particles. A Zetasizer Nano ZS (Malvern Instruments Ltd, Bedford, MA) was used to measure the dynamic light scattering which was detected and collected by a photo-detector at a fixed scattering angle of 173°. It uses a He-Ne laser of 633 nm wavelength. These results allow us to check the stability and follow the apparent increase in the mean diameter over time.

Electrophoretic mobility (EPM) measurements were also conducted using the same equipment (Zetasizer Nano ZS), which allow measuring the mobility of charged particles under the application of an electric field by the

Laser Doppler Electrophoresis technique. By applying an electric field to the colloidal suspension, particles migrate to one of the electrodes. This phenomenon is called electrophoresis. The measurable quantity is the electrophoretic mobility, which is the particle velocity per unit of electric field applied. The measurement procedure involves analysing the laser light scattered by particles when an electric field is applied to the suspension located in between two electrodes in a capillary. Scattered radiation by the moving charged particles experience a shift in frequency due to the Doppler effect, which is detected by the equipment and converted to the corresponding value of mobility. When needed, EPM values were converted to zeta potentials (ζ) using Henry's equation under the Smoluchowski approximation (Zetasizer Nano User Manual, Man0317 Issue 5.0, 2009).

A glass combined electrode (Orion 9103) was attached to a pH meter Orion 920A+ (Thermo Electron Corporation) and introduced in the samples to measure the pH.

2.4.3. Procedures

Characterization

The morphology of nano-ZnO was studied by TEM and SEM. The 20NP and 71NP nanoparticles powder was analysed at a concentration of 100 mg L^{-1} in two different media: a) dispersed in Milli-Q water and b) dispersed in a 0.1 mol L^{-1} KCl salt solution with pH adjusted to 8. Analyses were performed by Rachel Wallace at the Institute for Materials Research, University of Leeds (United Kingdom).

The BET surface area of both nano-ZnO samples was measured by J.J.Gámez from CCiT – University of Barcelona.

Effect of pH and ionic strength

Size distribution and EPM measurements of the nano-ZnO dispersions were conducted at different pH and salinity conditions. The effect of pH on the stability of nano-ZnO was tested at constant ionic strength (0.1 M KCl plus 0.02M Tris). The pH was ranged between 7 and 9, interval of interest in natural waters and biological fluids, and was adjusted with a standard solution of 0.1 M KOH or HCl. The amount of nano-ZnO was fixed by the necessary addition of an aliquot of the stock (1 g L^{-1}) as a function of the solubility at each pH to obtain a final 100 mg L^{-1} solid concentration.

The effect of ionic strength was tested at pH 8. The studied ionic strength was in the range of 0.1 mM to 1 M KCl.

The corresponding aliquot of nano-ZnO stock solution was diluted in the different aqueous solutions just before the size and EPM measurements were started. During each experiment, data were recorded for a period ranged between 0 and 180 minutes, in 90 and 5 second intervals, for DLS and EPM, respectively.

Concentration effect

Nano-ZnO stock was diluted in solution media containing 0.1 or 0.01 M KCl (plus 0.02 and 0.002 M Tris, respectively) at a fixed pH 8. A set of nano-ZnO dispersions were prepared in the range 100-400 mg L^{-1}. Hydrodynamic diameter was measured up to 80 min just after the addition of the stock to the media.

2.5. Results and Discussion

2.5.1. Morphological characterization (TEM and BET)

The particle size, size distribution and morphology information of the nanoparticles was provided by TEM (Fig. 2.1). TEM images can also be used to judge whether good dispersions have been achieved or whether aggregation is present in the system.

Figure 2.1a and 2.1b, show the images obtained by TEM of nano-ZnO dispersed in Milli-Q water. Notice that it can be seen the presence of small clusters. ZnO could not be effectively dispersed into primary particles in water regardless of ultrasonication, as there are aggregates with sizes larger than 100 nm. This may be due to insufficient power of the sonicator, or to some extent of sintering in the original commercial powders.

The size of the observed aggregates reached about 500 and 200 nm diameters for 71NP and 20NP, respectively. These results are consistent with those observed by DLS in the absence of background electrolyte (see section 2.5.2). The primary particle sizes agreed with those given by commercial brand, below 100 nm on average for 71NP, and about 20 nm for 20NP. It also can be seen that there is a greater heterogeneity of primary particle sizes for 71NP nano-ZnO, while 20NP samples show a lower polydispersity degree.

As shown in Figure 2.1c and 2.1d, the nano-ZnO primary particles tend to form irregular aggregates of different sizes when they are in a saline medium, in this case of 0.1 M KCl at pH 8. Furthermore, the observed aggregates are generally larger than the ones observed in Milli-Q water dispersions. It seems from the TEM micrographs that the particles aggregate when the ionic strength is increased. These results are also consistent with the data presented below from the DLS measurements.

In a BET analysis the specific surface area of nano-ZnO was measured as 31.8453 $m^2\ g^{-1}$ for 20NP and 11.5467 $m^2\ g^{-1}$ for 71NP. Therefore, as the diameter of the nanoparticle decreases, the surface area increases, as expected.

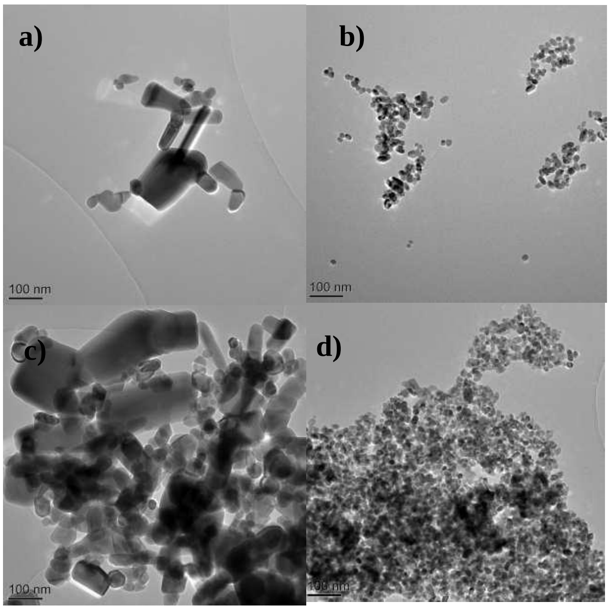

Figure 2.1. Representative TEM micrographs of nano-ZnO suspended in Milli-Q water at 19000 x magnification: a) 71NP and b) 20NP; and in 0.1 M KCl at pH 8 and 19000 x magnification: c) 71NP and d) 20NP.

2.5.2. Effect of ionic strength on the stability of nano-ZnO in aqueous solutions

Nano-ZnO aggregation kinetics

The stability of nano-ZnO and other metal oxide nanoparticles in aqueous solutions depends to a large extent on the ionic strength, *I*, of the media (*2*,*3*,*22*,*23*).

The hydrodynamic diameter of nano-ZnO measured as a function of time for different values of the ionic strength is shown in Figure 2.2. Ionic strengths employed in this study ranged from 1 to 100 mM KCl and the pH is fixed at 8 (0.02M Tris). At 1 mM, both nanoparticles are quite stable, no cluster aggregation is observed within the measurement time (80 min), remaining in a constant size of 361 ± 11 nm for 71NP nano-ZnO while 20NP remains at 171 ± 18 nm. At 5 mM ionic strength, a different behavior is observed between the different nano-ZnO since71NP aggregates faster than 20NP.

However, even faster aggregation of nano-ZnO during the analysis time is found when KCl concentration is above 10 mM. At 20 mM or higher, an increase in the electrolyte concentration has no influence on the aggregation rate. The size of both nano-ZnO aggregates, 71NP and 20NP, achieve maximum sizes around 2000 nm after 60 minutes from salt addition. Above 60 minutes, the hydrodynamic diameter of the aggregates apparently decreases. This effect is due to sedimentation of the biggest aggregates, which reduce the average size of the dispersed aggregates.

Electrolytes in colloidal systems are believed to control the thickness of electric double layer (EDL). The increase of the electrolyte concentration compresses the electrostatic double layer and hence promotes aggregation by reducing the electrostatic repulsion. This behavior has also been observed in other studies of ZnO NPs (*2*,*9*,*10*) or other metal NPs (*7*,*17*,*22*,*24*).

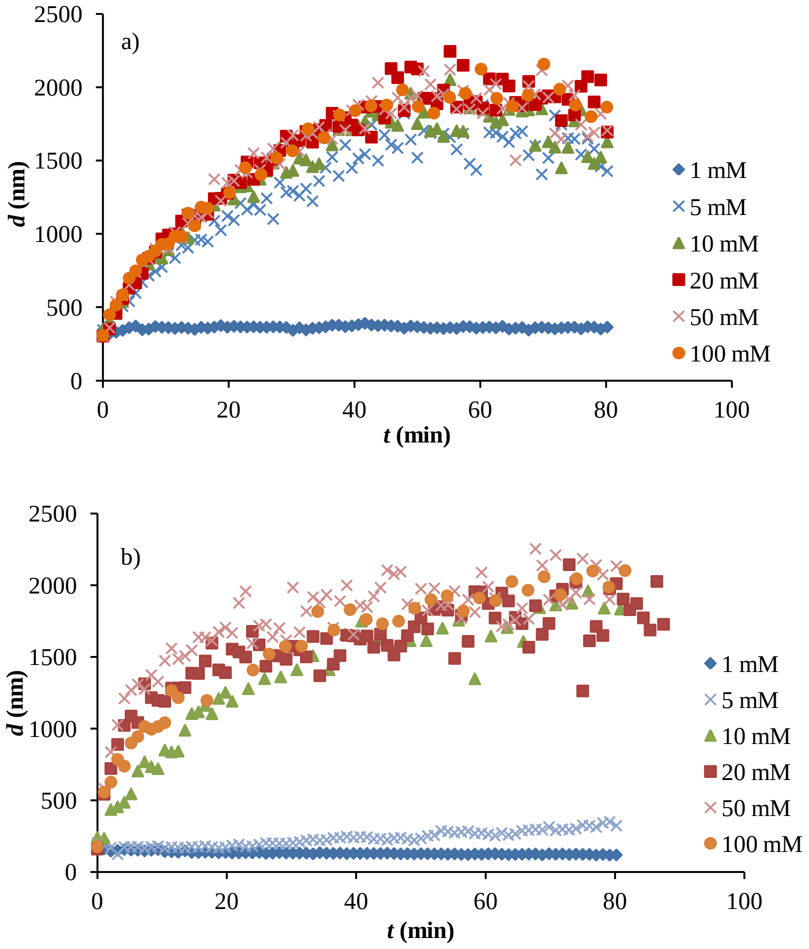

Figure 2.2. Aggregation kinetics of 100 mg L^{-1} nano-ZnO, a) 71NP and b) 20NP, as a function of time and ionic strength at fixed pH 8. Markers: experimental data.

The aggregation rate constant *k* under different electrolyte concentrations has been determined from the initial slopes of the aggregation curves of data showed in Figure 2.2. The obtained values are presented in Table 2.1 and Figure 2.3.

Table 2.1. Apparent aggregation rate constants *k* under different ionic strength for 100 mg L^{-1} 71NP and 20NP at pH 8.

I **(mM)**	$\mathbf{k_{71NP}}$ **(nm min^{-1})**	$\mathbf{K_{20NP}}$ **(nm min^{-1})**
1	3.87	0.11
5	25.13	0.167
10	36.36	31.37
20	37.74	85.68
50	42.48	101.59
100	41.35	

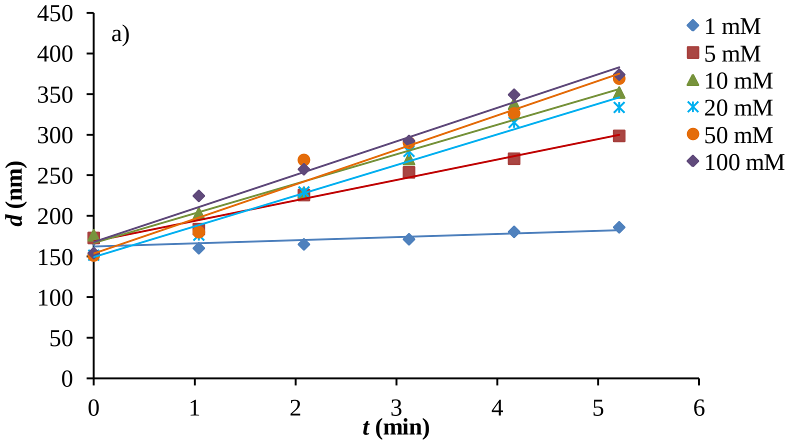

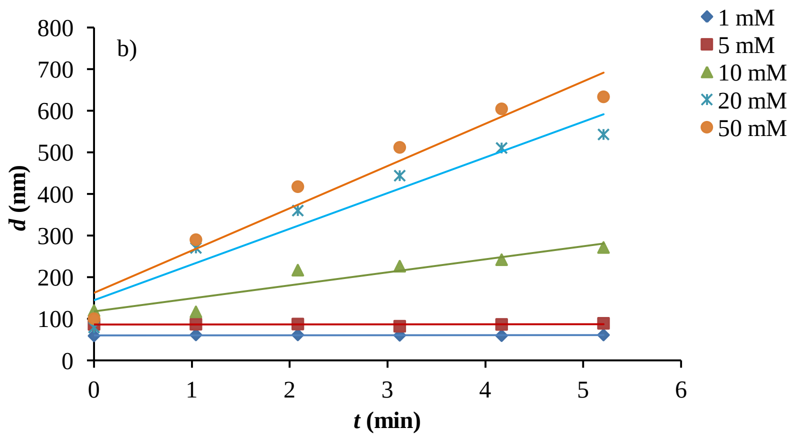

Figure 2.3. Slopes of the aggregation curves of data obtained from Figure 2.2 a) 71NP and b) 20NP).

The attachment efficiencies (α) of nano-ZnO as a function of KCl concentrations, ranging from 1 to 100 mM, are calculated by applying equation 2.10 and normalizing slopes with the k_{fast} values: 41,35 and 101,59 nm min^{-1} for 71NP and 20NP, respectively. Data are plotted in Figure 2.4. At low electrolyte concentrations, reaction-limited aggregation occurs since repulsive forces exist between equally charged nanoparticles. The critical coagulation concentration (CCC), obtained from the intersection of the lines extrapolation of attachment efficiency data to α close to unit, are 10.84 mM and 22.72 mM for 71NP and 20NP, respectively. Above this KCl concentration, diffusion-limited aggregation takes place, as the surface charge is sufficiently screened to eliminate the energy barrier aggregation. Above the respective CCC, the aggregation rate remains constant with the increase of the electrolyte concentration.

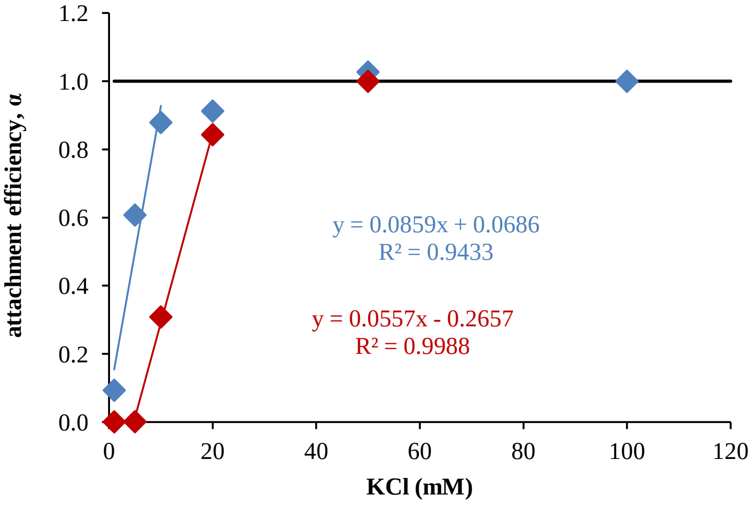

Figure 2.4. Attachment efficiencies as a function of KCl concentration obtained for 100 mg L^{-1} nano-ZnO (71NP, blue and 20NP, red) at pH 8.

According to Eq. 2.8, the fractal dimension of the formed aggregates, *FD*, has been fitted by plotting $\ln(1+\alpha k a N_0 t)$ versus $\ln(d/d_0)$ and using the attachment efficiencies previously calculated for each ionic strength. Figure 2.5 shows the linear regressions for each NP (71NP and 20 NP) at 20 mM ionic strength from whose slope the *FD* values are obtained. The fitted *FD* has a value of 1.97 for 71NP and 2.18 for 20NP.

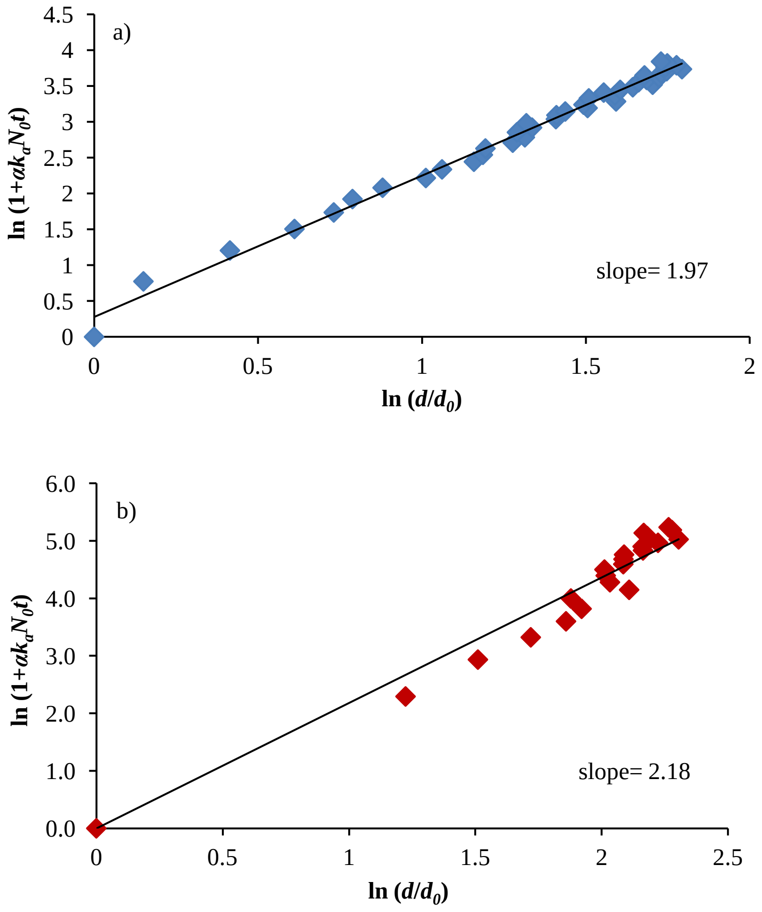

Figure 2.5. Fractal dimension fitting using experimental data obtained from Figure 2.2 a) 71NP; b) 20NP.

Finally, the aggregation kinetics is described using the *FD* and attachment efficiency parameters calculated above. Lines in Figure 2.6 correspond to the aggregation kinetics calculated by applying equation 2.8.

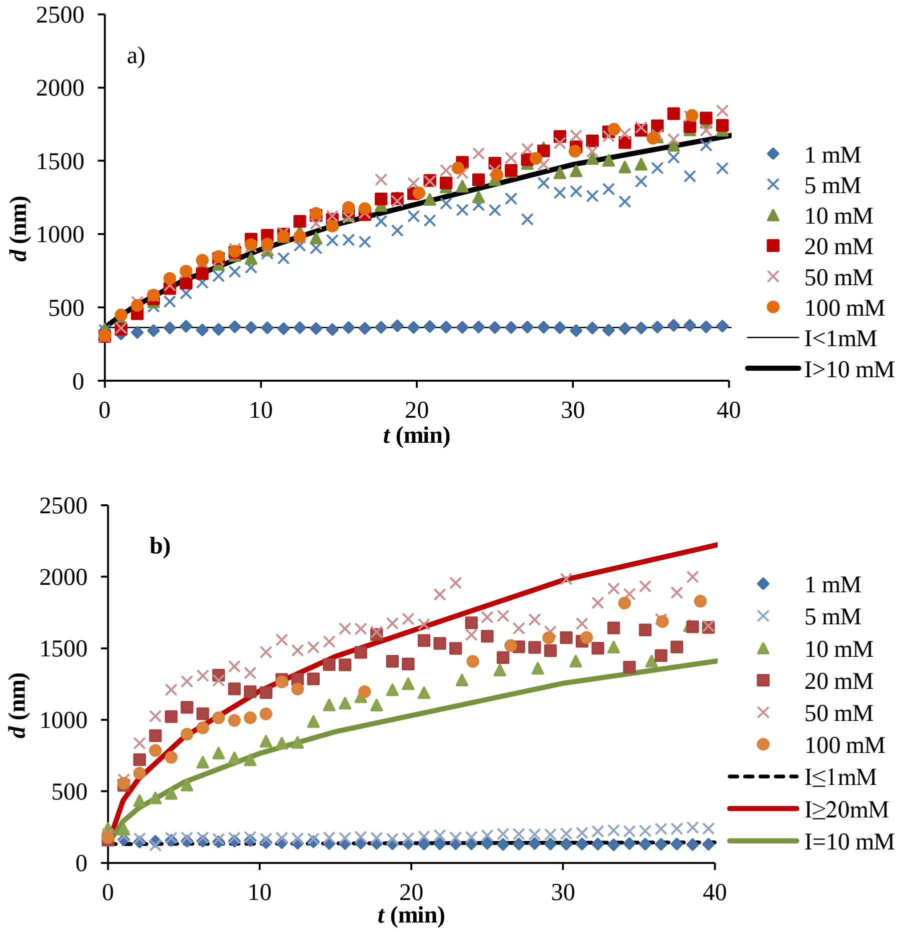

Figure 2.6. Theoretical aggregation kinetics (black lines) calculated by applying equation 2.7 for a) 71NP and b) 20NP at 100 mg L^{-1} and pH 8.

Nano-ZnO surface charge

The EPM of nano-ZnO in the aqueous solutions as a function of ionic strength at pH 8 has been measured, and the results are presented in Figure 2.7. Overall, both NPs present positive charge and, particularly, as the KCl content increase, from 0 to 1000 mM, the EPM decreases shifting from 2 ±

0.2 to -0.02 ± 0.04 µmcm $V^{-1}s^{-1}$ for 71NP and from 2.4 ± 0.2 to -0.1 ± 0.4 µmcm $V^{-1}s^{-1}$ for 20NP. Notice that the surface charge of 20NP is slightly more positive than 71NP in almost all the range of ionic strengths employed, which is in agreement with the larger CCC value observed for 20NP.

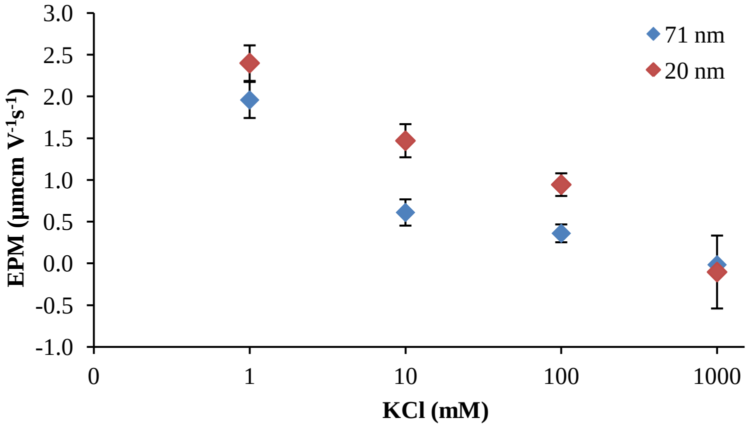

Figure 2.7. Electrophoretic mobility of 100 mg L^{-1} nano-ZnO (71NP, blue diamonds and 20NP, red diamonds) suspensions under different concentrations of KCl at pH 8.

DVLO analysis of the interactions between nano-ZnO NPs

The interaction forces between nano-ZnO in aqueous solutions can be described by DLVO theory, in which van der Waals attraction and EDL repulsion are accounted for. The sum of these two forces determines the net interactions between particles. Figure 2.8 plots the DVLO energy profiles of the ZnO NP-NP interactions as a function of the solution ionic strength. In the presence of low electrolyte concentrations, 1 mM KCl, the EDL repulsive energy between positively charged nano-ZnO is dominant and resulted in an energy barrier with a height of about 7.7 k_BT and 18.7k_BT for 71NP and 20NP, respectively. Then, nano-ZnO remains stable at 1mM as previously seen by DLS measurements (Figure 2.2). As ionic strength increases, interparticle repulsion decreases reducing the energy barrier. The same behavior has been seen for CeO_2 NPs in presence of KCl (*7*), magnetite NPs in NaCl (*16*) and other ZnO NPs (*25*).

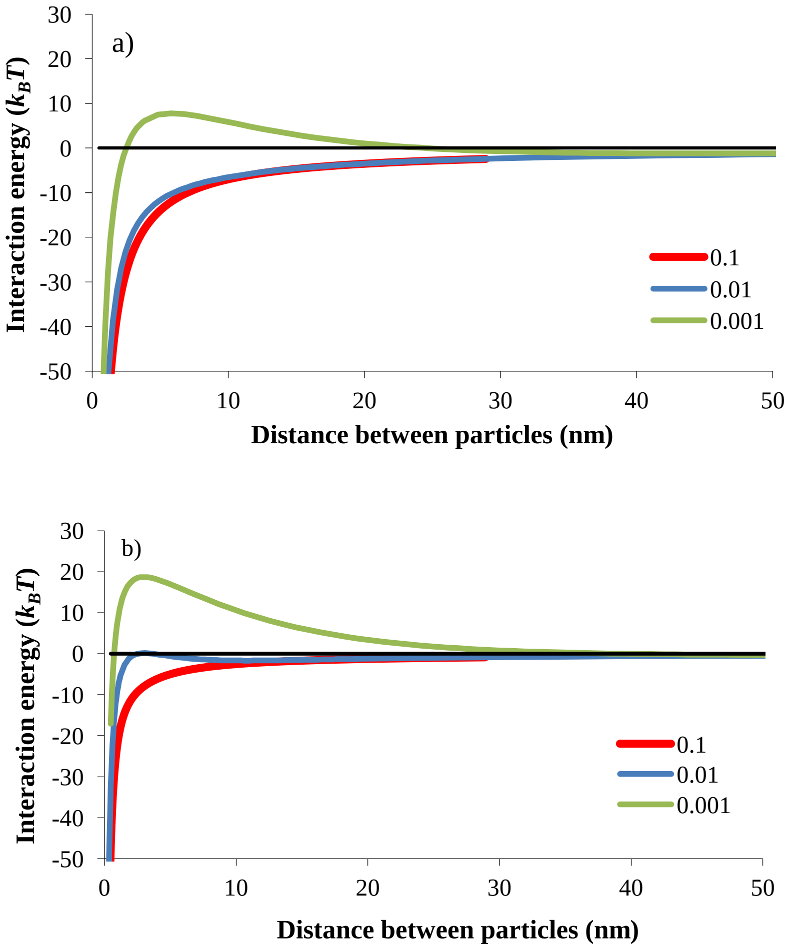

Figure 2.8. The net energy between nano-ZnO a) 71NP and b) 20NP particle suspensions for different KCl concentrations.

2.5.3. pH effect

Figure 2.9 plots the Z-average hydrodynamic diameter of nano-ZnO aggregates as a function of time for several pH values. The change in the pH between 7 and 9 do not cause changes in the aggregation process of the nano-ZnO at a concentration of 100 mg L^{-1} (NPs of 71 and 20 nm) when the ionic strength is kept constant at 0.1 M KCl (plus 0.02 M Tris). NPs tend to aggregate in all the pH range and follow a similar pattern of aggregation at the different pHs, although differences are observed depending on the type of nanoparticle. The initial average diameter for 71NP corresponds to 308 nm, reaching a hydrodynamic diameter of 2059 ± 110 nm at 50 minutes of measurement. Notice that after 50 min, the aggregate size of the NPs begins to decline. This is due to the sedimentation of NPs, as previously seen in the study of aggregation as function of ionic strength, which leads to a lower average size of the NPs that remain suspended at the height of the optical path of the DLS.

In contrast, the initial z-average hydrodynamic diameter of 20NP corresponds to 175 nm and reaches a stable diameter of 1993 ± 211 nm at 50 min. Above that, the average diameter seems to remain constant, probably due to a smaller effective density of aggregates

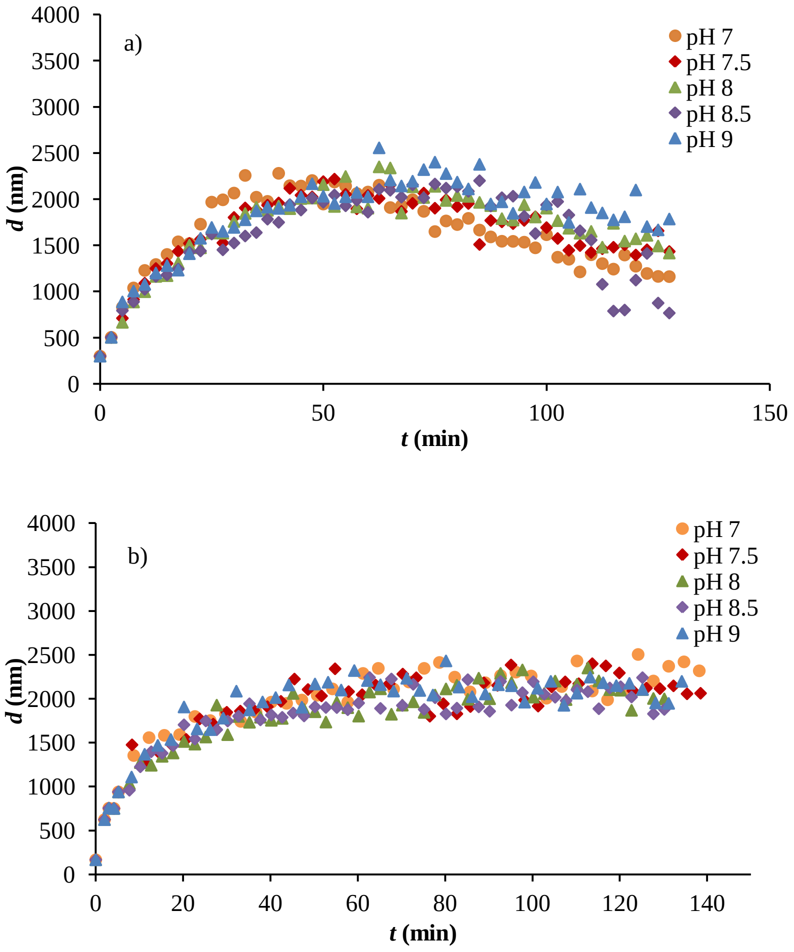

Figure 2.9. Hydrodynamic diameter of nano-ZnO aggregates (a) 71NP and b) 20NP) as a function of time and pH at 0.1 M KCl (plus 0.02 M Tris) ionic strength.

The electrophoretic mobilities of the ZnO NPs in 0.1 M KCl (plus 0.02 M Tris) solutions are presented as a function of pH in Figure 2.10. The nano-ZnO dispersions exhibit positive values at the lower pHs (pH<8) and become negative from pH 8 to 9. The instability of the aggregates in solution, measured by DLS as a function of time (Figure 2.9), agrees with the relatively small absolute values of EPM obtained. In all the studied pH range, the surface charge of the aggregates is not enough to prevent the aggregation process by electrostatic repulsions. These results are also in agreement with those obtained applying the DLVO theory where the energy barrier disappears allowing the nano-ZnO aggregation in all the studied pHs.

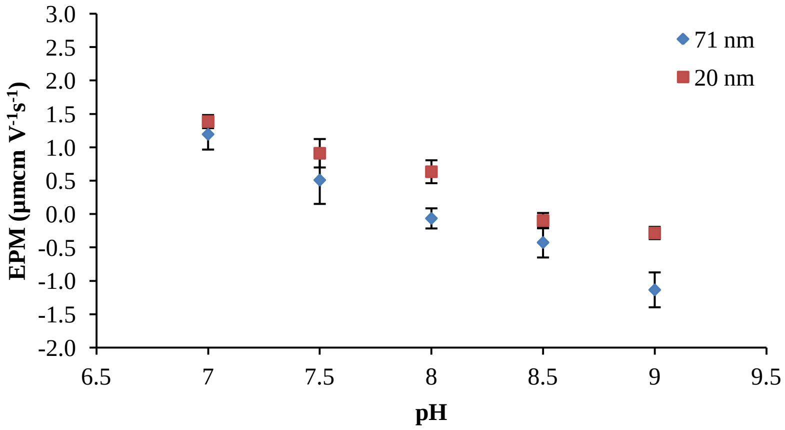

Figure 2.10. Electrophoretic mobility of 100 mg L^{-1} nano-ZnO (71NP, blue diamonds and 20NP, red squares) as a function of pH at a fixed ionic strength 0.1 M (KCl plus 0.02 M Tris).

2.5.4. Effect of particle concentration

Figure 2.11 plots the z-average hydrodynamic diameter of 71NP and 20NP ZnO aggregates as a function of time at different nanoparticle concentrations in the range 100-400 mg L^{-1}. Data show that the increase in NP concentration enhances their aggregation rate, presumably due to the higher probability of particle collisions (*26*) in agreement with Eqn. 2.9. Keller A. *et al*. have reported similar behavior for TiO_2 nanoparticles (*27*).

Notice that experimental values (markers) agree well with theoretical values (solid lines) obtained from the aggregation kinetic model explained above (see section 2.3.1) using fractal dimensions of 1.98 and 2.1 for 71NP and 20NP, respectively.

The disagreement between experimental and theoretical values at times higher than 40 minutes is due to the sedimentation of the bigger aggregates.

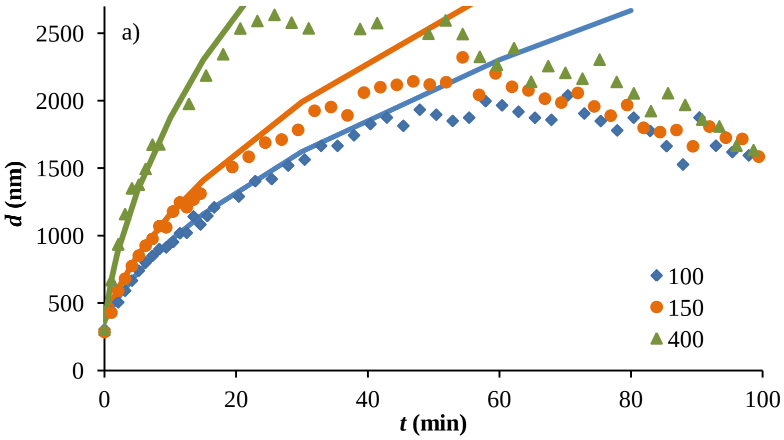

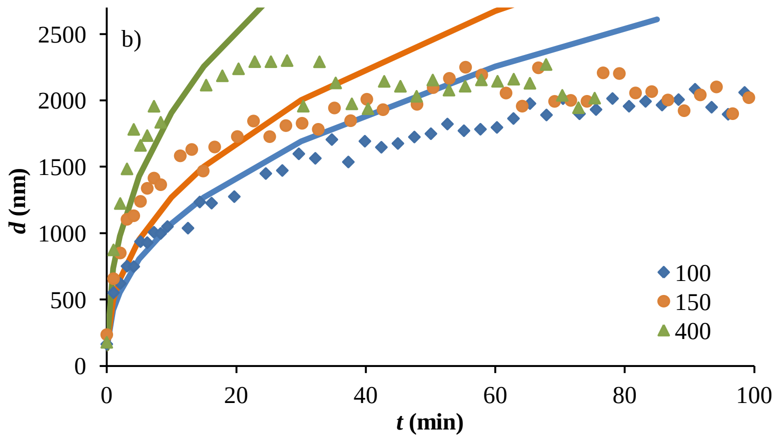

Figure 2.11. Nano-ZnO z-average hydrodynamic diameter (*d*) as a function of time and concentration of NPs (blue 100 mg L^{-1}, orange 150 mg L^{-1} and green 400 mg L^{-1}) for a) 71NP and b) 20NP. The pH is fixed at 8 and the ionic strength at 0.1 M KCl (plus 0.02 M Tris). Lines correspond to the theoretical calculations by applying equation 2.7.

2.6. Conclusions

In this study the effect of ionic strength, pH and nanoparticle concentration on the aggregation of nano-ZnO was investigated. These factors influence the stability of ZnO NPs in water affecting their fate in the aqueous environment. Several interesting implications of nanoparticle aggregation are obtained from this study.

In the case of the ionic strength, it is seen that with the addition of KCl there is an increase in the aggregation rate of ZnO NPs, that can be explained as due to the decrease of the energy barrier between nanoparticles at high ionic strength. At pH 8, the critical coagulation concentrations of KCl for nano-ZnO are approximately 10.84 mM and 22.72 mM for 71NP and 20NP, respectively. These results are consistent with the trends expected from the

DLVO theory, which indicate that higher electrolyte concentrations reduce the net energy barriers, enhancing the aggregation of the nano-ZnO.

Aggregation does not show a pH dependence within the employed pH range (between 7 and 9), when the ionic strength is relatively high (0.1 M KCl). The electrophoretic mobilities change from positive to negative values as pH increases.. However, no apparent effects are observed on the aggregation kinetics by varying the pH.

Particle concentration changes the collision frequency between particles. Here it is used a simple model of aggregation which allows to determine the aggregation kinetics of nanoparticles at different concentrations.

Therefore, based on these results, ZnO nanoparticles could either be stable or aggregate very fast, depending on the specific environmental ionic strength, pH and nanoparticle concentration conditions. Nevertheless, in real water samples such as lake water or wastewater, nanoparticles aggregate more slowly than that in synthetic solutions due to the existence of dissolved organic matter as humic substances.

2.7. References

1. Ali, M.; Winterer, M. ZnO Nanocrystals: Surprisingly 'Alive'. *Chemistry of Materials* **2010,** *22*, 85.

2. Zhou, D. X.; Keller, A. A. Role of morphology in the aggregation kinetics of ZnO nanoparticles. *Water Res* **2010,** *44*, 2948.

3. Zhang, Y.; Chen, Y. S.; Westerhoff, P.; Crittenden, J. Impact of natural organic matter and divalent cations on the stability of aqueous nanoparticles. *Water Res* **2009,** *43*, 4249.

4. Yosep Han; Donghyun Kim; Gukhwa Hwang; Byoungcheun Lee; Igchun Eom; Pil Je Kim; Meiping Tong; Hyunjung Kim Aggregation and dissolution of ZnO nanoparticles synthesized by different methods: Influence of ionic strength and humic acid. *Colloid Surface A* **2014,** *451*, 7.

5. Omar, F. M.; Aziz, H. A.; Stoll, S. Aggregation and disaggregation of ZnO nanoparticles: Influence of pH and adsorption of Suwannee River humic acid. *Sci Total Environ* **2014,** *468*, 195.

6. Nowack, B.; Bucheli, T. D. Occurrence, behavior and effects of nanoparticles in the environment. *Environ Pollut* **2007,** *150*, 5.

7. Li, K. G.; Zhang, W.; Huang, Y.; Chen, Y. S. Aggregation kinetics of CeO2 nanoparticles in KCl and CaCl2 solutions: measurements and modeling. *J Nanopart Res* **2011,** *13*, 6483.

8. El Badawy, A. M.; Luxton, T. P.; Silva, R. G.; Scheckel, K. G.; Suidan, M. T.; Tolaymat, T. M. Impact of Environmental Conditions (pH, Ionic Strength, and Electrolyte Type) on the Surface Charge and Aggregation of Silver Nanoparticles Suspensions. *Environ Sci Technol* **2010,** *44*, 1260.

9. Bian, S. W.; Mudunkotuwa, I. A.; Rupasinghe, T.; Grassian, V. H. Aggregation and Dissolution of 4 nm ZnO Nanoparticles in Aqueous Environments: Influence of pH, Ionic Strength, Size, and Adsorption of Humic Acid. *Langmuir* **2011,** *27*, 6059.

10. Tso, C. P.; Zhung, C. M.; Shih, Y. H.; Tseng, Y. M.; Wu, S. C.; Doong, R. A. Stability of metal oxide nanoparticles in aqueous solutions. *Water Sci Technol* **2010,** *61*, 127.

11. Derjaguin, B.; Landau, L. Theory of the Stability of Strongly Charged Lyophobic Sols and of the Adhesion of Strongly Charged-Particles in Solutions of Electrolytes. *Progress in Surface Science* **1993,** *43*, 30.

12. Gregory, J. Particles in Water: Properties and Processes. *IWA* **2005**.

13. Gmachowski, L. Mass-radius relation for fractal aggregates of polydisperse particles. *Colloid Surface A* **2003,** *224*, 45.

14. Schudel, M.; Behrens, S. H.; Holthoff, H.; Kretzschmar, R.; Borkovec, M. Absolute aggregation rate constants of hematite particles in aqueous suspensions: A comparison of two different surface morphologies. *J Colloid Interf Sci* **1997,** *196*, 241.

15. Mylon, S. E.; Chen, K. L.; Elimelech, M. Influence of natural organic matter and ionic composition on the kinetics and structure of hematite colloid aggregation: Implications to iron depletion in estuaries. *Langmuir* **2004,** *20*, 9000.

16. Hu, J. D.; Zevi, Y.; Kou, X. M.; Xiao, J.; Wang, X. J.; Jin, Y. Effect of dissolved organic matter on the stability of magnetite nanoparticles under different pH and ionic strength conditions. *Sci Total Environ* **2010,** *408*, 3477.

17. Chen, K. L.; Mylon, S. E.; Elimelech, M. Aggregation kinetics of alginate-coated hematite nanoparticles in monovalent and divalent electrolytes. *Environ Sci Technol* **2006,** *40*, 1516.

18. Chen, K. L.; Mylon, S. E.; Elimelech, M. Enhanced aggregation of alginate-coated iron oxide (hematite) nanoparticles in the presence of calcium, strontium, and barium cations. *Langmuir* **2007,** *23*, 5920.

19. Petosa, A. R.; Jaisi, D. P.; Quevedo, I. R.; Elimelech, M.; Tufenkji, N. Aggregation and deposition of engineered nanomaterials in aquatic environments: role of physicochemical interactions. *Environ Sci Technol* **2010,** *44*, 6532.

20. Hassellov, M.; Readman, J. W.; Ranville, J. F.; Tiede, K. Nanoparticle analysis and characterization methodologies in environmental risk assessment of engineered nanoparticles. *Ecotoxicology* **2008,** *17*, 344.

21. Filella, M.; Zhang, J. W.; Newman, M. E.; Buffle, J. Analytical applications of photon correlation spectroscopy for size distribution measurements of natural colloidal suspensions: Capabilities and limitations. *Colloid Surface A* **1997,** *120*, 27.

22. French, R. A.; Jacobson, A. R.; Kim, B.; Isley, S. L.; Penn, R. L.; Baveye, P. C. Influence of ionic strength, pH, and cation valence on

aggregation kinetics of titanium dioxide nanoparticles. *Environ Sci Technol* **2009,** *43*, 1354.

23. Zhang, Y.; Chen, Y. S.; Westerhoff, P.; Hristovski, K.; Crittenden, J. C. Stability of commercial metal oxide nanoparticles in water. *Water Res* **2008,** *42*, 2204.

24. Shih, Y. H.; Zhuang, C. M.; Tso, C. P.; Lin, C. H. The effect of electrolytes on the aggregation kinetics of titanium dioxide nanoparticle aggregates. *J Nanopart Res* **2012,** *14*, 924.

25. Liu, W. S.; Peng, Y. H.; Shiung, C. E.; Shih, Y. H. The effect of cations on the aggregation of commercial ZnO nanoparticle suspension. *J Nanopart Res* **2012,** *14*, 1259.

26. Baalousha, M. Aggregation and disaggregation of iron oxide nanoparticles: Influence of particle concentration, pH and natural organic matter. *Sci Total Environ* **2009,** *407*, 2093.

27. Keller, A. A.; Wang, H. T.; Zhou, D. X.; Lenihan, H. S.; Cherr, G.; Cardinale, B. J.; Miller, R.; Ji, Z. X. Stability and Aggregation of Metal Oxide Nanoparticles in Natural Aqueous Matrices. *Environ Sci Technol* **2010,** *44*, 1962.

Chapter 3

Interaction of ZnO nanoparticles with dissolved organic matter

3.1. Abstract

ZnO NPs strongly aggregate when ionic strength increases above 20 mM. However, this work indicates that Humic Acids (HA) present in the environmental waters act as a strong stabilizer of ZnO dispersions. Adsorption of HA on ZnO surface has been quantified with Langmuir isotherms. For HA concentrations above 8 mg L^{-1}, ZnO dispersions become stable at an ionic strength of 0.1 M. The stabilization effect is explained as due to the electrostatic repulsion between NPs due to the negative charge of the adsorbed HA. Less effective adsorption of the HA has been found as pH increases.

Stabilization of ZnO dispersions with HA can also be used as a way of selecting the average size of the ZnO aggregates by just controlling the time of the HA addition after sonication. This control allows a detailed study of the settling of the ZnO dispersions. A model based on the Stokes law has been used to fit sedimentation data of ZnO dispersions obtained with UV-Vis spectrophotometry.

3.2. Introduction

Among various materials, ZnO nanoparticles (nano-ZnO) have emerged as one of the most widely used nanomaterials in commercial products with applications such as cosmetics, pharmaceuticals, catalysis, dye-sensitized solar cells, sensors, sunscreens, coatings, optics and electronic materials (*1-3*). Because of the increase of their production and use, it is inevitable that a large amount of nanoparticles (NPs) will be discharged into the environment with expected rapid increases during next decade. Those NPs may end up in the environment, and their fate and transformation processes are difficult to evaluate and control. For this reason, there is now a wide debate about the possible risks associated with nanomaterials, including the risks for environment (*4*). Several studies have reported the adverse effects of nano-ZnO to plants, animals, bacteria and algae (*5*-*9*).

Environmental factors such as pH, ionic strength and the presence of dissolved organic matter (DOM) may result in physicochemical transformations of nanomaterials and induce their mobilization in the environment (*10*-*12*). Recently, Yang *et al*. (*13*) reported that humic acid (HA) adsorption enhances the NPs toxicity towards aquatic life as they become more mobile and dispersed in natural waters. Since NOM adsorption modifies the nanoparticle surface properties, it is important to study the changes that adsorption may have on their behavior.

This study focuses on the effects of the adsorption of humic acid (HA) onto nano-ZnO. HA was selected because of its unique polyelectrolytic and ion binding behavior, and the fact that it is an important constituent of natural dissolved/colloidal organic matter, playing an significant role in the geochemical cycles of many organic and inorganic compounds in soils and aquatic systems.

3.3. Theory

3.3.1. Adsorption isotherms

The adsorption of HA on the surface of nano-ZnO at constant temperature can be described by adsorption isotherms. These isotherms represent the amount of solute adsorbed onto the solid surface at equilibrium versus the concentration in the aqueous phase. The HA adsorption isotherms obtained experimentally resemble the shape of the classical Langmuir isotherms (see Results and Discussion) and therefore, the Langmuir Equation 3.1 was applied in this study as the adsorption model.

A detailed description of the Langmuir model can be found in any general text about colloidal physical chemistry (*14*). This model leads to the following expression for the amount of adsorbed humic acid, Γ, as a function of the humic acid concentration c_{HA} remaining in solution:

$$\Gamma = \frac{\Gamma_{\mathrm{max}} K c_{\mathrm{HA}}}{1 + K c_{\mathrm{HA}}} \tag{3.1}$$

where Γ_{max} represents the maximum amount adsorbed per ZnO mass unit, and K is a constant that represents the affinity of the adsorbate for the adsorbent.

3.3.2. Sedimentation

The model used in this work for the semi-quantitative description of the sedimentation experiments done by UV-vis spectrophotometry is based on a similar model previously described (*15*), which has been modified to consider the sample polydispersity.

It is considered that the dispersion of NPs form a water column in absence of shaking or stirring (*i.e.*, the advective forces are negligible). The NP dispersion consists of aggregates of constant size (which means that aggregation kinetics along the settling process is considered negligible). Nevertheless, we do take into account size heterogeneity of the particles, by considering a certain size distribution (polydispersity). The NP clusters are assumed independent and non-interacting (*i.e.,* the finite-volume, electrostatic, dispersive and hydrodynamic interactions are negligible). This assumption is valid for low NP concentrations (in volume fraction) and relatively high ionic strengths. Finally, the Reynolds number is assumed to be much smaller than one (laminar regime).

In this model the particles may settle down due to the balance between viscous drag and gravity forces. In steady state, this motion may be described by the Stokes law for spherical particles:

$$V = \frac{gd^2}{18\mu}\left(\rho_s - \rho_L\right) \tag{3.2}$$

where g is the gravity acceleration, d is the particle diameter, μ is the viscosity, and ρ_i is the density of the solid (S) and liquid (L) phases. Sedimentation is expected to be important in ZnO particles, since their bulk density is 5.6 g cm^{-3} (*16*).

Equation 3.2 is valid for spherical, compact particles. However, NPs in aqueous dispersion often form aggregates with complex structures. The settling velocity of these aggregates (V_{agg}) may be described to a good approximation using this extension of Stokes law (*15,17*)

$$V_{agg} = \frac{g}{18\mu}\left(\rho_{agg} - \rho_L\right) d_0^{3-FD} d^{FD-1} \tag{3.3}$$

Here, d_0 is the diameter of the primary particles (which may be obtained by TEM), d is the diameter of the aggregate (which can be measured by DLS), and FD is the fractal dimension, which is a measure of the structure of the cluster (*i.e.*: compact aggregates will have *FD* close to 3, and practically linear aggregates will have *FD* close to 1).

In addition to gravitational settling, the particles may also diffuse in all directions due to Brownian motion, with a diffusion coefficient given by the Stokes-Einstein equation:

$$D = \frac{k_B T}{3\pi d \mu} \tag{3.4}$$

where k_B is the Boltzmann's constant and T the absolute temperature.

We include the expressions for diffusion and settling into the conservation equation:

$$\frac{\partial n_i}{\partial t} = Di \frac{\partial^2 n_i}{\partial x^2} - V_{aggi} \frac{\partial n_i}{\partial x} \qquad \text{i=1...N} \tag{3.5}$$

where n_i stands for the normalized concentration of NP clusters of size *i* (we allow for a particle size distribution over *N* groups of aggregates of different sizes).

The values of the different physicochemical and geometric parameters used in the model are listed in Tables 3.1 and 3.2, respectively.

Table 3.1. Input parameters for the sedimentation-diffusion model (unless otherwise specified).

Parameter	value
ρ_L (kg m^{-3})	1.0×10^{3}
ρ_S (kg m^{-3})	5.6×10^{3}
μ (mPas^{-1})	0.89
d_0 (nm)	20 or 71
d (nm)	(from DLS)
N° of size classes (N)	20
FD	2.5

Table 3.2. Geometric parameters of the liquid column and discretization steps in the sedimentation-diffusion model applied to the description of UV-vis and DLS (Dynamic Light Scattering) data.

	x_a (mm)	x_b (mm)	l (mm)	Δx (mm)	Δt (s)
UV-vis	6	13	20	0.1	300
DLS	3	3	10	0.1	300

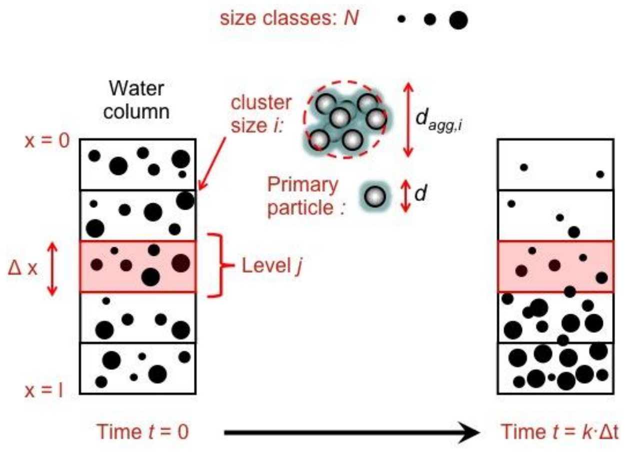

Figure 3.1. Schematic representation of the discretized transport model.

This model has been numerically solved by Dr. Calin David, who has kindly provided the calculations for comparison with the experimental results presented in this work.

3.4. Experimental section

3.4.1. Reagents

Stock solutions of nano-ZnO were obtained from dry powder nano-ZnO from two sources: Sigma-Aldrich (diameter of primary particle about 71 nm, labelled as 71NP) and Io·li·tec (Ionic Liquid Technologies GmbH, average diameter about 20nm, labelled as 20NP). The stock was prepared adding the nanoparticle powders into Milli-Q water (Synergy UV, Millipore) (1 g L^{-1}) without any other additive or background electrolyte and sonicating for 30 min.

To maintain the pH fixed, a buffer solution of Tris from Merck was used.

Potassium nitrate (Fluka, Trace Select) was used as supporting electrolyte. HNO_3 and/or KOH standard 0.1 M solutions (Fluka) were employed to adjust the pH.

Humic acid (HA) was purchased as lyophilized commercial HA (Sigma-Aldrich) and was purified using a standard purification procedure (see section 3.4.3.1.) and lyophilisation (*18*).

For the Humic acid purification procedure, hydrofluoric acid 48% (Panreac) and hydrochloric acid ≥ 37% (Aldrich) were employed. Also NaOH 0.1 and 1 M were used.

3.4.2. Instrumentation

The size distributions of nano-ZnO and their aggregates in solution were measured as hydrodynamic diameters using Dynamic Light Scattering (DLS) at 173º on a Zeta Sizer Nano ZS equipment (Malvern, Bedford, MA), which employs a He-Ne laser of 633 nm wavelength. The number-weighted particle size distributions were calculated from the DLS autocorrelation function according to the ISO13321 standard using Malvern software package (see Chapter 2 for more information). The results allowed to check the dispersion stability and to follow the average diameter of the aggregates with time.

Electrophoretic mobility (EPM) measurements were also conducted using the same equipment (Zetasizer Nano ZS), which allowed to measure the mobility of charged particles under the application of an electric field by a technique called Laser Doppler Electrophoresis.

The characteristic UV-vis absorption spectra of the nano-ZnO dispersions, as well as the changes in HA content, were recorded using a Perkin-Elmer Lambda XLS and a Specord 210 (Analytik Jena UK) spectrophotometers.

An ultrasonic bath (Branson 3210, 100 W) was use to break the aggregates formed in the stock nano-ZnO dispersions.

A glass combined electrode (Orion 9103) was attached to a pH meter Orion 920A+ (Thermo Electron Corporation) and introduced in the samples to control the pH.

Fourier transform infrared (FTIR) spectroscopy was used to investigate the adsorption of HA onto nano-ZnO. The FTIR spectrum was recorded with a Spectrophotometer FTIR Jasco 6200.

Inductively Coupled Plasma Optical Emission Spectrometry (ICP-OES) (Spectro Analytical Instruments and Activa-S, Horiba Scientific) was used to determine total Zn content in all 2.5% HNO_3 acidified samples.

Visual MINTEQ database was used to predict the metal speciation (*19*).

3.4.3. Methods

3.4.3.1. Humic acid purification

The extraction and isolation of humic acids from natural sediments and soils is a laborious process and require long periods of work. In order to reduce the extraction time, many researchers have used commercially available so-called "humic acids" in their studies. These humic acids have received some criticism (*20,21*), one of the major limitations is the lack of information relating to its origin and methods of extraction, but most researchers assumed that the commercial humic acids are representative of soil and water humic substances.

In this work commercial Sigma-Aldrich HA has been used. It is essential to purify the HA to avoid that the mineral constituents disturb the measurements and influence the behavior of HA.

Apart from the discrepancies of using commercial HA, other problems have appeared for the HA purification. The HA used in this work has been purified and characterized by other researchers and it has been concluded that it reflects many aspects found in natural HA, therefore it can be used as analogue for soil type HA in the following studies.

The purification procedure has sequentially followed these steps:

10 g of commercial Aldrich HA (Aldrich Chemie; code: H1, 675-2) were added to 800 mL of milli-Q water. 5 mL of concentrated hydrofluoric acid 48% (Panreac) and 8 mL of concentrated hydrochloric acid ≥ 37% (Aldrich) were subsequently added. The solution was stirred for 24 hours and afterwards centrifuged (Hettich Zentrifugen, EBA 21) at 6000 rpm during 30 minutes. Pellet was collected and suspended with 10 mL of HCl 1 M. The solution was centrifuged at 6000 rpm during 5 minutes and repeated twice. This step removes silica and other soluble minerals. The humic acid residue was dissolved in 500 mL NaOH aprox. 0.1 M plus adjusted to pH 10 and stirred for 24 hours. The suspension was brought to pH 2 with 36 mL 1 M HCl, stirred for 24 hours and centrifuged for 30 min at 6000 rpm. The humic acid precipitate was then dialysed against milli-Q water for about two weeks. Finally the sample was shaken with a Dowex 50WX4-50 ion-exchange resin (Aldrich) for three weeks to remove all trace metals. The humic acid obtained in this way is in its proton form, and it was freeze dried and stored in a glass container. From the lyophilized product, it was prepared a stock solution at a concentration of 500 mg L^{-1}, in MilliQ water, and pH was adjusted to 6 with 1 M KOH and/or HNO3. The stock was stored in the dark at 4 ºC.

The final samples were prepared by diluting the stock solution of HA, previously filtered through 0.45 µm PTFE membrane filters, in the solutions prepared with electrolyte (MilliQ water with adjusted pH and ionic strength) to give concentrations between 1 and 200 mg L^{-1} HA.

3.4.3.2. Humic acid adsorption onto nano-ZnO

In order to obtain the adsorption isotherms, HA solutions were prepared in 25 mL glass vials containing milliQ water with an ionic strength of 0.1 M KNO_3 and buffered with Tris 0.02 M. Different amounts of HA stock solution (filtered through 0.45 µm Whatman membrane filter) were added to reach HA concentrations ranged from 5 to 200 mg L^{-1}. An aliquot of concentrated nano-ZnO stock solution (20NP or 71NP) was then added to the solutions to yeld a final nano-ZnO concentration of 100 mg L^{-1}. All of the suspensions were adjusted to different pHs ranging from 7.5 to 9.0 with 0.1 M HNO_3 or KOH at the beginning of the adsorption experiments.

The samples, at a constant ZnO concentration but variable HA content, were shaken for 24 hours (to ensure that HA adsorption onto nano-ZnO has reached equilibrium (*22*)) at 40 rpm on an orbital shaking incubator (Labnet 211DS), where the temperature was kept constant at 25 ºC. In these conditions dispersions remained stable and homogeneous. No significant variations in pH were observed at the end of the adsorption experiment.

After incubation, the suspensions were centrifuged at 18.000 rpm for 30 minutes in an ultracentrifuge (Mikro 22R microcentrifuge, Hettich), and supernatants were extracted and analyzed by measuring the optical absorbance at 350 nm using a UV-Vis Lambda XLS spectrophotometer (PerkinElmer). By centrifugation, nano-ZnO aggregates coated with HA sediment, while the dissolved HA remained suspended. The HA adsorbed onto the surface of the nano-ZnO particles was calculated by mass difference between the HA concentration present in the supernatant and the initial HA amount (sample without centrifugation). The results were corrected taking into account the residual amount of humic acid that settles down in the absence of ZnO after centrifugation in the same conditions.

3.4.3.3. Characterization of the HA coated nano-ZnO agglomerates

Infrared spectra of nano-ZnO coated with HA

Five milligrams of HA, nano-ZnO, or HA-coated nano-ZnO were mixed gently with 95 mg of KBr as a background solid using a pestle and mortar and analyzed. FTIR spectra were recorded from 400 to 4000 cm^{-1} with 8 cm^{-1} resolution over 200 averaged scans. The FTIR spectra of HA was obtained by analyzing directly the purified and subsequently lyophilized HA. The HA coated nano-ZnO sample was obtained from a dispersion of 100 mg L^{-1} 20NP nano-ZnO in presence of 25 mg L^{-1} HA, I= 0.1 M (KNO_3 plus 0.02 M Tris) and pH 7.91. The sample was incubated for 24 hours at 40 rpm on an orbital shaker with constant temperature of 25ºC. The suspension was then centrifuged at 6000 rpm for 30 min and the precipitated material was freeze-dried. Nano-ZnO was measured directly from commercial 20NP nano-ZnO dry powder.

Size and morphology

Plunge-freezing TEM was used to characterize the two types of nanoparticles in absence and presence of different concentrations of HA. Plunge-freezing TEM allowed determining the aggregation state of ZnO nanoparticles since samples were measured as aqueous dispersions avoiding artifacts derived from the drying in the conventional grid used for TEM (*23*).

A dispersion without HA was prepared by adding an aliquot of concentrated nano-ZnO stock solution (250 mg L^{-1}) to a media containing 0.1 M ionic strength with KNO_3 as background electrolyte and buffered with 0.02 M Tris to fix a pH value of 8.0. In the case of samples with HA, aliquots of concentrated HA stock solution (500 mg L^{-1}, filtered through 0.45 µm Whatman membrane filters) were added to obtain a range of HA concentrations between 5 and 15 mg L^{-1}. Plunge freezing TEM measurements were performed by Rachel Wallace and Nicole Hondow, from University of Leeds (UK).

Agglomerate size distribution and surface charge

The effect of HA on the stability of nano-ZnO dispersions was determined by measuring the aggregate sizes and EPMs via DLS/Laser Doppler Electrophoresis. Two series of samples were measured: i) samples prepared as described above in the adsorption study section (see section 3.4.3.2.), and ii) samples prepared by diluting a stock solution of nano-ZnO (1 g L^{-1}) into a media with an ionic strength of 0.1 M KNO_3 at pH 8 (0.02 M Tris) and in the presence of HA at concentrations ranging from 0.5 to 60 mg L^{-1} HA.

Solubility

Dissolution experiments of 71NP and 20NP nano-ZnO were performed by analyzing the zinc content present in the supernatant collected from the HA adsorption studies. From these samples, the concentration of zinc ions was determined by ICP-OES after addition of HNO_3 up to a 2.5% concentration.

The total metal content present in purified and lyophilized HA was also measured by ICP-OES after digestion.

Sedimentation stability

Sedimentation dynamics of HA coated nano-ZnO was studied by measuring the absorbance of nano-ZnO, at 376 and 360 nm for 71NP and 20NP, respectively, as a function of time. Dispersions were prepared with a nano-ZnO concentration of 100 mg L^{-1}, in media of an ionic strength of 0.1M KNO_3 and pH adjusted to 8.0 (Tris buffer, 0.02 M).

These experiments were carried out to study the sedimentation rates as a function of the initial aggregate diameter, which ranged between 250 and 1500 nm. These aggregate sizes were adjusted through the addition of HA (5 mg L^{-1} for 71NP and 10 mg L^{-1} for 20NP) to the nano-ZnO dispersions at a given time after sonication and addition of saline media. The addition of electrolyte establishes the onset of the aggregation process, while the HA addition effectively stops it, yielding coated NP clusters of controlled size and electrostatically stabilized. This allows “freezing” of the kinetic aggregation process and uncoupling it from the transport processes. Depending on the time at which the HA was added after sonication (0, 10 and 30 minutes), aggregates of different sizes were obtained (see Figure 3.2).

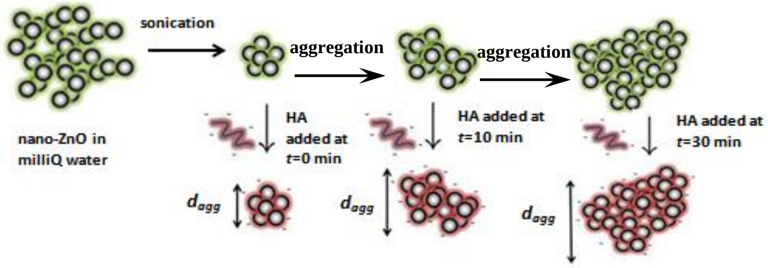

Figure 3.2. Representative scheme of the process to adjust the nano-ZnO aggregate sizes by the addition of HA at different time intervals.

3.5. Results and Discussion

3.5.1. Humic acid adsorption onto nano-ZnO

Two representative isotherms corresponding to humic acid adsorption onto nano-ZnO aggregates are shown in Figure 3.3, for both, 20NP and 71NP. The HA adsorption is fitted using the Langmuir adsorption model (lines), which has also been employed in other studies with inorganic mineral surfaces (*22*,*24*-*27*). In order to check the ability of the Langmuir model to fit the current data, adsorption values are plotted as $1/\Gamma$ *vs.* $1/c_{HA,SN}$ (subindex *SN* stands for concentrations measured in the supernatant):

$$\frac{1}{\Gamma} = \frac{1}{\Gamma_{\mathrm{max}} K} \frac{1}{c_{\mathrm{HA,SN}}} + \frac{1}{\Gamma_{\mathrm{max}}} \qquad (3.6)$$

Figure 3.3b shows the linearized isotherms corresponding to HA coated nano-ZnO at pH 8 and 0.1 M ionic strength. As can be seen, a good linear correlation is observed, supporting the validity of the Langmuir model to describe the adsorption data. Using equation 3.6 the model parameters $\Gamma_{\max}$ and K are obtained for each particle size. Table 3.3 summarizes these results.

The HA/nano-ZnO adsorption isotherms show an initial steep slope (adsorption increases as the concentration of added HA increases) and a plateau equilibrium HA concentrations above c_{HA} 0.02 and 0.16 g L^{-1} for 71NP and 20NP respectively (Figure 3.3), which indicates saturation of the ZnO surface. Similar behavior was observed for the adsorption of humic substances on ZnO nanoparticles (28), as well as on titanium oxide surfaces (24,29), other nano-metal oxides and carbon-based nanomaterials (22,25) and iron oxides (25).

Table 3.3. Langmuir model parameters for HA/nano-ZnO adsorption isotherms in 0.1M KNO_3 at pH 8 (from data shown in Figure 3.3).

Parameter	**Value**
$\Gamma_{\mathrm{max,20NP}}$ ($g_{\mathrm{HA}}\ g_{\mathrm{ZnO}}^{-1}$)	0.162
K_{20NP} (L g^{-1})	1934
$\Gamma_{\mathrm{max,70NP}}$ ($g_{\mathrm{HA}}\ g_{\mathrm{ZnO}}^{-1}$)	0.037
K_{71NP} (L g^{-1})	246

As can be observed, the amount of HA adsorbed on 20NP is much greater than that observed for 71NP nano-ZnO at comparable HA concentrations, on the basis of nano-ZnO mass loading. This is due to the much larger specific surface area of the 20NP sample. In fact, normalization of adsorbed HA amounts to the specific surface areas measured from N_2-BET analysis, of 31.8453 m² g^{-1} and 11.5467 m² g^{-1} for 20NP and 71NP, respectively (see chapter 2), reveals similar values of the maximum adsorption per surface area unit (Figure 3.3c) (*24*).

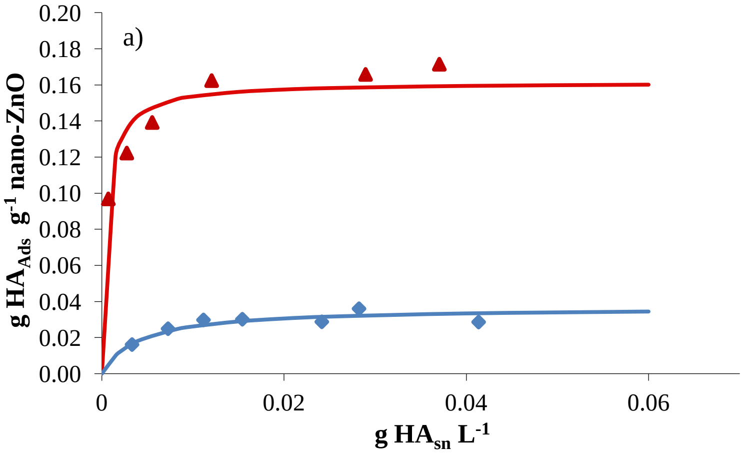

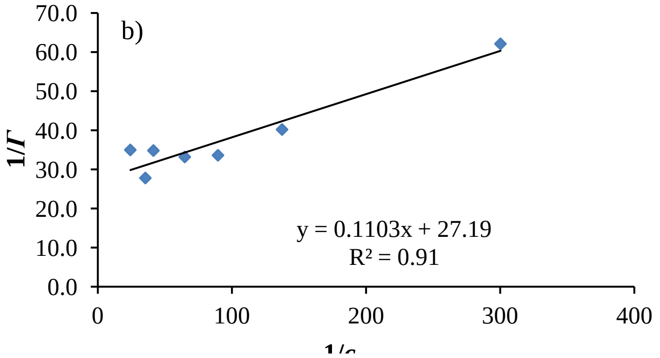
b)
70.0
60.0
50.0
40.0
30.0
20.0
10.0
0.0
1/*Γ*
y = 0.1103x + 27.19
R² = 0.91
0
100
200
300
400

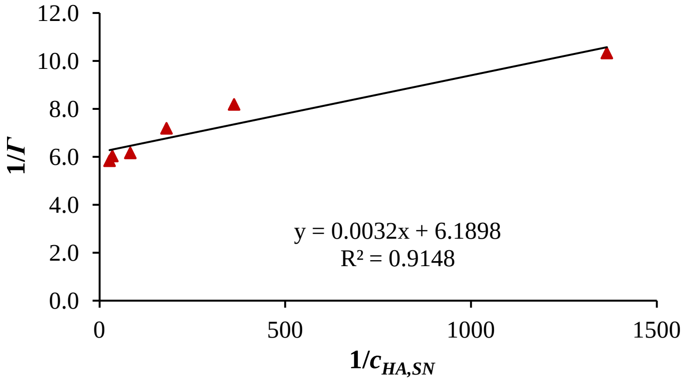
12.0
10.0
8.0
6.0
4.0
2.0
0.0
1/*Γ*
y = 0.0032x + 6.1898
R² = 0.9148
0
500
1000
1500
1/$c_{HA,SN}$

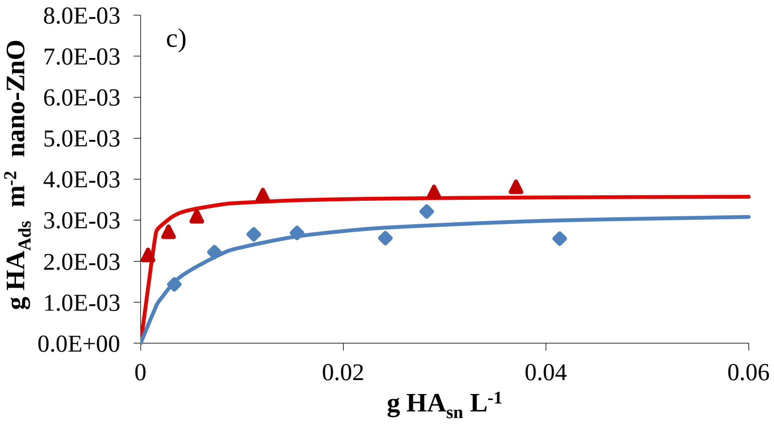

Figure 3.3. Adsorption isotherms of purified Aldrich HA on nano-ZnO at pH 8 (0.02 M Tris) and ionic strength 0.1M KNO_3, measured by centrifugation and UV-vis spectroscopy analysis of the supernatant. a) HA adsorbed per gram of ZnO *vs.* the concentration of HA remaining in the supernatant at equilibrium, b) linear regressions and c) adsorption values normalized to the specific surface area measured from N_2-BET analysis. Symbols: 20NP (red triangles); 71NP (blue diamonds). Lines: Langmuir fits.

However, the smaller ZnO NPs show stronger binding affinities for HA, as the fitted values of K indicate. This effect may be partially related to the higher charge of the smaller NPs and, most likely, to the particular structure of the NPs: NPs of 20 nm show higher porosity than 71 NPs (as indicated by TEM and BET experiments) which could lead to effectively stronger surface binding sites.

The influence of pH in the HA adsorption onto nano-ZnO was also analyzed. Figure 3.4 plots the adsorption isotherms of HA onto nano-ZnO at four pH values (7.4, 7.8, 8.3 and 8.8). The adsorption isotherms showed an initial steep slope and reached a plateau at an elevated equilibrium HA concentration (as seen in Figure 3.3a). Adsorption data can be fitted with the

Langmuir adsorption model using the linearization procedure indicated in equation 3.6. Resulting model parameters Γ_{max}, and K are listed in Table 3.4 for each particle size and pH. At pH ≤ 8 the surface of nano-ZnO is positively charged (see Chapter 2) enhancing the adsorption of the negatively charged HA, a behavior that has also been reported in the literature for other oxides (*27,30-32*). At increasing pH values, the carboxyl and phenolic groups (the main ionizable groups in HA) dissociate, and the negative charge of the HA increases (*33*). As a consequence, at pH above 8, adsorption is unfavored by electrostatic interactions because of the electrostatic repulsion between HA molecules and the negatively charged nano-ZnO surface, which, in theory, should lead to a decrease in the values of K. This seems to be the case of the 20NP sample, as reflected by the trend in the K values reported in Table 3.4. For the 70 NPs, however, the results follow the opposite tendency, although the fitting of the Langmuir model is less accurate indicating the influence of some heterogeneity of these surface interactions. Notice that, interestingly enough, the affinity of 71nm NPs tends to a similar value to that of the 20 nm NPs. This fact might be due to the electrostatic swelling of the HA as pH increases, which seems to constrain the accessibility of HA to the same sites in both the 20 and 71 nm NPs.

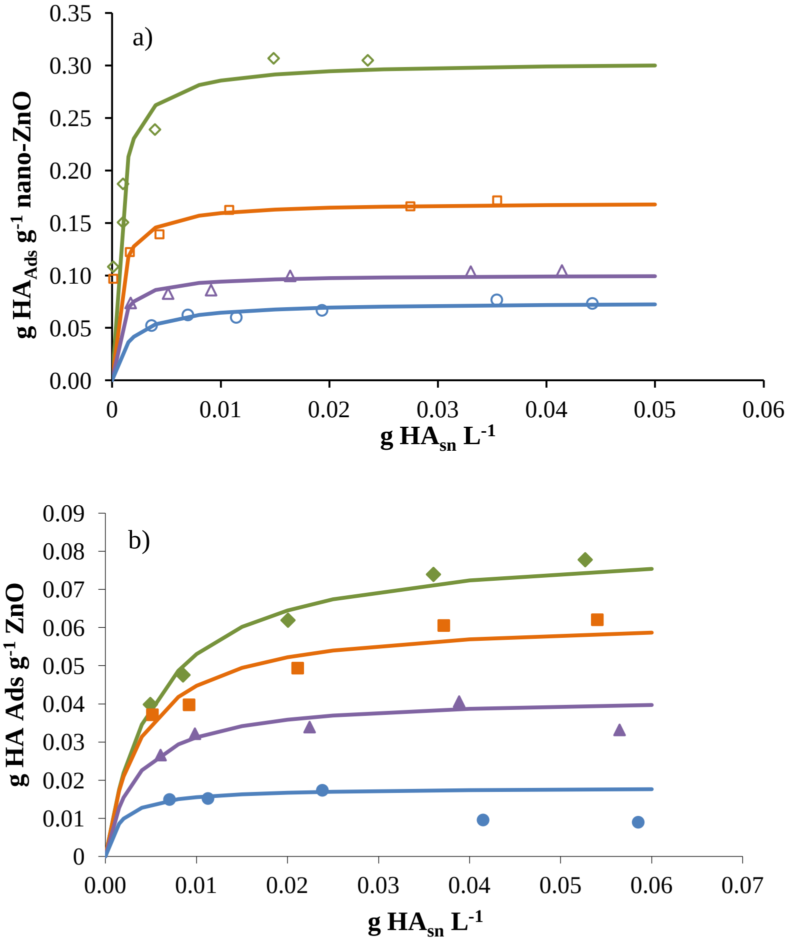

Figure 3.4. Adsorption isotherms of HA on 100 mg L^{-1} nano-ZnO a) 20NP and b) 71NP. *I*= 0.1 M KNO_3 plus 0.02 M Tris, at four different pH (green diamonds pH=7.4; orange squares pH=7.8; violet triangles pH=8.3 and blue circles pH=8.8). Lines are model fits according to equation 3.1.

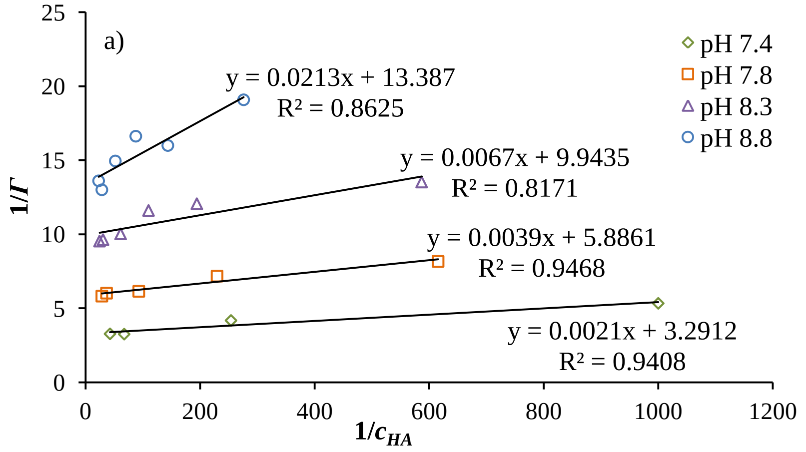

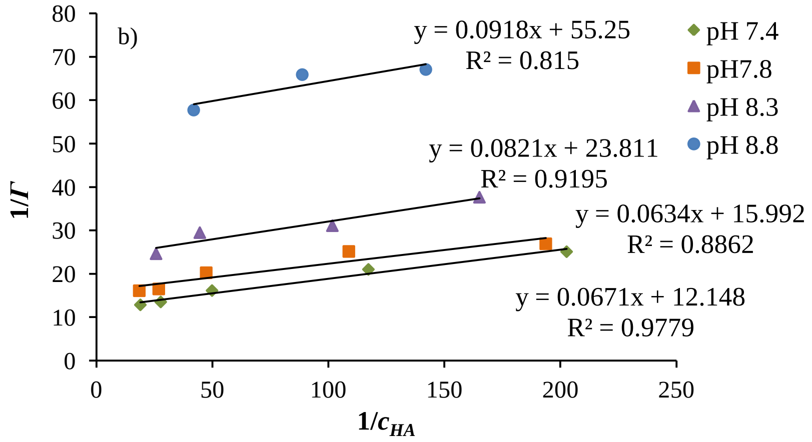

Figure 3.5. Linear regression of data corresponding to Figure 3.4 a) 20NP and b) 71NP.

Table 3.4. Langmuir model parameters for HA on nano-ZnO adsorption isotherms (from data plotted in Figure 3.4).

Parameter	**pH 7.4**	**pH 7.8**	**pH 8.3**	**pH 8.8**
$\Gamma_{max,20NP}$ (g_{HA} g_{ZnO}^{-1})	0.304	0.170	0.101	0.075
K_{20NP} (L g^{-1})	1567.238	1509.256	1484.403	628.498
$\Gamma_{max,70NP}$ (g_{HA} g_{ZnO}^{-1})	0.082	0.063	0.042	0.018
K_{71NP} (L g^{-1})	181.043	252.240	290.024	601.852

The maximum adsorption values, Γ_{max}, show significant pH dependence (Figures 3.4 and 3.6). The largest adsorption values are obtained at the lowest pH of the study (pH 7.4), *i.e.*: 0.304 and 0.082 g_{HA} g_{ZnO}^{-1} for the 20 and 71 nm NPs, respectively. The decrease of Γ_{max} as pH increases may be the result of several factors such as i) the decreasing surface charge of the ZnO; ii) the increasing size of the HA molecule as pH increases due to the intramolecular repulsion; etc.

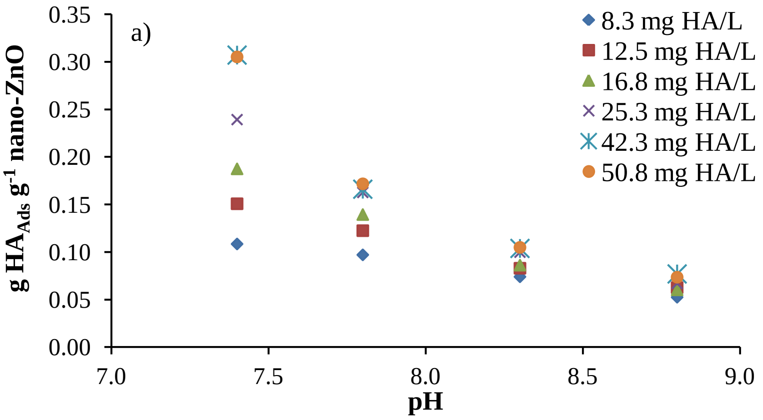

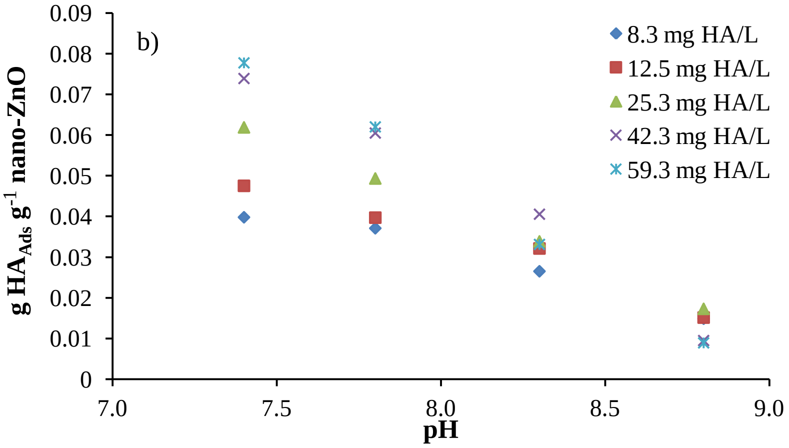

Figure 3.6. pH dependence on the adsorption of HA onto nano-ZnO (a) 20NP and b) 71NP) at different HA loadings in 0.1 M KNO_3 (plus 0.02 M Tris) as a function of pH. The values indicated in the legend correspond to the total (initial) HA concentrations.

In addition to the UV-Vis measurements of the HA adsorption onto the nano-ZnO NPs, FTIR spectra of nano-ZnO, HA and nano-ZnO coated with HA have also been recorded.

Figure 3.7 presents the FTIR spectra of HA, nano-ZnO and HA coated nano-ZnO. For nano-ZnO, Yang *et al*. (*22*) have analyzed and described the major absorption bands in FTIR spectra. One of these corresponds to the peak at 456 cm^{-1} and it is attributed to the Zn-O stretching vibration. This is the most important peak of this spectrum and it is also recognized in the coated nano-ZnO. The broad absorption band at 2500-3700 cm^{-1} in the ZnO spectrum can be assigned to hydroxyl group stretching coming from residual water molecules attached to the ZnO surface. Similarly, the peaks at 1630 and 1473 cm^{-1} are residual peaks of water attached to the ZnO surface or traces of other contaminants like carbonates (*34*,*35*).

The IR spectra of HA is consistent with those generally shown by humic substances in aquatic systems (*36*). Gu *et al*. (*25*) described that the major absorption bands are in the regions of 2918 and 2860 cm^{-1} (C-H stretching of $–CH_3$ and CH_2 groups), 1712 cm^{-1} (C-O stretching of COOH), 1595 cm^{-1} (C=O stretching of COO-, ketonic C=O and aromatic C=C conjugated with COO^-), 1383 cm^{-1} (CH deformation of CH_3 and CH_2 and COO^- asymmetric stretching), 1100-1300 cm^{-1} (OH stretching of phenolic OH and C-O stretching and OH deformation) and 1034 cm^{-1} (C-O stretching of carbohydrates and polysaccharide-like substances). In the region of 3400 cm^{-1} Shin *et al*. (*37*) described a band associated with OH stretching of carboxyl, phenol and alcohol, and Wahab *et al*. associates the peak centered at 2369 cm^{-1} with the presence of CO_2 (*35*).

The comparison of the three spectra shown in Fig. 3.7 evidences that most of the peaks of HA as well as those of ZnO appear in the spectra of the nano-ZnO coated with HA. The main modifications appear in the fingerprint region of the IR spectra and correspond to the changes in the frequencies of the normal modes of vibration that involve the chain of the HA, which are quite sensitive to the interactions with the ZnO surface. Gu *et al*. (*25*) and Yang *et al*. (*22*) described the effect of interactions between HA and nano-ZnO on the IR spectra. For HA bound to nano-ZnO, the peaks at 2918 and 2850 cm^{-1} were associated to C-H stretching of aliphatic $–CH_2$ and $–CH_3$ groups of HA. The peak at 1712 cm^{-1} corresponding to the C-O stretching of carboxylic groups is shifted to 1600 cm^{-1}, indicating that COO^- functional groups of HA may be directly bound to the nano-ZnO surface. The complexation between COO^- of HA and nano-ZnO is also evidenced by the appearance of a new strong band at 1400 cm^{-1}. This interpretation has also been reported in studies of soil fulvic acid interacting with Fe to form iron fulvate-like complexes with goethite (*38*). Another important feature in the spectra is the decrease in the observed bands of the aliphatic –OH region (1300-1100 cm^{-1}) for HA adsorbed on nano-ZnO with respect to the pure HA, which indicates the participation of phenolic (*39*) and other C-O groups in surface complexation, although it could also be ascribed to the replacement and release of nano-ZnO-adsorbed carbonate after HA coating (*40*). Finally, HA adsorbed on zinc oxide shows a relatively strong adsorption band at 1100 cm^{-1}, which can be attributed to the adsorbed carbohydrates or polysaccharide-like substances. The shift of this band (with respect to pure HA) may also indicate the complexation of C-O functional groups of HA with zinc oxide surface and/or a contribution of H-bonding mechanisms.

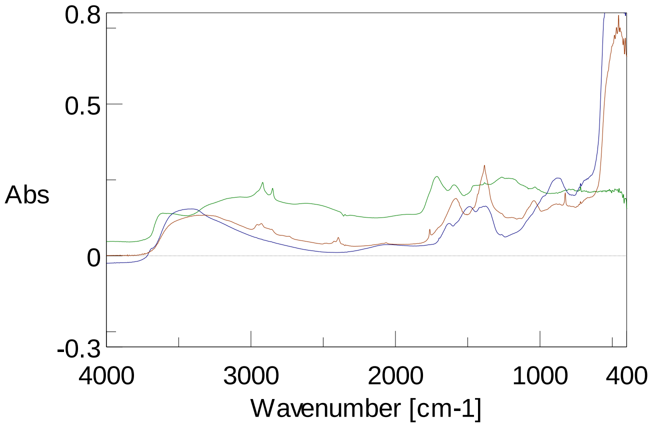

Figure 3.7. FTIR spectra of bulk HA (green), 20NP nano-ZnO (blue) and HA coated nano-ZnO (red). Experimental conditions are explained in section 3.4.3.2.

3.5.2. Stabilization of aggregates in the presence of humic acid

The ability of the HA to stabilize nano-ZnO was evaluated by examining the z-average hydrodynamic diameter of the aggregates for a varying HA concentration in the range (8.3-60 mg L $^{-1}$) and different pH values in the range (7.42-8.75). Figure 3.8 shows the average hydrodynamic diameters after 24 hours. In the absence of HA, an ionic strength of 0.1 M KNO_3 (0.02 M Tris) quickly induced the aggregation of nano-ZnO over time (see Chapter 2). In contrast, the presence of HA efficiently stabilized the nano-ZnO preventing their aggregation even at low concentrations, leading to relatively small sizes of the aggregates, which remained constant over time. For instance, with the addition of only 8.3 mg L $^{-1}$ HA the 71NP nano-ZnO showed stable average diameters of 336 ± 36 nm within the pH range of 7.42 to 8.75 (Figure 3.8b). However, 20NP nano-ZnO dispersions are only stabilized by this HA concentration above pH 7.81 (Figure 3.8a). The resulting diameter of the aggregates at the largest pH values is 160 ± 5 nm. The different behavior with respect to aggregation of 20NP and 71NP at pH 7.42 may be due to both the effect of pH on the HA conformation and the higher specific surface area of the 20NP derived from the smaller size of the aggregates. At pH 7.42, HA concentrations below 25 mg·L^{-1} are not enough to cover the entire surfaces of the 20NP nano-ZnO aggregates (as shown in the adsorption isotherms described in the previous section), and a similar thing happens at pH 7.81 with 8.3 mg L $^{-1}$ HA. Therefore, the remaining “free” surface may interact with HA adsorbed on other NPs leading to a ‘”bridging effect’’ (*28,41*). This effect is reduced when the HA content increases, since then there is enough humic acid to totally cover the particle surface without bridging, which is less entropically favored. This effect is not observed for 71NP at the lowest HA concentration since the specific surface area of 71NP is 4 times lower. The structural conformation of the humic acid macromolecules is ruled by pH and ionic strength (*42*). At low pH, interactions due to hydrogen bonds, van der Waal's forces and π-orbitals in conjugated aromatic rings within the humic macromolecules, favor a more compact conformation of the HA macromolecules and intermolecular association (*43*). Moreover, intermolecular interactions may induce the formation of dipoles through the delocalization of aromatic-ring π-electrons, thus favoring the aggregation of the macromolecule humic. Conversely, at neutral to alkaline media, the molecule tends to be extended as a result of intramolecular electrostatic repulsion. This effect may have an influence on the surface area fraction of ZnO actually covered by the adsorbed HA.

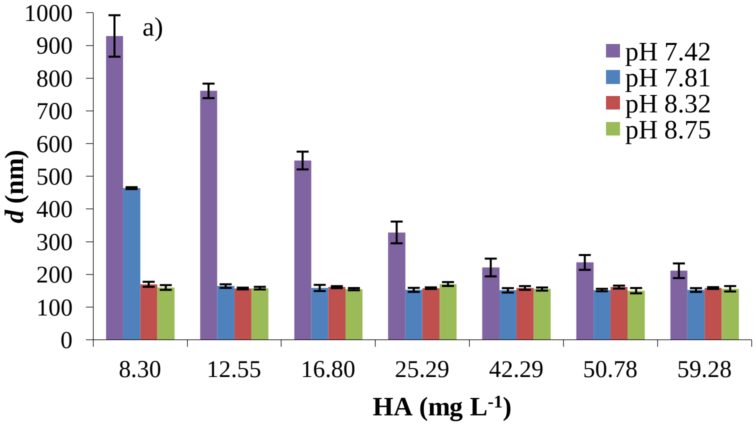

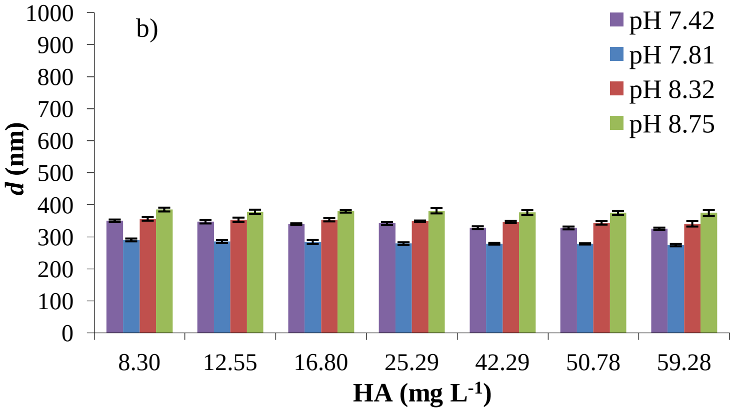

Figure 3.8. Z-average diameters of HA coated nano-ZnO dispersions at 100 mg L^{-1} of a) 20NP and b) 71NP) as a function of HA concentration and pH (violet pH=7.42; blue pH=7.81; red pH=8.32 and green pH=8.75). Media: 0.1 M KNO_3 plus 0.02 M Tris.

In order to get a further insight of the mechanisms through which HA hinders the aggregation of nano-ZnO, the impact of HA on nano-ZnO surface charge as a function of pH and HA concentration was evaluated. Figure 3.9 shows the variation of the EPM values of coated HA nano-ZnO with pH. The measurements were done at a ZnO concentration of 100 mg L^{-1}, in 0.1 M KNO_3 media with 0.02 M Tris to adjust the pH at different values (between 7.5 and 9), and with a constant HA concentration of 25.3 mg L^{-1}.

In absence of HA, EPM values decrease from positive to negative values with increasing pH, with a point of zero charge (PZC) at *ca.* pH 8 for 71NP and 8.5 for 20NP (see Chapter 2), which by definition is the pH where the net charge is zero. In presence of HA (25.3 mg L^{-1}), at the same conditions of ionic strength and pH, the EPM curve has negative values in the whole pH range tested. With 25.3 mg L^{-1} HA at pHs lower than the PZC, negatively charged HA neutralizes the positive charges on nano-ZnO, and therefore decreases the EPM. This is due to the fact that HA macromolecules carry negatively charged functional groups, including carboxylic (-COOH) and phenolic groups (-OH) (*30,44-46*). The presence of these groups provides negative charge (*46*), which increases the electrostatic repulsion and stabilizes the nano-ZnO aggregates (*28*).

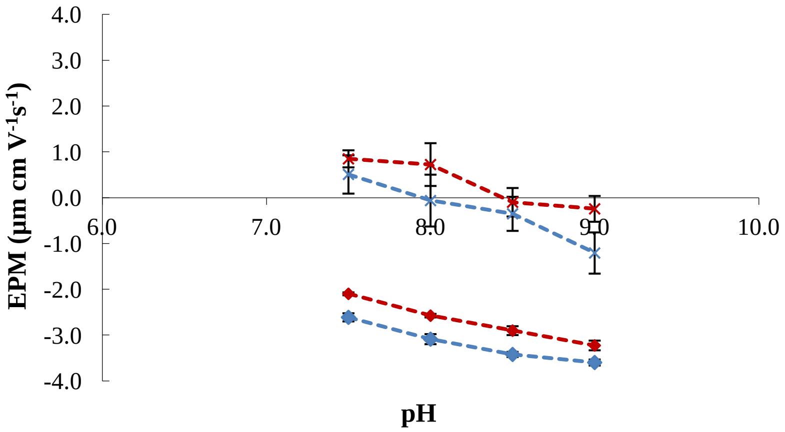

Figure 3. 9. Electrophoretic mobility of 100 mg L^{-1} nano-ZnO dispersions (20NP, red, and 71NP, blue) as a function of pH in the absence (crosses) and presence (diamonds) of 25.3 mg L^{-1} HA at a total ionic strength of 0.1 M (0.02 M Tris). The dashed lines are plotted as a guide to the readers' eyes.

In addition, no significant changes are observed in the EPM values as the HA concentration increases from 8.3 to 60 mg L^{-1} (Figure 3.10).

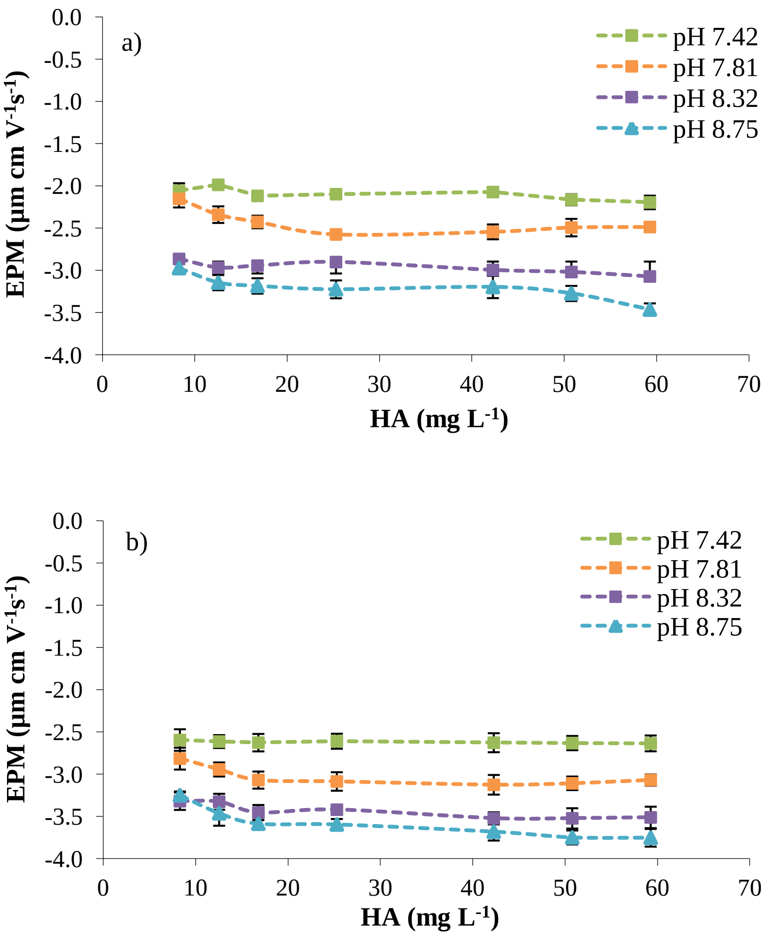

Figure 3.10. Electrophoretic mobility of 100 mg L^{-1} nano-ZnO dispersions (a) 20NP and b) 71NP) as a function of HA concentration and pH, at 0.1 M ionic strength (plus 0.02 M Tris).

In order to examine the effect of HA on nano-ZnO aggregation after HA adsorption, plunge-freezing TEM images were obtained. Figure 3.11 shows that nano-ZnO appeared to be largely agglomerated in the absence of HA at this ionic strength. On the contrary, in presence of low concentrations of HA, the micrographs show nano-ZnO clusters that are much smaller in size, due to the electrostatic stabilization mechanism (in good agreement with the DLS and EPM measurements presented above).

Moreover, it can be observed that the primary particles of 20NP and, especially, 71NP show a non-uniform morphology. 20NP are around 20 nm in diameter and 71NP have a wide size distribution, consisted with the manufacturer reported value.

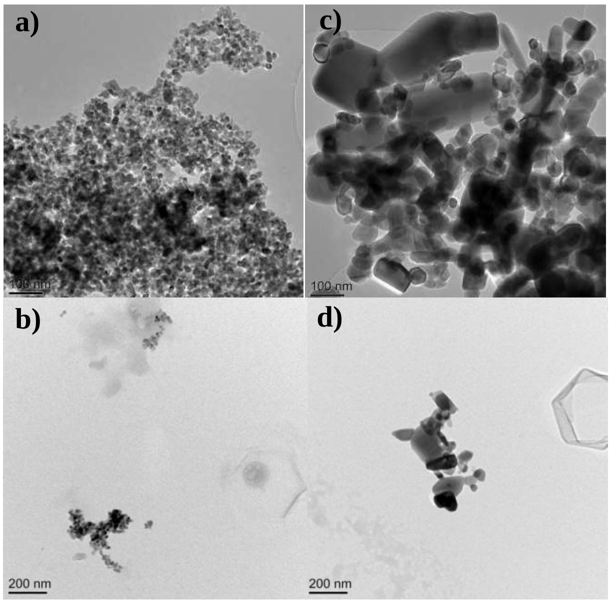

Figure 3.11. TEM micrographs of nano-ZnO suspended in 0.1 M KNO_3 (plus 0.02 M Tris) and pH 8 a) for 20NP and c)71NP (both at 19.000 x) and plunge-freezing TEM in presence of 15 and 5 mg L^{-1} HA for b) 20NP and d) 71NP.

3.5.3. Solubility of HA coated nano-ZnO

The dissolution process of ZnO:

$$ZnO_{s,zincite} + H_2O \overset{K_{sp}}{\longleftrightarrow} Zn^{2+} + 2OH^- \qquad (3.7)$$

can be described by the solubility product K_{sp} which depends, among other factors, on the pH of the solution and the size of the nano-ZnO. The solubility equation can be rewritten as

$$\log\left(\frac{[Zn^{2+}]}{M}\right) = \log\left(\frac{K_{ps}}{\gamma_{Zn^{2+}} K_w^2}\right) - 2pH \qquad (3.8)$$

being $\gamma_{Zn^{2+}}$ the activity coefficient for Zn^{2+} ions and K_w the ionic product of water. Equation 3.8 indicates a linear dependence of the logarithm of the free Zn^{2+} concentration with respect to pH (*47*), so that a decrease of one-half a unit of pH leads to an increase of one order of magnitude in the free metal concentration and, consequently, in the solubility. Thus, we can say that the solubitity of ZnO is strongly pH dependent.

There is also a specific size effect on the values of k_{ps} that leads to a slight increase in solubility with decreasing size (see Chapter 4), although it is quantitatively less important than pH.

Previous studies have shown that adsorbed natural organic matter can either inhibit or promote the rate of dissolution of metal oxides by steric protection or ligand-promotion processes, respectively. Shao-Wei Bian *et al*. (*39*) studies of ZnO nanoparticles have shown that humic acid does not have a significant effect on the rate of dissolution of ZnO nanoparticles at three different pH conditions (pH 6.0, 3.0, and 1.0). They consider that this may be due to the low coverage of the ZnO surface by the dissolved humic acid under the conditions of the experiment. The effect of humic acid content on the dissolution of nano-ZnO at four different pH values is depicted in Figure 3.12. It is shown that the solubility of nano-ZnO increases as pH decreases. This behavior agrees quantitatively with Equation 3.8, which indicates the free Zn^{2+} concentration that fulfills the solubility equilibrium at each pH. However, the dissolved fraction involves not only the Zn^{2+} ions, but also all the soluble complexes of Zn (with organic and inorganic ligands). Therefore, the ZnO solubility in presence of HA should increase with respect to that in pure water at the same pH, due to the formation of Zn-HA complexes. Figure 3.12 shows the calculated total dissolved Zn concentrations in solution according to Visual MINTEQ speciation code (lines in Fig. 3.12), using the generic NICA parameters to describe the complexation with HA. It can be observed that the theoretical values agree quite well with the experimental data (markers on Fig. 3.12) except for the smaller pH considered, pH=7,4, where a noticeable difference between solid lines and markers arise. This difference can be explained by an incomplete saturation of the solution in the timescale of the measurement, small changes in pH during adsorption, etc.

The influence of the HA concentration on the solubility is relatively small, according to the results depicted in Figure 3.12. Notice that markers corresponding to the highest HA concentration tend to correspond to the highest dissolved Zn concentrations at a given pH, despite the very small differences among HA concentrations. The generic NICA Donnan parameters seem to be useful to describe the Zn-HA complexation above pH 7.5.

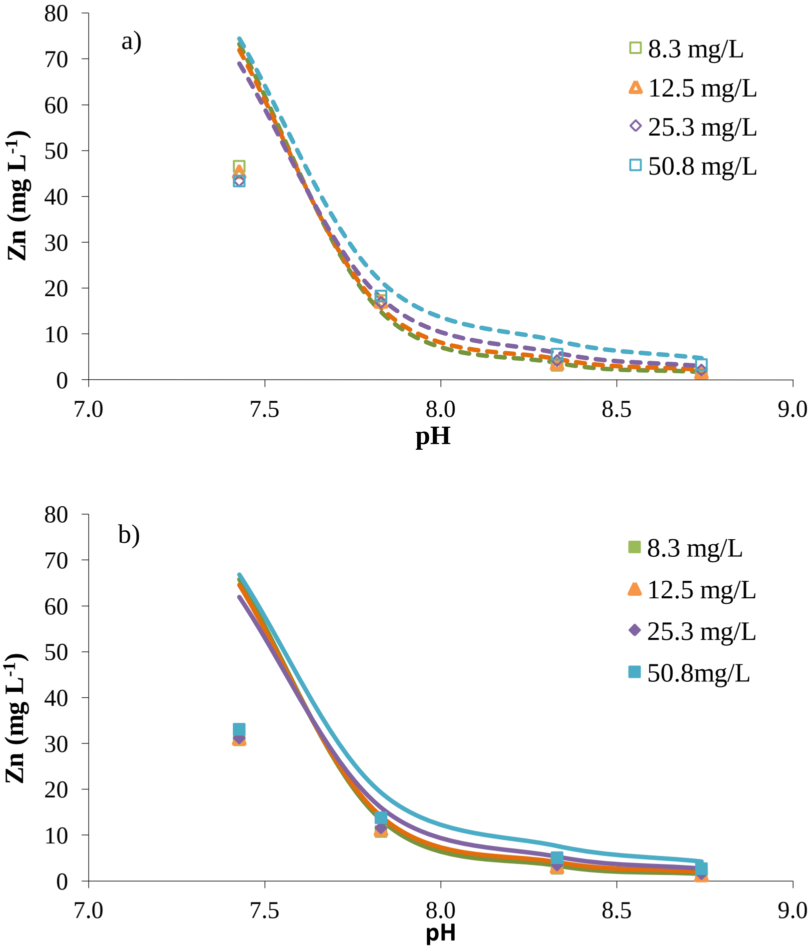

Figure 3.12. Amount of dissolved Zn (mg L^{-1}) as a function of pH and HA concentration (values indicated in the legend correspond to total concentrations) at 298K, for a) 20NP; b) 71NP. Each sample consisted of 100 mg L^{-1} of solid nano-ZnO in 0.1 M KNO_3 plus 0.02 M Tris. Lines represent Visual MINTEQ calculations.

The amount of background Zn was independently measured in digested aliquots of the pure HA, yielding a content of 0.0042 mg Zn per gram of

HA. These negligible blank values were not taken into account in the Visual MINTEQ calculations.

Differences in solubility relative to size have been observed using a set of NPs ranging from 6 to 71 nm NPs (*47*). Figure 3.12 shows the equilibrium Zn concentration in solutions of ZnO NPs of different diameter of the primary particle. At 24 hours and pH 7.43, the solubilities of 20NP and 71NP are 44.7 ± 1.6 mg L^{-1} and 32 ± 1 mg L^{-1}, respectively. Differences are not so noticeable at larger pH values, *e.g.*: at pH 8.7 with solubilities of 2.2 ± 0.8 mg L^{-1} (20NP) and 1.8 ± 0.6 mg L^{-1} (71NP). Moreover, smaller primary particle size and larger specific surface area result in faster dissolution kinetics of ZnO particles according to literature (*34,39,48*).

3.5.4. Sedimentation stability

In order to study the sedimentation of nano-ZnO, dispersions with different average agglomerate sizes were prepared by adding a fixed amount of HA to a fresh dispersion at different times of 0, 10 and 30 minutes after sonication, according to the procedure described in section 3.3.3.3. and Figure 3.2. Sizes between 280 and 1600 nm (Table 3.5 and Figure 3.13), as measured with DLS, were obtained. The aggregates have a strong repulsive electric double layer that keeps the suspensions stable, over the time of the settling experiments.

Table 3.5. Average sizes of the aggregates in the samples used for settling experiments, obtained with different delays in the addition of HA after sonication. These data correspond to the % volume distributions represented below.

***t* (min)**	**71NP (*d*.nm)**	**20NP (*d*.nm)**
0	380 ± 5	280 ± 40
10	870 ± 30	630 ± 50
30	1500 ± 180	960 ± 220

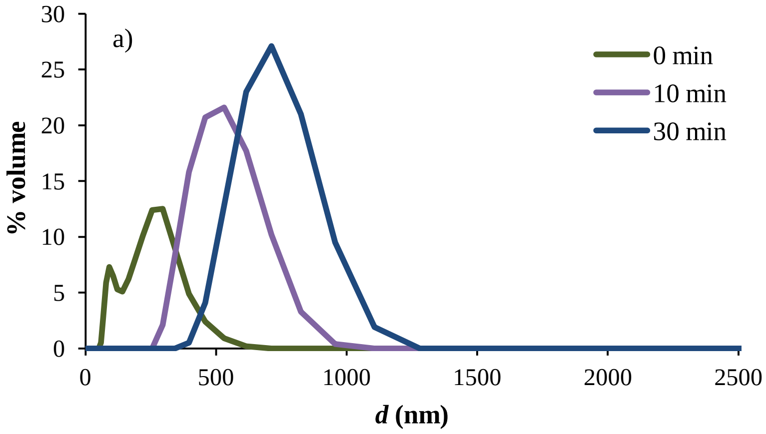

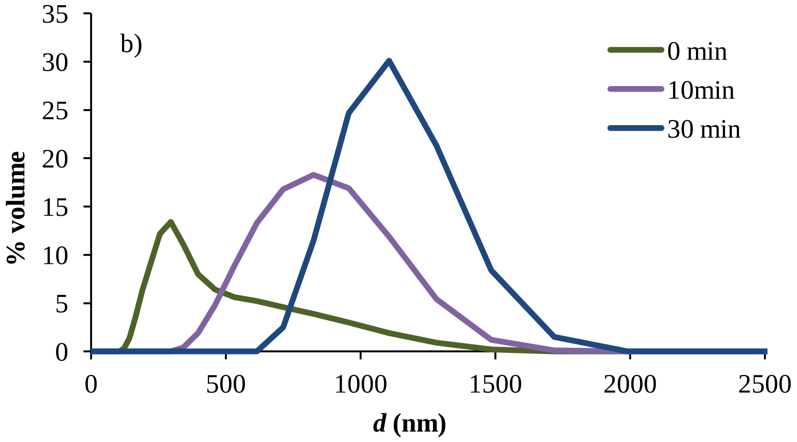

Figure 3.13. Experimental DLS measurements on % volume corresponding to the samples employed in sedimentation experiments: a)71NP and b) 20NP (see Figure 3.14 for detailed experimental conditions).

It was observed that according to the initial size of the aggregates, nano-ZnO settles at different rates (Figure 3.14).

As expected, the concentration of larger particles decays more quickly than that of the smaller particles, which may remain in solution for longer times. For the dispersion of average size 1500 ± 180 nm, the concentration of suspended 71NP aggregates decrease more than 70% in 2.5 h. The remaining fraction in solution increases as the sizes of nano-ZnO aggregates decrease, leading to characteristic shapes in the curves displayed in Figure 3.14: notice that they are not completely smooth but show some steps. These steps reflect the distribution of sizes for a given average value. Thus, for the average size of 1500 nm, the line in Figure 3.14 shows a step at t=1,4 h. This step is due to the complete fast settling of the largest NP aggregates. From that point, settling is mainly determined by the remaining aggregates of lower size. Thus, for a multimodal size distribution, the markers in Figure 3.14 show the presence of characteristic inflection points in the sedimentation profile. For long enough times, only the smallest particles remain in suspension.

Different sedimentation patterns were observed between the two types of nanoparticles. In the case of 20NP, the sedimentation was slower (Figure 3.14b). The larger aggregates (960 ± 220 nm) took 20 h to reach 80% sedimentation. The smallest aggregates almost do not settle and the suspensions remained stable over a long period of time. Aggregates of 280 ± 40 nm size only achieved a 10% settling at 15 h and 630 ± 50 nm aggregates reached only 20 % sedimentation, at 20 hours. These differences may be explained by the fact that the aggregates formed by 20NP are less dense than the 71NP, forming less compact structures with increased branching.

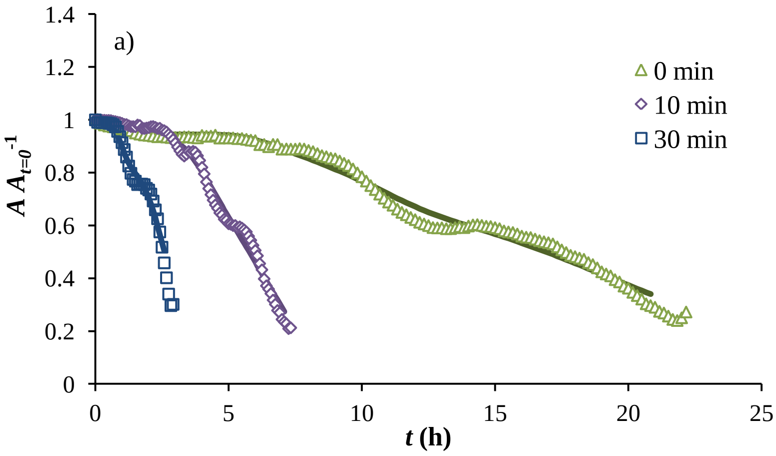

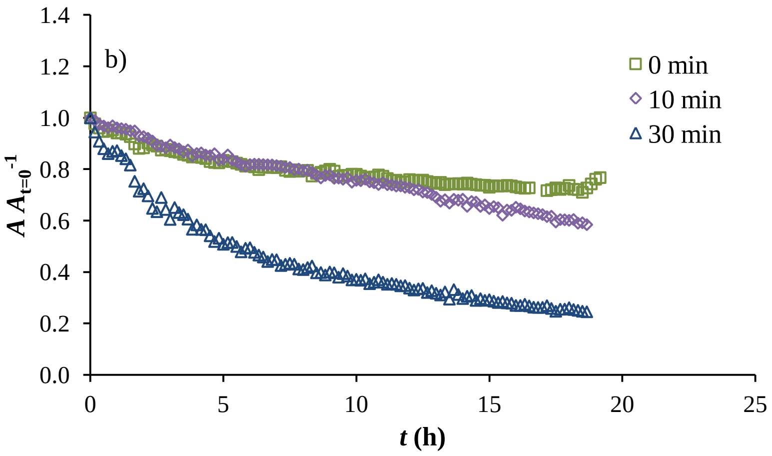

Figure 3.14. Nano-ZnO sedimentation plots for a) 71NP and b) 20NP as a function of time at 100 mg L^{-1}, I= 0.1M KNO_3 and pH fixed at 8 with 0.02 M Tris buffer. HA concentrations: 5 and 10 mg L^{-1}, for 71NP and 20NP, respectively. The continuous line in a) corresponds to the fitted sedimentation-diffusion model described in section 3.3.2.

When aggregation during the settling process can be neglected, the vertical transport of a polydisperse ensemble of NP aggregates throughout a quiescent water column is a balance between diffusion and gravitational settling, as mentioned in section 3.3.2.

The model detailed in that section describes accurately the sedimentation/centrifugation profiles, by fitting the sample size distribution (which agrees with DLS data) and the effective density of the aggregates (see continuous line in Figure 3.14a).

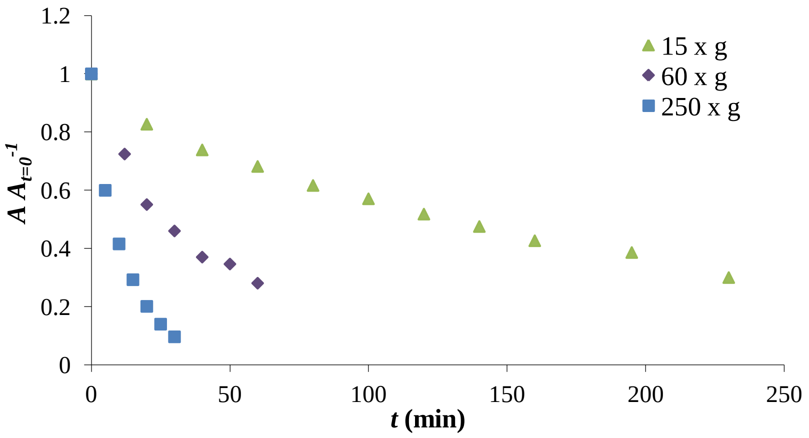

Figure 3.15. Settling of 20NP ha-coated nano-ZnO under a centrifugal field, as a function of time and acceleration (15 x g, 60 x g and 250 x g) (pH 8, I= 0.1 M KNO3 plus 0.02 M Tris, 100 mg L^{-1} nano-ZnO).

Finally, the sedimentation of samples of HA coated 20NP nano-ZnO (having average aggregate diameters of 260 nm, as measured by DLS) was studied using varying centrifugal fields. The resulting plots of the normalized adsorbance measured in the supernatant as a function of time and acceleration are shown in Figure 3.15. The analysis of these results using the sedimentation/diffusion model of fractal NP aggregates (section 3.3.2) allowed us to estimate an average density of the aggregates of ρ_{eff} = 2.3 g cm^{-3}.

3.6. Conclusions

This study shows the effect of the solution chemistry (particle properties, pH and content of HA) on the aggregation, dissolution and sedimentation process of nano-ZnO at a given ionic strength. The understanding of the interactions between HA and nano-ZnO is helpful for the prediction of the transport and fate of ZnO NPs in the environment.

In particular, the present study has analized the impact of humic acid on the behavior of nano-ZnO. DLS and electrophoretic mobility measurements have been used to investigate the stability of suspensions containing nano-ZnO in the presence of HA. At 0.1 M ionic strength, HA above a critical concentration shows an inhibition of the aggregation of ZnO NPs. The observed stabilization was due to the electrostatic repulsions among coated aggregates with a corresponding shift of the electrophoretic mobility to negative values. However, a concentration of HA as small as 8.3 mg L^{-1}, does not completely inhibit aggregation of the 20NP particles at low pH, probably due to a bridging mechanism among the partially covered aggregates.

The dissolution of HA coated nano-ZnO showed a dependence on pH and size. Smaller nanoparticles show higher solubility compared to larger particles. On the other hand, the nano-ZnO dissolution shows a negligible dependence on the amount of HA added, between 8.3 and 60 mg L^{-1}, in all the pH range studied (7.42-8.75).

Adsorption experiments have shown that the adsorption of HA onto nano-ZnO can be accurately described with a Langmuir isotherm model. The adsorption parameter $\Gamma_{\max}$ increases as pH decreases. At low pH, the negatively charged HA adsorbs on positive and neutral NPs resulting in charge inversion. Nevertheless, HA is also adsorbed on negatively charged nano-ZnO indicating that other interaction mechanisms apart from electrostatics may play an important role. The FTIR spectrum suggests that carboxylate and phenolic groups participate in the complexation with the nano-ZnO surface.

Finally, the implementation of the sedimentation model discussed above allows determining the characteristic settling times of the nano-ZnO aggregates in quiescent media. This process depends on the sizes and fractal dimension of the aggregates formed, as well as the density of the medium.

3.7. References

1. Ju-Nam, Y.; Lead, J. R. Manufactured nanoparticles: An overview of their chemistry, interactions and potential environmental implications. *Sci Total Environ* **2008,** *400*, 396.

2. Becheri, A.; Durr, M.; Lo Nostro, P.; Baglioni, P. Synthesis and characterization of zinc oxide nanoparticles: application to textiles as UV-absorbers. *J Nanopart Res* **2008,** *10*, 679.

3. Tang, X. S.; Choo, E. S. G.; Li, L.; Ding, J.; Xue, J. M. Synthesis of ZnO Nanoparticles with Tunable Emission Colors and Their Cell Labeling Applications. *Chemistry of Materials* **2010,** *22*, 3383.

4. Park, S.; Woodhall, J.; Ma, G. B.; Veinot, J. G. C.; Cresser, M. S.; Boxall, A. B. A. Regulatory ecotoxicity testing of engineered nanoparticles: are the results relevant to the natural environment? *Nanotoxicology* **2014,** *8*, 583.

5. Xia, T.; Kovochich, M.; Liong, M.; Madler, L.; Gilbert, B.; Shi, H. B.; Yeh, J. I.; Zink, J. I.; Nel, A. E. Comparison of the Mechanism of Toxicity of Zinc Oxide and Cerium Oxide Nanoparticles Based on Dissolution and Oxidative Stress Properties. *Acs Nano* **2008,** *2*, 2121.

6. Nel, A.; Xia, T.; Madler, L.; Li, N. Toxic potential of materials at the nanolevel. *Science* **2006,** *311*, 622.

7. Brayner, R.; Dahoumane, S. A.; Yepremian, C.; Djediat, C.; Meyer, M.; Coute, A.; Fievet, F. ZnO Nanoparticles: Synthesis,

Characterization, and Ecotoxicological Studies. *Langmuir* **2010,** *26*, 6522.

8. Beckett, W. S.; Chalupa, D. F.; Pauly-Brown, A.; Speers, D. M.; Stewart, J. C.; Frampton, M. W.; Utell, M. J.; Huang, L. S.; Cox, C.; Zareba, W.; Oberdorster, G. Comparing inhaled ultrafine versus fine zinc oxide particles in healthy adults - A human inhalation study. *American Journal of Respiratory and Critical Care Medicine* **2005,** *171*, 1129.

9. Thwala, M.; Musee, N.; Sikhwivhilu, L.; Wepener, V. The oxidative toxicity of Ag and ZnO nanoparticles towards the aquatic plant Spirodela punctuta and the role of testing media parameters. *Environmental Science-Processes & Impacts* **2013,** *15*, 1830.

10. Zhang, Y.; Chen, Y. S.; Westerhoff, P.; Crittenden, J. Impact of natural organic matter and divalent cations on the stability of aqueous nanoparticles. *Water Res* **2009,** *43*, 4249.

11. Omar, F. M.; Aziz, H. A.; Stoll, S. Aggregation and disaggregation of ZnO nanoparticles: Influence of pH and adsorption of Suwannee River humic acid. *Sci Total Environ* **2014,** *468*, 195.

12. Dasari, T. P.; Hwang, H. M. The effect of humic acids on the cytotoxicity of silver nanoparticles to a natural aquatic bacterial assemblage. *Sci Total Environ* **2010,** *408*, 5817.

13. Yang, S. P.; Bar-Ilan, O.; Peterson, R. E.; Heideman, W.; Hamers, R. J.; Pedersen, J. A. Influence of Humic Acid on Titanium Dioxide Nanoparticle Toxicity to Developing Zebrafish. *Environ Sci Technol* **2013,** *47*, 4718.

14. Butt, H. J.; Karlheinz Graf; Michael Kappl *Physics and Chemistry of Interfaces,* 3 ed.; **2006**.

15. Hinderliter, P. M.; Minard, K. R.; Orr, G.; Chrisler, W. B.; Thrall, B. D.; Pounds, J. G.; Teeguarden, J. G. ISDD: A computational model of particle sedimentation, diffusion and target cell dosimetry for in vitro toxicity studies. *Part Fibre Toxicol* **2010,** *7*,36.

16. Wood, A.; Giersig, M.; Hilgendorff, M.; Vilas-Campos, A.; Liz-Marzan, L. M.; Mulvaney, P. Size effects in ZnO: The cluster to quantum dot transition. *Australian Journal of Chemistry* **2003,** *56*, 1051.

17. Elimelech, M.; Gregory, J.; Jia, X.; Williams, R. A.*Particle Deposition & Aggregation: Measurement, Modelling and Simulation,* Butterworth-Heinemann, Woburn, MA: **1995**.

18. Vermeer, A. W. P. Interactions between humic acid and hematite. *Doctoral Thesis*, **1996**.

19. Allison, J.; Brown, D.; Novo-Gradac, K.*A geochemical assessment model for environmental systems: version 3.0 user's manual;* **1991**.

20. Malcolm, R. L.; Maccarthy, P. Limitations in the Use of Commercial Humic Acids in Water and Soil Research. *Environ Sci Technol* **1986,** *20*, 904.

21. Chiou, C. T.; Kile, D. E.; Brinton, T. I.; Malcolm, R. L.; Leenheer, J. A.; Maccarthy, P. A Comparison of Water Solubility Enhancements of Organic Solutes by Aquatic Humic Materials and Commercial Humic Acids. *Environ Sci Technol* **1987,** *21*, 1231.

22. Yang, K.; Lin, D. H.; Xing, B. S. Interactions of Humic Acid with Nanosized Inorganic Oxides. *Langmuir* **2009,** *25*, 3571.

23. Hondow, N.; Brydson, R.; Wang, P. Y.; Holton, M. D.; Brown, M. R.; Rees, P.; Summers, H. D.; Brown, A. Quantitative characterization of nanoparticle agglomeration within biological media. *J Nanopart Res* **2012,** *14*, 977

24. Pettibone, J. M.; Cwiertny, D. M.; Scherer, M.; Grassian, V. H. Adsorption of organic acids on TiO2 nanoparticles: Effects of pH, nanoparticle size, and nanoparticle aggregation. *Langmuir* **2008,** *24*, 6659.

25. Gu, B. H.; Schmitt, J.; Chen, Z. H.; Liang, L. Y.; Mccarthy, J. F. Adsorption and Desorption of Natural Organic-Matter on Iron-Oxide - Mechanisms and Models. *Environ Sci Technol* **1994,** *28*, 38.

26. Kang, S. H.; Xing, B. S. Humic acid fractionation upon sequential adsorption onto goethite. *Langmuir* **2008,** *24*, 2525.

27. Illes, E.; Tombacz, E. The role of variable surface charge and surface complexation in the adsorption of humic acid on magnetite. *Colloid Surface A* **2003,** *230*, 99.

28. Zhou, D. X.; Keller, A. A. Role of morphology in the aggregation kinetics of ZnO nanoparticles. *Water Res* **2010,** *44*, 2948.

29. Lin, D. H.; Ji, J.; Long, Z. F.; Yang, K.; Wu, F. C. The influence of dissolved and surface-bound humic acid on the toxicity of TiO2 nanoparticles to Chlorella sp. *Water Res* **2012,** *46*, 4477.

30. Chekli, L.; Phuntsho, S.; Roy, M.; Shon, H. K. Characterisation of Fe-oxide nanoparticles coated with humic acid and Suwannee River natural organic matter. *Sci Total Environ* **2013,** *461*, 19.

31. Illes, E.; Tombacz, E. The effect of humic acid adsorption on pH-dependent surface charging and aggregation of magnetite nanoparticles. *J Colloid Interf Sci* **2006,** *295*, 115.

32. Boily, J. F.; Persson, P.; Sjoberg, S. Benzenecarboxylate surface complexation at the goethite (alpha-FeOOH)/water interface: II. Linking IR spectroscopic observations to mechanistic surface complexation models for phthalate, trimellitate, and pyromellitate. *Geochim Cosmochim Ac* **2000,** *64*, 3453.

33. Ramos-Tejada, M. M.; Ontiveros, A.; Viota, J. L.; Duran, J. D. G. Interfacial and rheological properties of humic acid/hematite suspensions. *J Colloid Interf Sci* **2003,** *268*, 85.

34. Yosep Han; Donghyun Kim; Gukhwa Hwang; Byoungcheun Lee; Igchun Eom; Pil Je Kim; Meiping Tong; Hyunjung Kim Aggregation and dissolution of ZnO nanoparticles synthesized by different methods: Influence of ionic strength and humic acid. *Colloid Surface A* **2014,** *451*, 7.

35. Wahab, R.; Ansari, S. G.; Kim, Y. S.; Dar, M. A.; Shin, H. S. Synthesis and characterization of hydrozincite and its conversion into

zinc oxide nanoparticles. *Journal of Alloys and Compounds* **2008,** *461*, 66.

36. Chat Pholnak; Chitnarong Sirisathikul; Sumetha Suwanboon; David James Harding Effects of Precursor Concentration and Reaction Time on Sonochemically Synthesized ZnO Nanoparticles. *Materials Reserch* **2014,** *17*, 405.

37. Shin, H. S.; Monsallier, J. M.; Choppin, G. R. Spectroscopic and chemical characterizations of molecular size fractionated humic acid. *Talanta* **1999,** *50*, 641.

38. Sposito, G.*The Surface Chemistry of Soils*, **1984**.

39. Bian, S. W.; Mudunkotuwa, I. A.; Rupasinghe, T.; Grassian, V. H. Aggregation and Dissolution of 4 nm ZnO Nanoparticles in Aqueous Environments: Influence of pH, Ionic Strength, Size, and Adsorption of Humic Acid. *Langmuir* **2011,** *27*, 6059.

40. Yang, K.; Xing, B. S. Sorption of Phenanthrene by Humic Acid-Coated Nanosized TiO(2) and ZnO. *Environ Sci Technol* **2009,** *43*, 1845.

41. Chen, K. L.; Mylon, S. E.; Elimelech, M. Enhanced aggregation of alginate-coated iron oxide (hematite) nanoparticles in the presence of calcium, strontium, and barium cations. *Langmuir* **2007,** *23*, 5920.

42. Prado, A. G. S.; Pertusatti, J.; Nunes, A. R. Aspects of Protonation and Deprotonation of Humic Acid Surface on Molecular Conformation. *Journal of the Brazilian Chemical Society* **2011,** *22*, 1478.

43. Zara, L. F.; Rosa, A. H.; Toscano, I. A. S.; Rocha, J. C. A structural conformation study of aquatic humic acid. *Journal of the Brazilian Chemical Society* **2006,** *17*, 1014.

44. Dickson, D.; Liu, G. L.; Li, C. Z.; Tachiev, G.; Cai, Y. Dispersion and stability of bare hematite nanoparticles: Effect of dispersion tools, nanoparticle concentration, humic acid and ionic strength. *Sci Total Environ* **2012,** *419*, 170.

45. Hajdu, A.; Illes, E.; Tombacz, E.; Borbath, I. Surface charging, polyanionic coating and colloid stability of magnetite nanoparticles. *Colloid Surface A* **2009,** *347*, 104.

46. Hu, J. D.; Zevi, Y.; Kou, X. M.; Xiao, J.; Wang, X. J.; Jin, Y. Effect of dissolved organic matter on the stability of magnetite nanoparticles under different pH and ionic strength conditions. *Sci Total Environ* **2010,** *408*, 3477.

47. David, Calin A.; Galceran, Josep; Rey-Castro, Carlos; Puy, Jaume; Companys, Encarnació; Salvador, José; Monné, Josep; Wallace, Rachel; Vakourov, Alex Dissolution Kinetics and Solubility of ZnO Nanoparticles Followed by AGNES. *The Journal of Physical Chemistry C* **2012,** *116*, 11758.

48. Han, J.; Qiu, W.; Gao, W. Potential dissolution and photo-dissolution of ZnO thin films. *J Hazard Mater* **2010,** *178*, 115.

Chapter 4

Determination of the DGT-labile fraction of zinc in dispersions of nano-Zn

Chapter 4.Determination of the DGT-labile fraction of zinc in dispersions of nano-ZnO

4.1. Abstract

ZnO nanoparticles (nano-ZnO) are encountered in a wide range of consumer products. As the use of these nanomaterials is rising, nano-ZnO can easily enter soil and water resources representing an increase in the concentration in the environment and exposure to organisms. Toxicological studies have shown that ZnO nanoparticles (NPs) are one of the most toxic NPs. However, it is unclear whether the toxicity is due to the dissolution to Zn^{2+}, to the NPs or to the combination of both.

In this work, the dissolved Zn fraction released from ZnO nanoparticles has been studied by the implementation of the Diffusive Gradients in Thin Films (DGT) technique. With this objective, different media conditions in presence of ZnO nanoparticles have been studied, including modifications of the pH of the media, addition of dissolved organic matter (humic acid, HA) or simple organic ligands (EDTA), among others. In DGT, metals are bound to a resin layer after passing thorough a membrane filter plus a diffusive gel. Theoretically, the filter (with a standard pore size of 0.45 µm) should block the penetration of large particle aggregates to the gel avoiding errors when measuring the available metal released from nanoparticles.

By modifying the pH of the dispersions it was observed an increase of the solubility with the decrease of the pH (from 8.5 to 7.5). As the changes on pH were so influencing on ZnO solubility, Tris pH buffer was used to maintain fixed the pH. Nevertheless, it was showed an increase of the

measured dissolved metal fraction presumably due to the formation of Zn-Tris complexes and the subsequent accumulation on the DGT devices.

In order to evaluate the possible penetration of nanoparticles through the device, experimental data were obtained using different DGT device conformations (type of diffusive gel and pore size of membrane filter).

4.2. Introduction

The behavior of nano-ZnO in aquatic systems depends on a large number of factors such as pH, ionic strength and content of dissolved organic matter (DOM) (*1*-*3*). These factors can all impact on the aggregation/settling/dissolution and availability of nanoparticles in water and, therefore, determine their toxicological and environmental impact. The study of the aggregation/settling of nano-ZnO has already been presented (see chapters 2 and 3), whereas the solubility/availability will be addressed in the present chapter.

There is currently a debate about whether the toxicity of ZnO NPs is due to their nanoscale properties, or to the fact of its relatively large solubility (*1*,*4*).

A recent toxicology study by H. Zhou et. al. showed that both released Zn^{2+} and NPs contribute to the toxicity of ZnO NPs (*5*) as previously reported by Poynton *et al*. (*6*) whose work suggested that both ZnO NPs and Zn^{2+} are toxic, but have different modes of action.

The release of metal ions from the NPs follows a time course that, in general, is poorly known. In addition, the experimental study of the solubility is hampered by the fact that the separation of the particles from the liquid phase is difficult because of the extremely small size of NPs.

In our research group, the voltammetric stripping technique called AGNES has been successfully used to measure the kinetics and equilibrium of the dissolution process of nano ZnO through the determination of the Zn^{2+} concentration in solution (*1*). This determination is done “in situ” without the need of any separation of the NPs. Notice, however, that this method is not directly determining the solubility but the free Zn concentration in solution. The knowledge of the solubility, then, requires the knowledge of the concentrations of ligands present in the system and the corresponding stability constants.

The free Zn concentration in solution is the relevant parameter to understand the toxicity effects as long as the FIAM or BLM models apply. These models are restricted to cases where the internalization flux is smaller than the maximum transport and releasing capacity. In general cases, the internalization should be related to the flux received by the sensing surface, which depends on a cascade of processes including dissolution, homogeneous reactions and transport.

Sensors that allow measuring metal fluxes are called dynamic sensors. Among them, Diffusion Gradients in Thin Films (DGT) devices have received a great interest due to their ability of measuring *in situ* the flux of the analyte that gets bound to a binding layer made up by a binding agent embedded in a gel covered by a diffusive gel that defines a diffusion domain (*7-9*). The DGT measurement process implies the diffusion of the analyte through a diffusive gel to accumulate in the resin layer. In this way, the results are independent on the convection so that DGT devices can be deployed in streams without influence of the water velocity.

DGT has been used to measure the availability of metal cations, anions and organic pollutants by using the corresponding suitable binding agents in the resin gel. Here in this work we would like to use DGT devices to measure the availability of Zn cations in a system with ZnO NPs at different pH as well as in presence of natural organic matter and some other ligands. We wonder whether only the metal cations and dissolved complexes can cross the diffusive gel. In that case, the flux will allow measuring the bioavailable metal concentration in solution, obtaining in this case a measure of the solubility of the ZnO when the measurement takes places in a system in equilibrium with the dissolution process. On the other hand, some of the NPs could penetrate into the diffusive gel, as we will investigate. Since the hydrogels typically used in DGT have an open pore structure, there is a possibility that NPs can diffuse through them and be measured by DGT (*9-11*), with increasing accumulations with respect to those corresponding to the dissolved metal in solution.

The DGT technique has been used in many toxicity studies to determine the labile metal fraction released by nanoparticles (*12-15*). Most of these studies were performed using Ag NPs or CuO NPs. Buffet, *et al.* (*12,13*) used DGT to detect the release of labile silver from NPs in algae culture media, seawater and sediments. Dissolution was assessed by comparison with results obtained the same media spiked with soluble silver salts instead of NPs. Buffet *et al*., no detect release of soluble copper from NPs by DGT in seawater (*14,16*). In overall, the metal accumulation in systems with NPs and with the soluble form of the metal was the same.

Schlich *et al*, (*17*) used DGT to determine the concentration of labile dissolved silver (assumed Ag^+) in soil pore water after amendment with different amounts of Ag NPs. DGT measurements revealed no differences between the free Ag^+ content of soils spiked with AgNPs and Ag nitrate. Odzak, N., *et al*. (*18*) studied the dissolution of Ag, ZnO, Cu and CuO NPs of different sizes and organic coatings in synthetic freshwater at pH 6.1-7.6. DGT was compared with dialysis (100-500 Da MWCO) and ultrafiltration (3kDa MWCO) methods. In the case of silver, DGT yielded lower values than the other methods, probably due to complexation of Ag^+ ions with the organic coatings. For the rest of the NPs, DGT results were in good agreement with ultrafiltration values.

Kunniger *et al.* (*19*) measured dissolved Ag species in runoff solutions from Ag-NP coated wooden façades, and reported less than 2% of total Ag in the form of labile species.

A recent work of H. Pouran *et al.* (*11*) applied the DGT technique in systems with ZnO NPs. They concluded that ZnO NPs can pass through the open pore diffusive layer used in standard DGT devices and be retained by the binding resin layer. However, they do not correctly assess the persistence (*20*) and behavior (aggregation state) of the NPs in the bulk solution throughout their study. Therefore, further development of the DGT technique to measure available concentrations of metal released from manufactured nanomaterials in the different environmental media (waters, soils, and sediments) and the investigation of the effects of pH, ionic strength, and solution chemistry on the performance of DGT in presence of nanomaterials are needed.

In the present work, the DGT technique has been implemented to determine the labile metal fraction in dispersions of ZnO NPs at different media conditions and the results obtained are compared with the expected metal accumulation due exclusively to the dissolved zinc species.

4.3. Experimental section

4.3.1. Reagents

Two different nanoparticles were used (NP71 and NP20). NP71 presented an average diameter of primary particle of about 71 nm (<100nm) and NP20 about 20 nm. ZnO nanomaterials were provided as commercial dry nanopowders from two sources, Sigma-Aldrich and Io·Li·Tec (Ionic Liquid Technologies GmbH), respectively. ZnO nanopowders were dispersed in Milli-Q water (Synergy UV purification system Millipore) without any additive or background electrolyte to obtain a concentrated stock solution (1 g L^{-1}). The stock solution was sonicated for 30 min. (Branson 3210, 100W) prior to its use.

Zinc stock solution was prepared from solid ($Zn(NO_3)_2 \cdot 4H_2O$, Merck) and cadmium was diluted from the Merck 1000 ppm standard solution ($Cd(NO_3)_2$ in HNO3 0.5 M, Merck).

A stock solution of EDTA was prepared at a concentration of 8 x 10^{-2} mol L^{-1} from the solid salt. An aliquot of the stock was added to the solution to obtain a final concentration of 8 x 10^{-5} mol L^{-1}.

Humic acid (HA) was used as organic matter model substance. Humic acid was purchased as lyophilized commercial HA (Aldrich), and it was further purified following standard purification and lyophilisation procedures (*21*) (see chapter 3). After lyophilisation, a stock solution was prepared at 500 mg L^{-1} concentration, using Milli-Q water, adjusted to pH 6 using KOH and/or HNO_3 (Fluka) and filtered through a 0.45 µm PTFE membrane filter (Whatman) to reject possible aggregates. This stock was kept in dark at 4 °C until use.

Potassium nitrate was used as background electrolyte and it was prepared from solid KNO_3 (Fluka, Trace Select). The ionic strength (I) was fixed at 0.1 M and buffered with 0.02 M Tris (Merck) or MOPS (Sigma-Aldrich) to obtain a stable pH between 7.5 and 8.5. To adjust the pH, standard 0.1 M solutions of HNO_3 and/or KOH were used (Fluka). Milli-Q water was employed in all the experiments.

Purified water-saturated nitrogen N_2 (99.999%) was used to prevent dissolution of CO_2.

Diluted solutions of zinc in HNO_3 3.25 % were prepared from 1000 ppm zinc standard solution ($Zn(NO_3)_2$ in HNO3 0.5 M, Merck) in order to perform the ICP-OES calibration. Diluted nitric acid was used as a blank.

Nitric acid (70%, Fisher, Analytical grade) was used to acidify the samples for their analysis of the total metal content.

4.3.2. Instrumentation

The hydrodynamic size distributions as well as the zeta potential of the aggregates present in the dispersions under the experimental conditions were followed by Dynamic Light Scattering (DLS) and Electrophoretic Mobility, respectively, with a Zetasizer Nano ZS (Malvern Instruments Ltd, Bedford, MA). The content of dissolved zinc was also measured by filtration (0.45 or 0.1 µm diameter pore filters, PTFE membrane filters, Whatman) and centrifugation of the bulk sample for 30 min at 18.000 rpm (Hettich MIKRO 22R microcentrifuge) and subsequent analysis of the supernatant by ICP-OES.

Finally, the UV-Visible spectrum of each sample was determined to verify the presence of the characteristic absorption peaks of nano-ZnO.

A pH meter Orion 920A+ (Thermo Electron Corporation) was used to measure pH in situ during the deployment of the DGT sensors. The monitored pH values were continuously recorded using a PC controlled by a special in-house application programmed in MatLab by Dr. Calin A. David.

Inductively Coupled Plasma Optical Emission Spectrometry (ICP-OES) (SpectroAnalytical Instruments and Activa-S, Horiba Scientific) was used to determine total zinc content in all samples after acidification with HNO_3 (at a final concentration of 3.25 %).

Visual MINTEQ speciation code was used to predict the metal speciation in the experimental conditions (*22*).

4.3.3. Procedures

Systems with increasing complexity were studied. As a first step, calibration of the technique in solutions with only a soluble salt of zinc and a salt of zinc in presence of HA was performed. Afterwards, experiments with nano-ZnO in absence or presence of HA or EDTA were carried out.

DGT holders, diffusive gels and Chelex-100 resin gels were purchased from DGT Research Ltd (Lancaster, UK) (*23*). The nominal thickness of Chelex-100 (*8*) resin gel and diffusive gel were 0.4 mm and 0.8 mm, respectively. Two kinds of diffusive gels, both of the same thickness, were used in order to test the possible NPs penetration into the DGT device: one gel has a pore size greater than 5 nm of diameter (polyacrylamide gel cross-linked with an agarose derivative, open pore (OP) gel, or APA) while the other, called restricted gel (RG), has an average pore size of about 1 nm (polyacrylamide gel cross-linked with N,N-methylene bisacrylamide) (*24*). Filter membranes of 0.125 mm thickness and 0.45 µm pore size (or, alternatively, 0.1 µm for the testing of possible NPs penetration) were obtained from Whatman. For a given experiment, 8-14 DGT units were deployed in the same container.

Prior to the exposure experiments, the DGT sensors were immersed 24 hours in a solution with the same pH and background electrolyte conditions (*25*).

Different configurations of the DGT sensors were tested: a) OP gel + 0.45 µm pore size filter , b) OP gel + 0.1 µm pore size filter, c) RG gel + 0.45 µm pore size filter and d) RG gel + 0.1 µm pore size filter.

The solutions were stirred at 240 rpm continuously throughout the experiments, the pH was measured also throughout all the deployment time and the temperature was fixed to 25 ± 0.1 ºC with a thermostatic bath (*26*).

The DGT sensors were taken out of the solution at different times between 2 and 30 hours. After deployment, the devices were removed, rinsed with Milli-Q water and immediately disassembled to extract the resin gel, which was placed in a 1.5 mL Eppendorf vial (*27*). One mL of 34.5 % HNO_3 was added to the vial and allowed to stand for 24 hours at room temperature to extract the metals from the Chelex resin. The recovery was independent of elution time (1h-1week) (*8*). The concentration of the nitric acid used for extract the metals was chosen to be sure that all the metals bound to the resin were totally extracted as was confirmed by previous studies (elution efficiency factor of 1) (*26*). Moreover, to evaluate the possible contamination during the deployment, one DGT unit was used as blank and analyzed in the same conditions as the others.

Trace metals were analyzed by using an inductively coupled plasma optical mass spectrometer (ICP-OES).

The amounts of ion in the resin gel as well as in the diffusive gel and the filter were then calculated using the known volumes of the layers and the elution factors.

4.3.3.1. Calibration of DGT devices in absence of NPs

Prior to the study of nano-ZnO solubility by DGT, the technique was tested with solutions of a soluble salt of zinc ($Zn(NO_3)_2$) using concentrations close to the solubility of ZnO at the pH and ionic strength of the experiment. Under these conditions, substantially all the zinc is in the form Zn^{2+} free ion, as checked with Visual MINTEQ.

The DGT devices were deployed in 2 L of solutions containing Zn with an ionic strength fixed at 0.1 M KNO_3 (plus 0.02 M Tris or MOPS buffers). The pH was adjusted at 7.7 or 8.05 with small additions of HNO_3 and KOH 0.1 M. The DGT sensors (5-10 depending on the experiment) were deployed together in the solution and they were sequentially removed at 2-4 hours intervals for a total period of 24 hours.

Throughout the deployment of the sensors, aliquots of the exposition solution were collected and analysed by ICP-OES at regular intervals to check the total Zn concentration for each experiment.

4.3.3.2. DTG experiments in presence of nanoparticles

For DGT experiments with nano-ZnO, 2 L of thermostated solutions were prepared for each experiment by adding KNO_3 until reaching an ionic strength of 0.1 M and plus 0.02 M Tris or MOPS buffer to maintain a constant pH in the range 7.5 - 8.5. This range of pH was chosen with the aim to cover the range of typical pH of both river waters and seawater. More acidic pHs were not used due to the high solubility of nano-ZnO as pH decreases.

The initial bulk concentration of nano-ZnO was chosen to get the same final concentration of nanoparticles (90 mg L^{-1}, or 1.1 x 10^{-3} mol L^{-1}) after dissolution of the ZnO until saturation at each pH value. Initial concentrations of ZnO in the dispersions were calculated with Visual MINTEQ. In some cases, a soluble salt of cadmium was added to test the efficiency of the measurements of the DGT devices in systems with presence of nanoparticles.

The final solution was stabilized during at least 12 hours prior to the deployment of the DGT sensors to ensure that the equilibrium was reached (*1*).

During all the experiments, aliquots of the exposure solution at the same height of DGT devices were collected at regular intervals to check several parameters: a) the total zinc concentration, b) the zinc content in the fraction filtered through filter membranes of 0.1 and 0.45 µm, c) the zinc content present on the supernatant after centrifugation for 30 min at 18.000 rpm and d) average size of the agglomerates by Dynamic Light Scattering (DLS).

4.3.3.3. System with nano-ZnO coated with HA

For the determination of the labile metal zinc released from HA coated nano-ZnO, the immersion solutions were prepared at pH 8.1, ionic strength 0.1 M KNO_3 and 0.02 M Tris buffer. HA was added to obtain 8.3 $mg\cdot L^{-1}$, and then the pH was checked and corrected, if necessary, prior to the addition of nano-ZnO concentrated stock. The dispersion was stabilized overnight to ensure that equilibrium was reached.

4.3.4. DGT calculations

Accumulation in DGT devices requires the diffusion of the metal ions through the membrane filter and diffusive hydrogel to finally accumulate in the binding layer. At the interface of the DGT with the sampling solution there is a region where the tangential velocity of the water decreases, creating a diffusive boundary layer (*28*), of thickness δ (*28*). The thickness of the DBL depends on the stirring conditions applying in the solution side and increases the actual thickness of the diffusion layer. In any case, when the diffusion coefficients do not vary noticeably between solution and gel, only one diffusion domain with thickness comprising diffusive gel, filter and DBL can be used.

The physical principles of DGT consist on the interplay between chemical kinetics and diffusive transport of the analytes thorough the diffusive gel.

The sensor is deployed in the aqueous sample under (ideally) constant convective conditions, for a given period of time (from 1h to a few days). After a short transient (which usually happens within the first hour of deployment) (*29*), metal fluxes thorough DGT devices reach a steady state regime. For systems where only metal is present, a linear concentration profile is established between the solution and the resin gel interface. Under conditions of fast and irreversible binding of the metal to the resin, the metal concentration drops to zero at the resin/diffusive gel interface and the concentration gradient is maintained as long as the binding layer is not saturated. Under these conditions, the flux, J (mol m^{-2} s^{-1}), of the different analyte species i through the diffusive layer, of thickness g (m), can be described by Fick's first law of diffusion (Equation 4.1):

$$J = \frac{Dc^*}{g} \tag{4.1}$$

where D is the diffusion coefficient of species in the diffusive layer (m^2 s^{-1}) and c^* the metal concentration in the bulk solution (mol m^{-3}).

A limit of the accuracy of the assayed concentration is imposed by uncertainty in the knowledge of the D values in the diffusive gel. Davison and Zhang measured the diffusion coefficient in the diffusive gel for most environmentally-significant trace metals and found that they are only slightly smaller (about 0.85 times) than the diffusion coefficient in water (*30*). The value of the diffusion coefficient of Zn and Cd at 25 ºC used in this work are listed in Table 4.1 (*31*,*32*). Diffusion coefficients in the membrane filter and DBL are assumed indistinguishable from those in the diffusive gel (*30*,*33*) so that g commonly represents the thickness of the gel (0.8 mm) plus the filter (0.125 mm) and the DBL. Reported values for DBL thickness lie in the range 0.1-0.2 mm (*26,28,30,32,33*).

Once the deployment time is finished, the sensor is retrieved from the solution, disassembled, the analytes are eluted from the resin layer with nitric acid solutions and, finally, the amount of analyte accumulated in the sensor (n, in moles) is quantified using the ICP-OES analytical technique, using the following equation:

$$n = \frac{c_e(V_g+V_e)}{f_e} \tag{4.2}$$

where c_e is the concentration of metal in the eluted volume (mol m^3), V_g is the volume of the resin layer (m^3), V_e is the volume of the acid to elute the metal bound (m^3) and f_e the elution factor (considered as 1 in HNO_3 7.5 M, as determined previously by Sandrine Mongin (*26*)). Although the first papers published on DGT considered the volume of the resin gel as negligible (*8*), this parameter is not so small compared to the volume of HNO_3 required for elution of the Chelex. The value used in the following calculations is 0.18 mL, as reported by other authors in the literature (*26,33*).

Since the flux indicates the moles bound to the resin n, per unit of area, A (m^2), and unit of time t (s), and assuming that the resin layer acts as a perfect planar sink for the target ion (*34*), then the so-called *labile* concentration in the bulk sample solution, c^{DGT}, can be calculated as:

$$c^{DGT} = \frac{n_i g}{D_i A t} \tag{4.3}$$

Calculation of the metal accumulation in presence of metal complexes

The previous expressions are only for systems in absence of ligands where no metal complexes are present. When a ligand, L, is present in solution and gives rise to the formation of a complex with the metal, the accumulation is strongly dependent on both the mobility of the complex and the kinetics of dissociation. Whenever $K' = K\ c_L$ is K'>>1 (K and c_L being the complex formation constant and the free ligand concentration, respectively), the dominant metal species is the complex. When the free metal starts to develop a concentration profile, ML tends to dissociate, this dissociation buffers the metal depletion and contributes to the metal accumulation. If these complexes are *fully labile* (the dissociation of the complex is so fast as to achieve local equilibrium with the free metal in all the relevant spatial positions), the metal accumulation is given by (*24,30,35*).

$$n = \left[\frac{c_M^* D_M}{g} + \frac{c_{ML}^* D_{ML}}{g}\right] A t \tag{4.4}$$

indicating that a linear complex concentration profile has been developed so that the complex concentration has drop to zero at the resin/diffusive gel interface to be in equilibrium with the free metal.

Otherwise, when the complexes ML are relatively inert the dissociation of the complex is only partial within a layer where equilibrium is not achieved (*9,36,37*) which is generally known as the reaction layer.

A general expression for the flux can then be written as:

$$n = \left[\frac{c_M^* D_M}{g} + \frac{c_{ML}^* D_{ML}}{g}\xi\right] At \qquad (4.5)$$

where ξ, is the so-called *lability degree* of the complex, a parameter that quantifies the contribution of the complex dissociation to the bound metal flux (*29*) indicating the fraction of the actual with respect to the maximum contribution that would be reached if the complex was completely labile.

Therefore, c^{DGT} is called the *labile fraction* of dissolved M, which is often considered as an estimate of the bioavailable fraction (*38,39*).

Measures in presence of nanoparticles

In dispersions of nanoparticles, the ability of DGT to discriminate between the soluble metal and the solid NPs lies in the difference in their diffusion coefficients. A theoretical study by Van Leeuwen (*40*) has shown that the characteristic time to reach steady state flux of colloidal particles through the sensor should allow the discrimination between both. However, the actual capacity of nanoparticles to penetrate the DGT gel is still a matter of controversy (*9*). Pouran *et al.* proposed the inclusion of a dialysis membrane between the outer filter and the hydrogel (*10*) to prevent penetration of NPs into the diffusion gel, but their study does not report the monitoring of size distribution of NPs in the bulk solution throughout the experiments to discard complete dissolution. The objective of the present chapter, thus, will be to assess the validity of equations 4.4 and 4.5 to describe the experimental accumulation of zinc in equilibrated ZnO NP dispersions, as a result of their solubility.

The dissolution process of ZnO NPs was previously described (see eqn. 3.7 and 3.8). The theoretical calculation of the speciation in the bulk solution (c_M^* and c_{ML}^*) was carried out with Visual MINTEQ using the standard thermodynamic database, except for the parameters listed in Tables 4.2 and 4.3.

Table 4.1. Values corresponding to DGT sensor parameters.

parameter	**value**
D_{Zn} (m^2 s^{-1})	6.08×10^{-10}
$D_{ZnTris}{}^*$ (m^2 s^{-1})	5.47×10^{-10}
D_{Cd} (m^2 s^{-1})	6.09×10^{-10}
$D_{i,RG}$ (m^2 s^{-1})	$D_i \times 0.75$
A (m^2)	3.14×10^{-4}
g (m)	1.13×10^{-3}
V_{HNO3} (m^3)	1.00×10^{-6}
V_{gel} (m^3)	1.80×10^{-7}

* Diffusion coefficient of all Zn-Tris complex species

Table 4.2. Values of the conditional solubility product (K_{sp}) of ZnO NPs at I=0.1 mol L^{-1} and 298 K used for speciation calculations (from David *et al.* (*1*)).

ZnO NP	Log K_{sp}
bulk	-16.90
71NP	-16.81
20 NP	-16.76

Table 4.3. Values of the conditional equilibrium constants of Zn complexes with TRIS buffer at I=0.1 mol L^{-1} and 298 K used for speciation calculations (from C.A. David, personal communication).

Complex	Log K_i *
$ZnTRIS^{2+}$	0.64
$Zn(OH)TRIS^{+}$	-5.75

* The corresponding formation equations are:

$\mathrm{TRIS} + \mathrm{Zn}^{2+} \xrightleftharpoons{K_1} \mathrm{ZnTRIS}^{2+}$ and

$\mathrm{TRIS} + \mathrm{Zn}^{2+} + \mathrm{H_2O} \xrightleftharpoons{K_2} \mathrm{Zn(OH)TRIS}^{+} + \mathrm{H}^{+}$

4.4. Results and Discussion

4.4.1. Calibration of DGT devices

Experiments started with the simplest system made up by a soluble zinc salt without dispersion of ZnO NPs at the pH and ionic strength of interest. These accumulations are addressed to obtain reference values to calibrate DGT parameters. Three different media ($Zn(NO_3)_2$ plus Tris or MOPS buffer and with/without HA) have been studied. Additionally, calibrations of the technique with the two different types of gels (OP and RP) and filters employed were also performed.

4.4.1.1. DGT calibration in presence of pH buffer (Tris and MOPS)

Plots of the measured moles (*n*) of Zn versus time were obtained for each deployment solution containing different pH buffers.

The accumulation of Zn in solutions containing 1.69 x 10^{-4} M Zn and 0.02 M MOPS buffer is represented in Figure 4.1. It has been reported that MOPS does not complex Zn (*41*), so no contribution of the buffer to the metal accumulation was expected. The moles of metal given by DGT measurements agreed very well with the values calculated using Eqn 4.4 and the bulk solution concentrations determined by ICP-OES for Zn (red dotted line). Thus, the correlation between theoretical values (without considering zinc complexation by MOPS) and experimental values confirms both the diffusion coefficient for the free Zn and the thickness of the diffusion domain, g =1.13 x 10^{-3} m.

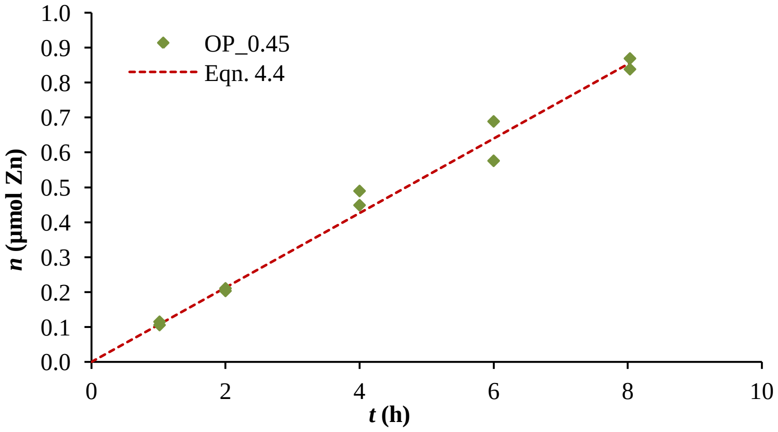

Figure 4.1. Measured moles of Zn in DGT devices deployed in a pH 7.7 solution in presence of 1.7 x 10^{-4} M Zn for up to 8 h. *I*= 0.1 M KNO_3 (buffered with 0.02 M MOPS). Markers: experimental measurements. Solid lines: predicted accumulation calculated using Eqn. 4.4.

The accumulation of Zn in the presence of 0.02 M Tris and two different concentrations of Zn, 1.7 x 10^{-4} M and 4.5 x 10^{-5} M, are depicted in Figure 4.2. Markers follow a linear trend indicating that the accumulated Zn is proportional to the contact time as predicted by equation 4.4.

The theoretical prediction needs to consider that Zn cations bind to Tris. As calculated with the speciation program Visual MINTEQ, in the solution containing 1.7 x 10^{-4} M Zn, a 79 % of the total dissolved Zn is complexed by Tris, however, when 4.5 x 10^{-5} M Zn is used, only a 46% is complexed.

Diffusion coefficients of complexes with organic ligands are usually smaller than those of simple inorganic complexes. Assuming that these complexes are fully labile we can use Eqn. (4.4) to reproduce the experimental accumulations. By fitting this equation to the experimental values (blue line in Fig. 4.2), the diffusion coefficient of Zn-Tris complexes was calculated as 0,9 times the diffusion coefficient of the metal. The fact that both sets of experiments yield a similar fitted value indicates that the effect of the filter pore size on the diffusion coefficients is negligible.

Accumulations calculated without taking into account Zn complexation by the buffer are represented with the dotted red line. The differences with the blue line are small but increase as the Zn concentration increases, due to the increase of the fraction complexed with Tris according to Visual MINTEQ results. The relatively small reduction of the accumulation when Tris complexes are included is due to the lower diffusion coefficient of ZnTris species with respect to that of free Zn.

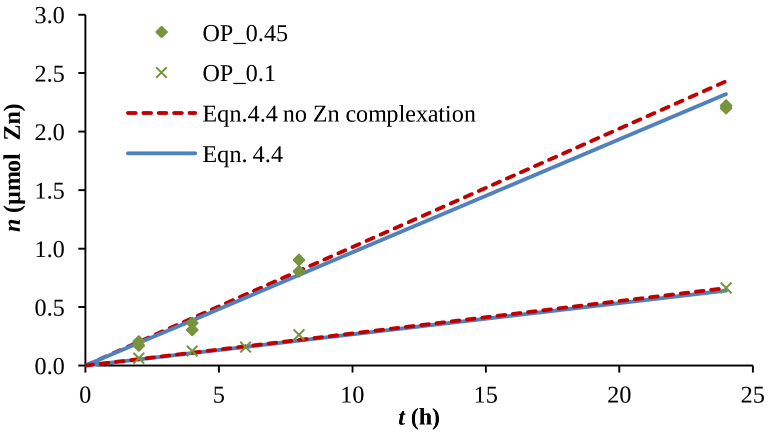

Figure 4.2. Moles of Zn accumulated by DGT (open pore gels) in presence of 1.69 x 10^{-4} and 4.53 x 10^{-5} M Zn. *I*= 0.1 M and pH 8.05 and 7.93 respectively (buffered with 0.02 M Tris). Markers: experimental measurements (diamonds and crosses correspond to devices with 0.45 and 0.1 µm pore membrane filters, respectively); lines: values according to eqn. (4.4) assuming no Zn-Tris complexation (red dotted line) and calculated with speciation program (blue continuous line).

The interpretation of the accumulation of Zn in presence of Tris is based on the assumption of a labile character of the Zn-Tris complex. In fact, the low values of the stability constant of ZnTris in comparison to other labile complexes studied by DGT, together with the Eigen ideas, supports this assumption. The values of the formation constants of the Tris complexes with Zn (as listed in Table 4.3) where determined through ancillary experiments using the AGNES technique (Calin A. David, personal communication).

In summary, from the comparison of the experimental data with eqn. 4.4 and Visual MINTEQ calculations, it can be concluded that the Zn-Tris complexes are fully labile with a diffusion coefficient near to the diffusion coefficient of the Zn metal ion (0.9 x D_{Zn}).

4.4.1.2. DGT calibration of different conformations of DGT devices

Different types of gels and filters are being used to measure the dissolved Zn fraction (“labile fraction”) released from nano-ZnO. Before analysing these experiments, accumulations of Zn using different combinations of gels and filters were performed to test the simple theoretical equation 4.4 as well as to fit the main parameters of the system in each type of gel.

DGTs with different gels and filters are immersed in stirred solution containing 1.98 x 10^{-4} M and 4.5 x 10^{-5} M $Zn(NO_3)_2$ for 2-24 h. The moles of Zn accumulated with time are shown in figure 4.3. In figure 4.3a, no differences are observed between devices using filters of 0.1 or 0.45 µm pore diameter. As mentioned above, the metal accumulation was also not affected by the filter pore size in the case of open pore gels.

Theoretical accumulations were computed with Eqn. 4.4 using the Zn diffusion coefficients corresponding to each gel, *i. e.* 4.59 x 10^{-10} m^2s^{-1} for *RG* gels (*31,42*), and 6.08 x 10^{-10} m^2s^{-1} for APA gels (*30-32*), as listed in Table 4.1. The resulting lines agree quite well the experimental accumulations (see blue lines in Fig.4.3).

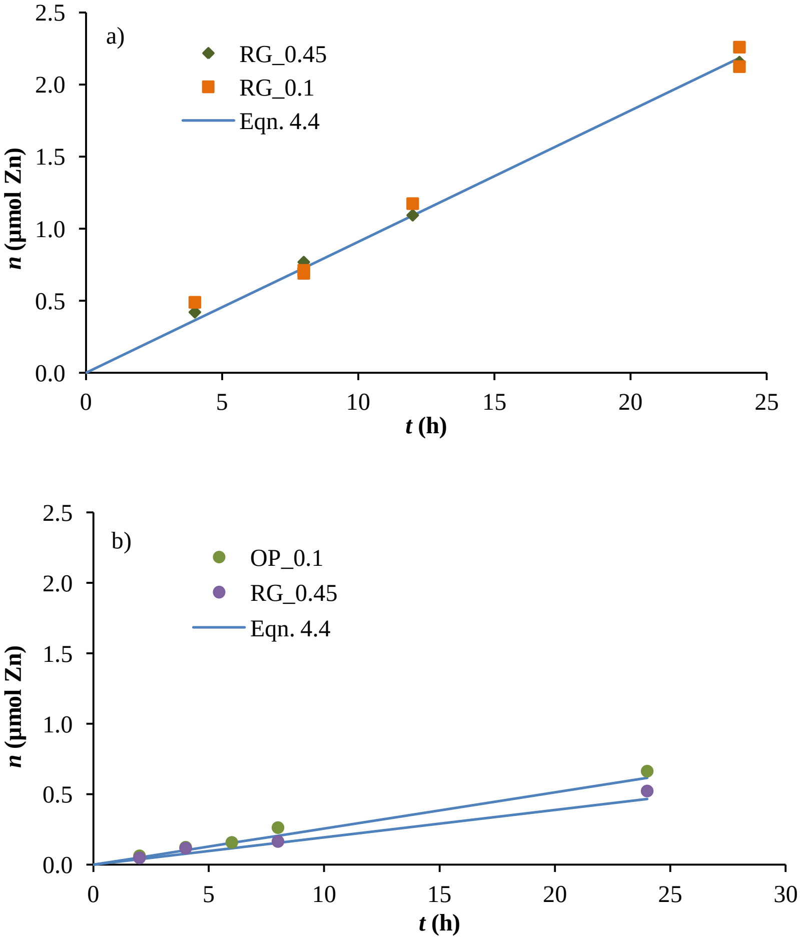
a)
RG_0.45
RG_0.1
Eqn. 4.4
n (µmol Zn)
0.0
0.5
1.0
1.5
2.0
2.5
0
5
10
15
20
25
t (h)
b)
OP_0.1
RG_0.45
Eqn. 4.4
n (µmol Zn)
0.0
0.5
1.0
1.5
2.0
2.5
0
5
10
15
20
25
30
t (h)

Figure 4.3. Number of µmoles of metal accumulated by DGT in a system with a) 1.98 x 10^{-4} M Zn using RG gels and 0.1 and 0.45 µm diameter pore filters and b) 4.5 x 10^{-5} M Zn using OP and RG gels with 0.1 and 0.45 µm diameter pore filters. Ionic strength 0.1 M and pH a) 7.72 and b) 7.93 (both buffered with 0.02 M Tris). Markers: experimental measurements using RG gels with 0.45 µm (green diamonds) and 0.1 µm (orange squares) diameter pore filter; OP gels and 0.1 µm (violet circles) blue lines: calculated values according to eqn. 4.4 for bulk Zn concentration.

4.4.1.3. DGT calibration in presence of humic acid

The accumulation of zinc as a function of time in a solution containing a concentration of HA of 3 mg L^{-1} and using 0.1 M KNO_3 with Tris buffer (0.02 M) and pH 8.33 was measured. A first estimation of the diffusion coefficient of HA in water can be obtained, assuming spherical geometry (*24*), with equation

$$D = \frac{3.3\ x\ 10^{-5}}{M_w^{\frac{1}{3}}} \qquad (4.6)$$

where M_w is the molecular weight of humic substances. With M_w= 6300 g mol^{-1}, as reported in (*24*), the calculated diffusion coefficient of HA in water becomes 1.97 x 10^{-10} m^2 s^{-1}. No unique values for the diffusion coefficients of humic substances in water are reported in the literature. Due to conformational changes and aggregation effects, measured diffusion coefficients are dependent on pH, ionic strength and concentration of the humic substances (*24,43,44*). In this work, D_{ZnHA} has been assumed equal to 3.65 x 10^{-11} m^2 s^{-1} (0.06 x D_{Zn}) which has been reported for APA gels (*24*). This value is clearly much lower than the diffusion coefficient of HA species measured in water. It can be understood as an effective value influenced by the interactions between the HA and the gel, since it has been reported that HA tends to accumulate in the gel by hydrophobic interactions (*45*).

Calculations with Visual MINTEQ, assuming the generic NICA parameters for the complexation of Zn with HA, indicate that Zn is mainly complexed by Tris (57.244 % of total Zn concentration is present as $ZnTrisOH^+$) or free zinc (23.8 %), and only 5.1 % of Zn is complexed to HA.

DGT accumulations in presence of Tris and HA are reported in Figure 4.4. Exprimental accumulations agree quite well with the theoretical accumulations calculated with equation 4.4 using the concentrations derived with Visual MINTEQ and diffusion coefficients D_{ZnTris}= 0.9 x D_{Zn}, as estimated above, and D_{ZnHA}= 0.06 x D_{Zn} as previously reported (*24,30,46*).

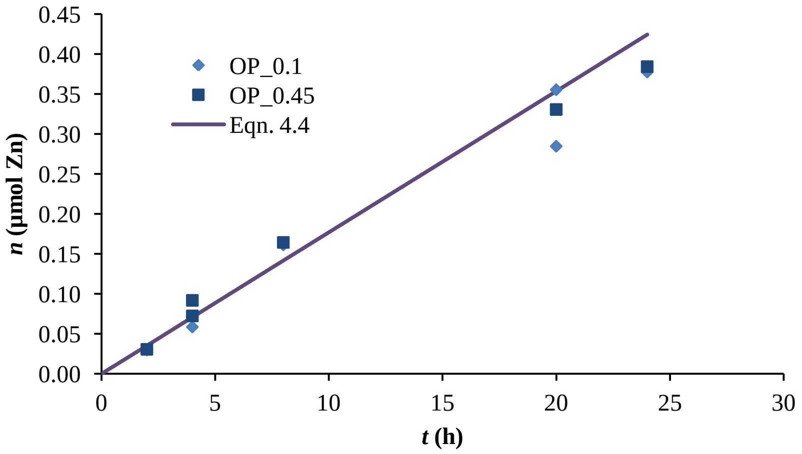

Figure 4.4. DGT (open pore gels) accumulation in presence of 3 mg·L^{-1} HA and a Zn concentration of 3.26 x 10^{-5} M. I = 0.1 M KNO_3 (buffered with 0.02 M Tris) and pH 8.33. Markers: experimental measurements with 0.45 µm (violet squares) and 0.1 µm pore size (blue diamonds); blue line: accumulation expected according to eqn. 4.4 and speciation calculated with Visual MINTEQ.

Two different filters (of 0.45 and 0.1 µm pore diameter) were also employed to test the effect of the pore size on the metal accumulation when HA is present in the immersion solution.

With the HA concentration used in the present work, 3 mg L^{-1}, there are no significant differences in the Zn accumulations between the two filters. This justifies that the diffusion coefficient of Zn bound to HA has no dependence on the size of the pore filters.

The moles of Zn accumulated in the filters were also measured (by elution of the filter membranes with nitric acid after deployment of the devices) in order to check if there is a significant retention of any Zn species on the filter, which proved to be negligible (0.004 ± 0.002 µmoles) with respect to the DGT accumulation in the resin discs.

4.4.2. DGT accumulations in systems containing ZnO NPs

4.4.2.1. Solubility of nano-ZnO

It has been previously reported that the diameter of the ZnO primary nanoparticles modify the solubility of the nanomaterial. This has an implication in the present work, where NPs of different diameter (20NP and 71NP) have been used (*1,47,48*). A first aim of this work was checking if this influence can be measured with DGT.

In principle, the DGT sensor response is expected to match with the concentration of Zn^{2+} and the labile complexes in solution (*e.g.* $Zn(OH)^+$, $Zn(NO_3)^+$, $ZnTris^{2+}$, etc.) according to Eqns. 4.4 and 4.5. In any case, we do not expect a direct contribution of NPs to the zinc accumulation, as even the smallest NPs (primary particles of 20 nm, assuming no aggregation) would have a diffusion coefficient (as estimated by Stokes-Einstein equation) of about 2×10^{-11} m^2s^{-1}, which is more than 1 order of magnitude lower than that of the Zn^{2+} ion, so that the NP diffusion from the solution through the sensor to the resin should, in principle, be negligible compared to the flux of free ions at the pH values of this study.

Figure 4.5 illustrates the accumulation of Zn with time in a suspension of 71NP (Figure 4.5a) at pH 7.72 and 20NP (Figure 4.5b) at pH 8.16. Green markers depict the experimental measurements while lines represent the theoretical accumulations calculated with equation 4.4 considering that the NPs cannot penetrate into the diffusive gel or this penetration is so slow, due to the low diffusion coefficient of the NPs, that no contribution to the metal accumulation arises. The rest of species present in bulk solution were calculated with Visual MINTEQ and the corresponding diffusion coefficients are the same as in the above sections. Differences among orange and blue lines result from the different solubility of bulk ZnO (orange line) and nano-ZnO (blue line). Experimental results, for 71NP and 20NP, agree better with theoretical calculations based on the solubility products determined for each size. These results clearly confirm the dependence of the solubility with nano-ZnO size.

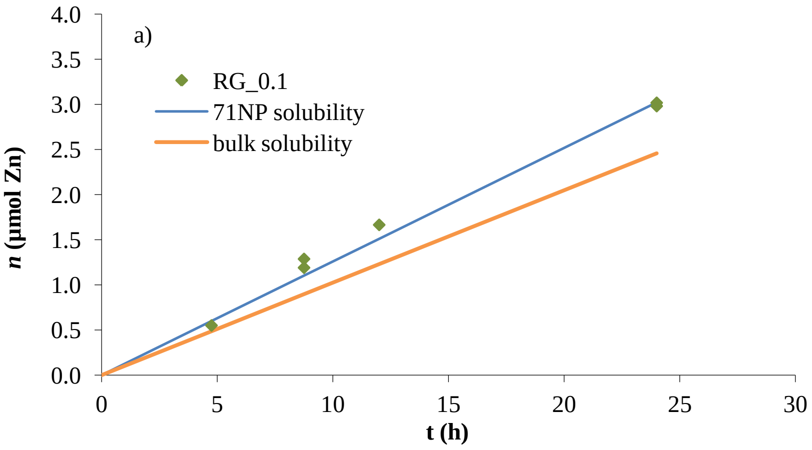

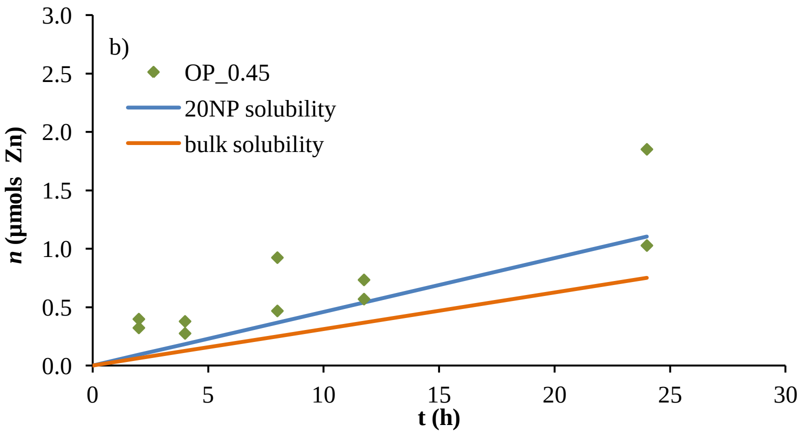

Figure 4.5. Moles of zinc accumulated with time in a deployment solution containing 90 mg L^{-1} nano-ZnO a) 71NP and b) 20NP. *I*= 0.1 M (0.02 M Tris), pH a) 7.7 and b) 8.16. Markers: experimental accumulation. Lines: theoretical accumulation calculated using bulk ZnO (orange line) and nano-ZnO solubility products (blue line), as listed in Table 4.2.

DGT measurements in aqueous dispersions of 20NP show poor reproducibility. This effect can be explained as an influence of the pH of the system, as explained below (see section 4.4.2.3.) or to the fact that some small particles may randomly penetrate into the sensor and dissolve within, thus contributing to the Zn accumulation.

4.4.2.2. Contribution of Zn-Tris complexes in systems with nano-ZnO

Due to the high dependence of the solubility of ZnO on pH, it is convenient the use of a buffer to keep the pH fixed.

Figure 4.6 shows the time dependence (4-24h) of the zinc accumulations in DGT devices deployed in a dispersion of 90 mg L^{-1} 71NP buffered with 0.02 M Tris. Theoretical accumulations calculated with the speciation program Visual MINTEQ for the experimental conditions detailed above, but in absence of Tris, are plotted as a violet line. Experimental accumulations are clearly above these theoretical values, which is explained by the increased solubility due to the presence of metal complexes formed with Tris. The agreement with equation 4.4 is greatly improved using the concentration of each species determined by Visual MINTEQ in presence of Tris and the corresponding diffusion coefficients (blue line).

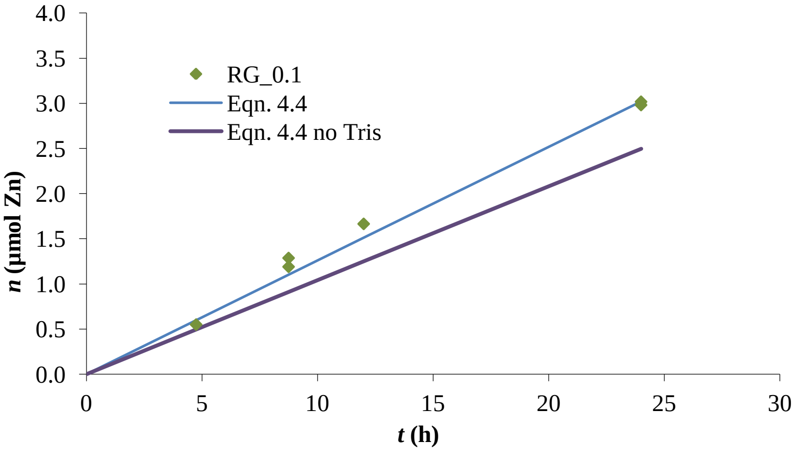

Figure 4.6. Moles of zinc accumulated vs. time in a deployment solution containing 90 mg·L^{-1} nano-ZnO 71 nm, *I*= 0.1 M (0.02 M Tris) and pH 7.7. Markers: experimental values. Lines: theoretical accumulation in presence of Tris (blue line) and in absence of Tris (violet line).

For a better understanding of the complex contribution to the DGT measurements, accumulations in a deployment solution containing 90 mg L^{-1} 71NP and buffered by MOPS (a non-complexing buffer) were done under identical experimental conditions to those corresponding to Fig. 4.6 (pH 7.7 and I=0.1M KNO_3).

The comparison between these accumulations (red markers in Fig. 4.7) and those obtained in presence of Tris (green markers in Fig. 4.7 or Fig. 4.6) shows that Tris increases the dissolved Zn fraction released from 71NP. Conversely, Zn is not complexed by MOPS buffer (*41*), and so the corresponding accumulations are smaller than those in presence of Tris. Differences are of the order of 25%. These results indicate that the DGT technique is an efficient method to measure the labile fraction dissolved from nano-ZnO, which includes the inorganic Zn and the Zn complexes formed with Tris, in this particular case.

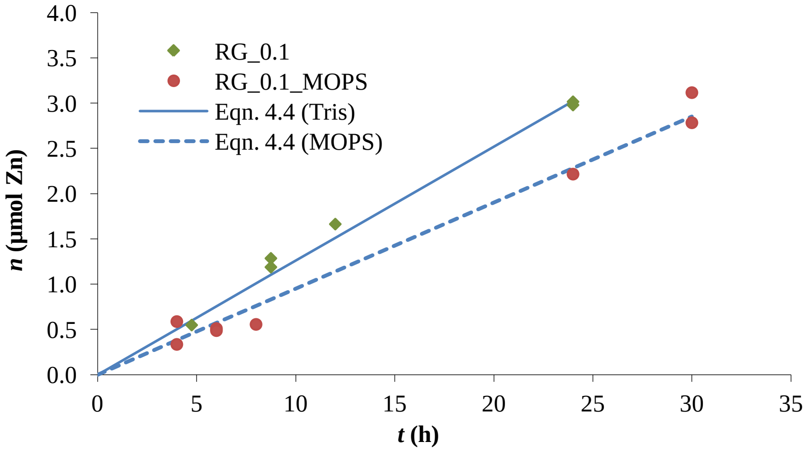

Figure 4.7. Moles of zinc accumulated by time in systems with two different buffers (Tris and MOPS). 90 mg L^{-1} 71NP, *I*= 0.1 M and pH 7.7. Markers: system with Tris buffer (green diamonds) and with MOPS buffer (red circles). Lines: theoretical accumulation in presence of Tris (continuous line) and MOPS (dashed line).

4.4.2.3. Impact of pH on the DGT measurements

To assess the effect of pH on the DGT measurements in presence of nanoparticles, DGT devices were immersed in nano-ZnO dispersions spanning the pH range of 7.58-8.45. The moles of Zn accumulated are plotted against time in Figure 4.8.

The solubility of nano-ZnO is extremely sensitive to changes in pH. A decrease of 1 pH unit implies an increase of 2 orders of magnitude in the Zn^{2+}concentration in solution, as deduced from the equilibrium solubility of nano-ZnO (*1*). Therefore, it is necessary to keep a tight control of pH throughout the experiments (Figure 4.8).

In all cases, the DGT devices were deployed in 71NP nano-ZnO dispersions with a final nano-ZnO concentration of 90 mg L^{-1} at equilibrium. To obtain the same ZnO concentration for each pH, different initial masses of nano-ZnO were being used (since solubility depends on pH). Blue lines represent the theoretical accumulations predicted by applying equation 4.4 using the total dissolved Zn calculated with Visual MINTEQ (tacking into account the dependence of the solubility with the NP size and the complexation with Tris). The agreement of experimental measurements (green diamonds) with theoretical measurements confirms the ability of the DGT technique to measure the dependence on pH of the solubility of the nano-ZnO.

As expected from the nano-ZnO solubility calculations, the moles of Zn measured are higher at pH 7.58 than at pH 8.05 and pH 8.45 (compare Figures 4.8a, 4.8b and 4.8c). However, it is observed a poor reproducibility on the accumulations when the pH of the solution is above 8.4. DLS measurements of the nano-ZnO aggregates formed in the deployment solutions at the three pH values are approximately the same (see Chapter 2), so it is not expected a difference on reproducibility between measurements due to differences in the effective particle size distributions.

One possible explanation of this poor reproducibility (and somewhat overestimated results) at high pH is that a fraction of smaller nanoparticles, may pass through the filter and dissolve inside the sensor. The released Zn^{2+} will increase the accumulation. As this penetration is small, random effects may lead to the lack of reproducibility. At low pH, the solubility greatly increases and so the relative contribution to the accumulation due to random penetration of NPs in the diffusive gel becomes negligible. It is reported in the literature the possibility that nanoparticles may accumulate inside the sensor gel (*40*), but we have not found any similar study with metal oxides.

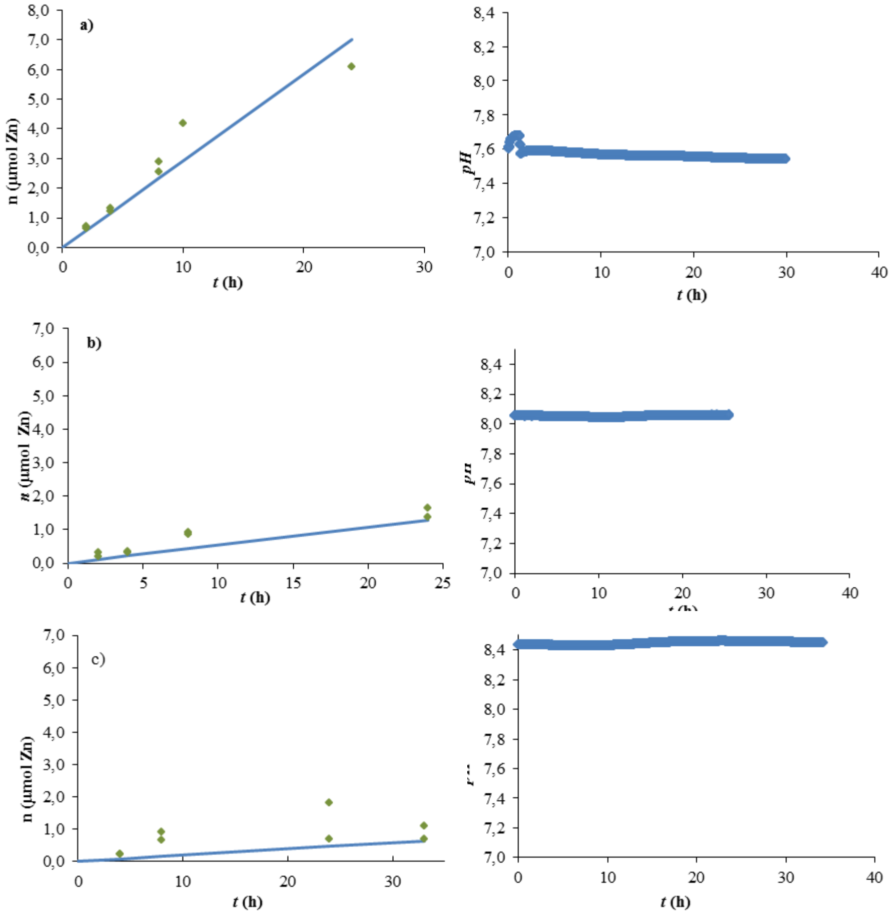

Figure 4.8. Left: Effect of pH on DGT measurements (open pore gels, 0.45 μm pore size filters) vs. time in presence of a final concentration of 90 mg L^{-1} of 71 nm nano-ZnO at 0.1 M ionic strength (0.02 M Tris) and three different pH values: a) 7.58, b) 8.05 and c) 8.45. Markers: experimental values. Line: theoretical values calculated using Eqn. 4.4 with the total dissolved zinc calculated with Visual MINTEQ (parameters from Tables 4.2 and 4.3) at each pH. Right: instantaneous pH values in the immersion solutions recorded throughout each experiment.

Figure 4.9 depicts the normalized Zn accumulations versus time calculated according to the following equation:

$$n_{norm} = n \Big/ (c^*_{Zn} D_{Zn} + c^*_{ZnTris} D_{ZnTris}) \qquad (4.\ 7)$$

The normalized Zn accumulation is used as ordinate axis in order to include in the same figure the results obtained for different pHs. Theoretic accumulations represented by the dotted line are calculated using equation 4.8, derived from the combination of equations 4.4 and 4.7

$$n_{norm} = \frac{A}{g} t \qquad (4.\ 8)$$

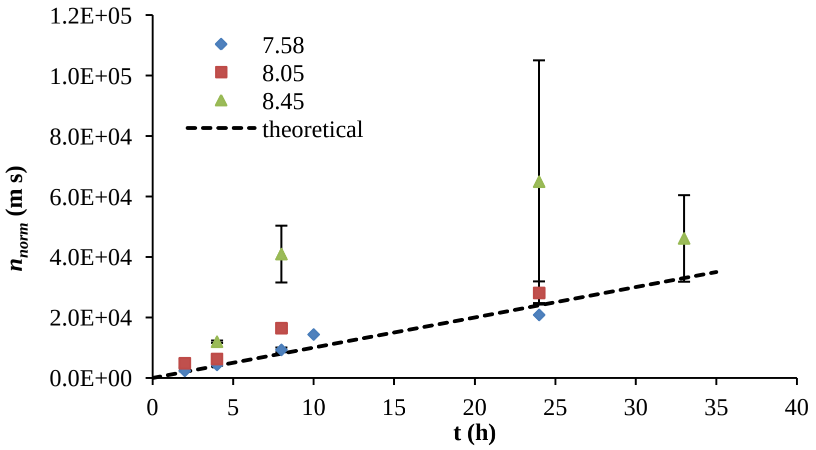

Figure 4.9. Normalized Zn accumulations versus time corresponding to the experiments shown in Figure 4.8. Line represents theoretical values calculated with equation 4.8. See Fig. 4.8 for experimental conditions.

In order to support the hypothesis that the poor reproducibility of the experimental measurements at high pH is related with specific particle effects (such a random penetration in the sensors), an additional experiment adding 8.6 x 10^{-6} M $Cd(NO_3)_2$ to the nano-ZnO dispersion was conducted at pH 8.59. The moles of Zn and Cd accumulated simultaneously in the same device for different deployment times are shown in figure 4.10. The Cd moles measured (orange crosses) are reproducible and in good agreement with the theoretical expectations (assuming negligible adsorption of Cd^{2+} ions on the NPs), while the simultaneous Zn accumulations in the same sensors showed a very poor reproducibility.

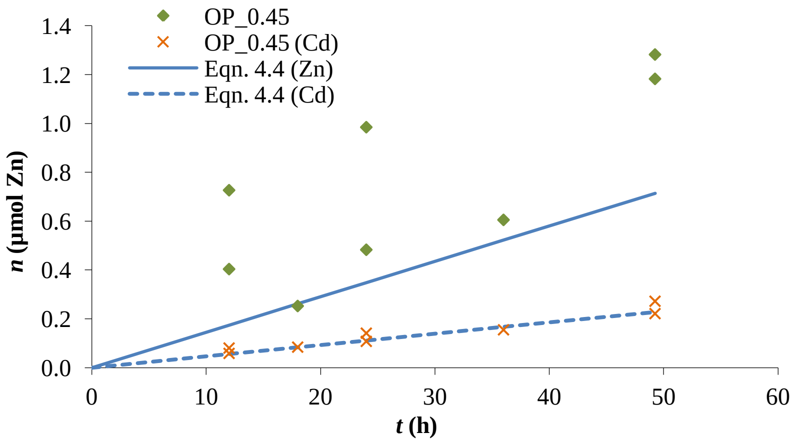

Figure 4.10. Moles of Zn and Cd simultaneously accumulated in the same devices versus time at pH 8.59, 90 mg L^{-1} 71NP nano-ZnO and 8.6 x 10^{-6} M Cd , *I*= 0.1 M (0.02 M Tris). Markers: green diamonds for Zn and orange crosses for Cd. Lines: theoretical accumulations calculated with Eq. 4.4.

These results suggest that the lack of reproducibility is not due to the limit of detection of DGT or other factors related to the gels reproducibility (pore size, thickness...).

4.4.2.4. The capacity of DGT

When a DGT measurement is carried out, it is necessary to ensure that the metal accumulation in the device is well below the maximum capacity (*26*) to avoid saturation effects. The time to reach saturation will vary depending on the concentrations of metals present in solution, pH, temperature and thickness of the diffusive gel layer. The achievement of saturation can be determined by a simple experiment where several sensors are deployed and retrieved at different times. In this particular case, the sensors are exposed to a solution of 4.48 x 10^{-4} M dissolved Zn from 130 mg L^{-1} 71NP nano-ZnO at pH 7.6 (with *I*= 0.1 M KNO_3 and 0.02 M Tris). Initially, the response is linear, but after 24 h the resin is completely saturated and cannot accumulate more Zn (Figure 4.11), leading to an estimated maximum binding corresponding to 6.18 ± 0.03 µmols of Zn per DGT sensor. From this result, and assuming the binding stoichiometry between Zn ions and resin groups as:

$$Zn + 2H_2R \underset{k_a}{\overset{k_d}{\rightleftharpoons}} ZnR_2 + 4H \tag{4.9}$$

$$Zn + 2H_2R \underset{k_a}{\overset{k_d}{\rightleftharpoons}} Zn\left(HR\right)_2 + 2H$$

an amount of resin sites of 12.36 µmols per sensor is obtained. This yields a concentration of sites in the resin layer of 0.137 mol L^{-1}, which is only slightly below 0.147 mol L^{-1} as determined for Cd by S. Mongin (*26*).

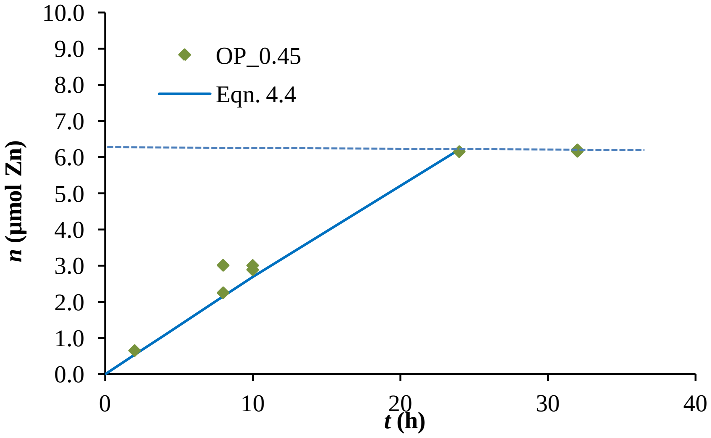

Figure 4.11. DGT-accumulated mass of Zn measured after different deployment times in a suspension of 130 mg L^{-1} 71NP nano-ZnO. I= 0.1 M KNO_3 (0.02 M Tris) at pH 7.6. Markers: experimental measurements. Continuous line: theoretical accumulations calculated by eqn. 4.4; dashed line: estimated maximum binding capacity.

The linear response between moles of metal and deployment time indicates that DGT can be used quantitatively, provided the capacity of the resin used is not exceeded (as in the case of the results presented in the present chapter).

4.4.3. DGT in presence of nano-ZnO and HA

As explained in Chapter 3, the addition of HA to the dispersions of nano-ZnO prevents the aggregation process that arises when the ionic strength is increased. When no HA is present in the deployment solution, nano-ZnO (in the same conditions of pH and salinity) tends to aggregate and from particles of around 1.5 µm while in presence of HA, stable and smaller aggregates are observed, as showed in Figure 4.12b (with average values around 70 nm). HA adsorbs on the nano-ZnO surface providing a negative surface charge so that small aggregates tend to stabilize by electrostatic repulsions (see Chapter 3). It is, therefore, interesting to assess the possible effect of the particle size distribution of the ZnO on the DGT measurements. Low concentrations of HA have been used in these experiments, in order to reproduce typical values found in natural waters.

The moles of Zn accumulated as a function of time in a solution of 100 mg L^{-1} 20NP nano-ZnO in presence of 8.3 mg L^{-1} HA and 0.1 M ionic strength (0.02 M Tris) are shown in figure 4.12a. The figure shows the expected linear increase in the accumulated moles with time. This indicates that the concentration gradient, as well as the flux of Zn, is constant and time-independent during the deployment time (*49*). Experimental accumulations are in good agreement with theoretical expectations calculated using eqn. 4.4 after a speciation computation with Visual MINTEQ was done and the diffusion coefficients of all the species were considered, as reported in the above sections. From the interpolation of the adsorption isotherms presented in Chapter 3, the concentration of HA remaining in solution after equilibration with the 20 NP nano-ZnO was estimated as 1.7 mg L^{-1} (out of the total amount of 8.3 mg L^{-1}). In these conditions, Visual MINTEQ (using the generic NICA parameters) predicts that only 2.5 % of the dissolved Zn is present as humic complexes. The diffusion coefficient of Zn complexes employed in the calculations is $D_{ZnHA}= 0.06 \times D_{Zn}$ (see section 4.3.1.3).

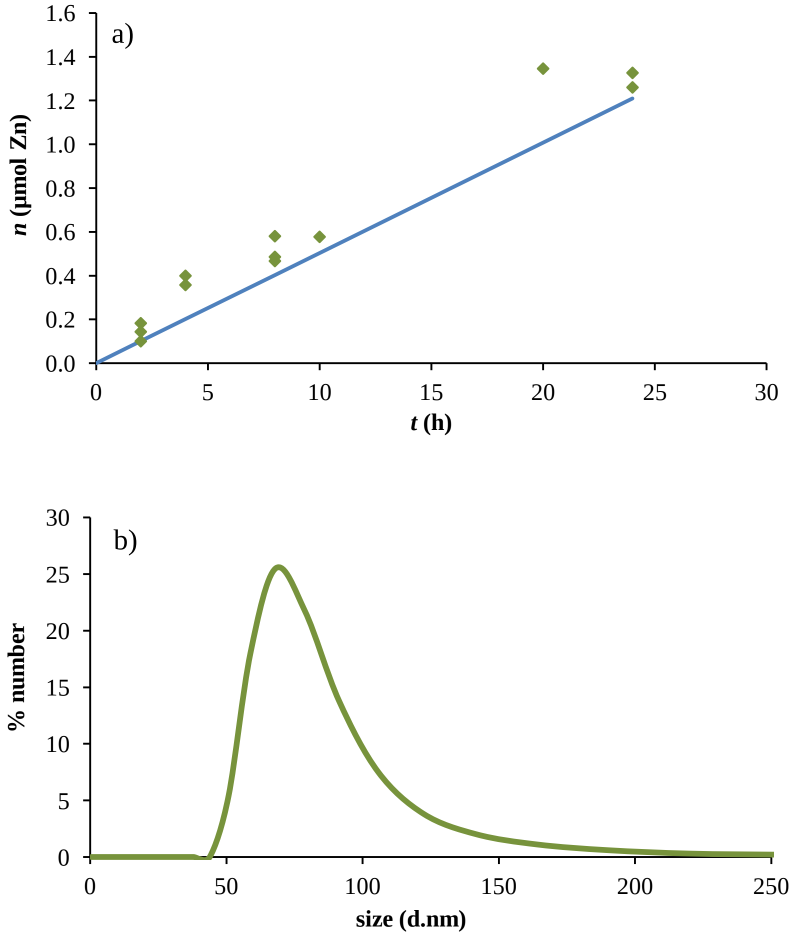

Figure 4.12. a) Time dependence of the accumulated moles of Zn during deployment in a dispersion of 100 mg L^{-1} nano-ZnO 20NP, with 8.3 mg L^{-1} HA, *I*= 0.1 M (0.02 M Tris) at pH 8.14 using open pore gels with 0.45 µm pore size filters . Markers: experimental data; line: theoretical accumulations calculated by eqn. 4.4; b) Number-weighed particle size distribution of the aggregates in the equilibrated immersion solution, as determined by DLS.

The results of Figure 4.12a can be compared with those shown in Figure 4.5b, obtained with the same DGT device configuration in very similar conditions (except for the presence of HA). Note that both sets of experimental data are rather similar, the accumulations being somewhat scattered and always lying above the theoretical calculations, which indicates some influence of particle penetration in both cases. This similarity suggests that the size distribution of the aggregates has a relatively small influence on the performance of DGT, which could seem contradictory with the hypothesis of a random penetration of particles and subsequent dissolution within the diffusion gels. However, the NP dispersion simple in absence of HA is extremely polydisperse (which means that size distributions measured by DLS may not show properly the smallest size fraction), and most of the largest aggregates of the immersion solution tend to settle down at DGT deployment conditions. Therefore, we cannot exclude the possibility that a significant population of relatively small clusters and aggregates (comparable in size to the average size distribution of the HA-coated ZnO) may still persist in the dispersions in absence of HA at the depth of the DGT devices.

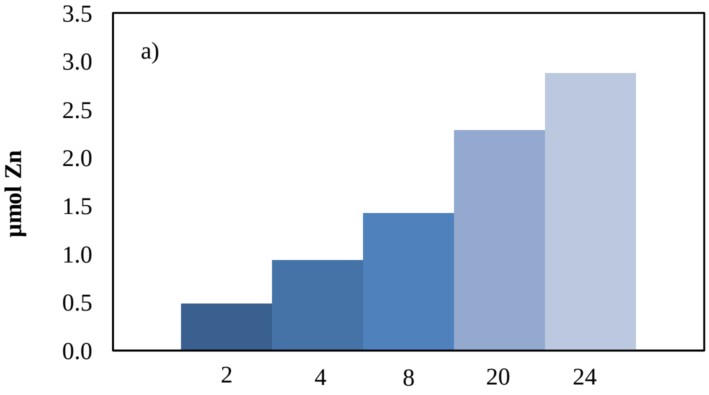

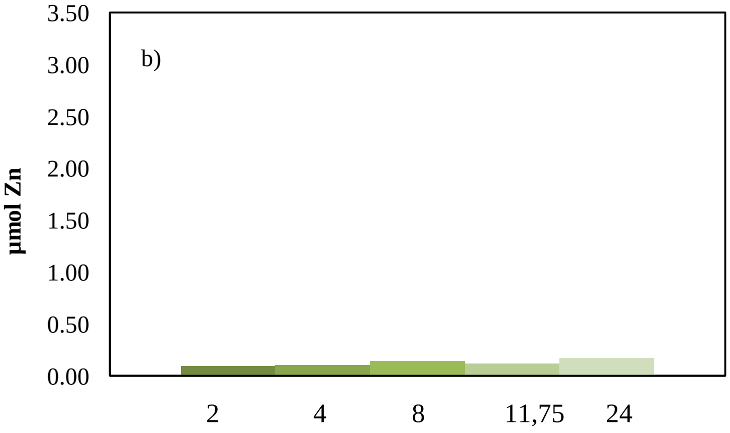

Figure 4.13. Measured moles of Zn in the front filter membrane (0.45 µm pore size) of DGT with time up to 24 h in a deployment solution of 100 mg L^{-1} 20NP nano-ZnO, a) 8.3 mg L^{-1} HA and b) in absence of HA. *I*= 0.1 M (0.08 M KNO_3 and 0.02 M Tris) with pH 8.1.

In addition to the analysis of the resin discs after the deployment, filters were also eluted in an acidic solution and analysed with ICP to determine the possible accumulation of NPs in them. Figure 4.13 shows the values of moles of Zn accumulated in the cellulose filter membranes (0.45 µm pore size). In absence of HA (Figure 13b), with 20NP, the Zn accumulations are negligible (0.126 ± 0.059 µmoles) whereas in presence of HA (Figure 13a) the accumulations increase almost linearly with time up to 2.87 µmoles at 24 h. We suggest that this strong adsorption is due to an affinity between groups of the cellulose filter and the groups of HA since the size of the coated nano-ZnO particles is smaller than the size of uncoated nano-ZnO (so physical trapping of ZnO in the filter fibers does not seem relevant). The nature of these interactions have to be studied, by analysing for instance different ionic strengths, but previous studies have reported that cellulose membrane filters would electrostatically bind free metals and positively charged complexes (*50*).

4.4.4. Comparison of DGT device configurations

Due to the limited reproducibility of the DGT accumulations at high pH in presence of nano-ZnO without HA, different gels (open pore (*OP*) and restricted (*RG*)) and filters (0.45 µm and 0.1 µm pore size) have been tested to assess whether these parameters, which in theory should modify the diffusion conditions, are relevant for the performance of the technique. The measured moles of Zn in different systems using different sensor conformations and pHs for the 71nm NPs were normalized with respect to the theoretical accumulations calculated with equation 4.4 (Table 4.4). A statistical comparison test between these averages indicated that no significant differences are obtained by changing the gels and filters with a 95 % confidence interval.

Table 4.4. Mean value of the experimental moles of Zn normalized with theoretical moles calculated by equation 4.4 (n/n_{theor}). Four different experiments are performed with different combinations of gels (OP and RG) and filters (0.45 µm and 0.1 µm pore size).

pH	OP gel + 0.45 µm size filter	OP gel + 0.1 µm size filter	RG gel + 0.45 µm size filter	RG gel + 0.1 µm size filter
7.72			1.1 ± 0.3	1.1 ± 0.1
7.93		1.5 ± 0.4		
7.97				1.3 ± 0.4
8.05	2.0 ± 0.6	1.1 ± 0.3	1.3 ± 0.4	

The concentration c_{DGT}, as defined in equation 4.3, resulting from all these experiments is presented in Figure 4.14 as a function of pH. Notice that c_{DGT} in these experiments should correspond to a value close to the total Zn concentration of the labile species in solution (free Zn plus Zn-Tris species and inorganic Zn complexes with NO_3^-, OH^-...) since all these species show a diffusion coefficient close to that of the free Zn^{2+}. Figure 4.14 also depicts a continuous line representing the theoretical dissolved Zn concentration in the bulk solutions calculated with Visual MINTEQ. The values of c_{DGT} show a good agreement with the continuous line confirming the usefulness of the straightforward c_{DGT} value to assess the solubility of the nano-ZnO. However, as mentioned in section 4.4.2.3, the experimental uncertainty increases with pH above 8.2.

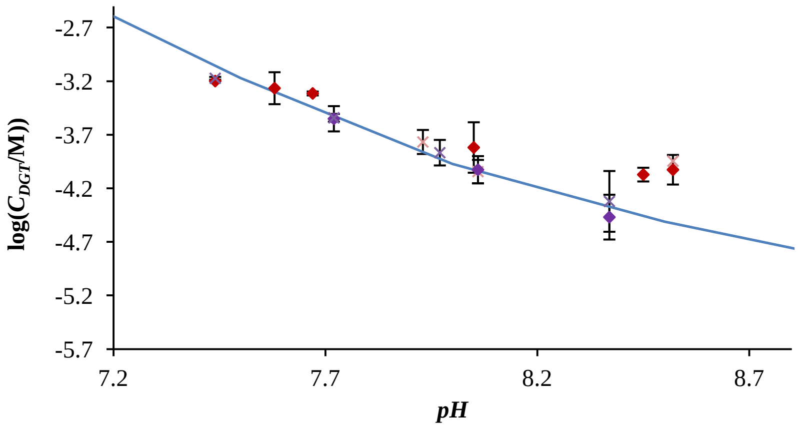

Figure 4.14. Labile concentration of Zn measured in 71NP ZnO dispersions with *I*= 0.1M (0.08 M KNO_3 plus 0.02 M Tris) and spanning a pH range of 7.44 - 8.45. Markers: experimental values obtained using different sensor configurations: OP gel + 0.45 µm pore size filter (red diamonds), OP gel + 0.1 µm pore size filter (red crosses), RG gel + 0.45 µm pore size filter (violet diamonds) and RG gel + 0.1 µm pore size filter (violet crosses). Line: theoretical total dissolved Zn concentration calculated with Visual MINTEQ.

4.4.5. Relation between labile fraction and solubility

As already mentioned in section 4.3.4., the metal accumulations in the DGT sensors allow the calculation of the concentration of labile Zn in the immersion solution (equation 4.4). It is interesting to compare these values with the dissolved Zn values determined by alternative techniques. Typical measurements of solubility of NPs are conducted using ultrafiltration and/or ultracentrifugation. To check the usefulness of filtration techniques, different samples of the deployment solution were analysed directly without any separation to get the total zinc present in the solution, after filtration (through

0.45 µm or 0.1 µm size pore filters) or after centrifugation (30 minutes at 18000 rpm). In all the cases, samples are acidified and measured by ICP-OES.

Figure 4.15 show the mean dissolved Zn concentrations obtained from DGT measurements at three different pHs, *i. e.*: 8.58 (blue), 8.05 (green) and 8.45 (violet), compared with the total Zn concentrations after filtration (F) or centrifugation (SN). Notice how at pH 7.58 and pH 8.05 the three methods give the same results, whereas at the highest pH DGT measurements yield somewhat larger and less reproducible results than those obtained after filtration or centrifugation. As discussed above, this could be ascribed to a relatively significant contribution of random particle penetration and dissolution into the DGT devices, which are in contact with the dispersions during relatively long deployment times. The presence of small NPs in the filtrates or supernatant, however, should be less relevant, due to the small contact times of the filtration operation and the highly aggregated state of the dispersions (which makes centrifugation very efficient in terms of the removal of particles).

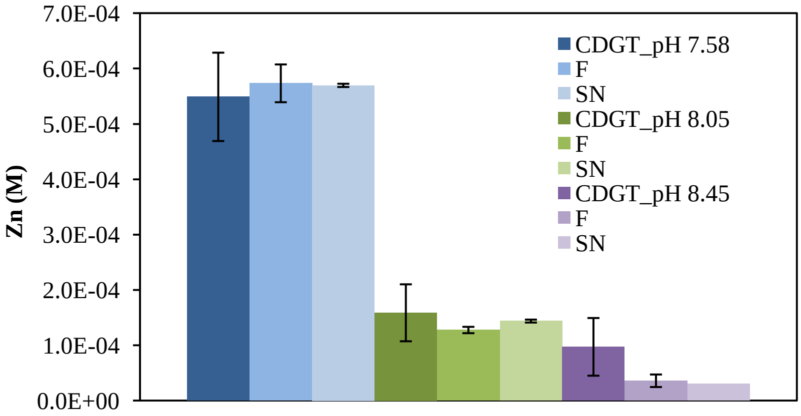

Figure 4.15. Zn concentration measured with DGT after filtration in the supernatant after centrifugation at three different pH: 7.58 (blue), 8.05 (green) and 8.45 (violet). *I*= 0.1 M (0.08M KNO_3 0.02 M Tris).

4.4.6. Presence of non-labile ligands

According to the results previously seen in Figure 4.15, the calculated DGT concentrations (c_{DGT}) are in agreement with the solubility values determined by filtration and centrifugation of the bulk solution. However, soluble species are not always "bioavailable" (or not to the same extent). In the presence of partially labile or inert complexing ligands, the DGT allows the estimation of the "bioavailable" fraction released from nano-ZnO, while filtration or centrifugation will include all species in solution independently of their dynamic characteristics ("labile" or "inert" nature).

To check these effects we studied the available fraction released from nano-ZnO dispersions containing the relatively strong binding agent, EDTA.

Figure 4.16 shows the Zn measured in a 100 mg L^{-1} 20NP dispersion in the presence of 80 µM EDTA at pH 8.125 and *I*= 0.1M (KNO_3 plus 0.02 M Tris). In these conditions, ZnEDTA complexes amounts the 56.9 % of the total dissolved Zn, whereas the remaining fraction is formed by the species showed in Table 4.5 (speciation values obtained by Visual MINTEQ). Experimental DGT values represented as blue diamonds (0.45 pore size filter) and red squares (0.1 pore size filter) are smaller than theoretical expectations obtained by Visual MINTEQ considering the complex as totally labile (blue line), calculated by applying equation 4.5 with the diffusion coefficient of Zn-EDTA equal to 0.7 x D_{Zn}, as reported in (*40,41*). Experimental DGT values are also smaller than values calculated from the filtered fraction (orange line), considered as free Zn with the corresponding diffusion coefficient.

When theoretical calculations consider the Zn-EDTA as inert species (violet line in Figure 4.16) the experimental accumulations are underestimated, indicating the partially labile character of the Zn-EDTA complexes.

Experimental accumulations can be used to fit the lability degree of the Zn-EDTA complexes. When $\xi_{Zn-EDTA} = 0.3$ the dotted green line is obtained, in good agreement with the experimental accumulations. Previous studies reported Zn-EDTA was not fully labile (*51,52*) as corroborated in Figure 4.16.

Table 4.5. Species distribution in the conditions described above.

% of total Zn	**Species name**
18.287	Zn^{+2}
19.962	$ZnTRISOH^{+}$
0.769	$ZnTRIS^{2+}$
1.169	$ZnOH^{+}$
1.508	$Zn(OH)_2$ (aq)
1.327	$ZnNO^{3+}$
0.012	$Zn(NO_3)_2$ (aq)
56.949	$ZnEDTA^{-2}$
0.015	$ZnOHEDTA^{-3}$

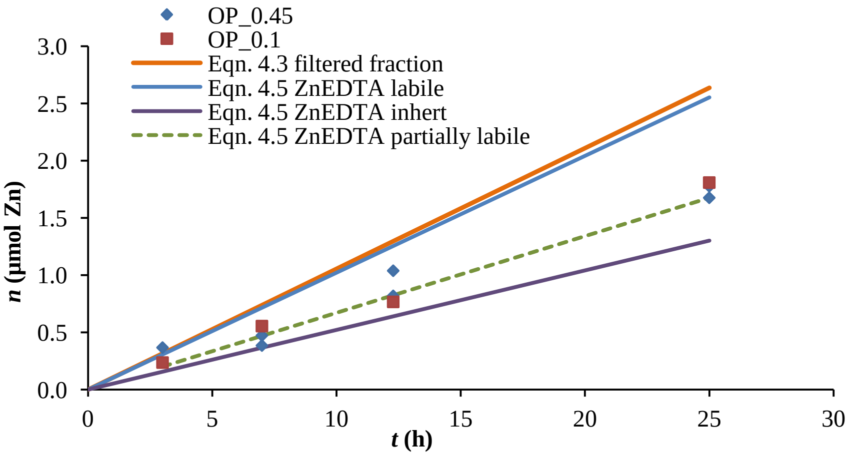

Figure 4.16. Measured moles of Zn for DGT sensors immersed in a nano-ZnO 20NP solution (100 mg L^{-1}) containing 8 x 10^{-5} M EDTA at different deployment times. I= 0.1 M (0.08 M KNO_3 plus 0.02 M Tris) and pH 8.12. Markers: experimental accumulations with OP gels and 0.45 µm (blue diamonds) or 0.1 µm (red squares) pore size filters. Orange line: theoretical accumulations calculated from eqn. 4.3 assuming c_{DGT} as equal to the experimental concentration measured in filtrated samples of the deployment solution; blue line: theoretical values calculated from eqn. 4.5 using bulk solution speciation concentrations (from Visual MINTEQ) assuming the ZnEDTA complexes as fully labile ($\xi = 1$) with D_{ZnEDTA}= 0.7*D_{Zn}; violet line: values calculated by applying eqn. 4.5 with D_{ZnEDTA}= 0.7*D_{Zn} and considering Zn-EDTA complexes as completely inert ($\xi = 0$); green dotted line: values calculated assuming D_{ZnEDTA}= 0.7*D_{Zn} and ξ =0.3.

4.5. Conclusions

DGT has been evidenced as an effective technique for measuring labile metal concentrations in nano-ZnO dispersions. It has been shown that, even in presence of small nanoparticles, the measurements are sensitive and reproducible. At some deployment nano-ZnO solutions, good agreement occurred between DGT measured metal and ICP measurements of total metal concentration after filtration or centrifugation, as well as with the predicted values obtained by Visual MINTEQ, in absence of inert metal complexes.

Solubility of nano-ZnO is dependent on the size of the primary NPs. The quantitative estimations of the solubility based on previous determinations using AGNES agree with the values of solubility determined in this work from the accumulations measured with DGT devices. This agreement gives further support to the accuracy of the DGT measurements and opens the way to measure the solubility of other nanoparticles with DGT overcoming the restrictions of AGNES.

The solubility of nano-ZnO shows an important dependence on pH changes. Due to this dependence, the pH has to be controlled during the experiments by using pH buffers as Tris or MOPS. In these cases, it has to be taken into account that the complexation of Zn by Tris buffer contributes to increase the NP solubility and, therefore, the metal accumulation in DGT (labile Zn fraction).

Measurements of the capacity of the resin to Zn ions have shown that up to 6.15 µmols of metal can be accumulated in the resin layer.

Above pH 8.4 the reproducibility of the experimental measurements decreases and the employment of RG gels and 0.1 µm size pore filters have no significant influence on the experimental uncertainty.

More definitive data is required to predict the possible penetration of the nanoparticles on the polyacrylamide gels, as the structure and diffusional properties of polyacrylamide gels are not clearly known (*24*).

The accumulations obtained by DGT in deployments with dispersions of NPs in presence of strong complexing ligands, such as EDTA, have little dependence on the EDTA concentration. These results indicate the low labile character of the Zn-EDTA complexes in DGT measurements.

The removal of the solid-liquid separation step together with the low cost of the sensors, enhance the interest for the application of DGT to the routine testing of the solubility of NPs in different aqueous media.

DGT is a potentially useful technique for long-term monitoring ecotoxicity studies supplying an *in situ* speciation measurement integrated over time.

4.6. References

1. David, C.; Galceran, J.; Rey-Castro, C.; Puy, J.; Companys, E.; Salvador, J.; Monne, J.; Wallace, R.; Vakourov, A. Dissolution Kinetics and Solubility of ZnO Nanoparticles Followed by AGNES. *The Journal of Physical Chemistry C* **2012,** *116*, 11758.

2. Zhou, D. X.; Keller, A. A. Role of morphology in the aggregation kinetics of ZnO nanoparticles. *Water Res* **2010,** *44*, 2948.

3. Bian, S. W.; Mudunkotuwa, I. A.; Rupasinghe, T.; Grassian, V. H. Aggregation and Dissolution of 4 nm ZnO Nanoparticles in Aqueous Environments: Influence of pH, Ionic Strength, Size, and Adsorption of Humic Acid. *Langmuir* **2011,** *27*, 6059.

4. Reed, R. B.; Ladner, D. A.; Higgins, C. P.; Westerhoff, P.; Ranville, J. F. Solubility of nano-zinc oxide in environmentally and biologically important matrices. *Environ Toxicol Chem* **2012,** *31*, 93.

5. Zhou, H.; Wanf, X.; Zhou, Y; Yao, H.; Ahmad, F. Evaluation of the toxicity of ZnO nanoparticles to Chlorella vulgaris by use of the chiral perturbation approach. *Anal Bioanal Chem* **2014,** *406*, 3689.

6. Poynton, H. C.; Lazorchak, J. M.; Impellitteri, C. A.; Smith, M. E.; Rogers, K.; Patra, M.; Hammer, K.; Allen, H.; Vulpe, C. D. Differential gene expression in Daphnia magna suggests distinct

modes of action and bioavailability for ZnO nanoparticles and Zn ions. *Environ Sci Technol* **2011,** *45*, 762.

7. Davison, W.; Zhang, H. In-Situ Speciation Measurements of Trace Components in Natural-Waters Using Thin-Film Gels. *Nature* **1994,** *367*, 546.

8. Zhang, H.; Davison, W. Performance-Characteristics of Diffusion Gradients in Thin-Films for the in-Situ Measurement of Trace-Metals in Aqueous-Solution. *Anal Chem* **1995,** *67*, 3391.

9. Davison, William; Zhang, Hao Progress in understanding the use of diffusive gradients in thin films (DGT) – back to basics. *Environ Chem* **2012,** *9*, 1.

10. Pouran, H.; Martin, F.; Zhang, H. Measurement of ZnO Nanoparticles Using Diffusive Gradients in Thin Films: Binding and Diffusional Characteristics. *Anal Chem* **2014,** *86*, 5906.

11. Pouran, H.; Llabjani, V.; Martin, F.; Zhang, H. Evaluating using ATR-FTIR spectroscopy the binding mechanisms of ZnO nanoparticles and Zn2+ to Chelex®-100 and Metsorb™. *Environ Sci Technol* **2013**.

12. Buffet, P. E.; Pan, J. F.; Poirier, L.; Amiard-Triquet, C.; Amiard, J. C.; Gaudin, P.; Faverney, C.; Guibbolini, M.; lliland, D.; Valsami-Jones, E.; Mouneyrac, C. Biochemical and behavioural responses of the endobenthic bivalve Scrobicularia plana to silver nanoparticles in seawater and microalgal food. *Ecotoxicology and Environmental Safety* **2013,** *89*, 117.

13. Buffet, P. E.; Zalouk-Vergnoux, A.; Châtel, A.; Berthet, B.; Métais, I.; Perrein-Ettajani, H.; Poirier, L.; Luna-Acosta, A.; Thomas-Guyon, H.; Risso-De Faverney, C.; Guibbolini, M.; Gilliland, D.; Valsami-Jones, E.; Mouneyrac, C A marine mesocosm study on the environmental fate of silver nanoparticles and toxicity effects on two endobenthic species: the ragworm Hediste diversicolor and the

bivalve mollusc Scrobicularia plana. *Sci Total Environ* **2013,** *470*, 1151.

14. Buffet, P. E.; Richard, M.; Caupos, F.; Vergnoux, A.; Perrein-Ettajani, H.; Luna-Acosta, A.; Akcha, F.; Amiard, J. C.; Amiard-Triquet, C.; Guibbolini, M.; Risso-De Faverney, C.; Thomas-Guyon, H.; Reip, P.; Dybowska, A.; Berhanu, D.; Valsami-Jones, E.; Mouneyrac, C. A mesocosm study of fate and effects of CuO nanoparticles on endobenthic species (Scrobicularia plana, Hediste diversicolor). *Environ Sci Technol* **2012,** *47*, 1620.

15. Navarro, E.; Piccapietra, F.; Wagner, B.; Marconi, F.; Kaegi, R.; Odzak, N.; Sigg, L.; Behra, R. Toxicity of Silver Nanoparticles to Chlamydomonas reinhardtii. *Environ Sci Technol* **2008,** *42*, 8959.

16. Buffet, P. E.; Tankoua, O. F.; Pan, J. F.; Berhanu, D.; Herrenknecht, C.; Poirier, L.; Amiard-Triquet, C.; Amiard, J. C.; Berard, J. B.; Risso, C.; Guibbolini, M.; Romeo, M.; Reip, P.; Valsami-Jones, E.; Mouneyrac, C. Behavioural and biochemical responses of two marine invertebrates Scrobicularia plana and Hediste diversicolor to copper oxide nanoparticles. *Chemosphere* **2011,** *84*, 166.

17. Schlich, K.; Klawonn, T.; Terytze, K.; Hund-Rinke, K. Effects of silver nanoparticles and silver nitrate in the earthworm reproduction test. *Environ Toxicol Chem* **2013,** *32*.

18. Odzak, N.; Kistler, D.; Behra, R.; Sigg, L. Dissolution of metal and metal oxide nanoparticles in aqueous media. *Environ Pollut* **2014,** *191*, 8.

19. Künniger, T; Gerecke, A. C.; Ulrich, A.; Huch, A.; Vonbank, R.; Heeb, M.; Wichser, A.; Haag, R.; Kunz, P.; Faller, M. Release and environmental impact of silver nanoparticles and conventional organic biocides from coated wooden façades. *Environ Pollut* **2014,** *184*, 464.

20. Muller, K. H.; Kulkarni, J.; Motskin, M.; Goode, A.; Winship, P.; Skepper, J. N.; Ryan, M. P.; Porter, A. E. pH-Dependent Toxicity of High Aspect Ratio ZnO Nanowires in Macrophages Due to Intracellular Dissolution. *Acs Nano* **2010,** *4,* 6767.

21. Vermeer, A. Interactions between humic acid and hematite. *Thesis* **1996**.

22. Gustafsson, J. P. Visual MINTEQ, version 3.0. *Department of Land and Water Resources Engineering.The Royal Institute of Technology* **2011,** *Sweden*.

23. Zhang, H.; Davison, W. Performance-characteristics of diffusion gradients in thin- films for the in-situ measurement of trace-metals in aqueous- solution. *Anal.Chem.* **1995,** *67*, 3391.

24. Zhang, H.; Davison, W. Diffusional characteristics of hydrogels used in DGT and DET techniques. *Anal Chim Acta* **1999,** *398*, 329.

25. Mudunkotuwa, I. A.; Rupasinghe, T.; Wu, C. M.; Grassian, V. H. Dissolution of ZnO Nanoparticles at Circumneutral pH: A Study of Size Effects in the Presence and Absence of Citric Acid. *Langmuir* **2012,** *28*.

26. Mongin, S. Contributions to the study of the availability of metal ions in aquatic systems. *Doctoral Thesis* **2012**.

27. Garmo, O. A.; Davison, W.; Zhang, H. Effects of Binding of Metals to the Hydrogel and Filter Membrane on the Accuracy of the Diffusive Gradients in Thin Films Technique. *Anal Chem* **2008,** *80,* 9220.

28. Garmo, O. A.; Naqvi, K. R.; Royset, O.; Steinnes, E. Estimation of diffusive boundary layer thickness in studies involving diffusive gradients in thin films (DGT). *Anal Bioanal Chem* **2006,** *386*, 2233.

29. Puy, J.; Uribe, R.; Mongin, S.; Galceran, J.; Cecilia, J.; Levy, J.; Zhang, H.; Davison, W. Lability Criteria in Diffusive Gradients in Thin Films. *Journal of Physical Chemistry A* **2012,** *116*, 6564.

30. Scally, S.; Davison, W.; Zhang, H. Diffusion coefficients of metals and metal complexes in hydrogels used in diffusive gradients in thin films. *Anal Chim Acta* **2006,** *558*, 222.

31. Zhang, H. In-situ speciation of Ni and Zn in freshwaters: Comparison hetween DGT measurements and speciation models. *Environ Sci Technol* **2004,** *38*, 1421.

32. Garmo, O. A.; Royset, O.; Steinnes, E.; Flaten, T. P. Performance study of diffusive gradients in thin films for 55 elements. *Anal Chem* **2003,** *75*, 3573.

33. Warnken, K. W.; Zhang, H.; Davison, W. Accuracy of the diffusive gradients in thin-films technique: Diffusive boundary layer and effective sampling area considerations. *Anal Chem* **2006,** *78*, 3780.

34. Mongin, S.; Uribe, R.; Rey-Castro, C.; Cecília, J.; Galceran, J.; Puy, J. Limits of the Linear Accumulation Regime of DGT Sensors. *Environ Sci Technol* **2013,** *47*, 10438.

35. Scally, S.; Davison, W.; Zhang, H. In situ measurements of dissociation kinetics and labilities of metal complexes in solution using DGT. *Environ.Sci.Technol.* **2003,** *37*, 1379.

36. Mongin, S.; Uribe, R.; Puy, J.; Cecilia, J.; Galceran, J.; Zhang, H.; Davison, W. Key Role of the Resin Layer Thickness in the Lability of Complexes Measured by DGT. *Environ Sci Technol* **2011,** *45*, 4869.

37. Uribe, R.; Mongin, S.; Puy, J.; Cecilia, J.; Galceran, J.; Zhang, H.; Davison, W. Contribution of Partially Labile Complexes to the DGT Metal Flux. *Environ Sci Technol* **2011,** *45*, 5317.

38. Ferreira, D.; Tousset, C.; Ridame, M.; Tusseau-Vuillemin, M. H. More than inorganic copper is bioavailable to aquatic mosses at environmentally relevant concentrations. *Environ Toxicol Chem* **2008,** *27*, 2108.

39. Bradac, P.; Behra, R.; Sigg, L. Accumulation of cadmium in periphyton under various freshwater speciation conditions. *Environ Sci Technol* **2009,** *43*, 7291.

40. Van Leeuwen, H. P. Steady-state DGT fluxes of nanoparticulate metal complexes. *Environ Chem* **2011,** *8*, 525.

41. Soares, H. M. V. M.; Pinho, S. C.; Barros, M. G. R. T. Influence of N-substituted aminosulfonic acids with a morpholinic ring pH buffers on the redox processes of copper or zinc ions: A contribution to speciation studies. *Electroanalysis* **1999,** *11*, 1312.

42. Uher, E.; Zhang, H.; Santos, S.; Tusseau-Vuillemin, M. H.; Gourlay-France, C. Impact of Biofouling on Diffusive Gradient in Thin Film Measurements in Water. *Anal Chem* **2012,** *84*, 3111.

43. Lead, J. R.; Starchev, K.; Wilkinson, K. J. Diffusion coefficients of humic substances in agarose gel and in water. *Environmental Science and Technology* **2003,** *37*, 482.

44. Pinheiro, J. P.; Mota, A. M.; dOliveira, J. M. R.; Martinho, J. M. G. Dynamic properties of humic matter by dynamic light scattering and voltammetry. *Anal Chim Acta* **1996,** *329*, 15.

45. Van der Veeken, P. L.; Chakraborty, P.; Leeuwen, H. P. Accumulation of humic acid in DET/DGT gels. *Environ Sci Technol* **2010,** *44*, 4253.

46. Lead, J. R.; Starchev, K.; Wilkinson, K. J. Diffusion coefficients of humic substances in agarose gel and in water. *Environ.Sci.Technol.* **2003,** *37*, 482.

47. Yebra, D. M.; Kiil, S.; Weinell, C. E.; Dam-Johansen, K. Dissolution rate measurements of sea water soluble pigments for antifouling paints: ZnO. *Progress in Organic Coatings* **2006,** *56*, 327.

48. Imali A.Mudunkotuwa, Vicki H. Grassian The devil is in the details (or the surface): impact of surface structure and surface energetics on understanding the behavior of nanomaterials in the environment. *J Environ Monitor* **2011,** *13*, 1135.

49. Docekal, B.; Rezacova-Smetkova, V.; Docekalova, H. Effect of humic acid on metal uptake measured by diffusive gradients in thin films technique. *Chemical Papers-Chemicke Zvesti* **2005,** *59*, 298.

50. Weltje, L.; den Hollander, W.; Wolterbeek, H. T. Adsorption of metals to membrane filters in view of their speciation in nutrient solution. *Environ Toxicol Chem* **2003,** *22*, 265.

51. Wang, P.; Zhou, D. M.; Luo, X. S.; Li, L. Z. Effects of Zn-complexes on zinc uptake by wheat (Triticum aestivum) roots: a comprehensive consideration of physical, chemical and biological processes on biouptake. *Plant and Soil* **2009,** *316*, 177.

52. Tusseau-Vuillemin, M. H.; Gilbin, R.; Taillefert, M. A dynamic numerical model to characterize labile metal complexes collected with diffusion gradient in thin films devices. *Environ Sci Technol* **2003,** *37*, 1645.

Chapter 5

Measurement of Metals Using DGT: Impact of Ionic Strength and Kinetics of Dissociation of Complexes in the Resin Domain

Results contained in this chapter have been published in:

Analytical Chemistry 86 **2014**, *86* (15), pp 7740–7748

http://pubs.acs.org/doi/abs/10.1021/ac50167

Chapter 5. Measurement of Metals Using DGT: Impact of Ionic Strength and Kinetics of Dissociation of Complexes in the Resin Domain

5.1. Abstract

As the measurement of metals by DGT in low salinity media has been controversial, a thorough study of the impact of ionic strength is timely. DGT accumulations of Cd, Co and Ni in the presence of NTA at pH 7.5 with I in the range 10^{-4} M to 0.5 M were obtained. An observed decrease in the metal accumulation as the ionic strength of the system decreased is partially explained by the electrostatic repulsion between the negatively charged resin domain and the dominant negatively charged complex species M-NTA. This electrostatic effect reduces the complex penetration into the resin domain, especially for non-labile complexes which do not fully dissociate in the gel domain. Analytical expressions, based on the Donnan model were able to quantify these electrostatic effects. Additionally, the data indicate that the kinetic dissociation constant of M-NTA complexes in the resin layer is higher than Eigen predictions, suggesting a ligand assisted dissociation mechanism. As the ionic strength decreases, the rate of reaction in the resin layer decreases due to the repulsion between the negatively charged resin sites and the complex species. This decrease contributes to the decrease in metal accumulation. These novel, previously unconsidered, effects of ionic strength and the ligand assisted dissociation mechanism in the resin domain will affect DGT measurements made in freshwaters and soils.

5.2. Introduction

Dynamic measurement techniques can provide information on chemical speciation which is very relevant to understanding the transport and bioavailability of metal ions in natural environments (*1-4*). Natural waters contain a large number of small ligands and different proportions of dissolved organic matter which compete and interact with metals present in the system, modifying their mobility and availability. Any uptake of metals in this system is, in general, a dynamic process resulting from a cascade of interconversion processes, which tend to buffer the metal consumption at the surface of the sensor or living organism.

The widely used technique of Diffusion Gradients in Thin Films (DGT) (*5*) utilises simple devices for measuring *in situ* the labile species of most metal cations (*6*), some anions (*7*) and other hydrophilic compounds (*8*). It is based on the use of a hydrogel which defines a diffusion domain located on top of a binding layer containing a binding agent embedded in the same kind of hydrogel used in the diffusive layer. Both layers are mounted as discs in a plastic moulding.

The application of DGT in low ionic strength solutions, which has been carefully studied (*9*) and reviewed (*10*), is very relevant for freshwaters. Specific effects that contravene the normal assumption of a completely inert diffusion layer have been observed and discussed. For instance, enhanced metal accumulation by DGT has been reported (*11,12*) and explained by a pre-accumulation of the metal cations on the hydrogel due to the presence of some negative charges in the gel domain (*13-16*). This influence is only noticeable at low ionic strength (I <1 mM) (*9*). Exhaustive washing of the cast gels minimises or even slightly reverses the gel charge and consequently reduces or even reverses the enhanced accumulation. Cations can also bind specifically to the hydrogels and filter membranes used in DGT (*14,17,18*). Such weak binding (with the exception of Hg) at low density sites is largely independent of ionic strength and long deployment times reduce its influence on the DGT measurement.

Progress in the interpretation of DGT measurements in solutions containing metal complexes has been recently reported. Using a stack of multiple resin discs in the same DGT device, the distribution of the metal bound to the resin disc has been assessed, concluding that for most cations, at pH>=6, the binding is strong and fast, so that the resin disc acts as a perfect sink for the metal (*19*).

Studies of the contribution of complexes to the DGT accumulation (*20*,*21*) have shown that the resin disc plays an active role in the metal accumulation by extending the layer where there is net dissociation of the complex. Implications of these results for the practical use of DGT have been discussed (*22*-*24*).

Two new implications of complex penetration in the resin domain emerge in this work: a) electrostatic partitioning between gel and resin layers and b) modified complex dissociation rate constants in the resin layer. The resin disc is expected to exhibit a high negative charge due to the metal binding sites of the resin. At high ionic strength, electrostatic effects of these charged sites will be screened by the background electrolyte, but at low ionic strength, there will be an additional influence on the metal accumulation from the charge of the resin disc. This influence is expected to be mild for the free metal, since its concentration is assumed to be negligible at the resin disc surface (there is no penetration of free metal in the resin disc for most metal cations). However, this influence is expected to be relevant for charged partially labile complexes as the concentration of complex inside the resin disc will be modulated by the attractive or repulsive electrostatic effects of the resin disc. Regarding b), we show that Eigen predictions with the standard closest approach of the outer sphere complex cannot fit the experimental data.

It is the aim of this work to assess the influence of low ionic strengths on the DGT measurement of metals in solutions where there are charged complexes. Nitrilotriacetic acid (NTA) is used as a ligand, since it tends to form dominant negatively charged complexes with divalent cations. The three metals used Ni, Cd and Co, form complexes with a range of labilities. Section 5.3 presents the standard theoretical framework. Sections 5.4 and 5.5 discuss the experimental data. Section 5.6 incorporates electrostatics effects into the model. Section 5.7 interprets the obtained data with the new model.

5.3. Standard model assumptions and computation of the experimental lability degree

The complexation of Ni, Cd or Co ions with nitrilotriacetic (NTA) acid can be represented as

$$\mathrm{ML} \underset{k_\mathrm{a}}{\overset{k_\mathrm{d}}{\rightleftharpoons}} \mathrm{M} + \mathrm{L} \tag{5.1}$$

All these divalent cations (charges are omitted for simplicity) bind to the NTA^{3-} species giving rise to negatively charged complexes. Experimental conditions were selected so that M-NTA are the dominant metallic species in all the systems considered (*i.e.* the free metal concentration is negligible).

The equilibrium relationship can be expressed as

$$K = \frac{k_a}{k_\mathrm{d}} = \frac{c_\mathrm{ML}^*}{c_\mathrm{M}^* c_\mathrm{L}^*} \tag{5.2}$$

where K, k_a and k_d are respectively the equilibrium, and the association and dissociation rate constants of the complexation process (5.1) and c_i^* labels the concentration of species i in the bulk solution.

Previous work has led to a "standard model" (*20,21,25,26*) whose assumptions are:

i) M, L and ML diffuse in a domain which comprises a resin layer ($0 < x < r$) and a gel layer ($r < x < r + g$). Here, for the sake of simplicity diffusion characteristics in the gel layer, filter and diffusive boundary layer (DBL), (*27*) are considered identical. Thus, g can be seen as the aggregated diffusion distance for gel, filter and DBL thicknesses.

ii) The free metal concentration is negligible throughout the resin gel domain (perfect sink), due to its fast and strong binding to the resin sites. Evidence supporting this approximation is reported in section 5.4.1.

iii) Complexes penetrate into the resin gel, where they can still dissociate. New evidence for this hypothesis is reported in section 5.4.2. As a first approximation, binding sites are assumed to be evenly distributed (*28*) in the resin gel.

iv) No direct ternary binding of complex to the resin sites is considered (*29*).

Let J label the metal flux of M bound to the resin, *i.e.*, the moles of M bound to the resin per unit of time and area of the resin/gel interface. After a short transient, the rate of binding to the resin reaches a steady state. Under these conditions, the metal flux of M bound to the resin is time independent and equals the total metal flux (as M and ML) crossing the resin-gel interface.

From the definition of the lability degree (*30*), ξ, it follows that *J* can be split into the sum of the flux of the M free in the bulk solution (negligible under our experimental conditions) plus the fraction (ξ) of the maximum possible complex contribution (occurring for the case when the complex is fully labile). This maximum complex contribution can be computed as $D_{\mathrm{ML}} c^*_{\mathrm{ML}} / g$ (where D_j stands for the diffusion coefficient of species *j*) if we assume that the resin acts as a perfect sink for the free metal. So, the number of moles of M accumulated in a deployment time *t* crossing the sensor area *A* is

$$n_{\mathrm{M}} = JAt = \frac{D_{\mathrm{M}} c^*_{\mathrm{M}}}{g} At + \xi \frac{D_{\mathrm{ML}} c^*_{\mathrm{ML}}}{g} At \approx \xi \frac{D_{\mathrm{ML}} c^*_{\mathrm{T,M}}}{g} At \tag{5.3}$$

Now, if we repeat the same experiment, but without ligand:

$$n_{\mathrm{M}}^{no-ligand} = \frac{D_{\mathrm{M}} c_{\mathrm{M}}^{*,\, no-ligand}}{g} At \tag{5.4}$$

By dividing previous expressions, we can experimentally compute the lability degree of a complex ML as:

$$\xi_{\mathrm{ML}} = \frac{n_{\mathrm{M}} / c^*_{\mathrm{T,M}}}{\left(D_{\mathrm{ML}} / D_{\mathrm{M}}\right) n_{\mathrm{M}}^{no-ligand} / c_{\mathrm{M}}^{*,\, no-ligand}} \tag{5.5}$$

5.4. Material and methods

5.4.1. Experimental Details

DGT holders (piston type, 2 cm diameter window), polyacrylamide gel discs (diffusive disc, 0.8 mm thick, and Chelex resin disc, 0.4 mm thick) from DGT Research Ltd. were used. A 5 L polyethylene exposure chamber was thermostatted at 25 ± 0.1 °C and stirred at 240 rpm. The DGTs were deployed in solutions of 10^{-5} mol L^{-1} Cd and Co and 2.5 x 10^{-5} mol L^{-1} Ni (prepared from nitrate metal salts) with or without NTA (Fluka, analytical grade) at 8×10^{-5} mol L^{-1}concentration. The pH of the solution was adjusted to pH 7.5 with 1 mM MOPS (Sigma-Aldrich) pH-buffer and accumulations were conducted at ionic strength ranging from 10^{-4} to 0.5 mol L^{-1} $NaNO_3$ (Merck, Suprapur). Solutions and metal accumulations, once eluted in HNO_3, were analyzed by ICP-MS. In order to access to additional information on the phenomena responsible for the accumulations, DGT devices with 2 resin discs (2R) were used in addition to the standard devices with one resin disc (1R). Separate elution and analysis of both resin discs, front (F) close to the diffusive gel or back (B) at the bottom of the sensor, were conducted. Additional experimental details are given in the SI.

5.5. Experimental accumulations and lability degrees

5.5.1. Metal accumulations in systems without ligand

The effect of the ionic strength on metal accumulation when only metal is present in the system has been the subject of several previous studies. In some of them (*12,31*), constant metal accumulations appeared for I>0.001, while increased accumulations at lower ionic strength were justified by the electrostatic effects of some negatively charged groups in the diffusive gel.

Here, metal accumulations at pH 7.5 (obtained as described in Section 5.4) are reported in Table 5.1. Values are expressed as ratios of nmol of metal over bulk concentration to refer the measurements to a fixed metal concentration, avoiding dilution effects resulting from the additions of the background salt.

Table 5.1. Nanomoles of metal accumulated in DGT devices after 24 h deployment normalized to bulk concentrations in systems with ionic strength ranging from 1.22 to 98.5 mM. Experimental conditions: Background electrolyte $NaNO_3$, pH 7.5, $c^*_{\mathrm{T,Cd}} = c^*_{\mathrm{T,Co}} = 10^{-5}\ \mathrm{M}$, $c^*_{\mathrm{T,Ni}} = 2.5\times10^{-5}\ \mathrm{M}$. In different rows, data corresponding to total metal accumulation in DGT devices with only one resin disc (1R), two resin discs (2R), in the front resin disc (close to the gel disc) of the 2R configuration (F), in the back disc (B) and percentage of the metal accumulated in the back resin disc.

I **(mM)**	**sensor**	$\frac{n_{\mathrm{Co}}^{no-ligand}}{c_{\mathrm{T,Co}}^{*,\,no-ligand}}$ **(mL)**	$\frac{n_{\mathrm{Ni}}^{no-ligand}}{c_{\mathrm{T,Ni}}^{*,\,no-ligand}}$ **(mL)**	$\frac{n_{\mathrm{Cd}}^{no-ligand}}{c_{\mathrm{T,Cd}}^{*,\,no-ligand}}$ **(mL)**
1.22	1R	21±3	23±3	21±3
	2R	15.0±0.7	14.5±0.2	14.7±0.7
	F	14.1±0.3	13.6±0.1	13.8±0.2
	B	0.96±0.46	0.82±0.29	0.97±0.47
	% back	6.3±2.8	5.6±1.9	6.5±2.9
9.66	1R	22±5	22±6	21±5
	2R	15.4±0.4	15.0±0.6	15.0±0.3
	F	15.1±0.5	14.8±0.7	14.7±0.4
	B	0.28±0.08	0.24±0.05	0.28±0.07
	% back	1.8±0.6	1.6±0.4	1.9±0.5
98.50	1R	21±5	25±7	21±5
	2R	14.8±0.6	14.1±0.5	14.0±0.6
	F	14.5±0.6	13.8±0.5	13.7±0.6
	B	0.28±0.07	0.27±0.07	0.29±0.05
	% back	1.9±0.5	1.9±0.5	2.1±0.3

The results confirm that the metal accumulation at pH 7.5 is almost independent of ionic strength (*32*), indicating the negligible presence of charged groups in the diffusive gel, as expected for gels that are extensively washed prior to DGT assembly (*9*). These results also indicate that electrostatic effects of the resin charge on the free metal penetration in the resin domain are negligible and accordingly, the perfect sink assumption for free M, as stated in this work, is a reasonable approximation.

Using the simplest interpretation, $\frac{n}{c_{\mathrm{T,M}}} = \frac{D_{\mathrm{M}}A}{g}t$, data of Table 5.1 are used to fit an effective thickness of the diffusion domain. Using diffusion coefficients and area as reported in Table SI-5.4, the effective thickness of the diffusion layer is $g = 8.52 \times 10^{-4}$ m.

5.5.2. Metal accumulation and experimental lability degree, ξ, in M-NTA systems

The accumulated mass of Ni in devices with only one resin disc (1R) decreased with decreasing *I* by a factor greater than 30 in the range of *I* studied (see Table 5.2). Concomitantly, the decrease for Cd was almost negligible under the same conditions, while Co showed an intermediate dependency. The effect of the ionic strength on the Ni accumulation in NiNTA systems cannot be ascribed to a Donnan effect driven by a charged diffusive gel because Table 5.1 shows that the Donnan effect of the gel on the metal-only systems was negligible. This effect in the M-NTA systems must be even smaller due to the higher absolute value of electrical charge of the metal in comparison to the M-NTA complexes.

Table 5.2. Nanomoles of metal accumulated in DGT devices after 24 h deployment normalized by bulk concentrations in systems with ionic strength ranging from 1.22 to 98.5 mM. Experimental conditions: Backgroud electrolyte $NaNO_3$, pH 7.5, $c^*_{\mathrm{T,Cd}} = c^*_{\mathrm{T,Co}} = 10^{-5}\ \mathrm{M}$, $c^*_{\mathrm{T,Ni}} = 2.5\times10^{-5}\ \mathrm{M}$ and $c^*_{\mathrm{T,NTA}} = 8\times10^{-5}\ \mathrm{M}$. Meaning of the rows as in Table 5.1.

I **(mM)**	**sensor**	$n_{\mathrm{Co}} / c^*_{\mathrm{T,Co}}$ **(mL)**	$n_{\mathrm{Ni}} / c^*_{\mathrm{T,Ni}}$ **(mL)**	$n_{\mathrm{Cd}} / c^*_{\mathrm{T,Cd}}$ **(mL)**
1.45	1R	4.7±0.5	0.3±0.1	10.5±1.9
	2R	5.8±0.3	0.4±0.1	9.7±0.1
	F	2.9±0.1	0.21±0.04	6.6±0.3
	B	2.9.±0.4	0.23±0.02	3.1±0.4
	% back	49±4	53±3	32±4
10.5	1R	10.0±0.4	0.7±0.1	12.0±2.3
	2R	10.2±0.1	1.2±0.1	11.1±0.2
	F	6.7±0.2	0.6±0.1	9.2±0.1
	B	3.5±0.3	0.6±0.1	2.0±0.3
	% back	34±3	50±3	18±2
99.2	1R	15.9±3.3	6.0±0.9	14.3±3.1
	2R	15.5±0.1	7.6±0.3	13.8±0.1
	F	12.9±0.3	4.6±0.4	11.2±0.3
	B	2.6±0.4	3.0±0.1	2.6±0.4
	% back	17±2	40±3	19±3
471	1R	16.3±0.4	12.2±0.5	14.31±0.03
	2R	12.7±0.2	9.9±0.2	11.1±0.2
	F	12.2±0.4	7.0±0.5	10.5±0.4
	B	0.5±0.2	2.9±0.2	0.6±0.2
	% back	4±1	29±3	6±2

In systems where the dominant metal species is a partially labile complex, it has been shown that the major supply of metal for accumulation in a standard DGT device comes from complex dissociation inside the resin domain (*22*). Thus, we conclude that the large impact of I on the accumulation of M-NTA (*e.g.* in the case of NiNTA), must arise from an effect operating in the resin domain.

We, then, suggest that the decrease in the metal accumulation as ionic strength decreases is due to an electrostatic repulsion effect between the resin charges and the negatively charged M-NTA species. This repulsion increases as the screening effect of the background electrolyte decreases. The consequent partial exclusion of the complex from the resin domain reduces the accumulation rate. The effect is more important for NiNTA because this is the least labile complex. Labile complexes are less influenced due to their almost complete dissociation in a region close to the gel/resin interface (in the limit of fully labile complexes, penetration would not extend beyond the gel/resin interface).

Additional information on the phenomena responsible for these accumulations can be obtained with replicate experiments with sensors incorporating 2 resin discs. Notice in Table 5.2 that the percentage of metal accumulated in the back resin disc increases to 50% as the ionic strength decreases, especially for Ni and Co, this confirming the penetration of complexes into the resin domain. Having 50% of the mass in the back disc indicates the practical absence of dissociation in the gel domain, because, if there was dissociation in the gel domain, a relevant amount of metal would be bound to the front resin layer coming from the free M generated in the gel layer. In contrast, at high ionic strength, metal accumulation in the back resin layer is as high as 20% for Ni while it is almost negligible for Co and Cd (3 and 5% respectively), indicating that complexes of both metals are quite labile. The decrease in the total metal accumulation as the ionic strength decreases is consistent with reduced penetration of the complex, which lends support to our interpretation based on assuming that this is an effect of the resin.

The experimental lability degrees of Cd, Co and Ni NTA complexes at the different ionic strengths in the range 0.1 mM up to 0.5 M calculated for 1R devices with equation 5 are depicted as markers in Figure 5.1 (see numerical values in the SI, Tables SI-5.1-SI-5.3).

Below I=0.01M, the lability degree of NiNTA drops to almost zero, indicating that there is neither dissociation inside the resin (due to almost complete exclusion of NiNTA) nor in the gel domain.

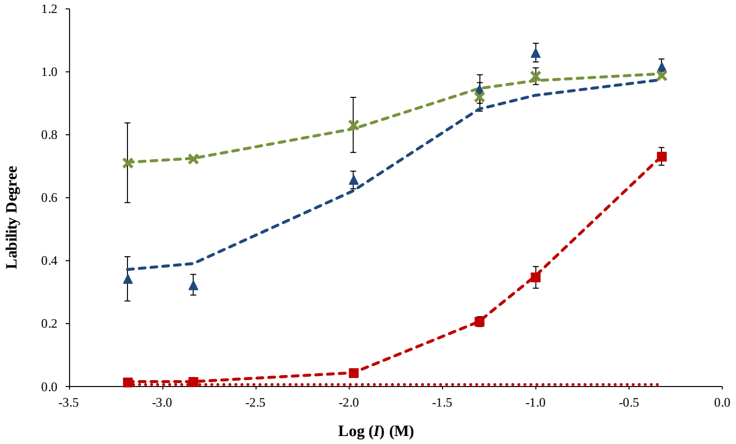

Figure 5.1. Lability degree (ξ_{ML}) of CdNTA, CoNTA and NiNTA complexes at ionic strengths in the range 0.1 mM – 0.5 M. Markers: ξ_{ML} calculated as indicated in eqn. 5.5 from experimental accumulations in single resin DGT devices for CdNTA (green crosses), CoNTA (blue triangles) and NiNTA (red circles). Error bars refer to standard deviations. Dashed lines: Fitted ξ_{ML} values according to eqn. (5.13) with parameters given in Table SI-5.5 and kd-value derived using Eqn 5.15 and values from those reported in the second column of Table 5.3; Red dotted line: Lability degree of NiNTA when dissociation kinetics in both gel and resin domains (without considering any electrostatic effect) follows Eigen values (column 3 in Table 5.3).

5.6. Model accounting for the Donnan repulsion

5.6.1. Formulation of the model

The observed results can be quantitatively described by extending the assumptions of the previous model (*20*,*21*,*25*,*26*) gathered in section 2:

v) There is a Donnan potential difference (Ψ, dependent on the ionic strength) at the interface between the resin phase and the gel phase.

As Chelex iminodiacetic acid groups are partially charged at common environmental pH, they can also be a source of electrostatic effects. The charge of the resin phase (Q) is expected to be higher than that of the diffusive gel, since the resin gel contains the charges of the polyacrylamide gel plus a larger charge resulting from the deprotonated Chelex sites.

vi) The electric potentials are homogeneous in each of the phases.

This hypothesis means that the background electrolyte ($NaNO_3$) together with the charge of the sites in the resin beads determine Ψ:

$$\Psi = \frac{RT}{F} \operatorname{arcsin h}\left(-\frac{Q}{2V_{\mathrm{r}} I} \right) \tag{5.6}$$

where V_{r} labels the volume of the resin domain (*33*).

The beads are known to be most prevalent near to the resin/gel interface. However, to keep the model sufficiently simple we assume that they produce a constant potential throughout the resin phase.

Effects of the metal and complex concentration profiles on the electrostatic potential are negligible, because, even at low ionic strength, metal concentrations are negligible compared with the concentration of the background electrolyte.

Assuming a homogeneous electrostatic potential along the resin domain also implies that the spatial distance between charges, l_C, in the resin domain is shorter than the Debye length, K^{-1}, $l_C < \kappa^{-1}$, where $\kappa^{-1} = \left(\varepsilon RT/2F^2 I\right)^{1/2}$. Actually, charges are packed in the resin beads. So the critical distance is the distance between beads. The calculation of this distance requires a detailed knowledge of the resin swelling. According to the manual of the supplier Bio-Rad, important changes of volume (up to 100%) arise for different ionic forms. Thus, we consider the smeared-out Donnan potential a first approximation to this problem, which could be refined in future work. A smeared-out Donnan potential has been used previously when considering the electrostatic effects of the diffusive gel in DGT accumulations (*13*). The present application focuses on the resin charge.

As discussed in (*34,35*), the assumption of a step potential at the resin-gel interface is a reasonable approximation for the electric potential profile when $r >> \kappa^{-1}$, a condition verified in standard DGT devices.

vii) Boltzmann equilibrium conditions rule the ratio of concentrations at the resin-gel interface and transient effects (in the building up of the Donnan potential) can be neglected.

The assumed step potential at the resin gel interface together with assumed equilibrium concentration profiles imply that concentration profiles of charged species are discontinuous (see Fig. SI-5.3). The discontinuity is determined by the Boltzmann factor, Π, which relates the complex concentrations at both sides of the resin/gel interface (represented as $c_{\mathrm{ML}}^{r^-}$ and $c_{\mathrm{ML}}^{r^+}$, respectively)

$$\Pi = \frac{c_{\mathrm{ML}}^{r^+}}{c_{\mathrm{ML}}^{r^-}} = \exp\left(-\frac{F\Psi}{RT}\right) \tag{5.7}$$

Free metal is not influenced by Donnan effects inside the resin domain, since we assume that the resin surface acts as a perfect sink for the metal.

With these hypotheses, the expression for the metal flux derived in Uribe *et al.*, (*21*) can be extended to take into account a possible electrostatic effect of the resin (see SI):

$$J = \frac{D_{\mathrm{M}} c_{\mathrm{M}}^{*}}{g} + \frac{D_{\mathrm{ML}} c_{\mathrm{ML}}^{*}}{g}\left[1 - \frac{\left(1+\varepsilon K^{'}\right)}{\varepsilon K^{'} + \frac{g}{m}\coth\left(\frac{g}{m}\right) + \frac{g}{\lambda_{\mathrm{ML}}}\frac{\left(1+\varepsilon K^{'}\right)}{\Pi}\tanh\left(\frac{r}{\lambda_{\mathrm{ML}}}\right)}\right] \tag{5.8}$$

where all the symbols have the standard meaning:

$$K^{'} = Kc_{\mathrm{L}}^{*} \tag{5.9}$$

$$\varepsilon = \frac{D_{\mathrm{ML}}}{D_{\mathrm{M}}} \tag{5.10}$$

$$m = \sqrt{\frac{D_{\mathrm{ML}}}{k_{\mathrm{d}}\left(1+\varepsilon K'\right)}} \tag{5.11}$$

and

$$\lambda_{\mathrm{ML}} = \sqrt{\frac{D_{\mathrm{ML}}}{k_{\mathrm{d}}}} \tag{5.12}$$

The derivation of eqn. (5.8) is detailed in the Supporting Information for a more general case when the diffusion coefficients of ML in the resin ($D_{\mathrm{ML}}^{\mathrm{R}}$) and gel (D_{ML}) could be different and the observed dissociation rate constant in the resin ($k_{\mathrm{d}}^{\mathrm{R}}$) might be different from that in gel layer (k_{d}).

Comparison of eqn (5.8) with eqn. (5.3) leads to the model expression for the lability degree:

$$\xi = 1 - \frac{1+\varepsilon K^{'}}{\varepsilon K^{'} + \dfrac{g}{m}\coth\left(\dfrac{g}{m}\right) + \dfrac{g}{\lambda_{\mathrm{ML}}}\dfrac{\left(1+\varepsilon K^{'}\right)}{\Pi}\tanh\left(\dfrac{r}{\lambda_{\mathrm{ML}}}\right)} \tag{5.13}$$

5.6.2. Fitting procedure

Using data in Fig. 5.1, we plan to estimate the values of the kinetic dissociation constants of the respective complexes (3 parameters), as well as the Boltzmann factor at each ionic strength (6 parameters). Not all points are equally sensitive to the 9 parameters, so, a convenient fitting procedure should be applied to avoid local minima.

a) Fitting the NiNTA kinetic dissociation constant

Let us assume that the electrostatic effects can reasonably be neglected (Π = 1) at the highest ionic strength, I = 0.5M (for the sake of simplicity we refer to the nominal I as in Table 5.4). Using eqns. 5.9-5.13, the kinetic dissociation constant of NiNTA can be found from the experimental lability degree of the NiNTA complex at I = 0.5 M taking g as fitted above, $K^{'} = 6.06\times10^{4}$ (given by Visual MINTEQ for the data of the experiment) and ε=0.7 (*20,36*). The resulting k_d-value is reported in the first column of Table 5.3.

This procedure cannot be used to determine the k_d -values of the CdNTA or CoNTA species, since these complexes are labile at I = 0.5 M and their respective metal accumulations are then independent of k_d and only limited by the diffusive transport of the complex.

Table 5.3. Estimated dissociation rate constants by solving eqn. (5.13) for ξ from experimental data reported as markers in Fig. 5.1. First column: k_d values resulting from fitting a common value for the dissociation rate constant in the gel and resin domains. Second column: k_d values resulting from fitting and extrapolating a specific dissociation rate constant applying only in the resin domain (k_d^R). Third column: k_d values resulting from Eigen expectations, labelled $k_{d,E}$.

	Fitted k_d (s^{-1}) (only one value for both gel and resin domains)	Fitted k_d^R (s^{-1}) for resin domain at I=0.5M	k_d (s^{-1}) calculated using Eigen´s ideas ($k_{d,E}$)
k_d NiNTA	6.29×10^{-3}	6.36×10^{-3}	7.77×10^{-6}
k_d CoNTA	2.77	0.98	7.38×10^{-3}
k_d CdNTA	12.92	4.01	4.19

Table 5.4. Boltzmann factor (π and Donnan potential (Ψ) values estimated by fitting experimental data in MNTA systems at pH 7.

nominal I (M)	real I (M)	Π	Π considering 2 dissociation mechanisms ($k_{\mathrm{d,E}}$ and $k_{\mathrm{d}}^{\mathrm{R}}$)	Ψ (mV)	$\left\lvert\frac{Q}{V_{\mathrm{r}}}\right\rvert$ (mol·L^{-1})
5×10^{-4}	6.46×10^{-4}	1322.5	15.2	-69.9	0.010
1×10^{-3}	1.45×10^{-3}	923.0	14.4	-68.5	0.021
0.01	1.05×10^{-2}	74.9	6.4	-47.5	0.065
0.05	4.96×10^{-2}	10.9	1.8	-15.7	0.065
0.1	9.92×10^{-2}	5.2	1.3	-7.3	0.057
0.5	4.71×10^{-1}	1.0	1.0	0.0	0.000

b) Fitting the Boltzmann factors, Π, and the dissociation rate constants

Once k_{d} of NiNTA is known, Π values can be computed by fitting the experimentally measured lability degrees of NiNTA at ionic strengths 0.1 to 0.01 M using eqn. (5.13) (see third column in Table 5.4).

With Π =74.9, a kinetic dissociation constant for CdNTA and CoNTA complexes can be computed using eqn. (5.13) at I=0.01M. This experiment is used, since both CoNTA and CdNTA are non labile at this ionic strength, so that the lability degree is now dependent on the kinetic dissociation constant. The resulting k_{d}-values are reported in Table 5.3. These values (k_{d} for CdNTA and CoNTA) can be used to calculate the remaining Π values at I = 1.5×10^{-3}M and 5×10^{-4}M, since the important exclusion of the NiNTA from penetration in the resin domain at this ionic strength renders this complex almost fully inert, so that Ni accumulation becomes insensitive to the actual Donnan exclusion factor. Π -values are gathered in Table 5.4 and they should hold for all divalent metals, since Π -values are only dependent on the charge of the resin and the ionic strength.

5.7. Dissociation kinetics in the resin domain. Ligand assisted dissociation

Fitted k_d-values can be compared with the expected ones deduced using Eigen's method which prescribes:

$$k_\mathrm{d} = \frac{K^{os} k_{-w}}{K} \tag{5.14}$$

where the outer sphere stability constant K^{os} is assessed as the electrostatic interaction energy between two point charges of values 2 and -3 corresponding to the free metal and ligand, respectively (*37*). Eigen predicted values, $k_\mathrm{d,E}$, computed using the standard closest approach between the point charges in the outer sphere complex, 0.5 nm, are also included in Table 5.3. The substantial differences between the fitted k_d values and $k_\mathrm{d,E}$ point to other factors not considered in the Eigen mechanism playing a key role in CoNTA and NiNTA dissociation. The reasonable agreement between k_d and $k_\mathrm{d,E}$ for CdNTA indicate that these factors are not present in this system. As NiNTA dissociation takes place almost entirely in the resin domain, a ligand assisted mechanism might be responsible for this accelerated NiNTA dissociation in the presence of the resin. In the other limit, Cd dissociation takes place at the gel/resin interface and penetration into the resin layer is not physically relevant due to the labile character of this complex. The kinetic constant is then close to Eigen expectations. Co is an intermediate case. Thus, two parallel routes for metal accumulation appear in the resin domain: dissociation (which can follow Eigen) followed by the binding of the free metal to the resin and the direct reaction of the complex with the resin site (see details in section 1.5 of the SI). The need to consider alternatives to the basic Eigen mechanism follows from the accumulation data of the three cations covering a wide range of labilities. Arvajeh *et al.* (*24*) value for the kinetic dissociation constant of the NiNTA also differed from that obtained using the standard Eigen framework, but they obtained a fit by using a specific value for the shortest closest approach.

The model developed here is quite simplistic. For example, no effect of ionic strength on the pore size distribution of the gel is assumed from $I = 5\times10^{-4}$M to 0.5M; common diffusion coefficients in the DBL, gel and resin domains are used. Consideration of these effects would produce some changes in the fitted parameters, but it is unlikely to account for the mismatch of three orders of magnitude between k_{d} and $k_{\mathrm{d,E}}$.

As the fitting of k_{d} the dissociation rate constant for NiNTA relies on the Ni accumulation at I = 0.5M, replicate measurements (n=6) were undertaken for these conditions. On the other hand, sticking to the Eigen value, the corresponding lability degree of the NiNTA would be only 0.006 in the most favourable conditions (assuming $\Pi = 1$ for all ionic strengths), far from the experimental values as indicated in Fig. 5.1 (dotted line).

The theoretical derivation of eqn. (5.7) can then be refined by distinguishing two parallel dissociation mechanisms in the resin domain (which act jointly) plus the dissociation in the gel domain according to the Eigen mechanism.

The corresponding k_{d} values will be labelled $k_{\mathrm{d}}^{\mathrm{R}}$ and $k_{\mathrm{d,E}}$, respectively. The final expression is formally identical to eqn. (5.7), but *m* has to be computed using $k_{\mathrm{d,E}}$ in eqn. 5.11 and λ_{ML} has to be computed with $k_{\mathrm{d}}^{\mathrm{R}}$ in eqn. 5.12 as indicated in the SI.

The application of this refined expression (5.7) to the experimental data needs still to consider the effect of the ionic strength on $k_{\mathrm{d}}^{\mathrm{R}}$. As $k_{\mathrm{d}}^{\mathrm{R}} >> k_{\mathrm{d,E}}$, we conclude that $k_{\mathrm{d}}^{\mathrm{R}}$ essentially corresponds to the ligand assisted mechanism. As both, the resin sites and complexes are negatively charged, a decrease of $k_{\mathrm{d}}^{\mathrm{R}}$ as the ionic strength decreases is expected. This decrease is also consistent with the increase of the percentage in the back resin disc of Ni reported in Table 5.2. Otherwise, this increase could not be justified since the exclusion of the complex from penetration in the resin domain should lead to a reduction of the percentage in the back resin disc in the 2-R experiments. Assuming the Debye Hückel dependence,

$$\log k_{\mathrm{d}}^{\mathrm{R}} = \log k_{\mathrm{d}}^{\mathrm{R},\infty} + 1.02 z_{\mathrm{R}} z_{\mathrm{MNTA}} I^{1/2} \tag{5.15}$$

where $k_{\mathrm{d}}^{\mathrm{R},\infty}$ is the value of the kinetic dissociation constant at infinite dilution and $z_{\mathrm{R}} z_{\mathrm{MNTA}}$ is the product of the charges of the reacting ions. z_{R} will be taken as 2 assuming that 2 deprotonated functional groups are involved in the resin site. Notice that this is the most favourable mechanism from an energetic point of view (no need to expend energy in extracting protons).

The decrease of Ni accumulation as the ionic strength decreases stems then from two effects: the electrostatic repulsion of negatively charged partially labile complexes (*i.e.* less concentration in the resin layer) and the decrease of the ligand assisted dissociation rate.

With the refined expression (5.7), we start a new fitting procedure using the values of the Eigen expectations reported in Table 5.3 for the gel domain, aiming at finding $k_{\mathrm{d}}^{\mathrm{R}}$ in the resin with the same procedure as described above, *i. e.*, assuming $\Pi = 1$ at I = 0.5M, extrapolating $k_{\mathrm{d}}^{\mathrm{R}}$ to all the ionic strength values using Eqn. 5.15 and finding, finally, the remaining π values. The obtained values of $k_{\mathrm{d}}^{\mathrm{R},\infty}$ are 0.17, 4.14×10^{-2}, 2.7×10^{-4} s^{-1} for Cd, Co and Ni, respectively. Final results are reported in Table 5.3 for the dissociation constants and in Table 5.4 for the Donnan factors. Notice that, although the model has been modified by including the Eigen values in the gel, fitted k_{d}-values inside the resin layer ($k_{\mathrm{d}}^{\mathrm{R}}$ values reported in the second column) do not differ significantly from those fitted previously (first column), indicating that dissociation in the resin domain is the main mechanism of releasing metal to be bound by the resin.

Experimental and predicted lability degree values are depicted in Figure 5.1, which shows a good agreement between both sets of values. Conversely, the new resulting Π values reported in column 4 of Table 5.4 are considerably reduced from those in column 3, because the decrease of Ni accumulation is mainly ascribed to the change in $k_{\mathrm{d}}^{\mathrm{R}}$ with ionic strength. Additional independent support for the Π values thus obtained can be gained from measuring the concentrations of Na^{+} ions in the resin domain in comparison to the solution. A quite reasonable agreement is obtained between the π values that can be derived from the Na^{+} measurements reported in Table SI-5.5 compared to those reported in Table 5.4, obtained by the fitting of the lability degree as outlined above. Finally, the expected percentage of mass of Ni bound to the back resin disc derived from the model increases from 39 to 48%, in reasonable agreement with the experimental measurements reported in Table 5.2.

Further work is needed to confirm this mechanism more generally. However, if the considerable enhancement of kinetic dissociation constants compared to predictions based on the Eigen mechanism (overcoming the repulsion effect) holds for all complexes in the resin domain, complexes measured by DGT will be far more labile than previously expected. Both phenomena (repulsion and non-Eigen behavior), with opposite effects, might affect DGT measurements of metals. However, for NiNTA complexes, the increase of the lability due to the kinetic dissociation enhancement is much more important than the repulsion effect of the resin. Notice that the accumulation would be almost negligible if the Eigen dissociation mechanism applied to NiNTA complexes (see horizontal dotted line in Fig. 5.1 corresponding to $\xi = 0.006$). The enhancement of metal accumulations due to the ligand assisted dissociation in the resin domain can, then, explain the unexpectedly high Ni concentrations measured by in situ DGT deployments in natural waters, as found in (*38*).

The π -value in the fourth column of Table 5.4 for the lowest ionic strength is estimated to be 15 (accepting the limitations of this rough model and the available data). Donnan factors of this order have been found for proton or metal accumulations in the Donnan volume of Humic Acids (*33,39-41*). A graphical representation of the resin effect on the complex concentration profile is found in Fig. 5.2 (see red crosses markers) at pH= 7.5 and I= 0.1M. Notice the drop in the NiNTA concentration profile at $x = r$, the resin gel interface. The ratio between the concentrations at both sides of the interface is just the factor Π whose value is 1.3 as indicated in Table 5.4 for I= 0.1M. For the 2R devices, the complex concentration profile, also depicted in Fig. 5.2, is lower than in the 1R device. This reduces the complex concentration available for dissociation and consequently the expected accumulated mass in the 2R should be less than double of that in 1R devices as observed.

Values reported in Table 5.4 also suggest that pH in the resin domain can decrease by more than 1 unit for sufficiently low ionic strengths due to the Donnan attractive effect of the resin domain over the protons. However, other effects not considered here, as for instance the proton binding to NTA when M dissociates, can modify this pH. Protons can also play a role in the ligand assisted dissociation of MNTA. The consideration of this effect would modify the fitted Π values, but a dedicated experimental study needs to be conducted to evaluate this effect.

5.8. Density of charge of the resin

A final step is the estimation of the charge of the resin in each experiment. Combining Eqns. (5.6) and (5.7), we have

$$\ln \Pi = \operatorname{arcsin h}\left(-\frac{Q}{2V_{\mathrm{r}}I}\right) \tag{5.16}$$

from which the density of charge in the resin domain, -Q/V_{r}, can be determined at each ionic strength. Notice that both the ionic strength and pH in the resin domain (determined by pH in the bulk and the Boltzmann factor) influence the density of charge in the resin domain. Results of -Q/V_{r} are then particular for each ionic strength and are reported in Table 5.4. Alternatively, values of $-Q/V_r$ can be calculated from the mass of chelex used per disc, the protonation constants of the chelex, $pK_{a,1}$=3.2 and $pK_{a,2}$=8.9 (*42*,*43*), and the pH of the resin. The calculated values lie in the range 0.038-0.040 depending on the ionic strength, in broad agreement with the values reported in Table 5.4, especially if we take into account that the chelex beads are not perfectly distributed in the resin disc due to some settling during casting.

5.9. Conclusions

Ligand assisted dissociation in the resin disc, together with Donnan effects, are relevant to understanding the measurement of metals at low ionic strength using DGT devices, as established for partially labile M-NTA complexes. Donnan effects arise from the negatively charged deprotonated groups of the resin beads, which tend to reduce the concentration of negatively charged species that penetrate into the resin, in this case M-NTA complexes. Measurement of free metals are relatively unaffected by ionic strength since they minimally penetrate, being bound at the resin-gel interface.

A model that considers Donnan potentials derived from the resin charges, the screening of the background electrolyte and the transport and complexation reactions of the chemical species has been developed and used to fit satisfactorily the accumulation data.

The fitting process demonstrated the important role of ligand assisted dissociation of the complexes which overwhelms the contribution of the parallel Eigen route in the resin domain. Due to this effect, metal accumulation in DGT devices is higher than expected from dissociation constants derived using Eigen assumptions. The ligand assisted rate constant is also dependent on the ionic strength, being the main factor responsible for the reduction of the metal accumulation as the ionic strength decreases.

Donnan factors reported in Table 5.4 can be used for any DGT experiment at pH 7.5, whenever the standard mass of Chelex in the resin disc is used, as in the present work. Complexes with charge *z* need to correct the Boltzmann factor as Π^{-z}.

This new understanding provides a unified explanation for several data sets obtained at low ionic strength.

5.10. Acknowledgments

Financial support from the Spanish Ministry of Education and Science (Projects CTQ2009-07831 and CTM2012-39183) and from the "Comissionat per a Universitats i Recerca del Departament d'Innovació, Universitat i Empresa de la Generalitat de Catalunya" (2009SGR00465) is acknowledged.

■ ASSOCIATED CONTENT

S Supporting Information

Additional information as noted in the text. This material is available free of charge via the Internet at http://pubs.acs.org.

5.11. References

1. Buffle, J.; Wilkinson, K. J.; van Leeuwen, H. P. Chemodynamics and Bioavailability in Natural Waters. *Environ Sci Technol* **2009**, *43,* 7170.

2. Mota, A. M.; Pinheiro, J. P.; Goncalves, M. L. S. Electrochemical Methods for Speciation of Trace Elements in Marine Waters. Dynamic Aspects. *J.Phys.Chem.A* **2012**, *116,* 6433.

3. Town, R. M.; van Leeuwen, H. P.; Buffle, J. Chemodynamics of soft nanoparticulate complexes: Cu(II) and Ni(II) complexes with fulvic acids and aquatic humic acids. *Environ Sci Technol* **2012**, *46,* 10487.

4. Bravin, M. N.; Garnier, C.; Lenoble, V.; Gerard, F.; Dudal, Y.; Hinsinger, P. Root-induced changes in pH and dissolved organic matter binding capacity affect copper dynamic speciation in the rhizosphere. *Geochim Cosmochim Ac* **2012**, *84,* 256.

5. Davison, W.; Zhang, H. In-Situ Speciation Measurements of Trace Components in Natural-Waters Using Thin-Film Gels. *Nature* **1994**, *367,* 546.

6. Garmo, O. A.; Royset, O.; Steinnes, E.; Flaten, T. P. Performance study of diffusive gradients in thin films for 55 elements. *Anal Chem* **2003**, *75,* 3573.

7. Osterlund, H.; Chlot, S.; Faarinen, M.; Widerlund, A.; Rodushkin, I.; Ingri, J.; Baxter, DC. Simultaneous measurements of As, Mo, Sb, V and W using a ferrihydrite diffusive gradients in thin films (DGT) device. *Anal Chim Acta* **2010**, *682,* 59.

8. A novel passive water sampler for in situ sampling of antibiotics. *J Environ Monitor* **2012**, *14,* 1523.

9. Warnken, K. W.; Zhang, H.; Davison, W. Trace metal measurements in low ionic strength synthetic solutions by diffusive gradients in thin films. *Anal Chem* **2005**, *77,* 5440.

10. Davison, William; Zhang, Hao Progress in understanding the use of diffusive gradients in thin films (DGT) – back to basics. *Environ Chem* **2012**, *9*, 1.

11. Alfaro-De la Torre, M.; Beaulieu, P. Y.; Tessier, A. In situ measurement of trace metals in lakewater using the dialysis and DGT techniques. *Anal Chim Acta* **2000**, *418*, 68.

12. Use of the diffusion gradient thin film method to measure trace metals in fresh waters at low ionic strength. *Anal Chim Acta* **2002**, *42*, 9250.

13. Yezek, L. P.; Van der Veeken, P. L.; Van Leeuwen, H. P. Donnan Effects in Metal Speciation Analysis by DET/DGT. *Environ Sci Technol* **2008**, *42*, 9250.

14. Yezek, L. P.; Van Leeuwen, H. P. Donnan Effects in the Steady-State Diffusion of Metal Ions through Charged Thin Films. *Langmuir* **2005**, *21*, 10342.

15. Van der Veeken, P. L.; Pinheiro, J. P.; Van Leeuwen, H. P. Metal Speciation by DGT/DET in Colloidal Complex Systems. *Environ Sci Technol* **2008**, *42*, 8835.

16. Van der Veeken, P. L.; Van Leeuwen, H. P. DGT/DET Gel Partition Features of Humic Acid/Metal Species. *Environ Sci Technol* **2010**, *44*, 5523.

17. Garmo, O. A.; Davison, W.; Zhang, H. Interactions of trace metals with hydrogels and filter membranes used in DET and DGT techniques. *Environ Sci Technol* **2008**, *42*, 5682.

18. Garmo, O. A.; Davison, W.; Zhang, H. Effects of Binding of Metals to the Hydrogel and Filter Membrane on the Accuracy of the Diffusive Gradients in Thin Films Technique. *Anal Chem* **2008**, *80*, 9220.

19.Levy, J. L.; Zhang, H.; Davison, W.; Puy, J.; Galceran, J. Assessment of trace metal binding kinetics in the resin phase of diffusive gradients in thin films. *Anal Chim Acta* **2012**, *717*, 143.

20. Mongin, S.; Uribe, R.; Puy, J.; Cecilia, J.; Galceran, J.; Zhang, H.; Davison, W. Key Role of the Resin Layer Thickness in the Lability of Complexes Measured by DGT. *Environ Sci Technol* **2011**, *45*, 4869.

21. Uribe, R.; Mongin, S.; Puy, J.; Cecilia, J.; Galceran, J.; Zhang, H.; Davison, W. Contribution of Partially Labile Complexes to the DGT Metal Flux. *Environ Sci Technol* **2011**, *45*, 5317.

22. Puy, J.; Uribe, R.; Mongin, S.; Galceran, J.; Cecilia, J.; Levy, J.; Zhang, H.; Davison, W. Lability Criteria in Diffusive Gradients in Thin Films. *Journal of Physical Chemistry A* **2012**, *116*, 6564.

23. Uribe, R.; Puy, J.; Cecilia, J.; Galceran, J. Kinetic mixture effects in diffusion gradients in thin films (DGT). *Phys Chem Chem Phys* **2013**, *15*, 11349.

24. ArvaJeh, M. R. S.; Lehto, N.; Garmo, O. A.; Zhang, H. Kinetic Studies of Ni Organic Complexes Using Diffusive Gradients in Thin Films (DGT) with Double Binding Layers and a Dynamic Numerical Model. *Environ Sci Technol* **2013**, *47*, 463.

25. Tusseau-Vuillemin, M. H.; Gilbin, R.; Taillefert, M. A dynamic numerical model to characterize labile metal complexes collected with diffusion gradient in thin films devices. *Environ Sci Technol* **2003**, *37*, 1645.

26. Lehto, N. J.; Davison, W.; Zhang, H.; Tych, W. An evaluation of DGT performance using a dynamic numerical model. *Environ Sci Technol* **2006**, *40*, 6368.

27. Warnken, K. W.; Davison, W.; Zhang, H.; Galceran, J.; Puy, J. In situ measurements of metal complex exchange kinetics in freshwater. *Environ Sci Technol* **2007**, *41*, 3179.

28. Zhang, H.; Davison, W. Direct in situ measurements of labile inorganic and organically bound metal species in synthetic solutions and natural waters using diffusive gradients in thin films. *Anal Chem* **2000**, *72*, 4447.

29. Chakrabarti, C. L.; Lu, Y.; Gregorie, D. C.; Back, M. H.; Schrroeder, W. H. Kinetic studies of metal speciation using chelex cation exchange resin: application to cadmium, copper and lead speciation in river water and snow. *Environ Sci Technol* **1994**, *28*, 1957.

30. Galceran, J.; Puy, J.; Salvador, J.; Cecilia, J.; van Leeuwen, H. P. Voltammetric lability of metal complexes at spherical microelectrodes with various radii. *J Electroanal Chem* **2001**, *505,* 85.

31. Peters, A. J.; Zhang, H.; Davison, W. Performance of the diffusive gradients in thin films technique for measurement of trace metals in low ionic strength freshwaters. *Anal Chim Acta* **2003**, *478*, 237.

32. Panther, J. G.; Whelsh, D. T.; Teasdale, P. R. Simultaneous measurement of trace metal and oxyanion concentrations in water using diffusive gradients in thin films with a Chelex-Metsorb mixed binding layer. *Anal Chem* **2014**, *86*, 427.

33. Companys, E.; Garces, J. L.; Salvador, J.; Galceran, J.; Puy, J.; Mas, F. Electrostatic and specific binding to macromolecular ligands - A general analytical expression for the Donnan volume. *Colloid Surface A* **2007**, *306*, 2.

34. Ohshima, H. Electrical Phenomena at Interfaces: Fundamentals, Measurements, and Applications. *Furusawa,K.* **1998**, *Eds. 2nd, Marcel Dekker: New York,* Chapter 1.

35. Van Leeuwen, H. P.; Galceran, J. Physicochemical kinetics and transport at chemical-biological surfaces. *John Wiley* **2004**, *Chichester, UK*, Chapter 3.

36. Mongin, S.; Uribe, R.; Rey-Castro, C.; Cecília, J.; Galceran, J.; Puy, J. Limits of the Linear Accumulation Regime of DGT Sensors. *Environ Sci Technol* **2013**, *47*, 10438.

37. Morel, F. M.; Hering, J. G. Principles and Applications of Aquatic Chemistry. *John Wiley* **1993**, *New York*, Chapter 3.

38. Warnken, K. W.; Lawlor, A. J.; Lofts, S.; Tipping, E.; Davison, W.; Zhang, H. In Situ Speciation Measurements of Trace Metals in Headwater Streams. *Environ Sci Technol* **2009**, *43*, 7230.

39. Benedetti, M.; Van Riemsdijk, W.; Koopal, L. K. Humic substances considered as a heterogeneous Donnan gel phase. *Environ Sci Technol* **1996**, *30*, 1805.

40. Kinniburgh, D. G.; van Riemsdijk, W. H.; Koopal, L. K.; Borkovec, M.; Benedetti, M.; Avena, M. J. Ion binding to natural organic matter: competition, heterogeneity, stoichiometry and thermodynamic consistency. *Colloid Surface A* **1999**, *151*, 147.

41. Saito, T.; Nagasaki, S.; Tanaka, S.; Koopal, L. K. Electrostatic interaction models for ion binding to humic substances. *Colloid Surface A* **2005**, *265*, 104.

42. Alberti, G.; Guiso, M.; Biesuz, R. Usage of Empore membrane in alcoholic media for copper(II) distribution studies. *Talanta* **2009**, *79*, 603.

43. Alberti, G.; Biesuz, R. Empore (TM) membrane vs. Chelex 100: Thermodynamic and kinetic studies on metals sorption. *React Funct Polym* **2011**, *71*, 588.

Measurement of Metals Using DGT: Impact of Ionic Strength and Kinetics of Dissociation of Complexes in the Resin Domain

SUPPORTING INFORMATION

Supplementary information available:

1. Mathematical formulation

The mathematical formulation and solution of the present problem has to consider the transport and reaction phenomena of all the species in the diffusive gel and resin domains. Diffusion is originated by the reaction of metal to the resin sites while migration effects might appear due to the uncompleted screening of the charge of the resin sites. Under the hypotheses reported in the running text, a constant potential applies both in the gel and resin domains with the change in electric potential being located at the resin-gel interface and determined by a step function, so migration terms are not needed in the continuity or flux equations. Advection is not necessary, either, because the diffusive gel restricts the movement of solution masses and the diffusive boundary layer (DBL) is treated under Nernst approximation of an equivalent distance with only diffusion. An approximate steady-state solution can then be straightforwardly obtained as outlined below.

The Model

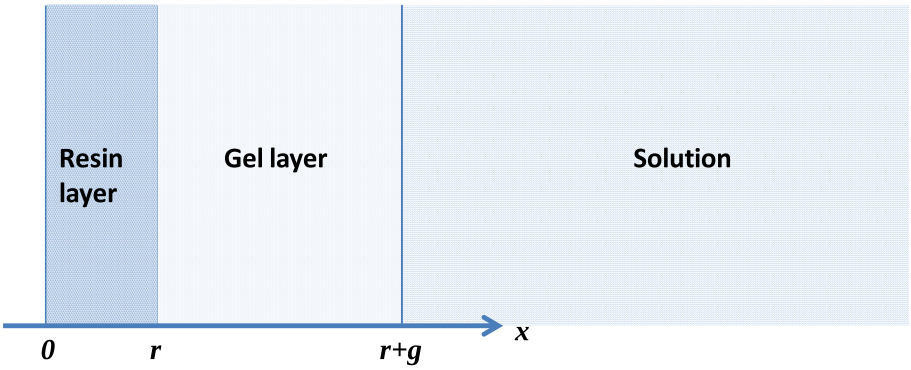

Figure SI-5.1. Schematic representation of a DGT device.

Let D_i and D_i^{R} stand for the diffusion coefficients of species *i* in the diffusive gel or in the resin domain, respectively and let c_i stand for the concentration of species *i* at a given spatial position *x*. Because of the steady-state regime, the variable time is not present. Total concentrations are denoted as $c_{\mathrm{T},i}$.

We are also assuming that the resin acts as a perfect sink for free metal, saturation effects of the resin are negligible, there is an excess of ligand with respect to metal in solution (*i.e.* the free ligand concentration can be taken as constant $c_{\mathrm{L}}(x) = c_{\mathrm{L}}^{*}\ \forall x$, regardless of ML formation), and that the complex can penetrate and diffuse within the resin layer (where its dissociation still takes place).

Under these conditions, the system reaches a quasi-steady state in which any free metal, M, arriving to or being generated by dissociation of the complex in the resin layer becomes instantaneously bound to the resin (perfect sink). The complex penetrating into the resin layer disappears by dissociation (notice that direct reaction of the complex with the resin leads to a parallel mathematical formulation as shown in section SI-1.5). We aim to find an analytical solution for the metal flux, lability degree and concentration profiles corresponding to this steady state.

The steady-state transport equations for the different species can, then, be written as:

For the metal:

$$c_{\mathrm{M}}(0 < x \leq r) = 0 \tag{SI-1}$$

$$0 = D_{\mathrm{M}} \frac{d^2 c_{\mathrm{M}}}{dx^2} - k_{\mathrm{a}} c_{\mathrm{L}}^{*} c_{\mathrm{M}} + k_{\mathrm{d}} c_{\mathrm{ML}}, \quad \text{if} \quad r < x < r + g \tag{SI-2}$$

For the complex:

$$0 = D_{\mathrm{ML}}^{\mathrm{R}} \frac{d^2 c_{\mathrm{ML}}}{dx^2} - k_{\mathrm{d}}^{\mathrm{R}} c_{\mathrm{ML}}, \quad \text{if} \quad 0 < x < r \tag{SI-3}$$

(superscript R indicates that is the value corresponding to the resin domain, and can be the result of one or more parallel routes)

and

$$0 = D_{\mathrm{ML}}^{\mathrm{R}} \frac{d^2 c_{\mathrm{ML}}}{dx^2} + k_{\mathrm{a}} c_{\mathrm{L}}^{*} c_{\mathrm{M}} - k_{\mathrm{d}} c_{\mathrm{ML}}, \quad \text{if} \quad r < x < r + g \tag{SI-4}$$

Boundary conditions

Boundary conditions at $x = r + g$ correspond to bulk concentrations:

$$c_{\mathrm{M}}(r + g) = c_{\mathrm{M}}^{*}, \qquad c_{\mathrm{ML}}(r + g) = c_{\mathrm{ML}}^{*} \tag{SI-5}$$

Boundary conditions at $x = r$:

As we assume a difference of electrostatic potential between the resin and gel domains, the relationship between the complex concentrations at both sides of the resin-gel surface, $c_{\mathrm{ML}}^{r^-}$ and $c_{\mathrm{ML}}^{r^+}$, reads

$$\Pi = \frac{c_{\mathrm{ML}}^{r^+}}{c_{\mathrm{ML}}^{r^-}} = \exp\left(-\frac{zF\Psi}{RT}\right) \qquad \text{(SI-6)}$$

where Π is the Boltzmann factor, and Ψ is the difference of potential between the resin and the gel domains. We are, thus, assuming that the electrostatic potential is determined by the background salt and the charge of the resin sites; concentrations at both sides of the resin-gel interface adapt to the Boltzmann equilibrium relationship and $r >> \kappa^{-1}$ as indicated in the assumptions explicitly reported in the running text.

Changes of free metal concentrations inside the resin domain (due to Donnan effects) are negligible, since we assume that the resin surface acts as a perfect sink for the metal,

$$c_{\mathrm{M}}(x \le r) = 0 \qquad \text{(SI-7)}$$

Additionally, at the gel-resin interface the fluxes must be continuous, that is

$$D_{\mathrm{ML}}^{\mathrm{R}} \left.\frac{dc_{\mathrm{ML}}}{dx}\right|_{r^-} = D_{\mathrm{ML}} \left.\frac{dc_{\mathrm{ML}}}{dx}\right|_{r^+} \qquad \text{(SI-8)}$$

Boundary conditions at $x = 0$ stem from non-flux conditions:

$$\left.\frac{dc_{\mathrm{ML}}}{dx}\right|_{x=0} = 0 \qquad \text{(SI-9)}$$

Eqns. (SI-1)-(SI-4) with the boundary value problem ((SI-5)-(SI-9)) constitutes a system of equations that determines $c_{\mathrm{M}}(x)$ and $c_{\mathrm{ML}}(x)$.

1.1 Solving the diffusion-reaction equations in the resin layer

The reaction-diffusion equation of the complex in the resin layer can be rewritten as

$$\frac{d^2 c_{\mathrm{ML}}}{dx^2} = \frac{k_{\mathrm{d}}^{\mathrm{R}}}{D_{\mathrm{ML}}^{\mathrm{R}}} c_{\mathrm{ML}} = \frac{c_{\mathrm{ML}}}{\lambda_{\mathrm{ML}}^{\;2}} \qquad 0 < x \le r \qquad \text{(SI-10)}$$

with

$$\lambda_{\mathrm{ML}} = \sqrt{\frac{D_{\mathrm{ML}}^{\mathrm{R}}}{k_{\mathrm{d}}^{\mathrm{R}}}} \qquad \text{(SI-11)}$$

λ_{ML} has dimensions of a distance and can be seen as a “penetration parameter” related to the distance required for full dissociation of a complex diffusing into the resin layer as discussed in (*1*).

The general solution of Eqn (SI-10) can be written as

$$c_{\mathrm{ML}}\left(x < r\right) = Ae^{\frac{x}{\lambda_{\mathrm{ML}}}} + Be^{-\frac{x}{\lambda_{\mathrm{ML}}}} \qquad \text{(SI-12)}$$

where A and B are integration constants that have to fulfil the boundary value problem given by Eqns. (SI-8) and (SI-9).

The application of (SI-8) in equation (SI-12) leads to *A*=*B*, so that the solution can be rewritten as

$$c_{\mathrm{ML}}\left(x<r\right)=c_{\mathrm{ML}}\left(x=0\right)\cosh\left(\frac{x}{\lambda_{\mathrm{ML}}}\right) \qquad \text{(SI-13)}$$

Labelling the complex concentration at resin side of the frontier between the resin and diffusion layer (*x*=*r*) as $c_{\mathrm{ML}}^{r^-}$, one obtains

$$c_{\mathrm{ML}}^{r^-}=c_{\mathrm{ML}}\left(x=r^-\right)=c_{\mathrm{ML}}\left(x=0\right)\cosh\left(\frac{r}{\lambda_{\mathrm{ML}}}\right)$$

(SI-14)

The complex concentration profile inside the resin layer becomes

$$c_{\mathrm{ML}}\left(x<r\right)=c_{\mathrm{ML}}^{r^-}\frac{\cosh\left(\frac{x}{\lambda_{\mathrm{ML}}}\right)}{\cosh\left(\frac{r}{\lambda_{\mathrm{ML}}}\right)} \qquad \text{(SI-15)}$$

The application of Eqn. (SI-8) requires the knowledge of the flux of complex entering the resin layer, calculated from the resin side. From Eqn. (SI-15), it becomes

$$J_{\mathrm{ML}}=D_{\mathrm{ML}}^{\mathrm{R}}\left.\frac{dc_{\mathrm{ML}}}{dx}\right|_{x=r^-}=D_{\mathrm{ML}}^{\mathrm{R}}\frac{c_{\mathrm{ML}}^{r^-}}{\lambda_{\mathrm{ML}}}\tanh\left(\frac{r}{\lambda_{\mathrm{ML}}}\right)=k_{\mathrm{d}}^{\mathrm{R}}c_{\mathrm{ML}}^{r^-}\lambda_{\mathrm{ML}}\tanh\left(\frac{r}{\lambda_{\mathrm{ML}}}\right) \qquad \text{(SI-16)}$$

which using the Boltzmann relationship (SI-6) yields

$$J_{\mathrm{ML}}=\frac{k_{\mathrm{d}}^{\mathrm{R}}c_{\mathrm{ML}}^{r^+}\lambda_{\mathrm{ML}}}{\Pi}\tanh\left(\frac{r}{\lambda_{\mathrm{ML}}}\right) \qquad \text{(SI-17)}$$

1.2 Solving the diffusion reaction equations in the gel layer

In the gel layer, an equivalent system of equations to that given by Eqns (SI-1)- (SI-4) is

$$0=\frac{d^2}{dx^2}\left(D_{\mathrm{M}}c_{\mathrm{M}}+D_{\mathrm{ML}}c_{\mathrm{ML}}\right) \tag{SI-18}$$

$$0=\frac{d^2}{dx^2}\left(c_{\mathrm{ML}}-K^{'}c_{\mathrm{M}}\right)-\left(\frac{k_{\mathrm{d}}}{D_{\mathrm{ML}}}+\frac{k_{\mathrm{a}}c_{\mathrm{L}}^{*}}{D_{\mathrm{M}}}\right)\left(c_{\mathrm{ML}}-K^{'}c_{\mathrm{M}}\right) \tag{SI-19}$$

which has the advantage of allowing the uncoupling of the system.

Eqn. (SI-18) is just the addition of Eqns. (SI-2) and (SI-4). Its integration yields

$$D_{\mathrm{M}}c_{\mathrm{M}}+D_{\mathrm{ML}}c_{\mathrm{ML}}=D_{\mathrm{ML}}c_{\mathrm{ML}}^{r^{+}}+\frac{\left(D_{\mathrm{M}}c_{\mathrm{M}}^{*}+D_{\mathrm{ML}}c_{\mathrm{ML}}^{*}\right)-D_{\mathrm{ML}}c_{\mathrm{ML}}^{r^{+}}}{g}\left(x-r\right) \tag{SI-20}$$

The previous expression is a closed equation for the new variable

$$\phi=c_{\mathrm{ML}}-K^{'}c_{\mathrm{M}} \tag{SI-21}$$

We now introduce the parameter *m*, with dimensions of distance, which could be called a “disequilibration” parameter. It is related to the thickness of the reaction layer in the gel domain, *i. e.*, the thickness of the layer in the gel domain where M and ML are not in equilibrium, see reference (*1*):

$$m=\mu\sqrt{\frac{\varepsilon K'}{1+\varepsilon K'}} \tag{SI-22}$$

where μ is the classical definition of reaction layer introduced by Koutecky in planar semi-infinite diffusion (*2*):

$$\mu = \sqrt{\frac{D_{\mathrm{M}}}{k_{\mathrm{a}}^{'}}} \qquad \text{(SI-23)}$$

Thus, eqn. (SI-19) can be rewritten as

$$\frac{d^2}{dx^2}\phi = \frac{\phi}{m^2} \qquad \text{(SI-24)}$$

whose general solution is

$$\phi = A\sinh\left(\frac{g+r-x}{m}\right) + B\cosh\left(\frac{g+r-x}{m}\right) \qquad \text{(SI-25)}$$

where *A* and *B* are integration constants.

The boundary conditions are given by

$$\phi\left(x = g+r\right) = 0 \qquad \text{(SI-26)}$$

$$\phi\left(x = r\right) = c_{\mathrm{ML}}^{r^+} \qquad \text{(SI-27)}$$

which indicate that *B*=0 and $A = \frac{c_{\mathrm{ML}}^{r^+}}{\sinh\left(g/m\right)}$, so that

$$\phi = c_{\mathrm{ML}}^{r^+}\frac{\sinh\left(\left(g+r-x\right)/m\right)}{\sinh\left(g/m\right)} \qquad \text{(SI-28)}$$

Differentiating ϕ at $x=r$ according to expressions (SI-21) and (SI-28)

$$\left.\frac{d\phi}{dx}\right|_{x=r^+} = -\frac{c_{\mathrm{ML}}^{r^+}}{m}\coth\left(\frac{g}{m}\right) = \left.\frac{dc_{\mathrm{ML}}}{dx}\right|_{x=r^+} - K^{'} \left.\frac{dc_{\mathrm{M}}}{dx}\right|_{x=r^+} \tag{SI-29}$$

and differentiating (SI-20)

$$D_{\mathrm{M}}\left.\frac{dc_{\mathrm{M}}}{dx}\right|_{x=r^+} + D_{\mathrm{ML}}\left.\frac{dc_{\mathrm{ML}}}{dx}\right|_{x=r^+} = \frac{\left(D_{\mathrm{M}}c_{\mathrm{M}}^{*} + D_{\mathrm{ML}}c_{\mathrm{ML}}^{*}\right) - D_{\mathrm{ML}}c_{\mathrm{ML}}^{r^+}}{g} \tag{SI-30}$$

leads to an expression to compute the flux of ML entering into the resin layer in terms of the diffusive gel side variables as

$$J_{\mathrm{ML}} = D_{\mathrm{ML}}\left.\frac{dc_{\mathrm{ML}}}{dx}\right|_{x=r^+} = \frac{-D_{\mathrm{ML}}\, g\, c_{\mathrm{ML}}^{r^+}\coth\left(g/m\right)/m + \varepsilon K^{'}\left(D_{\mathrm{M}}c_{\mathrm{M}}^{*} + D_{\mathrm{ML}}c_{\mathrm{ML}}^{*} - D_{\mathrm{ML}}c_{\mathrm{ML}}^{r^+}\right)}{g\left(1+\varepsilon K^{'}\right)} \tag{SI-31}$$

As stated in (SI-8), the continuity of the flux requires the equality of J_{ML} calculated from (SI-31) and from (SI-17). One can solve this equation for $c_{\mathrm{ML}}^{r^+}$:

$$c_{\mathrm{ML}}^{r^+} = \frac{c_{\mathrm{ML}}^{*}\left(1+\varepsilon K^{'}\right)}{\varepsilon K^{'} + \frac{g}{m}\coth\left(\frac{g}{m}\right) + \frac{g}{\lambda_{\mathrm{ML}}}\frac{D_{\mathrm{ML}}^{\mathrm{R}}}{D_{\mathrm{ML}}}\frac{\left(1+\varepsilon K^{'}\right)}{\Pi}\tanh\frac{r}{\lambda_{\mathrm{ML}}}} \tag{SI-32}$$

1.3 Metal flux

Under steady-state conditions, the flux of metal bound to the resin layer, *J*, is the total metal flux entering the resin layer both as free metal and complex,

$$J = D_{\mathrm{M}} \left. \frac{dc_{\mathrm{M}}}{dx} \right|_{x=r} + D_{\mathrm{ML}} \left. \frac{dc_{\mathrm{ML}}}{dx} \right|_{x=r} \tag{SI-33}$$

and, due to the linearity of the profile of $D_{\mathrm{M}} c_{\mathrm{M}} + D_{\mathrm{ML}} c_{\mathrm{ML}}$ in the gel layer, as given by (SI-20),

$$J = D_{\mathrm{M}} \frac{c_{\mathrm{M}}^{*}}{g} + D_{\mathrm{ML}} \frac{c_{\mathrm{ML}}^{*} - c_{\mathrm{ML}}^{r^{+}}}{g} \tag{SI-34}$$

which, using (SI-32), becomes

$$J = D_{\mathrm{M}} \frac{c_{\mathrm{M}}^{*}}{g} + D_{\mathrm{ML}} \frac{c_{\mathrm{ML}}^{*}}{g} \left(1 - \frac{(1+\varepsilon K^{'})}{\varepsilon K^{'} + \dfrac{g}{m} \coth\left(\dfrac{g}{m}\right) + \dfrac{g}{\lambda_{\mathrm{ML}}} \dfrac{D_{\mathrm{ML}}^{\mathrm{R}}}{D_{\mathrm{ML}}} \dfrac{\left(1+\varepsilon K^{'}\right)}{\Pi} \tanh \dfrac{r}{\lambda_{\mathrm{ML}}}} \right) \tag{SI-35}$$

This equation simplifies to eqn. (5.8) in the running text of chapter 5 when $D_{\mathrm{ML,R}} = D_{\mathrm{ML}}$.

1.4 Lability degree

For a labile case, full dissociation of the complex at the resin-gel interface is also reached, so $c_{\mathrm{ML}}^{r} = 0$ and, according to (SI-30), the metal flux becomes

$$J_{\mathrm{labile}} = \frac{D_{\mathrm{M}} c_{\mathrm{M}}^{*}}{g} + \frac{D_{\mathrm{ML}} c_{\mathrm{ML}}^{*}}{g} \tag{SI-36}$$

In the opposite case, when the complex is inert, it does not contribute at all to the metal flux, $c_{\mathrm{ML}}^{r}=c_{\mathrm{ML}}^{*}$ and the metal flux bound to the resin is just due to the diffusion of the free metal present in the system

$$J_{\mathrm{free}}=J_{\mathrm{inert}}=\frac{D_{\mathrm{M}}c_{\mathrm{M}}^{*}}{g} \qquad (\mathrm{SI\text{-}37})$$

The lability degree (*3*) , defined as

$$\xi=\frac{J-J_{\mathrm{free}}}{J_{\mathrm{labile}}-J_{\mathrm{free}}} \qquad (\mathrm{SI\text{-}38})$$

can, by combining it with eqns. (SI-30), (SI-37) and (SI-36), be written as

$$\xi=1-\frac{c_{\mathrm{ML}}^{r^{+}}}{c_{\mathrm{ML}}^{*}} \qquad (\mathrm{SI\text{-}39})$$

or, using expression (SI-35)

$$\xi=1-\frac{(1+\varepsilon K^{'})}{\varepsilon K^{'}+\frac{g}{m}\coth\left(\frac{g}{m}\right)+\frac{g}{\lambda_{\mathrm{ML}}}\frac{D_{\mathrm{ML}}^{\mathrm{R}}}{D_{\mathrm{ML}}}\frac{\left(1+\varepsilon K^{'}\right)}{\Pi}\tanh\frac{r}{\lambda_{\mathrm{ML}}}} \qquad (\mathrm{SI\text{-}40})$$

or

$$\xi=1-\frac{\Pi(1+\varepsilon K^{'})}{\Pi\varepsilon K^{'}+\Pi\frac{g\sqrt{1+\varepsilon K^{'}}}{\mu\sqrt{\varepsilon K^{'}}}\coth\left(\frac{g\sqrt{1+\varepsilon K^{'}}}{\mu\sqrt{\varepsilon K^{'}}}\right)+\frac{D_{\mathrm{ML}}^{\mathrm{R}}}{D_{\mathrm{ML}}}\frac{g\left(1+\varepsilon K^{'}\right)}{\mu\sqrt{\varepsilon K^{'}}}\tanh\frac{r}{\mu\sqrt{\varepsilon K^{'}}}}$$

$$(\mathrm{SI\text{-}41})$$

This last equation can be used to retrieve $\xi = 1$ or $\xi = 0$ for the labile or inert limits by taking $\mu \to 0$ or $\mu \to \infty$, respectively.

1.5 Formulation when two routes of metal accumulation are considered in the resin domain

The full model that we are using to understand the metal accumulations in presence of NTA considers two parallel routes for the metal accumulation:

Route 1: dissociation of ML into M + L, and ulterior binding of M to the resin (R):

Step 1 (limiting step) $\mathrm{M} + \mathrm{L} \underset{k_\mathrm{a}}{\overset{k_\mathrm{d}}{\rightleftharpoons}} \mathrm{ML}$

Step 2 (fast) $\mathrm{M} + R \underset{k_\mathrm{a}}{\overset{k_\mathrm{d}}{\rightleftharpoons}} \mathrm{M}R$

Route 2: the direct reaction of R^{2-} to MNTA^- by a ligand assisted (LA) mechanism:

$$\mathrm{M}L + R \underset{k_\mathrm{a}}{\overset{k_\mathrm{d}}{\rightleftharpoons}} \mathrm{M}R + L$$

Considering both routes (but neglecting any release of M from the resin, and association of M to L due to the negligible metal concentration inside the resin), the ML balance equation in the resin domain under steady-state conditions reads:

$$0 = D_{\mathrm{ML}}^{\mathrm{R}} \frac{d^2 c_{\mathrm{ML}}}{dx^2} - \left(k_{\mathrm{d,LA}} + k_{\mathrm{d,ML}}\right) c_{\mathrm{ML}}, \quad \text{if} \quad 0 < x < r \qquad \text{(SI-42)}$$

By defining a total rate constant for ML dissociation (aggregating the effects of both routes)

$$k_{\mathrm{d}}^{\mathrm{R}} \equiv k_{\mathrm{d,LA}} + k_{\mathrm{d,ML}} \tag{SI-43}$$

one obtains

$$0 = D_{\mathrm{ML}}^{\mathrm{R}} \frac{d^2 c_{\mathrm{ML}}}{dx^2} - k_{\mathrm{d}}^{\mathrm{R}} c_{\mathrm{ML}} + k_{\mathrm{a}} c_{\mathrm{M}} c_{\mathrm{L}}, \quad \text{if} \quad 0 < x < r \tag{SI-44}$$

which coincides with (SI-3).

The rest of the formulation is parallel to section 1.1-1.3 replacing k_{d} with

$$k_{\mathrm{d}}^{\mathrm{R}} \equiv k_{\mathrm{d,LA}} + k_{\mathrm{d,ML}} \tag{SI-45}$$

2. Experimental details

2.1 Test solutions

Ultrapure water with resistivity ≥ 18 µS cm^{-1} (Synergy UV purification system Millipore) was used in all preparations. Metal stock solutions of 10 mM were prepared from nitrate salts ($Co(NO_3)_2\cdot 6H_2O$, $Ni(NO_3)_2\cdot 6H_2O$, Sigma-Aldrich and $Cd(NO_3)_2\cdot 4H_2O$ Merck). The stocks were not acidified to allow greater control of pH during solution preparation (*4,5*).

Test solutions were prepared with Milli-Q water and the ionic strength was adjusted to 1 mM by adding 0.5 mM $NaNO_3$ (Sigma Aldrich) and 1 mM MOPS (Sigma-Aldrich). For the experiments at nominal 0.1 mM, only 1 mM MOPS was used (without any other background salt). Metals were added to the solution to reach a concentration of 10^{-5} mol L^{-1} Co and Cd, and

2.5×10^{-5} mol L^{-1} for Ni. When necessary 8×10^{-5} mol L^{-1} of NTA (Fluka, analytical grade) was added. The pH of the solution was then adjusted to pH 7.5 by dropwise addition of 0.1 M NaOH (Merck) or HNO_3 (Fluka). Stirred solutions were left to equilibrate for 1 to 2 h.

2.2 Preparation of DGT devices

DGT pistons and caps (polyethylene, with a 2 cm diameter window), resin gel (iminodiacetate chelating resin Chelex-100 beads, embedded on polyacrylamide gel, 0.4 mm thick) and diffusive gel (polyacrylamide, 0.8 mm thick) were purchased from DGT Research Ltd. (Lancaster, UK, http://www.dgtresearch.com). Cellulose nitrate membrane filters (0.45 µm pore size, 0.125 mm thick) were purchased from Whatman.

DGT pistons and cap mouldings were pre-cleaned using three 2 h 10% HNO_3 (Fluka, Trace Select) soaks, 5 washes in Milli-Q and a final soak in Milli-Q overnight. Resin gel layers were then positioned on the piston.

Previous experiments using similarly treated diffusive gels (*6*) have shown the expected accumulation of metals from inorganic solution at $I \geq$ 1mM. These results suggested a slight positive charge on the diffusive gels. To minimize any charge effects, the diffusive gels were well washed until the pH of the wash water was <7, then conditioned and stored in 0.03 M $NaNO_3$ as described previously (*6*).

The diffusive gel was placed on top of the resin layer, followed by the Milli-Q rinsed filter membrane.

Caps were fitted to secure the gels. Devices were deployed immediately or stored in plastic bags with 1 mL of 0.03 M $NaNO_3$ to prevent dehydration of the gel layers (as for DGT blanks).

2.3 DGT deployments

DGT devices were deployed at random in a 12-device rack inside a 5L polyethylene test container. In the current tests, devices were deployed for 24 h. pH was monitored during the deployment with a glass electrode. Temperature was 25 ± 0.1 °C, controlled by using a thermostatic bath where the immersion solution container was introduced. Flow was kept constant by stirring at 240 rpm using an overhead stirrer. 1mL aliquots of the immersion solution were taken at regular intervals of time at the height of the sensors to control the total amount of metal.

Following deployment, the devices were retrieved, rinsed with Milli-Q water, the fitted cap was removed, and the resin layers carefully placed into 1.5 mL micro-centrifuge PVC tubes. Metals were eluted from retrieved resin membranes by immersing them in 1 mL of 4.4 M HNO_3 (Fischer Chemical) for at least 24 h to allow an efficient extraction of the metals from the resin.

Samples were diluted 50-fold and the concentration of metal was measured with inductively coupled plasma mass spectrometry (ICP-MS) (7700 Series, Agilent).

The mass of metal accumulated in the resin was calculated as follows:

$$n = c_{\mathrm{e}}\left(V_{\mathrm{e}} + V_{\mathrm{g}}\right) / f_e \tag{SI-46}$$

Where *n* is the amount of metal accumulated in the resin (moles of metal per gel), c_e is the concentration from ICP-MS measurements of the eluted resin gel (mol L^{-1}), V_e is the volume of eluent, V_g is the volume of the resin gel and f_e is the elution factor, typically 0.8 (*4*).

2.4 Section 3: Additional data and figures

Table SI-5.1 Experimental lability degrees at pH 7.5 of CdNTA, CoNTA and NiNTA complexes at the different ionic strengths calculated as indicated in Eqn (5.13) from experimental accumulations in 1R DGT devices.

ξ(experimental) at pH 7.5			
I (M)	**Co**	**Ni**	**Cd**
6.46×10^{-4}	0.34±0.07	0.018±0.003	0.71±0.13
1.45×10^{-3}	0.32±0.03	0.022±0.004	0.724±0.001
1.05×10^{-2}	0.66±0.03	0.04±0.01	0.83±0.09
4.96×10^{-2}	0.95±0.05	0.21±0.02	0.92±0.05
9.92×10^{-2}	1.06±0.03	0.35±0.03	0.99±0.03
4.71×10^{-1}	1.02±0.02	0.73±0.03	0.989±0.002
8.91×10^{-1}	0.89±0.06	0.84±0.03	0.91±0.04

Table SI-5.2 Fitted lability degrees at pH 7.5 of CdNTA, CoNTA and NiNTA complexes at the different ionic strengths calculated as indicated in Eqn. (5.13) with parameters given in Table 5.4, Table SI-5.4 and kd values reported in the first column of Table 5.3.

ξ (theoretical values using $k_{\mathrm{d,E}}$) at pH 7.5			
***I* (M)**	**Co**	**Ni**	**Cd**
6.46×10^{-4}	0.372	0.009	0.711
1.45×10^{-3}	0.390	0.010	0.724
1.05×10^{-2}	0.613	0.043	0.832
4.96×10^{-2}	0.875	0.207	0.945
9.92×10^{-2}	0.932	0.348	0.970
4.71×10^{-1}	0.985	0.732	0.993

Table SI-5.3 Fitted lability degrees at pH 7.5 of CdNTA, CoNTA and NiNTA complexes at the different ionic strengths calculated as indicated in Eqn. (5.13) with parameters given in Table 5.4 and the two k_{d} values ($k_{\mathrm{d,E}}$ and $k_{\mathrm{d}}^{\mathrm{R}}$) reported in Table 5.3.

ξ (theoretical values using $k_{\mathrm{d,E}}$ and $k_{\mathrm{d}}^{\mathrm{R}}$) at pH 7.5			
***I* (M)**	**Co**	**Ni**	**Cd**
6.46×10^{-4}	0.373	0.018	0.711
1.45×10^{-3}	0.392	0.020	0.724
1.05×10^{-2}	0.584	0.043	0.817
4.96×10^{-2}	0.889	0.207	0.948
9.92×10^{-2}	0.942	0.348	0.972
4.71×10^{-1}	0.988	0.732	0.994

Table SI-5.4 Used values corresponding to DGT sensors parameters

D_{Co} (m^2s^{-1})	6.68×10^{-10}
D_{Ni} (m^2s^{-1})	7.07×10^{-10}
D_{Cd} (m^2s^{-1})	6.85×10^{-10}
r (m)	4.00×10^{-04}
g (m)	8.52×10^{-04}
A (m^2)	3.14×10^{-04}

Table SI-5.5 Experimental values of the Boltzmann factor calculated from measured Na^+ inside and outside the resin domain.

µM Na^+_{inside}	**µM $Na^+_{outside}$**	**Π**
31.3	1.7	18.0
42.4	11.6	3.7
116.4	109.1	1.1
552.0	507.6	1.1

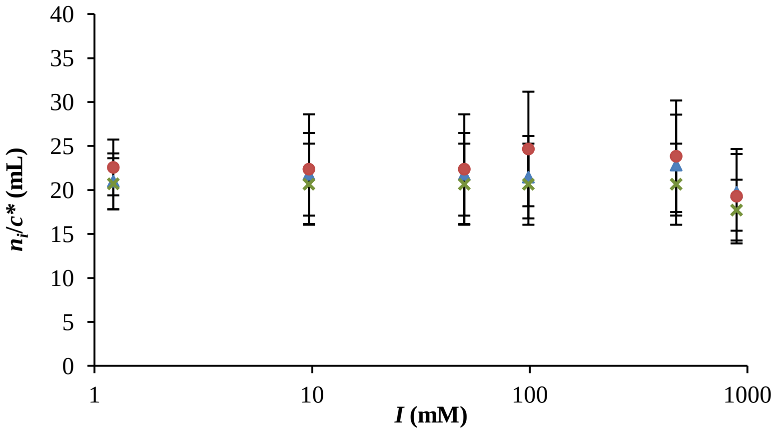

Figure SI-5.2. Nanomoles of Cd (green crosses), Co (blue triangles) and Ni (red circles), normalized with respect to bulk concentrations accumulated in DGT sensors at pH 7.5 after 24 h deployment. Parameters: $c^*_{\mathrm{T,Cd}} = c^*_{\mathrm{T,Co}} = 10^{-5}\ \mathrm{M}$, $c^*_{\mathrm{T,Ni}} = 2.5\times10^{-5}\ \mathrm{M}$ and values indicated in Table SI-5.4.

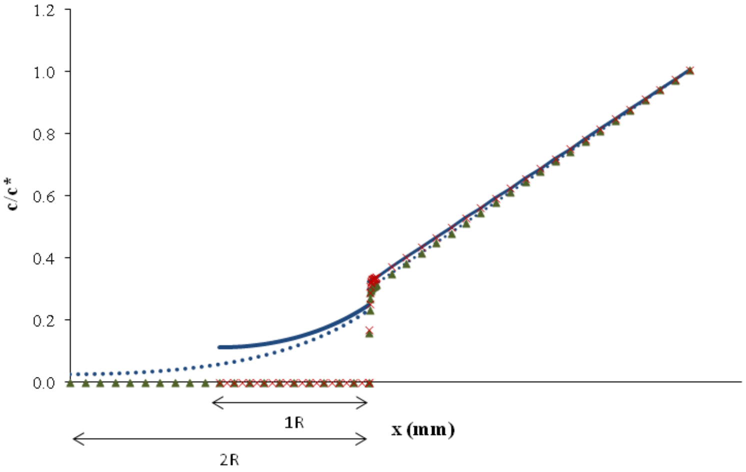

Figure SI-5.3 Normalized concentration (with respect to the corresponding bulk one) profiles of the system NiNTA at ionic strength 100 mM and pH =7.5 computed with the analytical model associated to eqn. 5.8 and the values of the parameters reported in column 2 and 3 of Table 5.3 and column 4 of Table 5.4. Markers denote $c_{\mathrm{Ni}^{2+}} / c^{*}_{\mathrm{Ni}^{2+}}$: red crosses for systems with 1R and green triangles for systems with 2R. Lines: continuous blue line for $c_{\mathrm{NiNTA}} / c^{*}_{\mathrm{NiNTA}}$ in systems with 1R and dotted blue line for $c_{\mathrm{NiNTA}} / c^{*}_{\mathrm{NiNTA}}$ in systems with 2R with parameters given in Table SI-5.5.

References

1. Uribe, R.; Mongin, S.; Puy, J.; Cecilia, J.; Galceran, J.; Zhang, H.; Davison, W. Contribution of Partially Labile Complexes to the DGT Metal Flux. *Environ.Sci.Technol.* **2011**, *45*, 5317.

2. Heyrovský, J.; Kuta, J.*Principles of Polarography*, Academic Press: New York, **1966**.

3. Galceran, J.; Puy, J.; Salvador, J.; Cecília, J.; van Leeuwen, H. P. Voltammetric lability of metal complexes at spherical microelectrodes with various radii. *J.Electroanal.Chem.* **2001**, *505*, 85.

4. Warnken, K. W.; Zhang, H.; Davison, W. Performance characteristics of suspended particulate reagent-iminodiacetate as a binding agent for diffusive gradients in thin films. *Anal.Chim.Acta* **2004**, *508,* 41.

5. Garmo, O. A.; Davison, W.; Zhang, H. Effects of Binding of Metals to the Hydrogel and Filter Membrane on the Accuracy of the Diffusive Gradients in Thin Films Technique. *Anal.Chem.* **2008**, *80*, 9220.

6. Warnken, K. W.; Zhang, H.; Davison, W. Trace metal measurements in low ionic strength synthetic solutions by diffusive gradients in thin films. *Anal.Chem.* **2005**, *77,* 5440.

Chapter 6

Additional evidences of kinetic and electrostatic effects on DGT devices

6.1. Abstract

The measurement of metals by DGT (Diffusive Gradients in Thin Films) in media with low ionic strengths (*I*) has been studied in Chapter 5. In the presence of partially labile negatively charged metal complexes, *e.g.* Ni-NTA, at pH 7.5 it was observed a decrease in the metal accumulation as *I* decreased. This effect was partly explained by an electrostatic repulsion between the negatively charged resin of the DGT device and the negatively charged metal-NTA species as well as by a decrease of the kinetic dissociation constant as *I* decreases due to an increasingly less efficient ligand assisted effect. In order to better understand these phenomena, two additional studies were undertaken. The first one is addressed to analyze systems with positively charged complexes. Sample solutions with Ethylenediamine (En) and Ni, Cd, Cu and Zn metal ions which react to give positively charged complexes were studied. An increase of the metal accumulation in the DGT devices as ionic strength decreases is reported. This behaviour is explained by the electrostatic attraction between the resin and the positively charged complexes which enhances de Donnan partitioning but also an increase of the kinetic exchange rate constant as *I* decreases. This kinetic effect is supported by a decrease in the % of mass accumulated in the back resin disc when DGT devices with a stack of two resin discs are used.

Moreover, a dependence of the lability of complexes on the En concentration is explained by the formation of the species MEn, MEn_2 and MEn_3, depending on the conditions.

A second study on the influence of pH on the metal accumulations in Ni, Cd or Co NTA systems at pH 6, 7.5 and 8 is reported. No significant differences were observed for labile CdNTA and CoNTA complexes. For the case of NiNTA, at high ionic strength, the lability decreases going from pH 7.5 to 6. A less effective ligand assisted effect is suggested as the responsible of this behavior. Conversely, at low ionic strength, the lability degree of the NiNTA increases at pH 6 with respect to pH 7.5. This behavior is explained by the dominant influence of the H on the NiNTA complexes in the gel domain due to the electrostatic exlusion of the NiNTA from penetration in the resin domain.

6.2. Introduction

DGT is nowadays a widely used technique for metal speciation and bioavailability in natural waters. Main advantages are the in situ measurement, which allows minimizing contaminations, and the easily transformation of the measurement on a “labile concentration” which is called c_{DGT}, or DGT labile concentration and in the simplest case becomes:

$$c_{\mathrm{DGT}}=\frac{n\,g}{D_{\mathrm{M}}At} \tag{6.1}$$

where n is the number of mols of metal accumulated, g the thickness of the diffusion domain (the sum of the thickness of the diffusive gel, the cellulose membrane filter and the diffusive boundary layer, DBL), D_{M} the diffusion coefficient of metal, A the area of the DGT window and t the deployment time.

In spite of these advantages, a systematic interpretation of DGT measurements in terms of physical parameters of the system remains a challenge. Parallel to the intensive work for developing new DGT applications, it has also been done an intensive work to improve the physical interpretation of the DGT measurements. This work has combined the use of numerical simulation tools (*1*-*3*) with the development of simple analytical expressions (*4*-*6*) to facilitate the physical interpretation of DGT measurements. From this work, interesting conclusions have emerged: the resin acts as a perfect sink for the metals unless a very low pH or too strong ligands are present in the system (*6*,*7*), penetration and dissociation of complexes in the resin disc is the main way of complex accumulation (*1*), and simple expressions for accumulations in ligand mixtures were reported (*4*) which allowed a physical definition of c_{DGT} in terms of the system parameters (*8*).

Recently (*9*), studying the influence of the ionic strength on the metal accumulation it has been reported that the resin can also be the responsible of some electrostatic and kinetic effects which strongly modify the metal accumulation. Thus, for high ionic strength, the fitting of the Ni accumulation in a system with NiNTA as dominant species has evidenced that the Eigen value of the kinetic dissociation constant of the NiNTA cannot justify the Ni accumulation. Instead, a three orders of magnitude higher kinetic dissociation constant is required. This has prompted to suggest that dissociation in the resin domain can benefit from a ligand assisted effect responsible for this increase of the kinetic constant. Cd complexes do not suffer this increase due to their labile behaviour which lead to full dissociation in the gel domain and prevents complex penetration.

This kinetic effect for NiNTA decreases as the ionic strength decreases due to the dependence of the kinetic constants of charged reactants on the ionic strength: as both, the resin sites and the complex species are negatively charged, there is an increasing repulsion as ionic strength decreases which tends to reduce the ligand assisted effect. Moreover, the negative charge of the resin domain induces a Donnan partitioning of the charged species, so that negatively charged complexes tend to be excluded from the resin domain, decreasing also in this way the corresponding metal accumulation.

It seems then timely to look for additional evidences of these electrostatic and kinetic effects. Two series of experiments were planned in this work. In a first strategy, positively partially labile complexes were studied in order to assess if electrostatic effects were opposite to those measured for the MNTA system, as expected if they were of electrostatic origin. In a second series of experiments, the influence of pH on the MNTA system was assessed. This influence is of special interest since the control of pH is, in principle, a way of regulation of the electrostatic charge of the resin and thus a way of modifying the electrostatic effects.

Accordingly, section 6.4.1 deals with DGT measurements in systems in presence of Ethyenediamine (En) which lead to positively charged complexes with divalent metal ions. Ionic strength values between 5mM and 1M are used. Section 6.4.2 reports the influence of the En concentration on the lability of complexes and Section 6.4.3 deals with the effects of pH on the M-NTA system.

6.3. Material and methods

6.3.1. Reagents

A metal stock solution at a concentration of 10^{-2} mol L^{-1} (except $2.5x10^{-2}$ mol L^{-1} Ni) was prepared from nitrate salts of $Cd(NO_3)_2{\cdot}4H_2O$, $Cu(NO_3){\cdot}3H_2O$, $Zn(NO_3)_2{\cdot}4H_2O$, $Co(NO_3)_2{\cdot}6H_2O$ (Merck) and $Ni(NO_3)_2{\cdot}6H_2O$ (Sigma-Aldrich) in Milli-Q water (Synergy UV, Millipore). The stocks were not acidified to allow greater control of pH during solution preparation (*10,11*). Metals were added to the solution to reach a concentration of 10^{-5} mol L^{-1} Cd, Co, Cu and Zn, and 2.5×10^{-5} mol L^{-1} for Ni.

Ethylenediamine (En) (Fluka), with the formula $C_2H_4(NH_2)_2$, was used as organic ligand.

When necessary, 8×10^{-5} mol L^{-1} of NTA (Fluka, analytical grade) was added.

Sodium nitrate was used to adjust the ionic strength in all the experiments and it was prepared from solid $NaNO_3$ (Fluka).

The pH of the solution was adjusted by drop wise addition of 0.1 mol L^{-1} NaOH or HNO_3 (Fluka).

Diluted solutions of metals and $NaNO_3$ in 2 %HNO_3 were prepared from 1000 ppm metal nitrate standard solutions in HNO_3 0.5 M (Merck) in order to perform the ICP-MS calibration. Diluted nitric acid, 2 %, was used as blank

Nitric acid (70%, Trace Metal Grade, Fisher Chemical) was used to acidify the samples to analyse the total metal content.

6.3.2. Instrumentation

Inductively coupled plasma mass spectrometry (ICP-MS, 7700 Series, Agilent) was used to determine the Na and total metal content in all the samples acidified at 2% HNO_3.

A pH meter Orion 920A+ (Thermo Electron Corporation) was used to measure the pH during the deployment of the DGT sensors**.**

Visual MINTEQ software was used to predict the metal speciation.

6.3.3. Procedures

Preparation, retrieval and analysis of DGT devices and experimental set up were described in chapter 5. In these studies, DGT devices with two resin discs were deployed (front and back as in Chapter 5).

DGT deployment solutions

Prior to the deployment, DGT devices were immersed for at least 12 hours in a pre-conditioning solution with the same pH and ionic strength as the sample solution. In all the cases three DGT devices were exposed to the deployment solution.

For the experiment with En, the solution contained 10^{-2} mol L^{-1} ethylenediamine and 10^{-5} mol L^{-1} Cd, Co, Cu and Zn, and 2.5×10^{-5} mol L^{-1} Ni. With such En concentration, 99% of metals became complexed by the ligand as predicted with Visual MINTEQ. The ionic strength (*I*) was scanned from 6.24 to 1000 mM using $NaNO_3$ and the pH was adjusted at 9 using small additions of diluted HNO_3 or NaOH.

To study the influence of the En concentration on the metal accumulation, 5 different concentrations were employed (0.05, 0.01, 0.03, 0.06 and 0.1 mol L^{-1}). The pH was fixed at 8 and a stock solution of metals was added to obtain a final concentration of 10^{-5} mol L^{-1} Cd, Co, Cu and Zn.

The effect of the pH was studied in systems with metal concentrations of 10^{-5} mol L^{-1} of Cd and Co and 2.5 x 10^{-5} mol L^{-1} of Ni. 8 x 10^{-5} mol L^{-1} of NTA was used in order to have 99% of the metal complexed.

Stirred solutions were left to equilibrate for 24 hours prior to the deployment of the DGT devices and additional times of 2 hours were used between changes in the ionic strength.

For all experiments, an extra DGT device was used as a blank. Aliquots of the bulk solution were collected at the beginning and the end of the deployment times to check the total Na and metal concentrations.

6.4. Results

6.4.1. Electrostatic effects at low ionic strength in presence of positively charged metal complexes: the case of Cd, Cu, Zn and Co with En

A first characteristic of the systems with Ni, Cd, Co, Zn or Cu with En is the formation of a mixture of complexes with different stoichiometric ratios: MEn, MEn_2 or MEn_3. Table 6.1 shows the speciation of the system as predicted with the speciation program Visual MINTEQ under pH, ligand and metal concentrations reported in the corresponding caption.

Table 6.1. Percentage of the species formed in the system metal-ethylenediamine at pH 9, En concentration of 0.01 mol L^{-1} and 10^{-5} mol L^{-1} Co, Cu, Cd and Zn and 2.5 x 10^{-5} mol L^{-1} Ni.

Component	**% of total concentration**	**Species name**
Ni^{+2}	7.805	Ni[En]2
	92.189	Ni[En]3
Cd^{+2}	3.189	Cd[En]
	92.45	Cd[En]2
	4.347	Cd[En]3
Co^{+2}	45.29	Co[En]2
	53.492	Co[En]3
	1.213	Co[En]
Zn^{+2}	0.424	Zn[En]
	34.669	Zn[En]2
	64.897	Zn[En]3
Cu^{+2}	100	Cu[En]2

DGT accumulations of Cd, Cu, Zn, Co and Ni in systems with total concentrations and pH as reported in Table 6.1 were undertaken in the presence of the ligand ethylenediamine (En) at concentration 0.01 mol L^{-1} and ionic strength values in the range comprised between 6.24 x 10^{-3} and 0.5 mol L^{-1}. Accumulation results are shown in Figure 6.1. Notice that, as predicted in Table 6.1, >99% of each metal is expected to be complexed with En so that the accumulation due to the free metal ion is negligible.

A first overview of Figure 6.1 indicates that, against the decrease of the metal accumulation as ionic strength decreases seen in the system MNTA as reported in Chapter 5, now, in presence of positively charged complexes, the accumulations increase as the ionic strength decreases. This is just the behaviour expected for positively charged complexes. However, the impact of the ionic strength is different for the different cations. For instance, there were only small differences between the accumulations of Zn, Cd and Ni in all the range of ionic strength studied. This behaviour can be understood if these metal-En complexes are labile. Under these conditions, no further increases of metal accumulation are possible since the accumulation is limited by the transport of the complex to the resin domain. In other words, no pre-accumulation of metal by a Donnan partitioning effect is possible in the resin domain since the concentration of these complexes at the resin/gel interface is small enough that the Donnan partitioning is negligible. It is also interesting to highlight that the accumulation at low ionic strength of Ni, Cd or Zn complexes almost coincide indicating a negligible dependence of the diffusion coefficient on the stoichiometry of the complex. When the contribution of the free metal is negligible, this accumulation can be used to fit the diffusion coefficient of the Ni, Cd and Zn En complexes. The convergence of the accumulation of Ni originated from the transport of the dominant $Ni(En)_3$ (>92%) with that of Cd originated from the transport and dissociation of $Cd(En)_2$ (>92%) or the accumulation of Zn originated from the transport and dissociation of a mixture of $Zn(En)_2$ (35%) and $Zn(En)_3$ (65%) indicates that the diffusion coefficient of the M En complexes is almost independent of the stoichiometric M to En ratio.

Conversely, Figure 6.1 also indicates that the accumulations of Cu and Co increase noticeably with the decrease of the ionic strength, *I*. For the case of Cu, at low *I* the accumulation reach the values of labile complexes while Co complexes do not reach such regime.

An increase in the accumulation as ionic strength decreases can be explained by the electrostatic attraction between negatively charged resin groups and the positively charged metal complexes which induces a Donnan partitioning at the resin/gel interface. However, we wonder whether ligand assisted effects similar to those reported for the MNTA system hold also in the present case.

Table 6.2 shows the percentage of metal accumulation in the back resin disc. For labile Ni, Cd and Zn complexes, no metal accumulation is expected in the back resin disc since full complex dissociation arises in the diffusive gel layer.

Partially labile complexes will exhibit non negligible accumulations in the back resin disc indicating the penetration and dissociation of the complex in the resin domain. This is the case of the Co and Cu complexes, in agreement with the above comments of the accumulation results.

No noticeable modification of the back percentage is expected from an increase of the complex concentration in the resin domain by an attractive electrostatic partitioning. Indeed, the electrostatic partitioning multiplies the complex concentration profile along the resin domain by the Donnan factor which will influence the release of metal by dissociation both in the back resin disc and in the entire resin domain. The total number of moles of metal bound in the resin has also to include the metal diffusing from the gel domain, *i. e.*, the free metal in the bulk solution and that resulting from dissociation of the complex in the reaction layer of the gel domain. Since this contribution is well below that of dissociation in the resin domain (for Cu and Co we can see in Fig. 6.1 small accumulations at high ionic strength), the % back will remain unaltered since the influence of the electrostatic partitioning in both the mols released in the back resin disc and the total number of moles released in all the resin domain cancels.

Conversely, a decrease of the back accumulation is expected from an increase of the kinetic dissociation constant since a faster dissociation leads to a steepest decay of the complex concentration along the resin domain and to a reduction of the metal accumulation in the back resin disc.

The different behavior of the electrostatic attraction and the kinetic effects on the variation of the % back as ionic strength changes makes the back percentage measurements of the highest interest to evidence if kinetic effects are present in the increase of the metal accumulation in the MEn systems as *I* decreases.

Table 6.2 shows a decrease in the back accumulation of the Co as *I* decreases. This effect suggests an increase in the dissociation kinetic constant and a non-negligible presence of a ligand assisted effect. For the Cu accumulation, 50 % of the metal is accumulated in the back resin disc along all the *I* range. In this case there is no ligand assisted effect or the dissociation constant is so small that the increase due to the ligand assisted is not high enough to lead to a reduction in the back percentage in the standard resin disc. The use of thicker resin discs might help in appreciating the presence of kinetic effects. However, as the Cu accumulated mass almost reach the labile limit, see Figure 6.1, we can conclude that in the case of Cu, the Donnan effects are more effective than the ligand assisted dissociation.

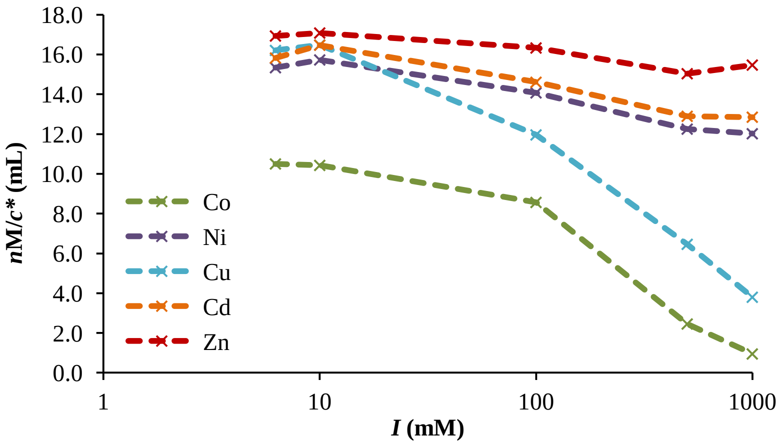

Figure 6.1. Moles of metal normalised with bulk concentration accumulated by DGT in a system with 10^{-5} mol L^{-1} Co, Cu, Cd and Zn and 2.5 x 10^{-5} mol L^{-1} Ni at pH 9 and 0.01 En for different ionic strengths. Markers: experimental measurements. Lines to connect the experimental measurements are depicted in the figure

Table 6.2. Back resin percentages of accumulated metals as function of ionic strength at a fixed pH 9.

I (mM)	**% Co back**	**% Ni back**	**% Cu back**	**% Zn back**	**% Cd back**
5	6.98	5.90	44.38	4.58	4.18
10	8.95	6.92	39.67	5.80	5.49
100	20.82	6.40	57.48	4.30	4.05
500	45.07	9.94	59.40	5.67	5.34
1000	40.29	11.28	50.12	3.91	3.50

6.4.2. Influence of the En concentration on the DGT metal accumulations when complexes are the dominant metal species

Systems with ML_2 and, in general, ML_n complexes require several dissociation steps to release free metal to buffer the metal consumption in a reaction layer. As explained in (*12*), the dissociation step

$$\mathrm{M+L} \underset{k_\mathrm{d}}{\overset{k_\mathrm{a}}{\rightleftharpoons}} \mathrm{ML} \tag{6.2}$$

is usually the rate limiting step in the dissociation of ML_n species.

In these cases, the formulation of the transport and reaction processes in systems containing ML_n complexes is equivalent to the formulation of a ML system, with the following changes:

$$k_\mathrm{d}^\mathrm{eff} = k_{\mathrm{d},1} \frac{1}{1+K_2^{'}+K_3^{'}K_2^{'}+\ldots+K_n^{'}..K_2^{'}} \tag{6.3}$$

$$k_\mathrm{a}^\mathrm{eff} = k_{a,1}^{'} \tag{6.4}$$

$$\begin{aligned} D_\mathrm{ML}^\mathrm{eff} = {} & D_\mathrm{ML} \frac{1}{1+K_2^{'}+K_3^{'}K_2^{'}+\ldots+K_n^{'}..K_2^{'}} + D_{\mathrm{ML}_2} \frac{K_2^{'}}{1+K_2^{'}+K_3^{'}K_2^{'}+\ldots+K_n^{'}..K_2^{'}} + \ldots \\ & + D_{\mathrm{ML}_n} \frac{K_n^{'}\ldots K_3^{'}K_2^{'}}{1+K_2^{'}+K_3^{'}K_2^{'}+\ldots+K_n^{'}..K_2^{'}} \end{aligned} \tag{6.5}$$

and

$$c_\mathrm{ML}^{eff} = c_{\mathrm{M},b} = c_\mathrm{ML} + c_{\mathrm{ML}_2} + \ldots + c_{\mathrm{ML}_n} \tag{6.6}$$

$$K^{\mathrm{eff}} = \frac{k_{\mathrm{a}}^{\mathrm{eff}}}{k_{\mathrm{d}}^{\mathrm{eff}}} = K_1^{'} + K_1^{'}K_2^{'} + ... + K_1^{'}..K_n^{'} = \sum_{i=1}^{n} \beta_i^{'} \qquad (6.7)$$

$$c_{\mathrm{ML}}^{eff*} = c_{\mathrm{M},b}^{*} = c_{\mathrm{ML}}^{*} + c_{\mathrm{ML}_2}^{*} + ... + c_{\mathrm{ML}_n}^{*} \qquad (6.8)$$

Details are given the appendix. Thus, defining effective parameters as given by equations (6.2-6.8), the expressions reported for the lability degree and metal accumulation in Chapter 5 can now be used for the MEn complexes.

A noticeable characteristic of the formulation given in Eqns (6.2-6.8) is the dependence of the effective kinetic dissociation constant on the ligand concentration (See Eqn. (6.3)). In general, a mild influence of the ligand concentration on the DGT accumulations is expected since, as explained elsewhere (*4*), in systems where complexes are the dominant metal species most of the metal accumulation comes from dissociation of complexes in the resin domain. Thus, an increase in the ligand concentration cannot shift the steady state towards an increased complex concentration whenever the resin acts as a perfect sink for the metal and free metal concentration is not available in such domain. Conversely, an increase of the ligand concentration in DGT can only reduce the ligand dissociation in the reaction layer in the gel domain leading to a mild impact on the metal accumulation.

However, for ML_n systems, the ligand concentration, c_{L}, influence the "effective" dissociation constant, $k_{\mathrm{d}}^{\mathrm{eff}}$, as indicated in Eqn. (6.3). Thus, the increase of c_{L} should induce a decrease of $k_{\mathrm{d}}^{\mathrm{eff}}$, decreasing the lability degree of the complex and the accumulation of metal in the M En system. This is expected for partially labile complexes, such as Cu-En and Co-En, for which the accumulation depends on $k_{\mathrm{d}}^{\mathrm{eff}}$. The accumulation of labile complexes is independent of the dissociation rate constant and only dependent on the transport so that almost a negligible effect is expected from an increase of c_{L} in such systems.

Figure 6.2 shows the effect of an increase of the En concentration (between 0.005 until 0.1 mol L^{-1}) on the accumulation of the Cd, Co, Zn and Cu in a system with total metal concentration 10^{-5} mol L^{-1}, pH 8 and I 0.1 mol L^{-1}. When En concentration amounts 5 x 10^{-3} mol L^{-1}, Figure 6.2 indicates that almost equal and maximum accumulations of Cd, Cu and Zn are obtained, suggesting that the labile limit is reached. Increasing the En concentration, the accumulations of Cu and Co decrease in agreement to the reduction of the corresponding $k_{\mathrm{d}}^{\mathrm{eff}}$. The increase of the En concentration does not influence the accumulation of Zn and Cd which remain as labile complexes, indicating that the resulting “effective” dissociation rate constant, although decreased, is still high enough for the labile behaviour. However, further increases in the En concentration may have an effect on the Zn and Cd accumulation.

Table 6.3 gathers the % back is these experiments. Negligible values are reported for Zn and Cd according to the labile behaviour of these complexes. For the case of Co and Cu the decrease of the accumulation as En increases is concomitant to an increase in the % back as expected from the decrease of the $k_{\mathrm{d}}^{\mathrm{eff}}$, as explained above.

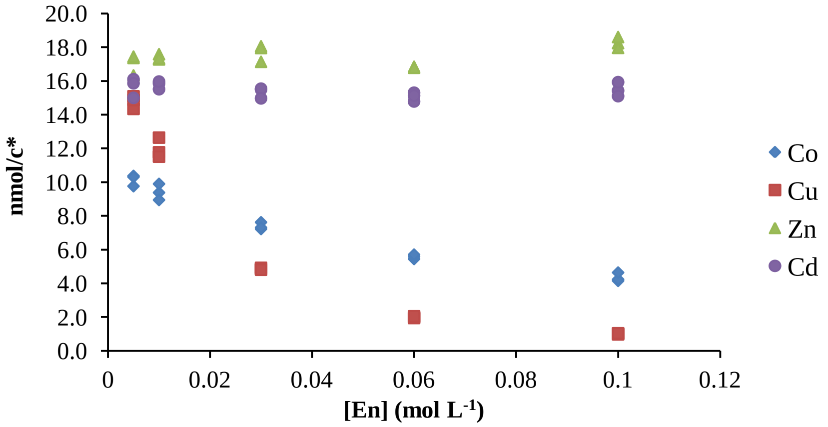

Figure 6.2. DGT accumulations in mols normalised with bulk concentration in a system with 10^{-5} mol L^{-1} Co, Cu, Cd and Zn at pH 8 and varying the concentration of the En ligand (between 0.005 and 0.1 mol L^{-1}).

Table 6.3. Percentage of metal accumulated in the back resin as function of En ligand concentration at pH 8 and *I* 0.1.

En (mol L^{-1})	**% Co back**	**% Cu back**	**% Zn back**	**% Cd back**
0.005	30.52	45.84	3.49	3.28
0.01	31.82	47.37	4.01	4.14
0.03	33.60	50.58	3.71	3.94
0.06	35.91	53.26	4.22	4.31
0.1	39.41	54.99	4.14	4.32

6.4.3. pH effect on metal accumulations in M-NTA systems

In this Section, the combined influence of pH and ionic strength on the metal accumulation in systems with dominant M-NTA complexes is discussed.

This work tries to extend the information on the DGT processes with special focus on evidencing i) if there are competition effects of the proton on the metal binding to the resin sites, ii) if there are H competition effects on the metal binding to the ligand, iii) the influence of these effects on the kinetics of dissociation and metal accumulation and iv) the influence of pH and ionic strength on the electrostatic effects. Three different pHs in the deployment solution, 6, 7.5 and 8 were studied. Reported protonation p*K* values of the chelex sites are $pK_{a,1}$=3.2 and $pK_{a,2}$=8.9 (*13,14*) which indicate that only mild differences due to changes of the electrostatic charge of the chelex can be expected in the pH range studied.

Figure 6.3 depicts the moles of metal accumulated in the DGT resin per unit of concentration of total metal in the bulk solution for all the cases. As can be seen in the figure, at high ionic strength no differences are reported for the labile complexes (CdNTA and CoNTA) with respect to changes in the accumulation due to a pH modification. For the NiNTA, a decrease of the metal accumulation as pH decreases is reported in Fig. 6.3. Since this complex is partially labile, Ni accumulations depend on the rate of dissociation of the NiNTA, thus indicating a decrease of the rate of the dissociation process as pH decreases. As explained in Chapter 5, this process is dominated by dissociation in the resin domain for which a kinetic dissociation constant higher than the value predicted by the Eigen mechanism has been suggested. The metal accumulation by dissociation of the NiNTA in the gel domain was negligible. We can then conclude that the effect of pH reported in Figure 6.3 is due to a decrease of the ligand assisted effect of the resin sites on the NiNTA dissociation in the resin domain as pH decreases. Actually, a decrease of pH should reduce the electrostatic charge of the resin groups which can then exhibit a better interaction with the negatively charged NiNTA complexes in order to facilitate the exchange of the Ni from the NTA to the resin site.

At low *I*, new effects arise: for all the cations, Figure 6.3 indicates that there is a systematic increase of the metal accumulation as pH decreases. This effect can be understood if we recall that, due to the electrostatic repulsion, the negatively charged MNTA species tend to be excluded from penetration in the resin domain at low ionic strength. The effect of the proton can be understood as an effect on the MNTA binding: a decrease of pH will weaken this binding by proton competition for the deprotonated groups of the NTA, this facilitating the dissociation process.

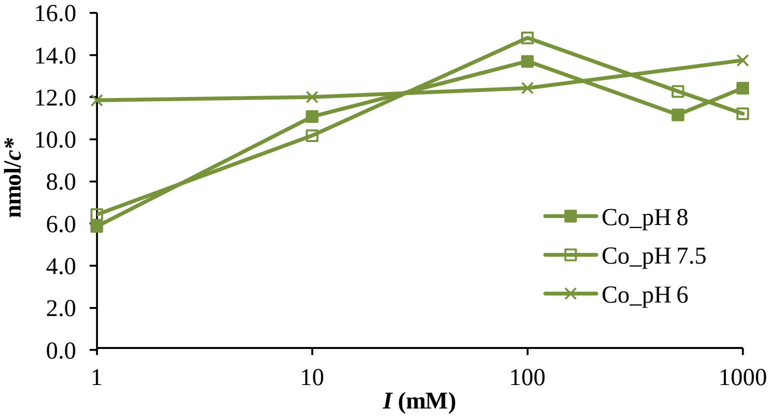

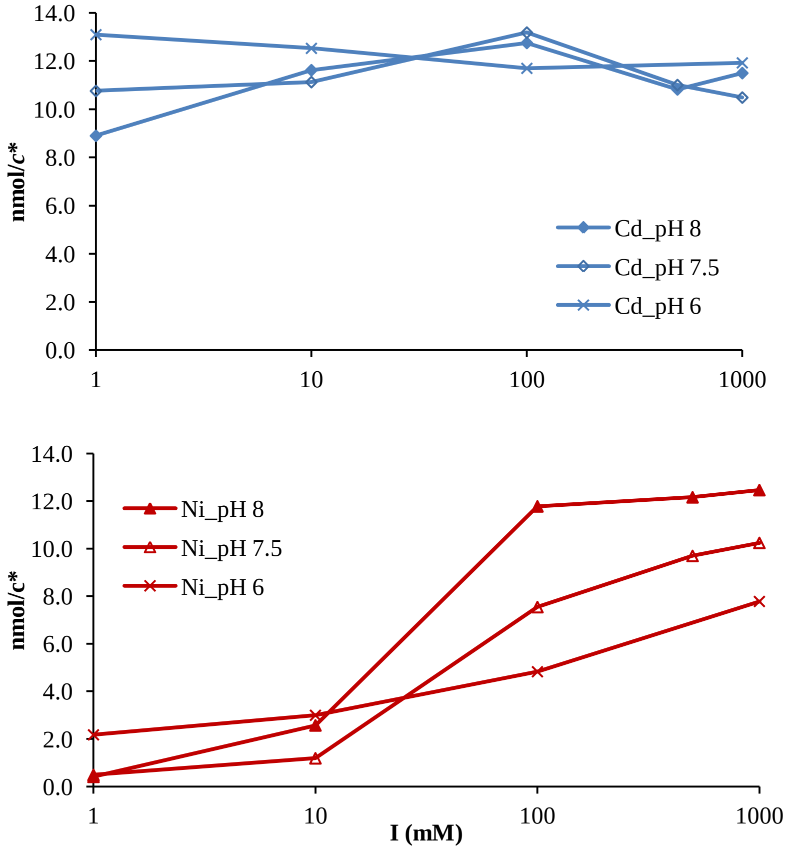

Figure 6.3. Moles of Co (green), Cd (blue) and Ni (red) in the presence of NTA normalised with *c** accumulated by DGT as function of ionic strength. Three different pHs: crosses for pH 6, empty markers for pH 7.5 and filled markers for pH 8. Total NTA concentration of 80 μM and total metal concentrations of 10 μM for Cd and Co and 25 μM for Ni. Lines to connect the experimental measurements are depicted in the figure.

As listed in Table 6.4, at high ionic strengths, the % of metal in the back resin disc increases as pH decreases in agreement with the decrease of the ligand assisted effect above explained.

At low ionic strengths, Table 6.4 indicates that the % back decreases as pH decreases in agreement to the increase of the rate of dissociation of the M-NTA in the gel domain due to the proton competition for the NTA functional groups.

Table 6.4 Percentage of metal accumulated in the back resin as function of pH and I for Co, Ni and Cd. Total NTA concentration of 80 μM and total metal concentrations of 10 μM for Cd and Co and 25 μM for Ni.

***I* (mM)**	**pH**	**% Co back**	**% Ni back**	**% Cd back**
1	6	25.08	48.68	13.96
	7.5	49.53	53.57	33.45
	8	41.52	48.25	23.49
10	6	30.37	51.60	20.84
	7.5	34.34	49.51	17.75
	8	21.48	46.80	10.12
100	6	21.30	48.17	27.86
	7.5	16.21	42.24	18.19
	8	14.15	34.49	17.65
500	7.5	4.67	28.58	6.28
	8	9.01	25.63	12.34
1000	6	22.48	45.67	32.61
	7.5	3.64	20.43	5.48
	8	5.60	12.97	8.06

6.5. Conclusions

The results shown in this chapter evidence the influence of the ionic strength, *I*, on the metal accumulations in the DGT devices. At low *I*, there are electrostatic effects that can increase or decrease the metal accumulation depending on the electrical charge of the partially labile complexes present in the system. As data of this chapter has shown, metal-NTA complexes decrease the metal accumulation as *I* decreases due to the negative charge of these complexes, while metal Ethylenediamine complexes increase the metal accumulation with the same variation of the ionic strength. Electrostatic effects do not take place on non-electrical charged complexes independently of their lability degree and do not lead to noticeable effects on labile complexes independently of their charge since these complexes fully dissociate before reaching the resin domain. This result clearly indicates that the electrostatic effects are due to the charge of the resin sites, a hypothesis suggested after realizing that dissociation of complexes in the resin domain is the main mechanism of metal accumulation in DGT devices.

However, results obtained in this chapter also indicate that the influence of the ionic strength in the metal accumulations also takes place through the influence of the ionic strength on the kinetic dissociation constant of the complexes. While the kinetic dissociation constant of the standard theory of metal complexation, relying on the Eigen mechanism, is independent of the ionic strength, the arising of an extra mechanism in the resin domain based on a ligand assisted effect makes the kinetic dissociation constant dependent on the ionic strength. This dependence goes parallel to the electrostatic effects so that the change in the metal accumulation results from a combined effect of both phenomena: electrostatic Donnan partiotioning and dependence of the kinetic dissociation constant on the ionic strength.

The presence of the ligand assisted effects is supported in the data reported in this chapter by the increase of the %back in the Ni accumulation or the decrease of the %back in the Co accumulation in the MNTA or MEn complexes, respectively. Electrostatic effects cannot increase the back accumulation in the DGT by a simple exclusion of the negatively charged complexes. A similar argument can be used for the M-En data.

M-En complexes also show that labile complexes fully dissociate in the diffusive gel layer and accordingly, the %back is negligible; there is a negligible dependence of the diffusion coefficient on the stoichiometry of the complex; a dominant influence of the ligand assisted dissociation as *I* decreases is reported for Co accumulations, while electrostatic effects seem to be dominant for the Cu accumulation in the Cu-En.

Additionally, the dependence of the lability on the En concentration has also been studied in this chapter. A mild influence of the ligand concentration on the DGT metal accumulations is expected when the resin acts as a perfect sink for the metal. However, for the case of ML_n systems (as is the case of MEn), the ligand concentration influence the “effective” dissociation constant of non-labile complexes decreasing the lability degree of the complex as the ligand concentration increases.

A last Section of this chapter shows the influence of pH on the metal accumulation in systems with MNTA complexes. At high *I* there are no differences on the metal accumulations coming from labile complexes (CdNTA and CoNTA) with pH modifications. Nevertheless, for the NiNTA case there is a surprising decrease of the Ni accumulation as pH decreases explained by a decrease of the ligand assisted effect of the resin sites due to the decrease of the pH.

Conversely, at low *I*, the dissociation process at the gel domain can become dominant due to the electrostatic exclusion of the MNTA complexes from the resin domain. The increase of the metal accumulation as pH decreases can then be explained by the competition of the proton for the deprotonated groups of the NTA which facilitates the dissociation of the metal in the gel domain.

The % of metal in the back resin disc at high *I* increases as pH decreases in the M-NTA system in agreement with the decrease of the ligand assisted effect. At low *I*, the % back decreases as pH decreases in agreement to the increase of metal dissociation in the gel domain.

6.6. References

1. Puy, J.; Uribe, R.; Mongin, S.; Galceran, J.; Cecilia, J.; Levy, J.; Zhang, H.; Davison, W. Lability Criteria in Diffusive Gradients in Thin Films. *Journal of Physical Chemistry A* **2012,** *116*, 6564.

2. Tusseau-Vuillemin, M. H.; Gilbin, R.; Taillefert, M. A dynamic numerical model to characterize labile metal complexes collected with diffusion gradient in thin films devices. *Environ Sci Technol* **2003,** *37*, 1645.

3. Lehto, N. J.; Davison, W.; Zhang, H.; Tych, W. An evaluation of DGT performance using a dynamic numerical model. *Environ Sci Technol* **2006,** *40*, 6368.

4. Uribe, R.; Puy, J.; Cecilia, J.; Galceran, J. Kinetic mixture effects in diffusion gradients in thin films (DGT). *Phys Chem Chem Phys* **2013,** *15*, 11349.

5. Uribe, R.; Mongin, S.; Puy, J.; Cecilia, J.; Galceran, J.; Zhang, H.; Davison, W. Contribution of Partially Labile Complexes to the DGT Metal Flux. *Environ Sci Technol* **2011,** *45*, 5317.

6. Levy, J. L.; Zhang, H.; Davison, W.; Puy, J.; Galceran, J. Assessment of trace metal binding kinetics in the resin phase of diffusive gradients in thin films. *Anal Chim Acta* **2012,** *717*, 143.

7. Mongin, Sandrine; Uribe, Ramiro; Rey-Castro, Carlos; Cecília, Joan; Galceran, Josep; Puy, Jaume Limits of the Linear Accumulation Regime of DGT Sensors. *Environ Sci Technol* **2013,** *47*.

8. Galceran, J.,Puy, J. Interpretation of DGT measurements. Review of a systematic approach. *Environ Chem* **2014.** In press

9. Puy, J.; Galceran, J.; Cruz-González, S.; David, C.; Uribe, R.; Lin, C. H.; Zhang, D.; Davison, W. Measurement of metals using DGT: impact of ionic strength and kinetics of dissociation of complexes in the resin domain. *Anal Chem* **2014,** *86*, 7740.

10. Bravin, M. N.; Garnier, C.; Lenoble, V.; Gerard, F.; Dudal, Y.; Hinsinger, P. Root-induced changes in pH and dissolved organic matter binding capacity affect copper dynamic speciation in the rhizosphere. *Geochim Cosmochim Ac* **2012,** *84*, 256.

11. Davison, W.; Zhang, H. In-Situ Speciation Measurements of Trace Components in Natural-Waters Using Thin-Film Gels. *Nature* **1994,** *367*, 546.

12. Puy, J.; Cecilia, J.; Galceran, J.; Town, R. M.; van Leeuwen, H. P. Voltammetric lability of multiligand complexes: the case of ML2. *J Electroanal Chem* **2004,** *571*, 121.

13. Alberti, G.; Guiso, M. G.; Biesuz, R. Usage of Empore (TM) membrane in alcoholic media for copper(II) distribution studies. *Talanta* **2009,** *79*, 603.

14. Alberti, G.; Biesuz, R. Empore (TM) membrane vs. Chelex 100: Thermodynamic and kinetic studies on metals sorption. *Reactive & Functional Polymers* **2011,** *71*, 588.

Chapter 7

General Discussion

"*Are nanotechnology products safe?"* this is a question frequently asked by scientists, consumers and by the public in general. Nanomaterials possess novel properties but, at the same time, present novel risks. Despite the investment in nanotechnology research, not very much is being spent on investigating its safety. In this work, two ZnO nanoparticles (NPs), 20NP (referring to ZnO NPs with primary particles of 20 nm average size) and 71NP (with an average size of 71nm), have been selected as a model of metal nanoparticles. The fate and impact of nanoparticles in the environment depends on their behavior as a response to environmental variables. The first part of this manuscript is devoted to the study of the stability and characterisation of ZnO nanoparticles in different aqueous media at environmentally relevant conditions. Several important implications concerning nanoparticle aggregation, sedimentation and dissolution are obtained from this study.

By TEM (transmission electron microscopy), the size and morphology of the NPs aggregates has been revealed. In milli-Q water, NPs tend to be stable, forming agglomerates with bigger sizes than those expected for the primary particles. The ultrasonication process is not enough to break the initial agglomerates to the primary particles (of 20 nm and 71 nm). When the NPs are dispersed in background electrolyte (100 mM KNO_3) enriched aqueous media, NPs tend to aggregate forming unstable dispersions with sizes around 1500-2000 nm.

The effect of the background electrolyte (KCl) on the stability of dispersions of NPs has been determined by DLS (Dynamic Light Scattering). The propensity of NPs to aggregate in aqueous environments determines not only their mobility, fate, and persistence, but also their toxicity. The size of the aggregates as a function of time and salt concentration revealed that, with the increase of the ionic strength, NPs tend to aggregate rapidly, reaching aggregate sizes of 2000 nm in 1 h. This behavior has also been described previously in ZnO and other type of metal oxide NPs (*1-4*). With the data obtained by DLS, the attachment efficiency (α) and the critical coagulation concentration (CCC) have been determined. The CCC corresponds to the lowest salt concentration at which diffusion-limited aggregation takes place, as the surface charge of nanoparticles is sufficiently screened to eliminate the energy barrier aggregation. The CCC for 71NP and 20NP were 10.84 mM and 22.72 mM KCl, respectively. Above these KCl concentrations, the aggregation rate remains constant with the increase of the electrolyte concentration.

With the calculated α and the DLS data, the fractal dimension of the aggregates (related with their morphology and structure) has been fitted and the obtained values corresponding to 71NP and 20NP were 1.97 and 2.20, respectively. Once attachment efficiencies and fractal dimensions are determined, the aggregation kinetics of nanoparticles as a function of time can be predicted by applying equation 2.7 (see chapter 2). The EPM (electrophoretic mobility) measurements provide information about the surface charge of dispersed nanoparticles. The effect of ionic strength has been studied by EPM. It has been shown that with the increase of the ionic strength, NPs tend to lose their positive charge, arriving to zero charge at 1000 mM ionic strength and pH 8.

Based on Derjaguin-Landau-Verwey-Overbeek (DLVO) theory, in which van der Waals attraction and electrostatic double layer repulsion between nanoparticles are accounted for, the interactive forces in NPs dispersions in the presence of electrolytes were evaluated. When the ionic strength is small enough to maintain the dispersion stable, the determined DLVO energy profiles show the presence of an energy barrier which inhibited the aggregation process.

When the pH of the dispersions of ZnO NPs was varied within a range of environmentally relevant values (at a fixed ionic strength of 100 mM), minimal effects were observed in the aggregation kinetics, while the EPM values changed from positive to negative by increasing the pH (from pH 7 to 9).

When different concentrations of NPs are employed in the same media conditions (pH and ionic strength), DLS data show an increase on the process aggregation with the increase of NP concentration. This is presumably due to the higher probability of particle collisions (*5*).

Humic acid (HA) is an important environmental compound largely present in natural aqueous media (surface waters, wastewaters, storm waters, etc.) (*2*). For this reason, the interactions between NPs and natural organic matter are of prime importance in understanding NPs fate and behavior. Humic acid has been selected as model of dissolved organic matter. The effect of the presence of HA on the behavior of ZnO NPs has also been characterized. Firstly, the adsorption of HA onto NPs was studied by UV-Vis spectrometry, which allowed to quantity the humic acid remaining in solution after the adsorption onto nanoparticles. Adsorption isotherms were plotted using the experimental data. These isotherms were fitted with the Langmuir adsorption model. The observed behavior agreed with previous literature reports on the adsorption of HA onto ZnO NPs (*1*) and other metal oxide nanoparticles (*6*-

8). From the fitting results, the $\Gamma_{\max}$ and K parameters were determined for each kind of nanoparticle. The amount of HA adsorbed onto 20NP was larger than that in 71NP, which can be explained by the larger specific surface area of the smaller NP and the increase in the porosity of the aggregates, as it was confirmed by N_2-BET analysis.

The influence of pH in the adsorption of HA onto NPs was studied. In all the tested pH range (between 7.4 and 8.8), adsorption isotherms follow the Langmuir isotherm model. The adsorption of HA increases with the decrease of the pH as ZnO NP are positively charged at these pH values (see chapter 2), enhancing the adsorption of the negatively charged HA due to electrostatic attraction (*9*). Conversely, at pH above 8, adsorption is unfavored by electrostatic repulsion between HA molecules and the negatively charged ZnO surface. This behavior was also reported in the literature for other oxides (*10-13*).

By comparing the IR spectra of pristine ZnO nanoparticles, pure HA, and HA coated NPs, it has been determined that, apart from electrostatic interactions, some chemical interactions between HA and ZnO surfaces may also exist.

The hydrodynamic diameter of the aggregates of ZnO coated with HA was studied by DLS. The adsorption of HA onto ZnO NPs provides negative charge to the aggregates stabilizing the dispersions of NPs in aqueous solution. Consequently, the presence of HA stabilized, or at least reduced, the aggregation rate of nanoparticles. Only at the lowest studied pHs and lowest HA concentration, NPs tend to aggregate due to the higher compaction of the HA at these pHs, which may induce a "bridging effect" among surrounding aggregates.

EPM measurements of the ZnO dispersions in presence of HA were performed. Results confirm the adsorption of HA and the change in the charge from positive, in absence of HA, to negative due to the negatively charged HA, which stabilizes the dispersion by electric repulsions.

Plunge-freezing TEM was used in order to examine the stabilization of the dispersions of NPs in the presence of HA. Plunge-freezing TEM allows evaluating the aggregation state of dispersions avoiding artifacts derived from the drying process involved in conventional TEM (*14*). Micrographs show the stabilization of NPs aggregate sizes at around 200 nm.

In the presence of HA, the solubility of NPs showed the same behavior than expected for the dispersions of NPs in the same conditions of ionic strength and pH but in absence of HA. Experimental measurements of the remaining dissolved Zn in solution after centrifugation agree with the theoretical values determined by the speciation program Visual MINTEQ using the generic NICA-Donnan parameters for HA. Nevertheless, at pH 7.4, experimental and theoretical data show differences presumably due to an incomplete dissolution process (*15*).

Sedimentation of aggregates of ZnO NPs of different sizes was studied by adding HA to the NPs dispersions at different aggregation times. This maintained stable the aggregates size by electrostatic repulsion and allowed determining the sedimentation rates as a function of the size of the aggregates. The application of a theoretical model based on the Stokes law was used to fit the sedimentation profiles of the aggregates. These results allow knowing the time scale in which nanoparticle aggregates settle in aqueous media, information of great relevance to toxicity studies.

The adverse effects of ZnO nanoparticles come from their specific properties related with the small size, but an important role of the release of free ions due to its relatively high solubility can also be expected. For this specific reason, the availability of the dissolved fraction of ZnO NPs in different aqueous solutions was studied. The Diffusive Gradients in Thin films (DGT) (*16,17*) is an analytical technique that measures the available metal fraction present in a solution. The DGT device has a binding layer covered with a diffusive gel layer and protected with a filter membrane. Metal ions diffuse thorough the filter and gel and react with the binding layer. Here, this technique has been employed to determine the available metal fraction released from ZnO NPs. The experimental measurement of the available dissolved fraction (which includes free ions plus the labile metal complexes present in the solution) in presence of the solid nanoparticles is challenging due to the small size of the particles.

The performance of the DTG technique in measuring the nanoparticle dissolution was extensively tested. Smaller nanoparticles show a greater extent of dissolution (*18*). This fact has also been observed in the DGT experimental data obtained in systems with two different sized ZnO NPs, of 20 nm and 71 nm.

The metal flux measured in presence of complexing pH buffers (Tris) was higher than that measured when a non complexing pH buffer (MOPS) was employed. This additional flux has to be taken into account in the solubility measurements.

The effect of the pH on the solubility of ZnO NPs showed that the highest DGT accumulations take place at the lowest pH (7.58), in agreement with the solubility of ZnO NPs determined by other techniques such as AGNES and ICP-OES. However, the worst reproducibility of the measurements was observed at the highest PHs, where the penetration of primary particles or small aggregates into the DGT device and their subsequent dissolution would have a more noticeable effect. Different hydrogel layers (open pore and restricted pore gels) and pore sizes of membrane filters (0.1 and 0.45 µm) where employed. Nevertheless, there was no improvement in the DGT measurements at the highest pHs. The nanoparticle dispersions were also filtered and/or centrifuged and the remaining metal filtered fractions and/or supernatants were measured by ICP-OES. The measurements of those fractions agree with the available fraction measured by DGT (c_{DGT}), except in presence of partially labile complexes, were DGT yielded values below the filtered or centrifuged fractions, suggesting that total solubility measurements could overestimate the metal availability in complex media. This fact demonstrates the importance of the use of the DGT technique for the measurement of the available metal fraction released from NPs compared with other conventional methods.

The second part of this thesis is devoted to the interpretation of the accumulation of metals in DGT devices in presence of charged partially labile metal complexes at different ionic strengths.

c_{DGT} measures the available metal concentration but, in fact, this is an effective property defined from the measurement of the metal accumulation after some deployment time. Experimental results indicate a strong decrease of the metal accumulation as ionic strength decreases for Ni while the decrease is almost negligible for Cd in a system with excess of the NTA ligand. An explanation of this behavior has been reached by assuming an electrostatic repulsion of the negatively charged complexes by the negatively charged resin sites. This repulsion increases as ionic strength decreases and is more effective over partially labile species due to the important penetration of these species in the resin domain.

Secondly, it is shown that theoretical Eigen predictions did not fit the experimental data. This is explained by ligand assisted dissociation of the complexes in the resin domain. Due to this effect, metal accumulation in DGT devices is higher than expected from the newly calculated dissociation constants.

Additional experiments with positively charged complexes have allowed corroborating the existence of electrostatic effects since M-Etdiam complexes, which are positively charged, showed an increase of the metal accumulation as the ionic strength decreases.

A last check was addressed to modify the charge by changing the pH. The obtained results indicate that the accumulation increases with pH, a result that can be understood as due to the increasing efficiency of the ligand assisted effect. At low pH, pH 6 in the case of NiNTA, metal accumulation at low ionic strength increases, a behavior that can be unsderstood as due to the dominant effect of the protons on the NiNTA dissociation in the gel domain.

References

1. Zhou, D. X.; Keller, A. A. Role of morphology in the aggregation kinetics of ZnO nanoparticles. *Water Res* **2010,** *44, 2948*.

2. Zhang, Y.; Chen, Y. S.; Westerhoff, P.; Crittenden, J. Impact of natural organic matter and divalent cations on the stability of aqueous nanoparticles. *Water Res* **2009,** *43*, 4249.

3. French, R. A.; Jacobson, A. R.; Kim, B.; Isley, S. L.; Penn, R. L.; Baveye, P. C. Influence of Ionic Strength, pH, and Cation Valence on Aggregation Kinetics of Titanium Dioxide Nanoparticles. *Environ Sci Technol* **2009,** *43*.

4. Zhang, Y.; Chen, Y. S.; Westerhoff, P.; Hristovski, K.; Crittenden, J. C. Stability of commercial metal oxide nanoparticles in water. *Water Res* **2008,** *42*, 2204.

5. Baalousha, M. Aggregation and disaggregation of iron oxide nanoparticles: Influence of particle concentration, pH and natural organic matter. *Sci Total Environ* **2009,** *407*, 2093.

6. Pettibone, J. M.; Cwiertny, D. M.; Scherer, M.; Grassian, V. H. Adsorption of organic acids on TiO2 nanoparticles: Effects of pH, nanoparticle size, and nanoparticle aggregation. *Langmuir* **2008,** *24*, 6659.

7. Gu, B. H.; Schmitt, J.; Chen, Z. H.; Liang, L. Y.; Mccarthy, J. F. Adsorption and Desorption of Natural Organic-Matter on Iron-Oxide - Mechanisms and Models. *Environ Sci Technol* **1994,** *28*, 38.

8. Lin, D. H.; Ji, J.; Long, Z. F.; Yang, K.; Wu, F. C. The influence of dissolved and surface-bound humic acid on the toxicity of TiO2 nanoparticles to Chlorella sp. *Water Res* **2012,** *46*, 4477.

9. Ramos-Tejada, M. M.; Ontiveros, A.; Viota, J. L.; Duran, J. D. G. Interfacial and rheological properties of humic acid/hematite suspensions. *J Colloid Interf Sci* **2003,** *268*.

10. Chekli, L.; Phuntsho, S.; Roy, M.; Shon, H. K. Characterisation of Fe-oxide nanoparticles coated with humic acid and Suwannee River natural organic matter. *Sci Total Environ* **2013,** *461*, 19.

11. Illes, E.; Tombacz, E. The role of variable surface charge and surface complexation in the adsorption of humic acid on magnetite. *Colloid Surface A* **2003,** *230*, 99.

12. Illes, E.; Tombacz, E. The effect of humic acid adsorption on pH-dependent surface charging and aggregation of magnetite nanoparticles. *J Colloid Interf Sci* **2006,** *295*, 115.

13. Boily, J. F.; Persson, P.; Sjoberg, S. Benzenecarboxylate surface complexation at the goethite (alpha-FeOOH)/water interface: II. Linking IR spectroscopic observations to mechanistic surface complexation models for phthalate, trimellitate, and pyromellitate. *Geochim Cosmochim Ac* **2000,** *64,* 3453.

14. Hondow, N.; Brydson, R.; Wang, P. Y.; Holton, M. D.; Brown, M. R.; Rees, P.; Summers, H. D.; Brown, A. Quantitative characterization of nanoparticle agglomeration within biological media. *J Nanopart Res* **2012,** *14,* 977.

15. Bian, S. W.; Mudunkotuwa, I. A.; Rupasinghe, T.; Grassian, V. H. Aggregation and Dissolution of 4 nm ZnO Nanoparticles in Aqueous Environments: Influence of pH, Ionic Strength, Size, and Adsorption of Humic Acid. *Langmuir* **2011,** *27,* 6059.

16. Davison, W.; Zhang, H. In-Situ Speciation Measurements of Trace Components in Natural-Waters Using Thin-Film Gels. *Nature* **1994,** *367*, 546.

17. Zhang, H.; Davison, W. Performance-Characteristics of Diffusion Gradients in Thin-Films for the in-Situ Measurement of Trace-Metals in Aqueous-Solution. *Anal Chem* **1995,** *67*, 3391.

18. Mudunkotuwa, I. A.; Rupasinghe, T.; Wu, C. M.; Grassian, V. H. Dissolution of ZnO Nanoparticles at Circumneutral pH: A Study of Size Effects in the Presence and Absence of Citric Acid. *Langmuir* **2012,** *28*.

Chapter 8

General Conclusions

In this thesis, the availability of metals in systems of environmental interest has been investigated. Part of the work has focused on the study of the behavior of dispersions of ZnO nanoparticles (NPs) in different media conditions, providing a context for understanding the stability of ZnO NPs in aqueous natural environments. The second part consists in the development of the analytical technique Diffusive Gradient in Thin films (DGT), for the measurement of the available metal fraction released from nanoparticles in aqueous dispersions and the metal flux measured from the contribution of metal complexes.

Even though detailed conclusions from the present work have been included in each chapter, the main conclusions can be summarized as follows:

1. The aggregation, sedimentation and solubilisation of nanoparticles are critic factors that affect both the fate of NPs in natural aqueous media, and its stability in biological fluids and the toxicity in cell culture.
2. Thorough characterization results revealed that the pH of the dispersions of ZnO NPs (in the range between 7 and 9) modify the surface charge of the nanoparticles, but it is not enough to make a change in the aggregation process. As the pH decreases, ZnO nanoparticles tend to charge positively, whereas with the increase of pH nanoparticles tend to become negatively charged. Because of the relatively high ionic strength employed (0.1 mol L^{-1} KCl), the charge of the nanoparticles is insufficient to prevent aggregation and stabilize the dispersions.

3. However, changes in the ionic strength of the media, affect both the surface charge of the nanoparticles and the aggregation process. The extent of aggregation for nano-ZnO increases with the increase of the ionic strength. At low ionic strengths ($I < 10^{-3}$ M), positively charged nanoparticles remains stable. In all the cases, the aggregation behavior is in agreement with the trends expected from the DLVO theory.
4. Particle concentration changes the collision frequency between particles. The increase in the NPs concentration increases the aggregation. With a simple model of aggregation the aggregation kinetics of nanoparticles at different concentrations has been determined.
5. NOM is an important factor that affects the stability of nanoparticles in water. In the presence of humic acid (HA), the aggregation process of ZnO NPs is inhibited for a given ionic strength and pH, above a critical concentration of humic acid. The negatively charged HA is adsorbed onto the surface of ZnO nanoparticles describing a Langmuir isotherm model enhancing the surface charge and stability.
6. The deposition rate of ZnO nanoparticles is highly sensitive to the sizes and fractal dimension of the NPs aggregates. HA has been used to stabilize the nano-ZnO aggregates in different sizes and by the implementation of a sedimentation model which takes into account the sizes, the behavior of the aggregates have been described, allowing determining the settling of NPs in different conditions. The

dissolution trend of nano-ZnO with the addition of humic acid is similar to the expected for nano-ZnO dispersions in the same conditions but in absence of HA.

7. In order to study the available metal fraction released from ZnO NPs, the DGT technique has been implemented.

a) DGT devices have been successfully applied for the determination of the Zn soluble fraction at pH range between 7.5 and 8.1. The results have shown an agreement with those predicted by speciation programs as Visual MINTEQ and by filtration and centrifugation of dispersions for the separation of the soluble fraction from NPs.

b) At pHs above 8.2, where the solubility of ZnO NPs is relatively low, the reproducibility of the DGT measurements showed a deterioration. These results indicate the possible penetration and solubilization of primary particles and/or small aggregates which contribute to the measurements.

c) The metal measured has shown an increase with the decrease of the pH as predicted by the solubility of ZnO NPs.

d) Smaller ZnO nanoparticles (20 nm) show a greater extent of dissolution compared to larger particles (71 nm) confirming the dependence of the solubility on the particle size.

8. The deployment of the DGT devices in low ionic strength solutions has been deeply studied. A reduction of the metal accumulation as ionic strength decreases has been found when negatively charged metal species are dominant while increasing metal accumulations have been found in the opposite case, i. e., when positively charged metal species are dominant. These effects are more important for partially labile complexes in comparison to the labile ones. Ligand assisted dissociation in the resin disc and Donnan effects have been used to understanding these measurements,

a) Ligand assisted dissociation allows higher kinetic dissociation constants for complexes in the resin domain in comparison to values predicted from the Eigen mechanism. Lability of complexes as measured by DGT is then increased.

b) Electrostatic factors arise between the negatively charged resin sites and electrically charged metal species.

c) Free metals are almost unaffected by ionic strength since they minimally penetrate to the resin disc, being bound at the resin-gel interface.

9. A numerical model that considers Donnan potentials derived from the resin charges, the screening of the background electrolyte and the transport and complexation reactions of the chemical species has been developed. The experimental results for the M-NTA system are accurately predicted. This new understanding provides a unified explanation for several data sets obtained at low ionic strength.

En esta tesis se ha investigado la disponibilidad de metales los sistemas de interés ambiental. Parte del trabajo se ha centrado en el estudio del comportamiento de dispersiones de nanopartículas (NPS) de ZnO en medios acuosos con distintas condiciones, proporcionando un contexto para la comprensión de la estabilidad de ZnO NPs en medios acuosos naturales. La segunda parte consiste en el desarrollo de la técnica analítica *Diffusive Gradient in Thin films* (DGT), para la medida de la fracción de metal disponible liberado por las nanopartículas en dispersiones acuosas y el flujo de metal medido de la contribución de complejos metálicos.

A pesar de que las conclusions del presente trabajo se han incluido en cada capítulo de forma detallada, las principales conclusiones se pueden resumir de la siguiente manera:

1. La agregación, sedimentación y solubilidad de las nanopartículas son factores críticos que afectan tanto el destino de NPs en medios acuosos naturales como a su estabilidad en los fluidos biológicos y la toxicidad en cultivos celulares.
2. A través de los resultados de la caracterización se ha observado que el pH de las dispersiones de ZnO NPs (en el rango entre 7 y 9) modifica la carga superficial de las nanopartículas, pero no es suficiente para provocar un cambio en el proceso de agregación. A medida que el pH disminuye, las nanopartículas de ZnO tienden a cargarse positivamente, mientras que con el aumento de pH las nanopartículas tienden a hacerlo negativamente. Debido a que la fuerza iónica empleada fue relativamente alta (0,1 mol L^{-1} KCl), la

carga de las nanopartículas fue insuficiente para prevenir la agregación y estabilizar las dispersiones.

3. Sin embargo, los cambios en la fuerza iónica del medio, afectan tanto a la carga superficial de las nanopartículas como al proceso de agregación. La agregación de las nanopartículas de ZnO aumenta con el aumento de la fuerza iónica. A bajas fuerzas iónicas ($I < 10^{-3}$ M), las nanopartículas se mantienen estables con carga positiva. En todos los casos, el comportamiento de agregación concuerda con las tendencias esperadas de la teoría DLVO.
4. La concentración de partículas modifica la frecuencia de colisión entre las partículas. El aumento en la concentración NPs aumenta la agregación. Con un modelo simple de agregación la cinética de agregación de las nanopartículas a diferentes concentraciones ha sido determinada.
5. DOM es un factor importante que afecta la estabilidad de las nanopartículas en los medios acuosos. En presencia de ácido húmico (HA), el proceso de agregación de NPs de ZnO es inhibido, a una fuerza iónica y pH dado, por encima de una concentración crítica de ácido húmico. El HA cargado negativamente se adsorbe sobre la superficie de las nanopartículas de ZnO que describiendo un modelo de isoterma Langmuir.
6. La velocidad de sedimentación de nanopartículas de ZnO es muya sensible a los tamaños y dimensiones fractales de los agregados de NPs. El HA se ha utilizado para estabilizar los agregados nanopartículas de ZnO en diferentes tamaños y por la aplicación de

un modelo de sedimentación que tiene en cuenta los tamaños, se han descrito el comportamiento de los agregados, lo que permite determinar la sedimentación de NPs en diferentes condiciones. La tendencia a la disolución de las nanopartículas de ZnO con la adición de ácido húmico es similar a la esperada para dispersiones de nanopartículas de ZnO en las mismas condiciones pero en ausencia de HA.

7. La técnica DGT se ha aplicado con el fin de estudiar la fracción de metal disponible liberado por las NPs de ZnO,
    a) Los sensores DGT se han empleado con éxito para la determinación de la fracción soluble de Zn en el rango de pH entre 7,5 y 8,1. Los resultados han mostrado concordancia con los predichos por programas de especiación como es el Visual MINTEQ y también por filtración y centrifugación de las dispersiones para la separación de la fracción soluble de NPs.
    b) A pHs por encima de 8,2, donde la solubilidad de ZnO NPs es relativamente baja, la reproducibilidad de las medidas con DGT mostró un deterioro. Estos resultados indican la posible penetración y la solubilización de partículas primarias y / o pequeños agregados que contribuyen a las medidas.
    c) El metal medido ha mostrado un aumento con la disminución del pH como se predice por la solubilidad de las NPs de ZnO.
    d) Las nanopartículas de ZnO de menor tamaño (20 nm) muestran un mayor grado de disolución en comparación con las partículas de mayor tamaño (71 nm) confirmando que la solubilidad depende del tamaño de partícula.

8. Se ha estudiado detalladamente el empleo de los dispositivos DGT en soluciones con baja fuerza iónica. Se ha encontrado una reducción de la acumulación de metales a medida que disminuye la fuerza iónica cuando las especies de complejo metal ligando son dominantes y poseen carga negativa mientras que en el caso contrario se ha observado un aumento de la acumulación de metales, es decir, cuando los complejos metálicos poseen con carga positiva. Estos efectos son más importantes para los complejos parcialmente lábiles en comparación con los lábiles. La disociación asistida por ligando en el disco de resina y los efectos de Donnan se han utilizado para explicar estos resultados.

a) La disociación asistida por ligando permite el aumento de las constantes cinéticas de disociación de los complejos en la capa de resina en comparación con los valores predichos por el mecanismo de Eigen. Las medidas de labilidad de los complejos medidos por DGT de esta forma se verán aumentadas.

b) Los factores electrostáticos surgen entre la cargada negativa de la resina y la carga negativa de las especies metálicas cargadas eléctricamente.

c) Los metales libres no se ven afectados por la fuerza iónica ya que penetran mínimamente en el disco de resina, se unen en la interfase resina-gel.

9. Se ha desarrollado un modelo numérico que considera los potenciales Donnan derivados de las cargas de la resina, el apantallamiento del electrolito de fondo y las reacciones de transporte y complejación de las especies químicas. Los resultados experimentales para el sistema M-NTA se predicen con precisión. Esta nueva comprensión ofrece una explicación unificada para varios conjuntos de datos obtenidos a baja fuerza iónica.